Cranfield University

Panagiotis Giannakakis

Design space exploration and performance modelling of advanced turbofan and open-rotor engines

SCHOOL OF ENGINEERING

EngD Thesis

Cranfield University
School of Engineering
EngD Thesis

2013

Panagiotis Giannakakis

Design space exploration and performance modelling of advanced turbofan and open-rotor engines

Supervisor: Dr. P. Laskaridis & Prof. R. Singh

This thesis is submitted in partial fullfillment of the requirements for the degree of Doctor of Engineering

This work is dedicated to
all the members of my family,
and to my patient Marie.

Acknowledgements

First of all, I would like to thank my supervisor Dr. Panagiotis Laskaridis for all the time, ideas and effort he has put in my project. Our long discussions instigated many of the themes presented here.

I would like to express my gratitude to Prof. Riti Singh for providing his insightful views throughout the course of this project. I also wish to thank Prof. Pericles Pilidis for teaching me gas turbine performance, for his trust and his advice in technical and personal level.

The financial support of the Boeing Commercial Aircraft Company and the invaluable advice of its engineers are gratefully acknowledged.

I am very thankful to Prof. Anestis Kalfas, who was always there to support, advise and motivate me. I wish to extend my gratitude to all the teachers that inspired and shaped me as an engineer and person throughout my studies.

Special thanks to all the staff of the Cranfield University Library for providing us with such a high quality of services. Thanks are also due to all the staff of the Department of Power and Propulsion for their valuable services and support.

Thanks are due to Konstantinos Kyprianidis for our interesting and stimulating discussions on the topics of engine performance, simulation and preliminary design. I owe a lot to Periklis Lolis, who provided his preliminary design and weight code, and dedicated a lot of time and patience to help me realise the turbofan design exploration study. The propeller part of this thesis would not exist without the invaluable contributions of Georgios Iosifidis and Ioannis Goulos, who embarked with me in this exciting trip in the fundamentals of propeller aerodynamics. I would also like to thank Jan Janikovic, Georgios Doulgeris and Theoklis Nikolaidis for our fruitful and interesting interactions, within the code development activities of the department.

I had the chance to work with many MSc students and gain through them much experience and knowledge. Many thanks to Egoitz Rodriguez, Chinmay Beura, Iker Manzanedo, Devaiah Nalianda, Benjamin Bruni, Alfonso Ortal Sevilla, Ilektra Kanaki, Jessica Gridel, Alicia Sanchez-Ortega and Steve Owen.

Many thanks to my colleagues Devaiah, Domenico, Eduardo and my tolerant officemate Alice, for sharing our thoughts and worries, and for making this personal research journey a bit less lonely.

I owe my fullest gratitude to my housemates Pavlos, Alekos, Peri, Giorgos and Fanis for being a real family to me and for all the moments we shared together. A big thank you to my friends in Cranfield, Asteris, Avgoustinos, Elias and Yiannis for lightening up my life there and for giving me so many nice memories. Because of my housemates and friends I will always think about the time in Cranfield in a sweet nostalgic tone.

I am deeply grateful to my old friends Sotos, Dionysis, Alexandros, Apostolis, and Teo for honouring me all these years with their support, camaraderie and care.

Finally, special thanks to my colleagues in YYPV, Snecma, for their warm welcome and for their understanding during the writing up of this thesis.

Abstract

This work focuses on the current civil engine design practice of increasing overall pressure ratio, turbine entry temperature and bypass ratio, and on the technologies required in order to sustain it. In this context, this thesis contributes towards clarifying the following gray aspects of future civil engine development:

- the connection between an aircraft application, the engine thermodynamic cycle and the advanced technologies of variable area fan nozzle and fan drive gearbox.
- the connection between the engine thermodynamic cycle and the fuel consumption penalties of extracting bleed or power in order to satisfy the aircraft needs.
- the scaling of propeller maps in order to enable extensive open-rotor studies similar to the ones carried out for turbofan engines.

The first two objectives are tackled by implementing a preliminary design framework, which comprises models that calculate the engine uninstalled performance, dimensions, weight, drag and installed performance. The framework produces designs that are in good agreement with current and near future civil engines. The need for a variable area fan nozzle is related to the fan surge margin at take-off, while the transition to a geared architecture is identified by tracking the variation of the low pressure turbine number of stages. The results show that the above enabling technologies will be prioritised for long range engines, due to their higher overall pressure ratio, higher bypass ratio and lower specific thrust. The analysis also shows that future lower specific thrust engines will suffer from higher secondary power extraction penalties.

A propeller modelling and optimisation method is created in order to accomplish the open-rotor aspect of this work. The propeller model follows the lifting-line approach and is found to perform well against experimental data available for the SR3 prop-fan. The model is used in order to predict the performance of propellers with the same distribution of airfoils and sweep, but with different design point power coefficient and advance ratio. The results demonstrate that all the investigated propellers can be modelled by a common map, which separately determines the ideal and viscous losses.

Contents

List of Figures

List of Tables

Nomenclature

Roman Symbols

A	blade element surface $[m^2]$
A_f	fan inlet area $[m^2]$
B	propeller blade pitch angle [degrees]
C_D	propeller blade element drag coefficient
$C_{D,a}$	afterbody drag coefficient
$C_{D,c}$	nacelle cowl drag coefficient
C_{Df}	propeller blade element friction drag coefficient
C_{Dpr}	propeller blade element pressure drag coefficient
C_F	circulation solution process total correction factor
C_{FL}	circulation solution process lift correction factor
$C_{F\phi}$	circulation solution process angle of attack correction factor
C_{FV}	circulation solution process velocity correction factor
c	propeller blade element chord length [m]
C_L	propeller blade element lift coefficient
C_{La}	propeller blade element lift coefficient slope
C_P	propeller power coefficient
C_T	propeller thrust coefficient
C_V	nozzle velocity coefficient

D	used as scalar denotes the propeller tip diameter [m]
d_a	afterbody diameter [m]
d_c	nacelle cowl diameter [m]
D_a	afterbody drag [N]
D_c	nacelle cowl drag [N]
D_n	total nacelle drag [N]
$\vec{D}$	drag [N]
$\vec{e}$	unit vector
$\vec{F}$	blade element total force vector
$\vec{GC}^*$	Biot-Savart geometric coefficient vector corresponding to the total circulation of a blade element
$\vec{GC}$	Biot-Savart geometric coefficient vector
g_w	wake azimuthal angle grading parameter
h	specific enthalpy [J/kg]
h_0	total specific enthalpy [J/kg]
$(h/t)_f$	fan inlet hub/tip ratio
$(h/t)_{lpt}$	low-pressure turbine inlet hub/tip ratio
J	propeller advance ratio
K_r	Walsh and Fletcher range factor [kg/N]
L	propeller blade element lift force [N]
L_a	afterbody length [m]
L_b	bypass duct inner line length [m]
L_c	nacelle cowl length [m]
$\frac{L}{D}$	length to diameter ratio
M	Mach number

M_e	Engine weight [kg]
M_h	propeller blade helical Mach number
m_{nac}	nacelle weight [kg]
d	cartesian distance
N	number of blade elements
n	propeller rotational speed [1/s]
N_B	number of propeller blades
$N_{lpt,stages}$	number of low-pressure turbine stages
N_{WP}	number of points on a wake filament
N_{WT}	number of wake turns
P	power [W]
P_{cp}	core power [W]
P_{cp}^*	core power after the extraction of off-takes [W]
P_{po}	shaft power off-takes extracted [W]
PR_{bs}	booster pressure ratio
PR_f	fan pressure ratio
PR_{hpc}	high-pressure compressor pressure ratio
Q	torque $[Nm]$
$r_{f,t}$	fan inlet tip radius [m]
$r_{lpt,m}$	low-pressure turbine inlet mean radius [m]
$r_{lpt,t}$	low-pressure turbine inlet tip radius [m]
$\vec{r}_{BE,(i)}$	i^{th} blade element position vector
T	thrust [N]
T_1	fan inlet total temperature [K]

T_2	booster inlet total temperature [K]
T_3	high-pressure compressor outlet temperature [K]
$U_{f,t}$	fan inlet tip blade speed [m/s]
$U_{lpt,m}$	low-pressure turbine inlet mean blade speed [m/s]
$\vec{U}$	vector of free stream velocity seen by a blade element
$\vec{u}$	vector of nacelle induced velocity seen by a blade element
V_0	free stream velocity [m/s]
V_c	cold jet velocity [m/s]
$V_{f,ax}$	fan inlet axial velocity [m/s]
V_h	hot jet velocity [m/s]
$V_{lpt,ax}$	low-pressure turbine inlet axial velocity [m/s]
V_m	mean jet velocity [m/s]
$V_{f,rel,t}$	fan inlet tip relative velocity [m/s]
$\vec{V}$	vector of total velocity seen by a blade element
W_{25}	high-pressure compressor inlet mass flow [kg/s]
W_b	bleed air mass flow [kg/s]
W_{bs}	booster inlet mass flow [kg/s]
W_{cl}	cooling flow [kg/s]
W_c	cold, bypass stream mass flow rate [kg/s]
W_f	fan inlet mass flow [kg/s]
W_{ff}	fuel flow [kg/s]
W_h	hot, core stream mass flow rate [kg/s]
W_{in}	engine inlet mass flow [kg/s]
W_{lpt}	low-pressure turbine inlet mass flow [kg/s]

X	X coordinate value
Y	Y coordinate value
Z	Z coordinate value

Greek Symbols

α	unit vector component coefficient or *cn* plane angle of attack [degrees]
β	ratio of bleed air mass flow upon core mass flow
$\Delta\beta$	blade geometry station twist angle [degrees]
Δh_b	bleed air enthalpy increase through the core [J/kg]
Δh_{bs}	booster enthalpy difference [J/kg]
Δh_{cp}	enthalpy produced by the core [J/kg]
Δh^*_{cp}	enthalpy produced by the core after the extraction of off-takes [J/kg]
Δh_f	fan enthalpy difference [J/kg]
Δh_{lpt}	low-pressure turbine enthalpy difference [J/kg]
$\Delta p/p$	relative total pressure loss [%]
η_0	engine total efficiency
η^*_0	engine total efficiency after the extraction of off-takes
η_{co}	engine core efficiency
η^*_{co}	engine core efficiency after the extraction of off-takes
η_f	fan isentropic efficiency
$\eta_{is,t}$	turbine isentropic efficiency
η_{lpt}	low-pressure turbine isentropic efficiency
$\eta_{p,bs}$	booster polytropic efficiency
$\eta_{p,c}$	compressor polytropic efficiency
$\eta_{p,f}$	fan polytropic efficiency

η_{pr}	engine propulsive efficiency
η_{pr}^{*}	engine propulsive efficiency after the extraction of off-takes
η_{prop}	propeller efficiency
η_{tr}	engine transmission efficiency
η_{tr}^{*}	engine transmission efficiency after the extraction of off-takes
Γ	Circulation
γ	heat capacity ratio
κ_i	interference drag factor
κ_{nac}	nacelle weight per square meter of surface $[kg/m^2]$
Λ	blade geometry station sweep angle [degrees]
Ω	propeller rotational speed [rad/s]
ω_{lp}	low-pressure spool rotational speed [rad/s]
ϕ_{az}	wake element azimuthal angle [rad]
ϕ_h	blade element helix angle [rad]
ρ	density $[kg/m^3]$
ρ_f	fan inlet density $[kg/m^3]$
ρ_{lpt}	low-pressure turbine inlet density $[kg/m^3]$
θ_B	blade element free velocity cn plane angle of attack [degrees]
V_∞	propeller axial free stream velocity [m/s]

Subscripts

0	used with enthalpy denotes the total conditions
3	high pressure compressor outlet station
4	combustor outlet station
a	air

B	corresponding to bound vorticity
c	chordwise component
f	free velocity component including free stream and nacelle induced velocities
g	gas products
i	blade element index
j	index of a wake filament point
k	trailing vortex filament radial index
l	propeller blade number index
m	mean or mean-line value
n	normalwise component
op	optimum
s	spanwise component
t	circulation solution process iteration number
TR	corresponding to trailing vorticity

Acronyms

ACARE	Advisory Council for Aeronautics Research in Europe
AF	propeller blade activity factor
BE	blade element
BPR	bypass ratio
far	fuel air ratio
FB	fuel burn [kg]
FCV	fuel calorific value [J/kg]
FPR	fan pressure ratio
HPC	high-pressure compressor

HP	high-pressure
HPT	high-pressure turbine
LP	low pressure
LPT	low pressure turbine
mCR	mid-cruise
OPR	overall pressure ratio
PR	pressure ratio
SFC	specific fuel consumption [kg/N/s]
SLS	sea level static
ST	specific thrust at ToC (unless otherwise specified) [m/s]
TET	turbine entry temperature, here used as combustor outlet temperature [K]
ToC	top-of-climb
TO	take-off
VFN	variable area fan nozzle

Chapter 1

Introduction

1.1 Research scope

The motivation for this research project stems from the pursuit for a more sustainable and environmentally friendly air transport. The goals set for 2020 by the Advisory Council for Aeronautics Research in Europe (ACARE) are a typical example of this turn towards a greener direction. According to ACARE, aircraft fuel consumption and CO_2 emissions should be reduced by 50%, noise by 50% and NO_x emissions by 80% until 2020 [1]. This work focuses on civil aero engine design and its impact on the installed specific fuel consumption.

The aero industry has until now followed the evolutionary path of increasing engine thermodynamic cycle temperatures and pressures, whilst also increasing the engine diameter for a given thrust. The first practice improves the thermal efficiency of the engine, while the second increases the propulsive efficiency. Many excellent references [2–4] written by industry experts, detail the limits gradually being reached by following the above design practice and list the following principal technologies as the means to keep engine design on a continuously improving path:

1. Variable area fan nozzle
2. Geared turbofan architecture
3. More electric technologies
4. Open-rotor configuration

The scope of this thesis is to contribute towards understanding many gray aspects of these technologies, including why they are required, for which application, under which conditions, what is their impact and how can they be accurately modelled.

1.2 Literature overview

Although the details of the literature review will be given within each chapter, this section aims to set the context for each of the technologies under investigation and to identify - at a top level - the gap this thesis endeavours to fill.

1.2.1 Variable area fan nozzle

Low fan pressure ratio engines will suffer from fan surge during take-off, due to the unchoking of the bypass nozzle that controls the fan running line [4]. A variable area fan nozzle could be used to provide an adequate surge margin and act as a technology that enables the design of low fan pressure ratio engines. Many different publications converge towards a low limit of 1.45, below which the variable nozzle would be required [3–8]. Although the above limit is well known, the conditions and application requirements that lead engine design towards it are not always clear.

From another point of view, Kyritsis investigated the off-design benefits of using a VFN, as well as the benefits of achieving a smaller and hotter core by opening the VFN at take-off [9]. His study was focused on a specific engine thermodynamic cycle and it would be interesting to expand his analysis to the entire turbofan design space.

1.2.2 Geared turbofan architecture

Following the current design trends, future engines will feature a lower specific thrust, higher diameter for a given thrust, and at the same time, a smaller and hotter engine core. The low-pressure shaft of these engines will have to rotate at lower rpm in order to avoid excessive fan tip compressibility losses. The lower LP spool rpm could compromise the efficiency of the LPT, increase its number of stages [10], or make it impossible to pass the LP shaft through the core [3]. A gearbox connecting the fan and the LPT would allow the two components to run at their optimal speeds and thus achieve higher efficiencies, lower number of stages and a lower LP spool diameter.

Although a lot of knowledge exists inside the design offices of engine manufacturers, there is still no publicly available study that connects the thermodynamics of the cycle with the need for a gearbox, and identifies which aircraft application is more likely to be the first requiring its introduction.

1.2.3 More electric technologies

An aircraft engine provides the aircraft with primary propulsive power and secondary power to drive the aircraft subsystems. The secondary power comes in the form of compressed bleed air and shaft power and impacts negatively the performance of the engine [4].

More electric technologies come to replace bleed air extraction with an equivalent shaft power extraction, which is used to drive separate compressors that provide the cabin with pressurised air in a more efficient way [11]. Many modern studies have investigated the potential benefits of different conventional and more electric configurations [11–16].

Nonetheless, there is still no formally proven and unique answer as to whether secondary power extraction induces or not greater penalties for certain engine designs. For example, will an engine with a low specific thrust suffer from greater off-take penalties relative to a high specific thrust engine? Answering such a kind of question could potentially indicate whether the more electric technologies should be prioritized for a long or short range application.

1.2.4 Open-rotor configuration

Higher engine diameters lead to propulsive efficiency gains, but they also result in higher nacelle weight and drag that penalise the aircraft fuel burn. In addition, the corresponding lower fan pressure ratios increase the negative impact of bypass duct pressure losses on the SFC of the engine [17]. Removing completely the bypass duct, in order to eliminate the above problems, leads to an open-rotor configuration, which could achieve very high propulsive efficiencies and fuel burn reductions [18].

In such a configuration the propeller provides the lion's share of the thrust, while the core mainly operates as the power generator that drives the propeller. As the propeller thrust power is the product of propeller efficiency times the power generated by the core, it becomes apparent that the performance simulation of the open-rotor engine relies upon the accurate prediction of the propeller performance at design and off-design conditions. Traditionally, propeller efficiency is represented in the form of characteristic curves or maps, in analogy to the way compressors and turbines are modelled. These characteristic curves relate the propeller efficiency with the non-dimensional parameters that govern the propeller performance. Let alone the difficulty in finding propeller maps in the open literature, there is as yet no physics based technique of scaling the map from one propeller design to another, a prerequisite feature for performance design studies of open-rotor engines.

Modern open-rotor performance studies either use a propeller map that corresponds to a specific geometry [19–24], or scale a map the same way a compressor map is scaled, simply by estimating the performance on the design point [22, 23]. Nevertheless, there is no formal proof that any of the above methods is correct, and no quantification of the error they introduce. In order to conduct the same kind of extensive design exploration as in the case of turbofan engines, a new propeller map scaling method needs to be created.

1.3 Project aim and objectives

The aim of this project is to perform an exploration of the advanced turbofan design space in order to identify the technologies required for different aircraft applications, and to develop a propeller modelling approach that will enable the same exercise to be conducted for an open-rotor configuration.

The work can be split into the following individual objectives:

1. the creation of an engine preliminary optimisation framework, which is able to calculate the uninstalled performance, dimensions, weight, and installed performance. The framework will be used in order to explain how the requirements of a given aircraft application lead to the selection of a thermodynamic cycle.
2. establishing the link between the engine thermodynamic cycle and the requirement for a variable area fan nozzle or a fan drive gearbox. Within the developed engine optimisation framework, this connection will be then used in order to find whether these enabling technologies should be prioritised for one aircraft application relative to another.
3. the derivation of algebraic expressions that calculate the fuel consumption penalty due to bleed and power extraction and the study of the thermodynamic cycle parameters effect. This entails answering the question whether future engines will face higher penalties and intensify thereby the demand for more efficient secondary power systems.
4. the creation of a propeller modelling method able to accurately model the performance of prop-fan geometries. This capability will enable the generation and study of full propeller maps for a given geometry.
5. the study of how the propeller map is affected when its design point changes, and the creation of a generic propeller representation. This will allow the same map to be used within extensive design parametric analyses, putting this way the foundations for future open-rotor design exploration studies.

1.4 Thesis structure

The thesis starts by tackling objectives 1 and 2 within chapter 2. This chapter begins with a brief account of engine efficiency and losses with the aim of identifying the parameters driving them. Already existing studies concerning the need for a variable area nozzle or a fan drive gearbox are reviewed. The method section presents the individual modules of the preliminary optimisation framework and sets up the design exercise. The results section starts with the uninstalled performance results, continues with the relation between the cycle parameters and the enabling technologies and concludes by the integration of all the above in an installed performance analysis.

Chapter 3 deals with the secondary power off-takes study of objective 3. The analysis starts by deriving formulas that calculate the effect of extracting bleed or power off-takes on the core, transmission and propulsive efficiency of the engine. The equations are subsequently validated by comparing their results against calculations conducted with an engine simulation model. The chapter ends with a discussion on the thermodynamic parameters that drive the efficiency penalties and the evolution of the penalties for future engine designs.

Chapter 4 presents the development of a propeller modelling method in order to accomplish the objective 4. The literature survey covers the fundamentals of propeller performance and reviews the available modelling methods. The development of the selected approach is then described in detail. The chapter ends with the validation of the method against experimental data and another higher fidelity method.

Chapter 5 starts by reviewing existing propeller map scaling approaches and by identifying their shortcomings. The propeller modelling method developed in chapter 4 is then used in order to generate a full propeller map and use it to study the variations of efficiency with the map parameters. A propeller optimisation framework is then set up in order to calculate the optimal blade geometry for different design point specifications. A full propeller map is then generated for each of the optimal geometries. The maps are analysed and compared in order to devise a map scaling technique and accomplish this way the objective 5.

The final chapter 6 summarises the most important findings of each technical part of this work, identifies the novelty and the contribution to knowledge and ends with some potential future work directions.

Chapter 2

Advanced turbofan design space exploration

2.1 Introduction

The work described in this chapter aims to demonstrate how a given aircraft application leads to the selection of an optimum thermodynamic cycle, and to identify which enabling technologies are required in order to implement it. The enabling technologies under investigation include the installation of a fan drive gearbox and the use of a variable area fan nozzle. It goes without saying that the presented topics have been extensively treated within the design offices of the engine manufacturers, whose wealth of knowledge on the topic is unrivalled. Nonetheless, their design choices are often driven by non-thermodynamic factors and by underlying assumptions which are not always visible to the academic reader. The presented analysis treats the subject from a clean sheet thermodynamic design perspective, in order to cast light to some of the current and future design trends of the advanced turbofan engine.

The chapter starts by laying the foundations of engine losses and their dependencies to the thermodynamic cycle parameters. Although seeming trivial, this topic is often a source of misconceptions and is vital for the analysis to follow. The next step involves reviewing the studies available on the literature showing the current trends of turbofan design, the limits being reached and the required new technologies. The method description starts by the presentation of the thermodynamic design framework used for the generation of results. This framework combines an optimisation method with tools that calculate the engine uninstalled performance, dimensions, weight, drag and installed performance. The method description ends with the formulation of the optimisation design problem, which also details the assumptions made for the case studies to follow. The case studies start from the optimisation of the uninstalled engine performance, in order to identify the effects of the main thermodynamic variables. The generated thermodynamic cycle data are then fed into the engine design and weight tool, which calculates the dimensions of the engine, the number of stages for each component and the engine weight. At this stage the analysis establishes the relation between the thermodynamic cycle parameters and the need for a variable area fan nozzle and a fan drive gearbox. The final stage of the analysis involves the calculation of the installed performance for a short and a long range aircraft mission. This calculation enables the positioning of the optimum engine designs on the created design space maps, in order to demonstrate whether the industry trends lead or not to the introduction of the aforementioned enabling technologies.

2.2 Engine Efficiency Fundamentals

The main power conversions that take place within a gas turbine aero-engine are depicted in the schematic representation shown in Fig. 2.1. Although the schematic shows a turbofan arrangement, the principles described apply also to turbojet and turboprop engines.

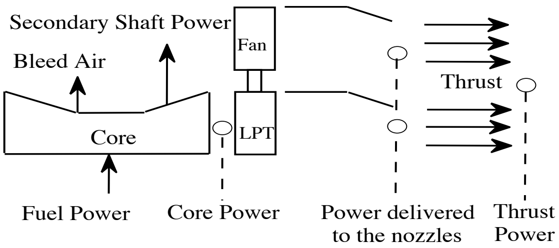

Figure 2.1: Schematic representation of a turbofan engine. The main power conversions are also shown. The term *core power* describes the mainstream product of the core, while the secondary power extraction consists of bleed air and shaft power.

Power enters the core of the engine in the form of fuel, which is burned inside the combustor. The core translates the fuel power into hot gas thermal power at the core exit (denoted as *core power* in Fig. 2.1), which is the mainstream product of the core. A lower amount of power is extracted from the core as bleed air and secondary shaft power, which comprise the total secondary power off-takes of the engine. At this point the core efficiency can be defined as the ratio of mainstream *core power* over the power provided by the fuel. The core efficiency, which corresponds to the thermal efficiency of a turboshaft engine, depends on the engine overall pressure ratio and turbine entry temperature, and on the isentropic efficiencies and pressure losses of the core components. It is common knowledge that for an ideal engine, the core efficiency always increases for an increasing overall pressure ratio (OPR), while an optimum OPR exists if the component isentropic efficiencies are lower than 100%. A different lower optimum value of OPR exists for the maximisation of the core specific power. These optimum OPR values depend on the turbine entry temperature (TET) and on the efficiency and pressure losses of the core components.

On the other hand, the effect of TET is a source of many misconceptions. It is a commonly held belief that the TET has no effect on the efficiency of an ideal engine, while it has a positive effect for a non-ideal engine. At the same time, an increase in TET always increases the specific power of the core and hence decreases its mass flow and size for a given power requirement. According to Birch [2], under constant technology level, after a certain value of TET, the resulting smaller core size and the increasing cooling requirement completely counteract the efficiency amelioration. Nonetheless, the pure thermodynamic effect of TET is considered always positive in terms of core efficiency. This widespread statement regarding the effect on efficiency has been proven wrong subsequently by Wilcock [25], Guha [26] and Kurzke [27]. The existence of this common misconception originates from the simplifications made mainly for teaching purposes, including constant heat capacities C_P or the non-taking into account of the fuel mass flow. Without these simplifications, the calculations result in the clear existence of an optimum TET, which maximises the core efficiency and that is present even without the losses induced by cooling bleeds or by smaller core components. The most sound explanation has been given by Kurzke [27], who attributed the existence of the optimum TET in the non-linear relation between the fuel injected in the combustor and the increase in temperature. As the temperature increases, one has to introduce disproportionally higher fuel, which finally leads to the deterioration of the engine core efficiency. Most surprisingly, in the extreme case where the components are ideal, the TET is found to have always a negative impact on core engine efficiency, a trend completely opposed to the common knowledge. Nonetheless, it must be underlined that high TETs will always be used as a way to decrease the core size and reduce its weight.

Kurzke's finding has been confirmed by the author and the problem has been identified in the combustor balance. The correct combustor balance as reported by Guha [26] is given by Eq. 2.1, where the subscript g corresponds to "gas" (air plus combustion products) and the subscript a corresponds to "air". This non-linear relation between the enthalpy at the combustor exit and the fuel air ratio is the reason for the existence of the TET optimum. If the term $(1 + far)$ is neglected, the result changes dramatically and no TET optimum exists any more. Surprisingly, this term was neglected in the in-house performance code (Turbomatch), and this was also the case with the excellent textbook of Walsh and Fletcher [28]. Turbomatch has been corrected in order to capture correctly this very important effect.

$$far \cdot FCV = (1 + far) \cdot h_{g04} - h_{a03} \tag{2.1}$$

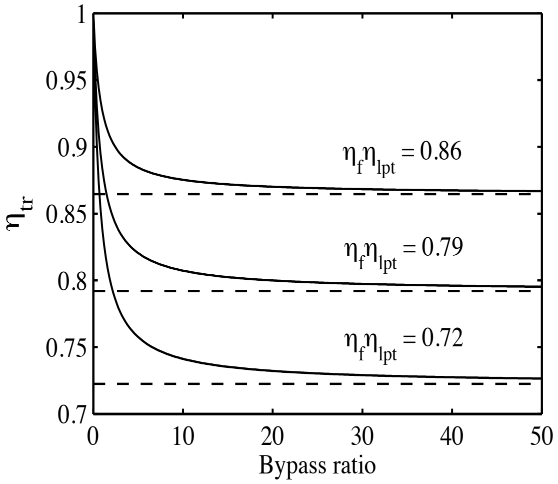

Figure 2.2: Variation of transmission efficiency with bypass ratio, fan and turbine efficiency.

Part of the hot gas power generated by the core is transmitted to the bypass propulsive nozzle through the low-pressure turbine, fan, and bypass duct, whereas the remaining power is transferred to the core nozzle. This power transfer is described by the so-called transmission efficiency, which is defined as the ratio of power delivered to the propulsive nozzles over the power generated by the core. The transmission efficiency is a function of the engine bypass ratio, the low-pressure turbine and fan isentropic efficiencies, the bypass and core duct pressure losses, while Guha [29] found that it also depends lightly on the specific thrust of the engine. For the calculation of the transmission efficiency many similar analytical expressions can be found in the literature [30–32]. Equation 2.2 is the one given in [32] and used for the analysis.

$$\eta_{tr} = \frac{1 + BPR}{1 + BPR/(\eta_f \eta_{lpt})} \tag{2.2}$$

Figure 2.2 shows the variation of transmission efficiency with bypass ratio for different sets of fan and low-pressure turbine isentropic efficiencies. The efficiency reduces as the bypass ratio increases due to the higher amount of energy that is transmitted via the higher losses path of the fan, low-pressure turbine, and bypass duct. At the one extreme, in the case of a turbojet engine with $BPR = 0$, the transmission efficiency is equal to

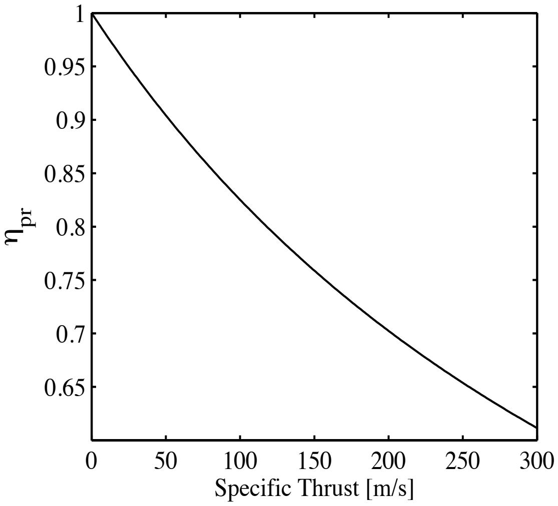

Figure 2.3: Variation of propulsive efficiency with specific thrust.

one. At the other extreme, when $BPR \rightarrow \infty$, all the energy is transferred to the bypass stream and therefore $\eta_{tr} \longrightarrow \eta_f \eta_{lpt}$.

Finally, as shown in Fig. 2.1, the power that reaches the propulsive nozzles is converted into thrust power by the expansion of the air and hot gases into the atmosphere. This last power conversion is described by the propulsive efficiency of the engine, which is defined as the ratio of the thrust power produced over the power delivered to the propulsive nozzles.

$$\eta_{pr} = \frac{1}{1 + ST/(2V_0)} \tag{2.3}$$

The propulsive efficiency of a turbojet is given by Eq. 2.3, the derivation of which can be found in many textbooks [33]. A graphical representation of Eq. 2.3 is shown in Fig. 2.3, where one can readily observe that as $ST \rightarrow 0, \eta_{pr} \rightarrow 1$. Equation 2.3 establishes the unique dependence of propulsive efficiency on the engine specific thrust. This is a rather intuitive result, if one considers that: 1) the propulsive efficiency represents the losses of kinetic energy ejected in the atmosphere without producing thrust, 2) the specific thrust is essentially equal to the increase in jet velocity as shown later by Eq. 2.6 and Eq. 2.7.

A similar expression can be derived for the case of separate flow turbofans, if one assumes an optimum ratio of cold to hot jet velocities as shown by Eq. 2.4. Guha [34] has proven that - for zero bypass duct pressure losses - the optimum ratio V_c/V_h equals the product of the fan and low pressure turbine isentropic efficiencies. Equations 2.5-2.7 are taken from the same reference [34] and define the kinetic energy in the nozzles, the mean jet velocity and the specific thrust. Equation 2.5 makes the assumption of full expansion at the nozzle exit, i.e. the static pressure is equal to the ambient and no pressure thrust component exists. Combining Eqs. 2.4-2.7 leads to Eq. 2.8, which is the expression of propulsive efficiency for a separate flow turbofan engine that has an optimum velocity ratio. This assumptions seems to be a valid one according to the optimisation results reported by Jackson [17] and Kyritsis [9]. It becomes apparent that in the case of a turbofan engine, the propulsive efficiency is also affected by BPR and the low pressure component efficiencies. However, their impact is much lesser relative to the impact of ST, which remains the driving parameter. It is also observed that when $\eta_f \eta_{lpt} \rightarrow 1$, the BPR drops from the equation and the expression reduces to Eq. 2.3. The performance results by Bruni [35] also confirm the dominance of the ST factor, relative to the BPR term. In general, the Eq. 2.3 could be used even for the case of a turbofan engine, within an error of 0-5%.

This discussion comes to clarify another common misconception regarding the relation between propulsive efficiency and BPR, also discussed by Refs. [2, 7, 29]. It is the ST and not the BPR, which drives the propulsive efficiency. The two are interrelated only if the core characteristics remain constant. For example, the BPR could be increased independently from ST if the TET was increased, leaving the propulsive efficiency completely unaffected.

$$\left(\frac{V_c}{V_h}\right)_{op} = \eta_f \eta_{lpt} \tag{2.4}$$

$$P_{nozzles} = 1/2 \cdot W_h \left(V_h^2 - V_0^2\right) + 1/2 \cdot BPR \cdot W_h \left(V_c^2 - V_0^2\right) \tag{2.5}$$

$$V_m = \frac{1}{1+BPR}\left[BPR + \frac{1}{\eta_f \eta_{lpt}}\right] V_c \tag{2.6}$$

$$ST = \frac{T}{W_h + W_c} = V_m - V_0 \tag{2.7}$$

$$\eta_{pr} = \frac{ST \cdot V_0}{1/2 \cdot (ST+V_0)^2 \cdot \underbrace{\left(\frac{\left(\frac{1}{(\eta_f \eta_{lpt})^2} + BPR\right)(1+BPR)}{\left(\frac{1}{(\eta_f \eta_{lpt})} + BPR\right)^2}\right)}_{BPR\ term} - 1/2 \cdot V_0^2} \tag{2.8}$$

Having defined the efficiencies of the aforementioned power transformations, the total engine efficiency can now be expressed as the product of their individual efficiencies:

$$\eta_0 = \eta_{co}\eta_{tr}\eta_{pr} = \frac{P_{core}}{P_{fuel}}\frac{P_{nozzles}}{P_{core}}\frac{P_{thrust}}{P_{nozzles}} = \frac{P_{thrust}}{P_{fuel}} \tag{2.9}$$

2.3 Low pressure system enabling technologies

After having explained the parameters driving engine efficiency, it becomes now clear why engine design has followed a path of increasing TET, OPR and decreasing specific thrust. Modern engines have take-off TETs in the order of 2000 K, maximum OPR which exceeds 50 and bypass ratios higher than 10 [29, 36]. Specific thrust values are more difficult to quote as they are not usually reported by the engine manufacturers.

According to Refs. [27, 36, 37], no further core efficiency benefits are expected from the increase of TET further than 2000 K. A further increase of around 3.5% is expected for the core efficiency, mainly through the increase of OPR [6, 27]. The authors of Refs. [2, 4, 17, 36] support that significant benefits can only arise from propulsive efficiency gains, if the specific thrust is further reduced. According to Jackson [17] and Birch [2] this could deliver an efficiency benefit close to 10% but only if the installation losses are kept under control. On the other hand, Young [38] claims that in the case of medium to long range aircraft, the specific thrust is not expected to reduce much further than the current levels. Each of the above studies has been done under a different set of assumptions and conducted at different times. Therefore it would be interesting to test the above statements under a common set of assumptions for short and long range missions, with current and future levels of technology.

Two low pressure system technologies are widely accepted as enablers of low specific thrust designs. The first is the variable area fan nozzle (VFN), which is required in order to control the fan surge at take-off conditions, from which suffer low fan pressure ratio (FPR) engines. According to the analysis of Guha [34] low FPRs directly result from a choice of a low specific thrust. Many different studies converge to the low limit FPR value of 1.45, under which a VFN would be required [3–8]. Jackson [17] also calculated the required percentage of fan nozzle area increase for a wide range of FPR values. Kyritsis [9] investigated how a VFN can be further used in order to optimise the off-design engine operation, or in order to enable a smaller and hotter core design. He studied the impact on a specific engine design and found that none of the two options results in interesting fuel benefits. Nonetheless, it would be interesting to expand this study on the whole of the engine design space and test whether there is a design region when this variable cycle technique brings significant fuel savings.

Contrary to the case of variable fan nozzles, there is no unique converged answer for the introduction of a fan drive gearbox. Some authors relate the introduction of gearbox to a bypass ratio greater than 10 [29, 36], while others for BPRs higher than 17 [30]. Zimbrick supported that a gearbox would be required in order to keep the number of low pressure turbine stages below 6 [8]. References [4, 6, 37] introduce the gearbox for engines which have an FPR lower than 1.4, while references [3, 7, 39] relate it to the specific thrust of the engine, claiming a lowest ST value of 100 m/s for an ungeared configuration.

The assumptions underlying the aforementioned claims are not given, but two main lines of thought recur in the literature. The first dictates that the gearbox should be introduced to avoid an exceedingly high number of LPT stages, which could possibly increase the weight, cost and length of the engine. The second perspective focuses on the fact that a core must be flexible enough in order to accommodate a whole family of engines [40]. Jacquet highlights the importance of the LP shaft diameter which must pass through the core, and constitutes the parameter driving the growth capability of the engine [41]. For constant fan power, the torque increases as the rotational speed decreases. A higher torque sizes a higher diameter LP shaft, which becomes increasingly difficult to fit through the HP shaft. Lower rotational speeds result from the constant fan tip speed assumption, which keeps the aerodynamic losses under control, when the diameter of the fan increases. Under a constant core assumption, the diameter of the fan can increase if a growth version of the engine is sought and that is how the engine growth capability is related to the flexibility of the core, and the LP shaft diameter. According to Borradaile [3] a core which has been designed for an engine of given specific thrust, immediately poses a torque limit on the LP shaft, which could only be overcome by introducing a gearbox or an aft-fan configuration.

The analysis by Kurzke is the only one existing in the open literature, which clearly describes its ground rules [36]. This study compares the characteristics of a conventional and a geared configuration, as the bypass ratio increases under a constant core assumption. Both the problem of increasing LPT stages number and LP shaft torque are demonstrated and the author concludes that at a BPR of 10 the two configurations are equal, with the geared architecture becoming more appealing as the BPR increases further. Kurzke clearly connects the use of a gearbox with BPR or specific thrust. It is reminded that under constant core conditions the two parameters are directly linked. Thus, it is unclear which of the two parameters is the one driving the phenomena, or whether the core characteristics have any influence. Furthermore, the aim of the paper is to compare the two configurations under the same thermodynamic cycle parameters. However, a geared configuration is expected to have a lower specific thrust optimum [5] and therefore a further propulsive efficiency benefit to unlock.

The work presented in this chapter aims to extend Kurzke's study and to fill the aforementioned gaps. Nevertheless, it has been chosen not to follow a constant core assumption, as this would require the selection of a core size according to some given engine family strategy. Such a selection could only be performed correctly within the preliminary design office of an engine manufacturer and is outside the scope of this work. Thus, the current analysis will mainly focus on the number of LPT stages aspect and its connection to the thermodynamic cycle characteristics.

2.4 Numerical methods and models used

2.4.1 Engine model - TURBOMATCH

The performance simulation is conducted using the Turbomatch code, developed in Cranfield University. This code is based on the equations of mass continuity and energy balance, combined with characteristic curves or ”maps” that describe the performance of the individual components. The set of the above non-linear equations is solved using an iterative Newton-Raphson solver. More details on Turbomatch can be sought in [42].

The code has been upgraded by the author on the following aspects:

Convergence robustness

- The component maps have been ”smoothed” in order to increase the accuracy of the interpolations.
- The non-linear Newton-Raphson solver has been upgraded by adding the backtracking capability, which improves the global convergence as described by Press et al [43]. This change was essential in order to avoid the numerous convergence problems encountered with the initial version of the code, which made the integration with an optimiser very difficult.
- In extreme cases, where one of the nozzles has barely enough pressure ratio to eject the fluid to the atmosphere, convergence problems can still occur. To tackle these problems the author added the capability of automatically adjusting the off-design steps requested by the user in order for them to be small enough for the solver to converge.
- The ability of convergence even outside the component maps was introduced. Before this change, if the solution tried to move outside the limits of a component map, the code would immediately intervene in the solution proposed by the solver and move the solution inside the allowed space. This could easily lead to singular Jacobian problems for solutions that lied close to the limits of the maps. Furthermore, this new capability allows the illustration of the fan surge problems from which suffer the low FPR fans.
- A solver guess has been added for the intake mass flow. Previously, the intake mass flow was only known when the first compressor of the flowpath was calculated. This meant that the initial mass flow at the intake had to be taken from the previous numerical step, in order to calculate the momentum drag. This numerical lag between the intake mass flow and the rest of the variables was found to lead to convergence problems.

- The turbine mass flow guess has been replaced by the turbine non-dimensional enthalpy drop, which corresponds to its pressure ratio. This modification allowed the solutions to lie in the choked region of the turbine map where the mass flow is constant.

The above convergence related modifications have an important impact on the robustness of the code. Before the modifications, the lowest achievable idle thrust was about 20% of the maximum take-off thrust, in the case of a separate flow turbofan engine. Moreover, in order to achieve this idle thrust, the user had to specify many small off-design steps from maximum take-off until idle. Getting closer to idle, these steps could be even less than 10 K of TET. After the aforementioned stability improvements, the lowest possible thrust can be as low as 7%, achievable with only one step from maximum take-off.

Features enrichment and improvements

- The capability of using the engine thrust as a power setting handle has been added. This allows the automatic adaptation of the engine TETs in order to satisfy the given thrust requirements. Previously, the user could only define a TET and calculate the thrust as a result. This meant that the TET had to be iterated by the user until the desired thrust value was achieved. In order to automate the process and enable the execution of thousands of optimisation cases, this task has been taken on by the code solver, which automatically calculates the required TET.
- A propeller component has been added in order to incorporate the findings on propeller modelling as described in chapters 4 and 5.
- The capability of defining the compressor polytropic efficiency has been added. This allowed the fair comparison between compressors of different pressure ratios as described by Saravanamuttoo et al [44]. The same process has not been introduced for turbines as their pressure ratio shows much lower variation. Furthermore, in the turbine case an additional iteration would be required, which would unnecessarily increase the complexity as described by Kyritsis [9].
- The combustor balance has been updated in order to take into account the injected fuel flow as described in section 2.2. This change resulted in optimum TETs lower by 200K, a result with significant impact on engine design and lifing considerations.
- The capability of programming one engine variable as a function of another was introduced. This improvement allowed the scheduling of bleed valves or variable stator vanes as a function of the power setting of the engine.

2.4.2 Engine preliminary design and weight estimation tool

The preliminary design tool is fed with the engine thermodynamic parameters generated by Turbomatch, conducts a preliminary sizing of the main components and estimates the weight of the engine. The tool has been created in Cranfield University by Lolis and a detailed description and validation can be found in his PhD thesis [45]. Apart from the engine thermodynamic data, the design code requires the definition of certain design assumptions for each component. These design assumptions include the definition of component input and output Mach numbers, hut to tip ratios, aerodynamic loadings and geometrical choices, like constant hub, tip or meanline. The whole engine meridional design is calculated by the code including the component number of stages, diameters, lengths, rotational speeds and the variation of aerodynamic and thermodynamic parameters within the component. The code has been validated by Lolis, achieving almost identical designs when compared to current engines and providing consistent weight predictions. The interaction between Turbomatch and the design code has been completely automated by Lolis, thereby giving the capability of running efficiently a large number of engine design studies.

2.4.3 Installed performance calculation

Having calculated the engine weight for each one of the engine thermodynamic cycles, two more elements are required before the calculation of the installed performance. The engine nacelle weight and drag. The nacelle weight is calculated using Eq. 2.10, as proposed by Jackson [17].

$$m_{nac} = \kappa_{nac} \cdot (2 \cdot L_c \cdot d_c + L_b \cdot d_a + 2 \cdot L_a \cdot d_a) \tag{2.10}$$

The coefficient κ_{nac} represents the nacelle weight per square meter of nacelle surface and Jackson calculated it equal to $24.88[kg/m^2]$ for an engine similar to the RR Trent 892. The explanation of the individual variables is given by Fig. 2.4. As shown in Eq. 2.10, Jackson multiplied by 2 every surface which is exposed to the atmosphere. In order to simplify the calculation and without losing much accuracy, this has not been taken into account for the case of the afterbody (described by the length L_a). Thus the two last terms collapse into one which equals to $(L_b + L_a) \cdot d_a$. This term can then be calculated if the length of the fan module is subtracted from the total engine length. The diameters d_c and d_a are taken equal to the fan and booster inlet tip diameters respectively.

Engine drag is the last required element and it is calculated using the method suggested by Walsh and Fletcher [28], also used by Jackson [17]. According to this approach, the nacelle drag can be calculated as the sum of the cowl and afterbody drag by Eq. 2.11-2.13. The factor κ_i represents the interference drag and according to Jackson it is taken

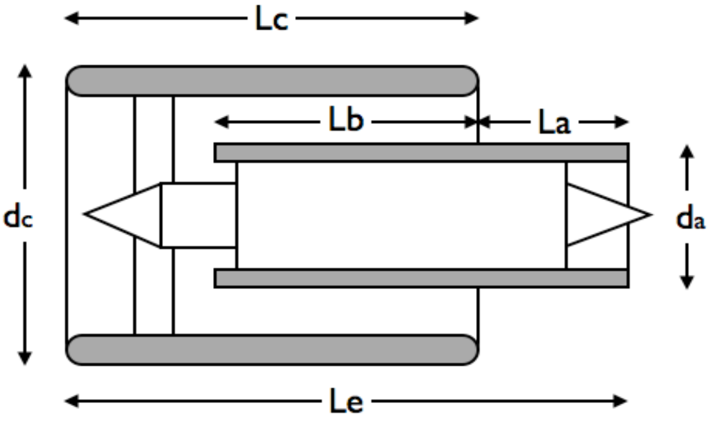

Figure 2.4: Engine schematic showing the definition of nacelle dimensions

equal to 1.2. According to Walsh and Fletcher [28] the drag coefficient C_D takes a value between 0.002-0.003. The value 0.003 is used by Jackson, while the low limit of 0.002 is chosen for this study. It must be highlighted that the velocity used for the calculation of the afterbody drag (Eq. 2.12) is not the free stream one, but the one ejected by the bypass nozzle. Finally, the cowl length to diameter ratio depends on the type of cowl and its technology. A long cowl would have values from 1.5 to 1.8, while an aggressive short cowl could have values even below 1 [17].

$$D_c = \kappa_i \cdot \frac{1}{2} \cdot \rho \cdot V_0^2 \cdot C_{D,c} \cdot \left[\pi \cdot \left(\frac{L}{D}\right)_c \cdot d_c^2\right] \tag{2.11}$$

$$D_a = \kappa_i \cdot \frac{1}{2} \cdot \rho \cdot V_c^2 \cdot C_{D,a} \cdot (\pi \cdot L_a \cdot d_a) \tag{2.12}$$

$$D_n = D_c + D_a \tag{2.13}$$

Knowing the uninstalled engine SFC, weight and drag, the installed performance can now be calculated using the range factor K_r introduced by Walsh and Fletcher [28], Eq. 2.14. The engine fuel burn FB is calculated using Eq. 2.15. The range factor is effectively an installed expression for the specific fuel consumption, expressed as total engine related mass divided by the installed engine thrust. Contrary to the uninstalled SFC, this expression takes into account the engine weight and drag variation. The equation considers that the required thrust at mid-cruise remains constant as the engine parameters vary and thus represents more accurately the case of re-engining a fixed aircraft. This approach would give somewhat conservative predictions if the aircraft was changing in relation to the efficiency to the engine.

$$K_r = \frac{M_e + FB}{T_{mCR} - D_n} \tag{2.14}$$

$$FB = T_{mCR} \cdot SFC_{mCR} \cdot \frac{Range}{V_0} \tag{2.15}$$

2.4.4 Optimisation method

The purpose of this section is not to describe in detail different optimisation algorithms but to justify the selection of the optimisation method used within the created engine optimisation framework. For further information the reader can refer to several good textbooks on this topic [46, 47]. The nature of the engine design problem falls into the category of non-linear constrained optimisation. The method selected is a Genetic Algorithm developed in Cranfield by Rogero [48] and used later on also by Celis [49].

The reason for starting the optimisation with a genetic algorithm emerges from the fact that the non-linear equations governing the design of the engine do not have a solution for any given set of design variables [50]. For instance, increasing too much the fan pressure ratio for a given set of (TET, OPR, BPR) can lead to a core nozzle pressure ratio which is lower than one, and hence to a non-feasible solution. Furthermore, gradient methods require that the function to be optimised is smooth enough for the determination of the gradients [51]. As seen in section 2.4.1, the prediction of engine performance relies a lot on the interpolation of characteristic curves and on iterative methods with given tolerances. At this moment, the tolerance of Turbomatch is in the order of 5×10^{-4}. This tolerance is adequate for engine simulation, but it is quite large if Turbomatch has to be used by another numerical method, such as an optimiser. Therefore, the discontinuities present on the characteristic curves and the inadequate convergence tolerance are potential sources of problems for gradient based methods. On the other hand, Genetic Algorithms have been successfully used in previous engine simulation studies at Cranfield University [48, 49, 52–54]. After experimenting with a gradient based approach included in Matlab and the GA optimiser available in the department, the latter has been chosen mainly due to its robustness and accurate results.

2.5 Engine design principles

During the preliminary design phase the engine thermodynamic cycle parameters are chosen in order to comply with the requirements of the following three major mission points [55, 56].

- **hot-day take-off (TO)** The requirements of the airframe manufacturer for a given runway length and a minimum climb rate pose a thrust requirement for the engine at this point. The highest engine temperatures and spool speeds are usually encountered at this point and that is why the mechanical design of the engine takes place here.

- **Top-of-climb (ToC)** At this point the fan experiences its highest non-dimensional mass flow and speed. Minimum time to cruise and air traffic control restrictions impose a thrust requirement for this point too.
- **Mid-cruise (mCR)** For civil aircraft the figure of merit is normally the mission block fuel. The greatest part of the fuel is burned at cruise and thus the SFC at a typical mid-cruise point constitutes an important performance metric.

The thermodynamic design point can be located either at top-of-climb [49, 55, 57] or at mid-cruise [51, 58]. In the first case the design points must be located in such a way on the component maps that the optimum component efficiencies occur at mid-cruise [57]. In the second case a margin must be allowed for the increased aerodynamic speed of the top-of-climb condition [58].

In order to fully define the thermodynamic design of a two-spool separate exhausts turbofan, where the design point is located at mid-cruise, the following thermodynamic parameters must be chosen [9]:

1. Bypass ratio at mCR
2. Fan pressure ratio at mCR
3. HP/LP pressure ratio split at mCR
4. Overall pressure ratio at mCR
5. Engine mass flow at mCR
6. Combustor outlet temperature at mCR
7. Combustor outlet temperature at ToC
8. Combustor outlet temperature at TO

The designed engine has to satisfy the following set of constraints, coming either from airframe requirements or technological limitations:

1. a mid-cruise nominal net thrust T_{mCR}
2. a hot-day take-off nominal net thrust T_{TO}
3. a top-of-climb nominal net thrust of T_{ToC}

4. a maximum fan diameter of d_f imposed by the airframer
5. a hot-day take-off maximum turbine entry temperature TET_{TO}
6. a hot-day take-off maximum high-pressure compressor exit temperature of $T_{3,TO}$

The fan diameter can be calculated at top-of-climb if typical values of the hub-tip ratio and inlet Mach number are assumed. The thrust at the take-off and top-of-climb points can be replaced by the ratios of thrust relative to the mid-cruise point, which do not depend on engine size but only on its thermodynamic parameters. Although traditionally only the maximum take-off TET is taken into account, according to Karanja [40] an eye must be kept at the levels of TET at climb and cruise in order to control the creep life of the engine. The compressor delivery temperature limit is imposed by the requirement for uncooled compressor blades, with an approximate limit of 990 [K] for nickel alloy blades [29]. Finally, the figure of merit can either be the engine specific fuel consumption, if only the uninstalled performance is optimised, or the mission block fuel in the case where the optimum installed performance is sought. In the context of this work the installed performance optimisation is optimised using the aforementioned range factor K_r presented in section 2.4.3.

2.6 Engine thermodynamic design approach

The selection of the thermodynamic parameters that define the engine cycle is normally conducted either by extensive parametric studies or numerical optimisation. Parametric studies give a physical insight on the phenomena that govern the engine performance, but they are not suitable for cases with more than 2-3 design variables and numerous design constraints. This is true especially when only one parameter is varied while all the others are constant at a non-optimum value [29]. Numerical optimisation can then be employed to find an optimum solution that satisfies all the design constraints [59]. Nonetheless, numerical optimisation results must always be critically filtered, otherwise they are just numbers coming out of a black box. Both the aforementioned approaches have their merits, and within the context of this thesis a combination of the two will be implemented.

To begin with, it must be noted that contrary to formal definitions, the turbine entry temperature (TET) signifies the combustor outlet temperature. That is the temperature before the mixing of the nozzle guide vanes cooling flow. The method used here for the thermodynamic cycle design is essentially similar to the approaches of Jackson [17] and Guha [29]. A typical mid-cruise point of given thrust is used as the engine design point. This choice is based on the fact that the engine off-design performance is calculated using component characteristic curves, interpolation and a numerical solver process, which at the moment is not accurate enough. On the other hand, the design point calculation uses no iterative process and thus achieves by default a very high accuracy. Thus this selection avoids the interaction of the engine off-design iterative process with the optimiser and enables a more robust and accurate optimisation. For a parametric variation of the design point turbine entry temperature, overall pressure ratio and bypass ratio, the fan pressure ratio is optimised for minimum design point SFC. The optimisation of the fan pressure ratio leads to an optimal ratio of velocities between the bypass and core nozzle as described by Guha [34]. This technique, also used by Jackson [17], intrinsically assumes that the FPR does not have an important impact on the fan weight. By using this design approach the main design variables have been essentially reduced to 3 (TET, OPR, BPR) and a clear graphical representation of the design space is enabled.

Kyritsis proved that the engine performance does not depend on its actual size, as long as there is no constant absolute demand for power or bleed off-takes [9]. Therefore, it has been decided not to include any normal off-takes and thereby avoid the iteration of inlet mass flow in order to match a given design point thrust. This technique simplified significantly the optimisation task. The effect of off-takes will be separately treated in chapter 3.

Having optimised the design point FPR for the given values of TET, OPR and BPR, the off-design conditions of ToC and TO can be now calculated using the thrust ratios (independent of design point thrust). These thrust ratios are automatically matched by Turbomatch using its internal iteration process that calculates the required off-design TETs. At this point the engine performance is known at all the three major design points for the given set of TET, OPR and BPR. An extensive variation of these three parameters unfolds the design space, where the benefits in SFC can be juxtaposed with the different engine design constraints, identifying this way the optimum feasible solution. The process can be repeated for different thermodynamic assumptions, notably for different component efficiencies. Nevertheless, the final optimal solution can not be identified yet, as at this point only the uninstalled performance is known.

The next step involves the calculation of engine enabling technologies using the produced uninstalled thermodynamic results. Plotting the fan surge margin at take-off for each engine design allows to identify the need for a variable fan nozzle. At this point, the engine mass flow is scaled to provide the required design point thrust and the performance results are passed on the preliminary design code in order to calculate the number of LPT stages, the dimensions of the engine and its weight. The dimensions of the engine are subsequently used in order to calculate the engine drag and finally the range factor K_r for a specified aircraft mission. This installed performance calculation is then repeated for long and short range missions. The data generation process is now completed and the analysis of the design space can be conducted. Tracing the installed performance on design space maps, enables the selection of an engine respecting the design constraints and allows the quantification of the impact of the aforementioned technologies.

2.7 Uninstalled performance study

2.7.1 Model configuration and assumptions

The baseline engine model employs a two-spool separate flow turbofan configuration as shown in Fig. 2.5. The basic thermodynamic design assumptions are shown in table 2.1. The polytropic efficiency is used for the compressors in order to isolate the effect of technology level from the effect of pressure ratio variations. On the other hand, the same approach is not followed for the turbines, because this capability is not supported by Turbomatch and its implementation would require additional iterations within the turbine module. The same approach was followed by Kyritsis [9]. This gives a somewhat pessimistic view of the turbine efficiency, which however does not give unrealistic results, because turbines have significantly lower pressure ratios relative to compressors. The nozzles are assumed to have an ideal velocity coefficient C_V as the characteristic curve available in Turbomatch gave unexpectedly low values. Jackson [17] also assumed an almost ideal value of 0.999.

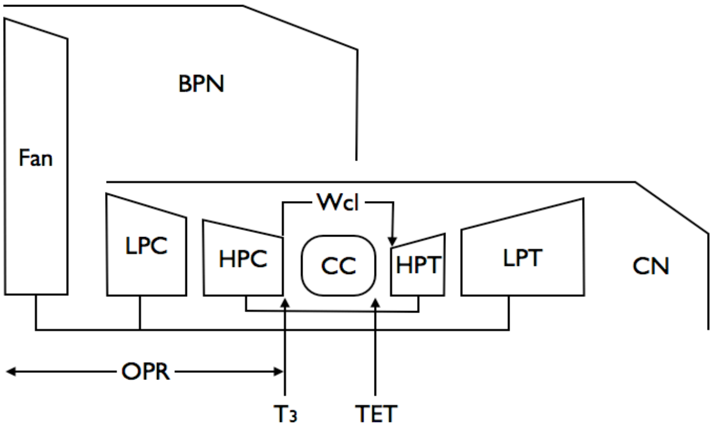

Figure 2.5: Engine configuration schematic showing the definition of OPR, T_3 and TET. The bypass and core nozzles are designated by BPN and CN respectively.

The fan module is modelled as a simple compressor component, as Turbomatch does not support a separated hub/tip modelling. In order to conserve the OPR as the fan pressure ratio varies during the optimisation, the model automatically adjusts the pressure ratio of the booster (LPC) and the HPC, by conserving their relative ratio of PR at the value shown in table 2.1. The additional optimisation of the pressure ratio split between the two compressors would require studying the impact of compressor pressure ratio on its polytropic efficiency, while also taking into account the variation of HPT stages. For example, the HPC pressure ratio could be limited in order to have only one HPT stage, limiting this way the number of expensive HPT parts. As the above considerations are outside the scope of this thesis, the simplifying assumption of constant pressure ratio split is made.

The relative cooling mass flow W_{cl}/W_{25} is considered constant as the OPR and TET vary. This essentially means that the cooling technology is adjusted in order to maintain a constant metal temperature, or that the maximum allowable metal temperature changes. A varying cooling mass flow would move the optimum results towards lower OPR and TET but its calculation falls outside the scope of this work.

Finally, table 2.1 shows the specifications of the three major design points. The two mid-cruise thrusts correspond to typical short range and long range aircraft and they will be used for the sizing calculations of the installed performance study, later on. The thrust ratios come from the airframe requirements and constitute typical short and long range values.

Table 2.1: Engine thermodynamic specifications

Parameter	Value	Parameter	Value
mid-cruise	35kft/0.8M/ISA	W_{cl}/W_3	10 [%]
top-of-climb	35kft/0.8M/ISA+10	$\eta_{p,c}$	0.85/0.90/0.95
take-off	SLS/ISA+15	$\eta_{is,t}$	0.85/0.90/0.95
Short range T_{mCR}	20 [kN]	PR_{HPC}/PR_{LPC}	11
Long range T_{mCR}	65 [kN]	C_V	1.0
T_{ToC}/T_{mCR}	1.325	Bypass duct $\Delta p/p$	1.5 [%]
T_{TO}/T_{mCR}	6.05	Burner $\Delta p/p$	4.0 [%]

2.7.2 Uninstalled performance results

Figure 2.6 shows the variation of the optimum FPR with design point (mCR) TET and BPR, while also illustrating the impact of the aforementioned parameters on the non-installed cruise SFC. The main observations stemming from this figure are the following:

- **For a constant BPR the optimum FPR increases as the TET increases.** The optimum FPR corresponds to the FPR which leads to an optimum ratio of jet velocities $V_c/V_h = \eta_f \eta_{lpt}$. Under constant BPR conditions the mass flows of the two streams are fixed. If the FPR also remained constant, the total fan power would stay the same and the same would apply for the LP turbine. Thus the turbine enthalpy drop would also be fixed. At the same time, the increase in TET would increase the specific power of the core, and thus for the same core mass flow more enthalpy would be available at core exit. At constant turbine power this increased enthalpy would translate to an increased core nozzle velocity. However, the bypass stream jet velocity would be the same as it is fixed by the FPR, and thus the jet velocity ratio would decrease away from its optimum value. Its a natural consequence that the FPR has to increase in order to increase the cold jet velocity, decrease its hot counterpart and bring back the velocity ratio at its optimum value.

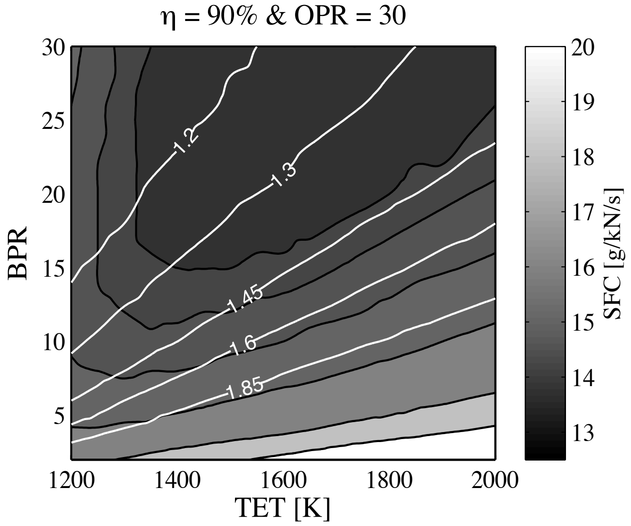

Figure 2.6: Baseline uninstalled SFC design map, also showing the variation of optimum FPR (white lines).

- **For a constant TET the optimum FPR decreases as the BPR increases.** With a fixed TET the specific enthalpy at the core exit is constant (enthalpy for unit mass). For a fixed FPR, the LPT enthalpy drop depends only on the ratio of LPT and fan mass flows, i.e. on the bypass ratio. For higher BPR the fan mass flow increases while the LPT mass flow is constant and thus the LPT turbine has to work harder and its enthalpy drop increases. This drops the velocity of the core nozzle and thus for fixed cold velocity (fixed FPR) unbalances the optimality of the velocity ratio. Therefore, the FPR has to be reduced in order to increase the velocity ratio to its optimal value. In reality, the LPT mass flow would not remain constant and it would adjust up or down in order to give a fixed thrust value. The direction of the LPT mass flow change would depend on whether or not the optimum BPR value has been exceeded or not. If the increase in BPR improves the efficiency then for the same thrust a smaller core would be needed and thus the LPT mass flow would decrease, together with a decrease in the fan mass flow, in order to keep the desired BPR value.

- **For a constant BPR there is an optimum TET which minimises SFC.** The existence of an optimum TET for a given BPR results from the trade-off between propulsive and core efficiency (the transmission efficiency being fixed by the constant BPR). For the given OPR and component efficiencies, the increase in the TET leads to an initial improvement of the core efficiency, until approximately a TET of about 1800 K. For higher component efficiencies or lower OPR this optimum TET would move towards lower values. In the extreme case where ideal component efficiencies were considered, the increase in TET would only have a negative impact on the efficiency for the reasons discussed in section 2.2. Concerning the propulsive efficiency, an increase of TET under constant BPR conditions leads to an increase in FPR and jet velocities and thus to a decrease of propulsive efficiency. For higher BPR the optimum TET, moves to the right due to the positive effect of reduced FPR and jet velocities.

- **For a constant TET there is an optimum BPR which minimises SFC.** This time the trade-off takes place between the propulsive and the transmission efficiency. As the BPR increases the FPR and jet velocities decrease and the propulsive efficiency improves. At the same time more energy travels through the bypass system and thus the transmission efficiency decreases. The transmission efficiency being of secondary importance, the optimum BPR presents quite high values. An increase in TET leads to increased jet velocities and thus the optimum BPR is moved to higher values.

The aforementioned analysis was conducted under constant OPR and component efficiency conditions. The effect of altering these conditions is treated by Fig. 2.7a and 2.7b, for which the following statements can be made:

- **An increase in the OPR leads to decreased optimum FPR values.** This statement stems from the current design trends of civil aircraft engines, but it is not necessarily correct according to the strict thermodynamic theory. In theory, there is an value of OPR which maximises the specific work output of the core. If the baseline value of OPR is lower than this value, the increase of OPR leads to an increase in specific work, while the opposite applies if the baseline value lies on the right of the value that maximises the specific work. Civil aircraft engines are designed for maximum efficiency and thus the OPR is always close to the value that maximises the efficiency and on the right of the maximum specific work point.

Thus, any increase in OPR naturally leads to a further decrease in the specific work output of the core. This decrease results in less energy being available for the LPT turbine and thus the FPR has to decrease in order to maintain a constant velocity ratio. As shown in Fig. 2.7a, this decrease is more important for low TETs than for high ones. This happens because at higher TETs, the increase in OPR results in a lower decrease of specific power.

- **Increased component efficiencies lead to higher optimum FPR values.** This results comes about due to two reasons. Firstly, the increased values of fan and LPT efficiency lead to higher ratios of cold to hot jet velocities. For the same energy available from the core, this naturally leads to higher fan pressure ratios. Moreover, the energy at the core exit increases due to the increased efficiencies and hence more power is available for the LPT. This augmented level of power has to be consumed by a higher FPR in order to keep the balance between the jet velocities.

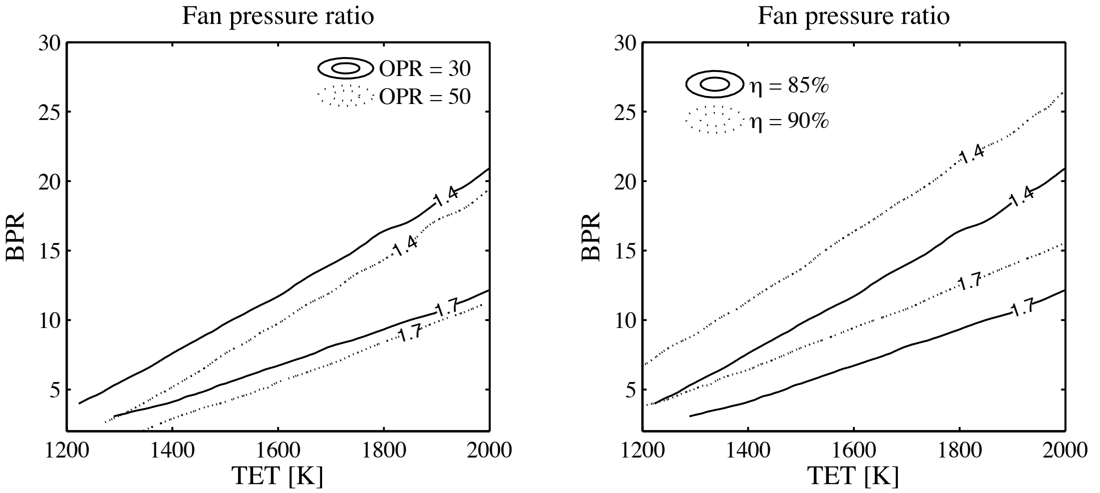

(a) The effect of OPR

(b) The effect of component efficiencies

Figure 2.7: The effect of OPR and component efficiencies on the optimum value of FPR.

Up to this point, the fan pressure ratio has been used as the indicator of propulsive efficiency and jet velocities. As shown by Eq. 2.8, the specific thrust ST is a more convenient η_{pr} indicator, while it has also the very important function of fixing the mass flow and diameter of the engine for a given thrust. Not unexpectedly, the two parameters are strongly interrelated, as proven by Guha [34]. Figure 2.8 proves this relation, by showing that all the points of different TET and BPR collapse into a single curve that relates the specific thrust with the fan pressure ratio. Henceforth the ST will be used analogously to FPR, as done in Fig. 2.9a, which corresponds to the analysis of Fig. 2.6. It must be underlined that throughout this chapter the term ST refers to the specific thrust at the top-of-climb point, as it is this point that sizes the fan diameter. It can be observed from Fig. 2.9a that there is an optimum value of ST which is around 75 m/s, a value which according to Guha [60] is much lower than the currently applied levels of ST. This difference is due to the effect of drag and weight, not captured by the uninstalled SFC, as explained in section 2.4.3.

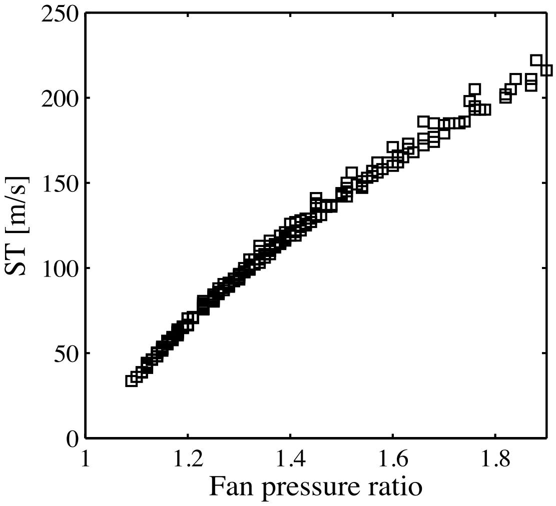

Figure 2.8: The relation between specific thrust (ST) and FPR ($\eta = 90\%$ $OPR = 30$). The plotted points represent results for the full range of TET and BPR.

Figure 2.9a shows another interesting aspect concerning the choice of TET. Following a constant ST line (e.g. $ST = 150m/s$) the engine soon reaches a point where a further increase in TET does not bring any benefits. Under constant ST conditions, the propulsive efficiency is fixed and the trade-off takes place between the core and transmission efficiencies. As the TET increases the core efficiency increases before it reaches an optimum value at about 1800-1900K. Results proving this statement can be found in the aforementioned works of Guha [26], Wilcock et al. [25] and Kurzke [27]. At the same time, for higher TETs the BPR increases in order to conserve a fixed value of ST. This increase in BPR brings about a degradation of the transmission efficiency. The ensemble of the above effects leads to the existence of an optimum TET very close to the currently used values. The phenomenon is accentuated if higher component efficiencies are used, as shown in Fig. 2.9b. The higher component efficiencies significantly decrease the TET value that optimises the core efficiency and hence from an efficiency point of view, increased TETs are completely uneconomical. Nonetheless, high TETs can still be used as a means to decrease the core size and weight. These results confirm the observations made by Guha [29], and are completely opposed to the widely held belief that from an efficiency point of view, high TETs are always beneficial.

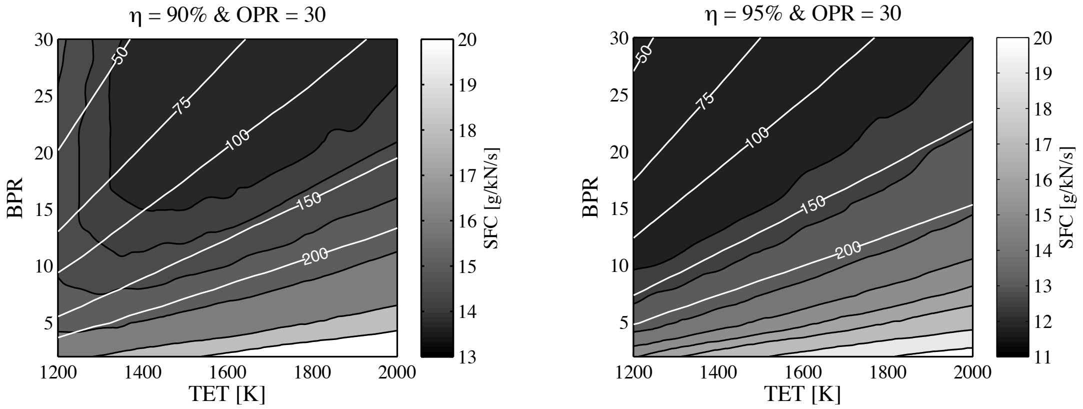

(a) Baseline map

(b) The effect of component efficiencies

Figure 2.9: The uninstalled SFC design map, using the specific thrust as a design parameter.

2.7.2.1 The TET ratio between take-off and climb

This short section deals with the TET ratio between take-off and climb/cruise and its variation throughout the design space. Jackson [7] stated that the lower the specific thrust the higher the TET at ToC relative to the ones observed at TO. This observation is confirmed by the results shown in Fig. 2.10, covering different TET, BPR, OPR and component efficiencies. There is a clear relation between ST and the ratio of TET, although there is some scatter of the points in the two extremities. This scatter is due to the variation of the fan efficiency for the extreme values of ST. As shown by Fig. 2.11, at very low ST the fan operating point at TO is above the surge line (see section 2.8.1), while at very high ST it moves towards the right extreme where the efficiency start degrading faster. Especially the points above the surge line are completely unrepresentative, as the fan efficiency results from extreme extrapolations.

The clear relation between the specific thrust and the TET ratio can be explained by the connection of ST to the jet velocities. A low ST leads to low jet velocities and a higher amount of thrust produced by the mass flow component. The higher the mass flow component of the thrust, the higher the sensitivity to the increases of Mach number and altitude. The sensitivity to Mach stems from the stronger component of momentum drag, which is proportional to the inlet mass flow of the engine. The sensitivity to the increase of altitude comes from the decrease in the air density, which directly impacts the mass flow and hence the thrust. Under constant TET between ToC and TO, and a fixed thrust at ToC, a higher thrust lapse rate leads to a higher thrust at TO. However, the thrust at TO is also fixed by aircraft requirements and thus the TET has to fall at TO in order to keep the thrust constant. That is the reason why lower ST, leads to TETs at climb which are closer to the ones at TO, or even higher. This conclusion shows another important impact of ST on engine design, operation and finally cost. Low ST engines, will experience much higher temperatures at climb and cruise (for a fixed maximum take-off temperature) and thus a significantly higher amount of their life will be consumed due to creep. At the same time, the cooling flow will probably have to be sized for the ToC point, if the maximum TET moves there. Alternatively, the design might choose to lower the temperatures at every operating point, or even to choose a higher ST, degrading this way the propulsive efficiency. The final decision, would depend on all the aforementioned aspects and is an answer that depends on the strategy and characteristics of the engine manufacturer.

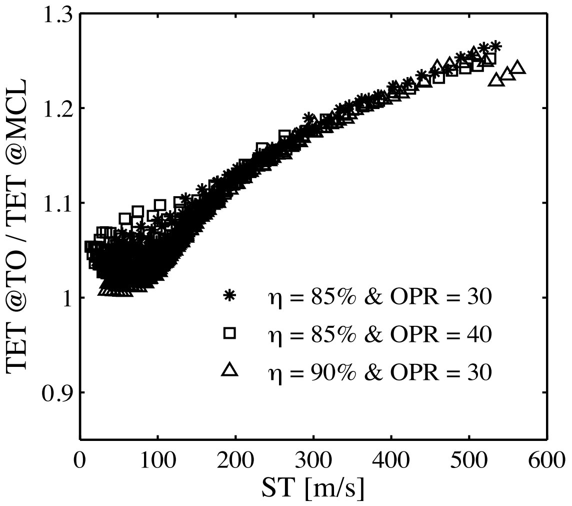

Figure 2.10: The relation between specific thrust (ST) and the ratio of TET between ToC and TO. The plotted points represent results for the full range of TET and BPR.

2.7.2.2 Design space limits for the selection of OPR

The overall pressure ratio (OPR) is selected in a way that optimises the efficiency of the core. The optimum OPR depends on the TET of the engine, according to the principle that a higher TET leads to a higher optimal OPR. Increasing the OPR further would degrade the core efficiency, unless a higher TET was employed. Figure 2.12 illustrates

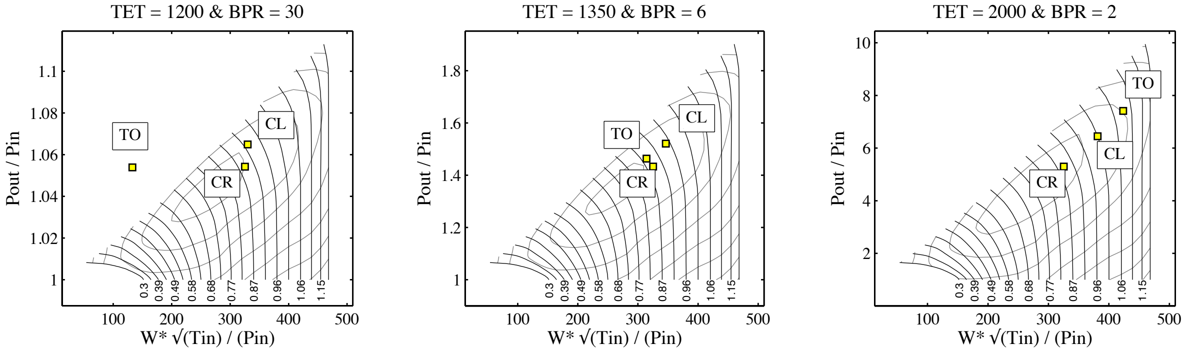

(a) Low ST

(b) Medium ST

(c) High ST

Figure 2.11: The effect of specific thrust (through the definition of TET and BPR) on the location of the TO point on the fan map ($\eta = 90\%\ OPR = 30$).

this effect for the entire design space of TET and BPR. The graphs are based on data for a baseline OPR of 30. Increasing the OPR to 40, 50 and 60 has a benefit on the right of the corresponding continuous line, one for each increased level of OPR (Fig. 2.12a). It is clear that increasing the OPR up to 60 has no benefit for TETs which are lower than about 1300K. Moreover, Fig. 2.12b shows that if the component efficiencies are increased the TET has a significantly lower impact on the optimum OPR, resulting in a benefit of increasing OPR for the whole design space. The effect of increased OPR seems also to have a weak dependence on BPR. Lower bypass ratio engines benefit from the decreased jet velocities as the core specific work decreases due to the higher OPR. Higher bypass ratio engines have already very low jet velocities and thus the effect of increasing OPR is lower.

Although the improvement of engine efficiency is the driving factor, the design choice is also limited by the maximum temperature at the exit of the compressor T_3, which normally occurs at TO. The dashed lines shown in Fig. 2.12 split the design space in the upper feasible region, and the lower non-feasible which exhibits T_3 higher than the limit of nickel based alloys (typically between 950-1000K). It is shown here, that the selection of OPR strongly depends on the selection of the BPR; in fact it can be observed that the dashed lines, resemble a lot to the constant specific thrust lines shown in Fig.2.9. Figure 2.13 proves this point by plotting the T_3 as a function of ST for the engines of the whole design space. It is clearly seen that the points collapse onto single curves of T_3 versus ST. The explanation for this phenomenon comes from the relation between ST and the ratio of TET between TO and ToC. For a given TET and OPR at cruise (or ToC), the TET and OPR at TO are lower for lower specific thrusts. In addition, figures 2.12b and 2.13b illustrate the beneficial effect of increasing the component efficiencies. Higher compressor efficiencies lead to lower exit temperatures for the same pressure ratio.

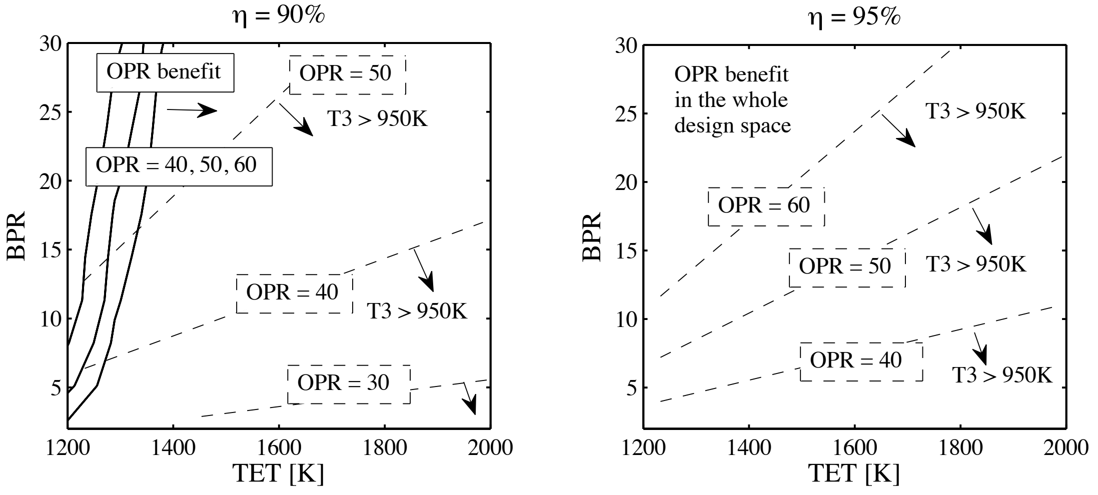

(a) (b)

Figure 2.12: The effect of component efficiencies and OPR on the maximum T_3 and on the uninstalled SFC. One continuous line for each increased level of OPR splits the design space in the right region where there is an SFC benefit and in the left where the SFC deteriorates. SFC benefit relative to OPR=30.

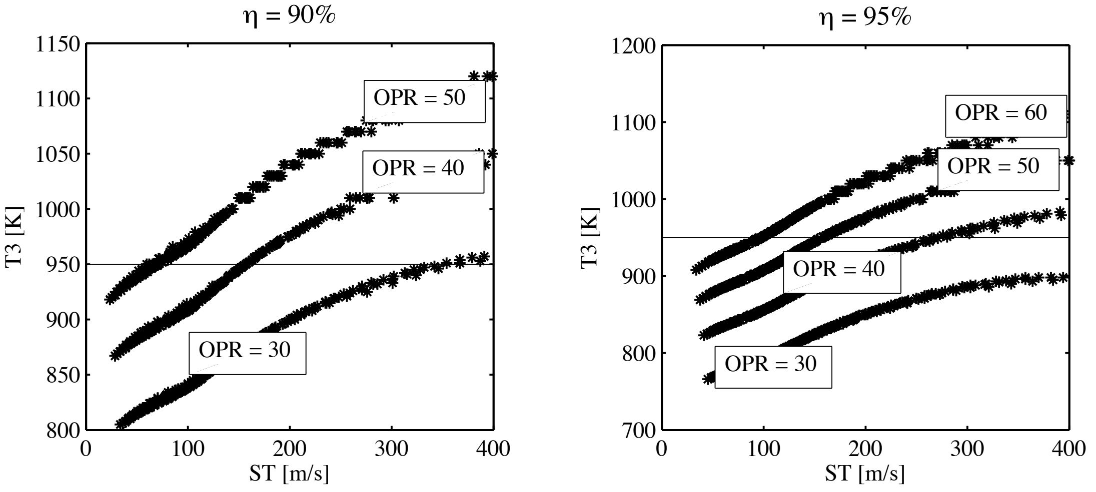

(a) (b)

Figure 2.13: The relation between OPR, specific thrust, component efficiencies and maximum T_3. The plotted points represent results for the full range of TET and BPR.

It is thus concluded that the increase of OPR, albeit beneficial for efficiency, must be accompanied by high compressor efficiencies, while it is also affected by the selection of the specific thrust of the engine. In a multi-design point code like the one described by Schutte [61], it would be possible not to include OPR as a design variable, but set instead the maximum value of T_3, which coupled with the selection of ST leads to a level of OPR.

2.8 LP system enabling technologies study

2.8.1 Variable area fan nozzle

Using simple assumptions and basic expressions that relate the bypass nozzle throat Mach number with its pressure ratio, Jackson [17] proved that low fan pressure ratio engines experience an increase of their pressure ratio at take-off. This results from the unchoking of the bypass nozzle that controls the operating point of the fan, limiting its mass flow capacity and leading it at surge as depicted in Fig. 2.11a. The lower the fan pressure ratio, the lower the nozzle pressure ratio and Mach number and hence the lower its mass flow capacity at take-off. This is illustrated by Fig. 2.14a which shows the relation between the fan Z parameter and its design pressure ratio, for engines of different TET, BPR, OPR and component efficiencies. The fan Z parameter is equal to 1 when the operating point is on the surge line, or 0.8 for a surge margin of 20%. Figure 2.14a confirms the unique dependency of the fan surge margin on its design point pressure ratio.

The fan operating point can be controlled by varying the bypass nozzle area. Opening the fan nozzle area increases the mass flow capacity and lowers the fan running line away from surge. This is shown by Fig. 2.14b where the relation between the surge margin and fan pressure ratio is repeated for different nozzle areas. Setting a Z parameter limit of about 0.82 (Fig. 2.14b) leads to a correlation between the fan pressure ratio and the required bypass nozzle area, as shown by Fig. 2.14c. The results of Jackson [17] are also depicted and good agreement is found between the two studies, although they are based on different engine configurations and assumptions. This is a strong indication that the required bypass nozzle area increase is only a function of the design point fan pressure ratio. As shown earlier, the fan pressure ratio is in turn strongly related to the specific thrust of the engine and therefore the required area increase could also be related with ST without a great loss of accuracy. Thus, the variation of the required area variation as an enabling technology has been established for the whole design space.

Having established the required area increase as a technology which enables lower FPRs, the next step considers its use for the achievement of variable cycle benefits. Kyritsis [9] proved that an increase of fan nozzle area at take-off leads to lower turbine entry temperatures under a fixed take-off thrust requirement. This lower TET results from the higher engine BPR and optimised fan efficiency achieved by opening the fan area. The effect of increased fan nozzle area on the ratio of TET between take-off and top-of-climb is depicted in Fig. 2.14d. The points of Fig. 2.10 were fitted by a curve and the process has been repeated for an area increase of 10 and 20 %. The transition to 10 and 20% was introduced at the specific thrusts which correspond to the respective values of fan pressure ratio as read from Fig. 2.14c.

It can be extracted from Fig. 2.14d, that for an engine with an ST of about 130 m/s, the 10% area increase reduces the ratio of TET from 1.083 to 1.05, bringing the TET at take-off closer to the one at ToC and mCR. For a hypothetical engine having a TET of 1800K at TO this would be translated in an increase in the ToC and mCR TET by approximately 50K. However, it must be underlined that this TET benefit strongly depends on the variations of fan efficiency as the area increases and the operating point moves on the fan map. In a similar single engine study, Kyritsis found that TET in flight increases by approximately 15K if the nozzle area is opened by 15% at take-off [9]. It is concluded that the use of increased fan nozzle area at take-off is analogous to increasing the take-off TET limit of the engine, as it allows higher in-flight TETs.

2.8.2 Gearbox study

2.8.2.1 Design assumptions

In order to proceed with the gearbox study, the thermodynamic analysis has to be extended by a preliminary design which translates the "pure" thermodynamic cycles in a real engine design. The most crucial design assumptions are listed in table 2.2, with most of the values being taken from the recommendations of Walsh and Fletcher [28].

The fan diameter is calculated using a given inlet Mach number and hub/tip ratio. The rotational speed of the low pressure spool is determined by a chosen fan tip Mach and the calculated tip diameter. The two compressors are designed for constant hub diameter and given inlet Mach numbers. The rotational speed of the high pressure spool is defined by the structural integrity of the high pressure turbine, given as a maximum AN^2 criterion. The high pressure turbine is designed for given inlet and outlet Mach numbers, a constant mean diameter and a typical aerodynamic loading. The same applies for the low pressure turbine, with the only difference being the constant hub configuration. This choice results in a simple design, which is realistic for engines with low number of stages, but leads to a somewhat pessimistic evaluation as the number of stages increases. In reality, the number of stages would be partially controlled by using an increasing hub diameter, upto the point that the design constraints are not violated.

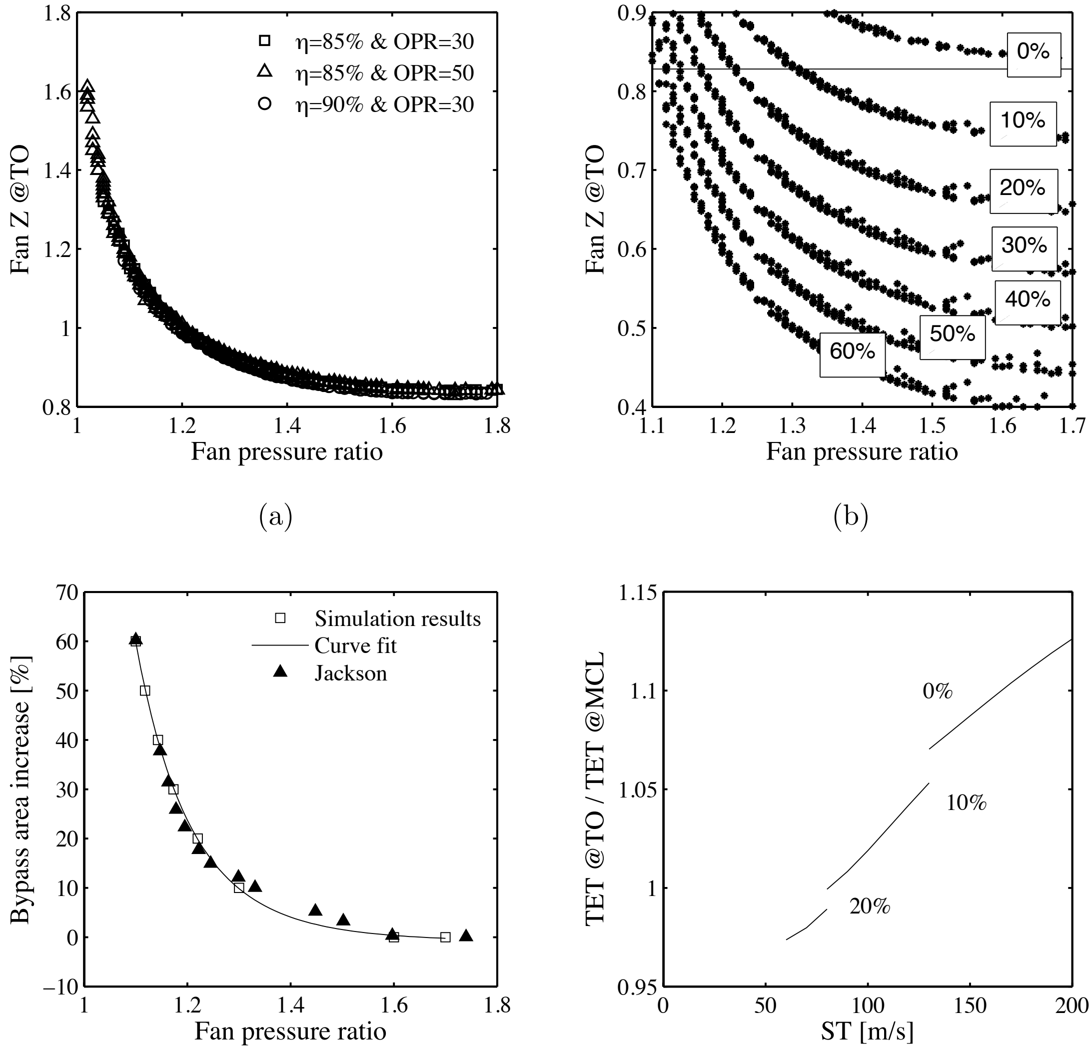

(a) (b)

(c) (d)

Figure 2.14: (a) The relation between FPR and the surge margin parameter for different component efficiencies and OPR, for the full range of TET and BPR. (b) The impact of varying the fan nozzle area at take-off on the fan surge margin parameter. (c) The required fan nozzle area increase at take-off in order to keep a safe fan margin. The results by Jackson can be found in [17]. (d) The impact of the fan nozzle area increase on the ratio of TET at take-off to the TET at mid-cruise.

Table 2.2: Basic preliminary design code assumptions

Parameter	Value
Fan inlet axial Mach	0.6
Fan h/t	0.32
Fan tip Mach	1.6
Booster configuration	constant hub
Booster inlet Mach	0.5
HPC configuration	constant tip
HPC inlet Mach	0.5
HPT configuration	constant mean
HPT inlet Mach	0.1
HPT outlet Mach	0.45
HPT AN^2	$50 \cdot 10^6$ $[rpm^2 m^2]$
HPT Aero Loading	2.8
LPT configuration	constant hub
LPT inlet Mach	0.45
LPT outlet Mach	0.40
LPT Aero Loading	2.5

2.8.2.2 Gearbox baseline results

The preliminary design code uses the thermodynamic data presented in the section 2.7.2, together with the design assumptions presented in the previous section and calculates the full engine configuration design, including the number of the low pressure turbine stages, which is the goal here. The results are shown in Fig. 2.15 for an OPR of 30 and component efficiencies equal to 90%. It is shown that the number of LPT stages increases for increasing bypass ratio or increasing turbine entry temperature. The analysis that follows attempts to shed some light on these trends.

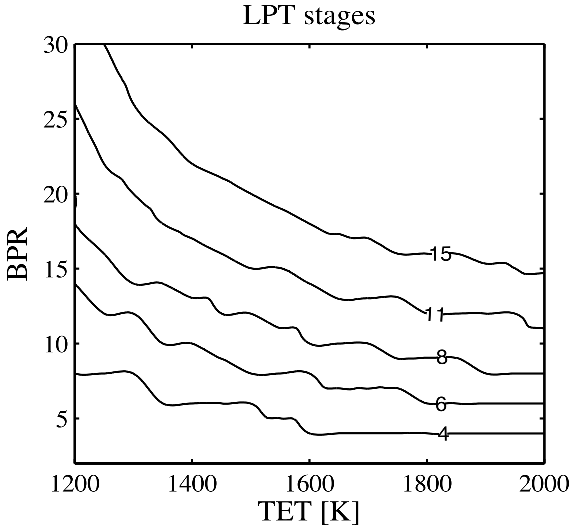

Figure 2.15: The relation between TET, BPR and the number of LPT stages ($\eta = 85\% \; OPR = 30$).

Using a simplified approach, the number of LPT stages can be calculated from the total enthalpy drop of the turbine and the chosen aerodynamic loading, which is equal to the ratio of the enthalpy drop per stage divided by the square of the mean blade speed. For the shake of simplicity, it is assumed that the enthalpy drop is equally divided between the stages and that the turbine uses a constant mean diameter configuration. Having made these assumptions, the number of stages can be calculated if the total enthalpy drop is divided by the enthalpy drop per stage, which is equal to the aerodynamic loading multiplied by the square of the mean blade speed (Eq. 2.16).

$$N_{lpt,stages} = \frac{\Delta h_{lpt}}{\left(\dfrac{\Delta h_{lpt}}{U^2_{lpt,m}}\right)_{stage} U^2_{lpt,m}} \tag{2.16}$$

The per stage aerodynamic loading being a design choice, it remains to be clarified how the thermodynamic cycle affects the total enthalpy drop of the turbine, and its mean blade speed. The low pressure spool power balance, given by Eq. 2.17, equates the turbine power with the power needed to drive the fan and the booster. By assuming that the injected fuel flow is negligible and by dividing by the common LPT and booster mass flow, the Eq. 2.18 is derived. The enthalpy differences for the two compressors are determined by their pressure ratios, for given polytropic efficiencies, as shown by Eq. 2.19. The booster pressure ratio can be calculated from the overall pressure ratio, and the assumption for a given pressure ratio split between the booster and the HPC, Eq. 2.20. Furthermore, the booster inlet temperature T_2 can be calculated from the fan inlet temperature T_1, the fan pressure ratio and polytropic efficiency. The low pressure turbine enthalpy difference is then calculated by Eq. 2.21, which is a function of the fan pressure ratio PR_f, the bypass ratio and the overall pressure ratio.

$$\Delta h_{lpt} \cdot W_{lpt} = \Delta h_f \cdot W_f + \Delta h_{bs} \cdot W_{bs} \tag{2.17}$$

$$\Delta h_{lpt} = (BPR + 1) \cdot \Delta h_f + \Delta h_{bs} \tag{2.18}$$

$$\Delta h_{lpt} = C_P \cdot (BPR + 1) \cdot T_1 \cdot \left(PR_f^{\dfrac{\gamma - 1}{\gamma \eta_{p,f}}} - 1 \right) + C_P \cdot T_2 \cdot \left(PR_{bs}^{\dfrac{\gamma - 1}{\gamma \eta_{p,bs}}} - 1 \right) \tag{2.19}$$

$$OPR = PR_f \cdot PR_{bs} \cdot PR_{hpc} = PR_f \cdot PR_{bs}^2 \cdot \frac{PR_{hpc}}{PR_{bs}} \Rightarrow PR_{bs} = \sqrt{\frac{OPR}{PR_f \dfrac{PR_{hpc}}{PR_{bs}}}} \tag{2.20}$$

$$\begin{aligned} \Delta h_{lpt} = C_P T_1 \cdot (BPR + 1) \left(PR_f^{\frac{\gamma - 1}{\gamma \eta_{p,f}}} - 1 \right) + \\ C_P T_1 \cdot PR_f^{\frac{\gamma - 1}{\gamma \eta_{p,f}}} \left[\left(\frac{OPR}{PR_f \frac{PR_{hpc}}{PR_{bs}}} \right)^{\frac{\gamma - 1}{2 \gamma \eta_{p,bs}}} - 1 \right] \end{aligned} \tag{2.21}$$

The results of Eq. 2.21 are compared with the rigorous cycle calculations, Fig. 2.16, and they show exceptionally good agreement both in trend and absolute values. In this graph the turbine entry temperature is used instead of the fan pressure ratio, with higher TETs corresponding to higher FPRs. It is therefore seen that under constant component efficiencies and OPR, the FPR and BPR are the factors driving the enthalpy drop in the LPT. The higher the FPR the higher the fan work and the higher the enthalpy drop demanded by the turbine. As the BPR increases under constant FPR, the fan work increases, the turbine mass flow falls and it has to compensate by increasing its enthalpy drop. As a matter of fact, the re-arrangement of variables from FPR-BPR to TET-BPR, shown in Fig. 2.16, indicates that the effect of FPR and BPR is better captured in a single dominant parameter of TET. Generally, higher turbine entry temperatures, reduce the core mass flow and thus increase the LPT enthalpy drop for the same fan power. This conclusion explains the increase in the number of LPT stages as the TET increases in Fig. 2.15.

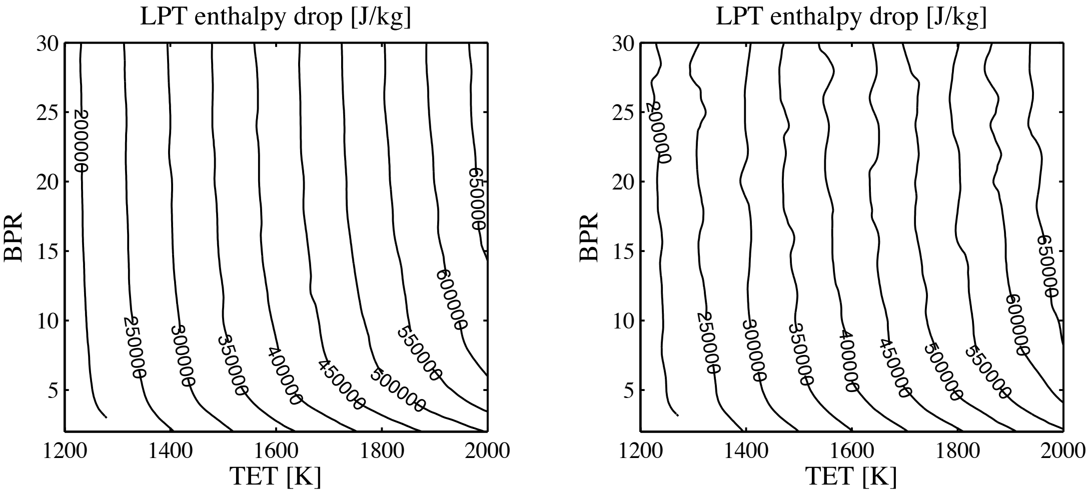

(a) Simulation results

(b) Equation 2.21 results

Figure 2.16: The relation between TET, BPR and the LPT enthalpy drop as predicted by the simulation framework and by the equation ($\eta = 85\%\ OPR = 30$).

The strong BPR dependence is however still not clear and the explanation will be sought in the calculation of the mean blade speed. The fan tip radius can be readily calculated from Eq. 2.22, if the fan mass flow, inlet axial velocity and hub/tip ratio are known. The tip radius is then used in Eq. 2.23, together with the chosen relative tip velocity $V_{f,rel,t}$ in order to calculate the rotational speed of the low pressure spool. The low pressure turbine inlet tip radius can be calculated by Eq. 2.24, if the turbine inlet mass flow, Mach number and hub/tip ratio are known. It can then be used in order to calculate the inlet mean radius, as shown by Eq. 2.25. The final low pressure turbine mean blade speed is calculated as the product of the LP spool rotational speed and the turbine inlet mean radius (Eq. 2.26), which combined with Eq. 2.23 and Eq. 2.25 results in the final Eq. 2.27.

$$W_f = \rho_f V_{f,ax} A_f = \rho_f V_{f,ax} \pi r_{f,t}^2 \left(1 - {(h/t)_f}^2\right) \Rightarrow r_{f,t} = \sqrt{\frac{W_f}{\rho_f V_{f,ax} \pi \left(1 - {(h/t)_f}^2\right)}} \tag{2.22}$$

$$\omega_{lp} = \frac{U_{f,t}}{r_{f,t}} = \frac{\sqrt{V_{f,rel,t}^2 - V_{f,ax}^2}}{\sqrt{\dfrac{W_f}{\rho_f V_{f,ax} \pi \left(1 - {(h/t)_f}^2\right)}}} \tag{2.23}$$

$$r_{lpt,t} = \sqrt{\frac{W_{lpt}}{\rho_{lpt} V_{lpt,ax} \pi \left(1 - {(h/t)_{lpt}}^2\right)}} \tag{2.24}$$

$$r_{lpt,m} = \frac{1}{2}\left(1 + \frac{1}{(h/t)_{lpt}}\right) \sqrt{\frac{W_{lpt}}{\rho_{lpt} V_{lpt,ax} \pi \left(1 - {(h/t)_{lpt}}^2\right)}} \tag{2.25}$$

$$U_{lpt,m} = r_{lpt,m} \cdot \omega_{lp} \tag{2.26}$$

$$U_{lpt,m} = \underbrace{\frac{1}{2}\left(1 + \frac{1}{(h/t)_{lpt}}\right)}_{Design\ term} \sqrt{\frac{1}{BPR} \frac{\rho_f}{\rho_{lpt}} \underbrace{\frac{\left(1 - {(h/t)_f}^2\right)}{\left(1 - {(h/t)_{lpt}}^2\right)} \frac{V_{f,ax}}{V_{lpt,ax}} \cdot \left(V_{f,rel,t}^2 - V_{f,ax}^2\right)}_{Design\ term}} \tag{2.27}$$

Three distinct terms are apparent in Eq. 2.27. A term which depends only on the design choices of velocities and hub/tip ratios, which is considered unaffected by thermodynamic cycle variations. A second term which depends on the density ratio between the fan and low pressure turbine inlet, which for this level of analysis will be considered constant. A last dominant term of BPR, which decreases the blade speed as BPR increases. In a real rigorous calculation, the velocity at the inlet of the low pressure turbine is determined by a choice of Mach number and thus depends on the variation of static pressures and temperatures. Furthermore, the density at the inlet of the LPT also depends on the static temperature and pressure at this point. Nonetheless, as shown in the comparative Fig. 2.17, Eq. 2.27 correctly captures the dominant effect of BPR. However, Fig. 2.17a shows that there is also a secondary effect of TET, which affects the density and velocity at the inlet of the turbine.

To sum up, under constant component efficiencies and OPR, the bypass ratio and the fan pressure ratio are the two dominant thermodynamic cycle parameters that drive the number of low pressure turbine stages. Higher bypass ratios lead to lower mean turbine blade speeds, lower enthalpy drop per stage and thus, for a given total enthalpy drop, higher number of stages. Higher fan pressure ratios result in higher fan work, increased enthalpy drop in the LPT and thus higher number of stages. Interestingly, the actual size of the engine is not present in the equations, neither in the form of a mass flow nor in the form of a diameter. This means that the results do not depend on the thrust requirement and the same design map (Fig. 2.15) can be used for short and long range applications.

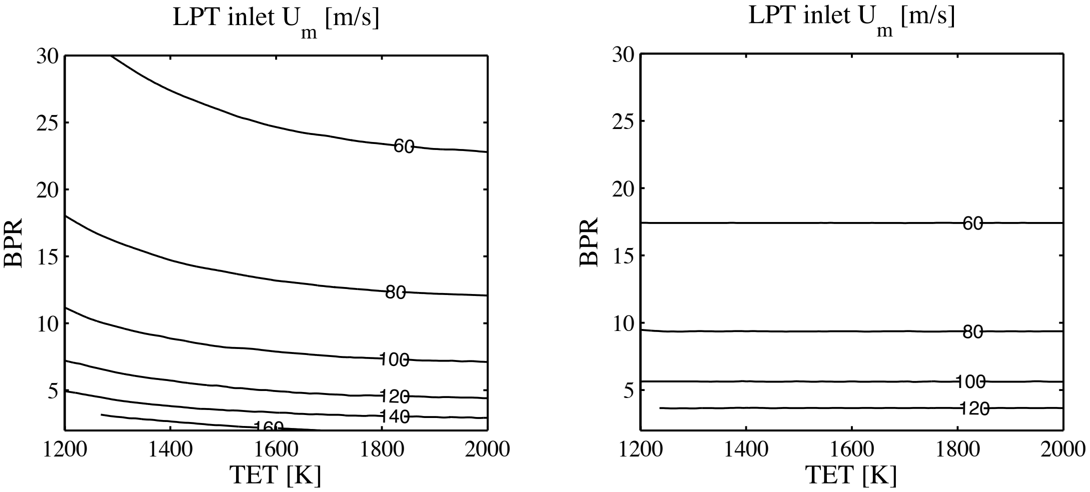

(a) Simulation results

(b) Equation 2.27 results

Figure 2.17: The relation between TET, BPR and the LPT mean blade speed as predicted by the equation for a constant density term or by the simulation framework with a real varying density term ($\eta = 85\%$ $OPR = 30$).

As so far the analysis has been carried out under constant component efficiencies and OPR, the next two sections will investigate the impact of changing these assumptions.

2.8.2.3 The effect of component efficiencies

According to Eq. 2.27 the component efficiencies have no important effect on the determination of the turbine mean blade speed. On the contrary, the efficiencies exist as terms in the equation that determines the required enthalpy drop in the LPT, Eq. 2.21. Higher component efficiencies are expected to reduce the enthalpy drop required for the same FPR and BPR. However, Fig. 2.18a shows that this effect is almost negligible, while there are also areas where the opposite trend is observed, probably due to secondary factors not captured in Eq. 2.21 and Eq. 2.27.

Although, there is no important effect on the FPR-BPR space, the same does not apply if the results are plotted in the usual TET-BPR space. As shown in Fig. 2.7b, an increase in component efficiencies tends to increase the fan pressure ratio under constant BPR and TET conditions. This increase in FPR leads to an augmented demand for LPT enthalpy drop according to Eq. 2.21 and hence increased number of LPT stages. This is illustrated by Fig. 2.18b where the iso-stages lines tend to go downwards in the TET-BPR space, following the opposite upwards movement of the iso-FPR lines of Fig. 2.7b.

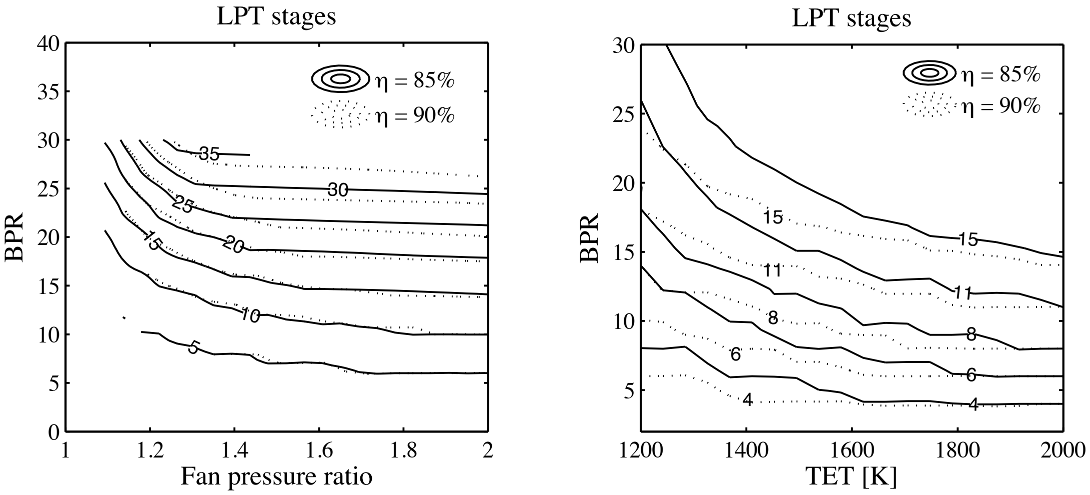

(a) FPR-BPR space (b) TET-BPR space

Figure 2.18: The effect of increased component efficiency on the number of stages (OPR = 30).

2.8.2.4 The effect of OPR

The impact of increasing the OPR is analysed with the help of figures 2.19 and 2.20. According to Eq. 2.21, in the FPR-BPR space, an increase in OPR rises the demand for power coming from the booster and hence requires a higher low pressure turbine enthalpy drop. This is also proven by Fig. 2.19a that depicts the lowering of the iso-enthalpy-drop lines for rising OPR. At the same time, the density term of Eq. 2.27 falls due to the increased LPT inlet density, and the mean blade speed drops, as seen in Fig. 2.19b. The combination of these two effects increases the number of stages in the FPR-BPR space, as illustrated by the downwards movement of the iso-stages lines in Fig. 2.20a.

The impact is slightly more complicated in the TET-BPR space shown in Fig. 2.20b. The aforementioned increase in the number of stages under constant FPR conditions, is counteracted by the decrease in optimum FPR depicted in Fig. 2.7a. The latter effect is stronger at the low end of TET and the former dominates for normal to high TETs. Thus, the dotted lines are higher than the continuous ones on the left side of Fig. 2.20b, while the opposite applies for the right side.

It can be concluded that for the greatest part of the TET-BPR design space, an increase of OPR results in a higher demand for low pressure turbine number of stages, due to the greater required enthalpy drop and the resulting lower mean blade speed.

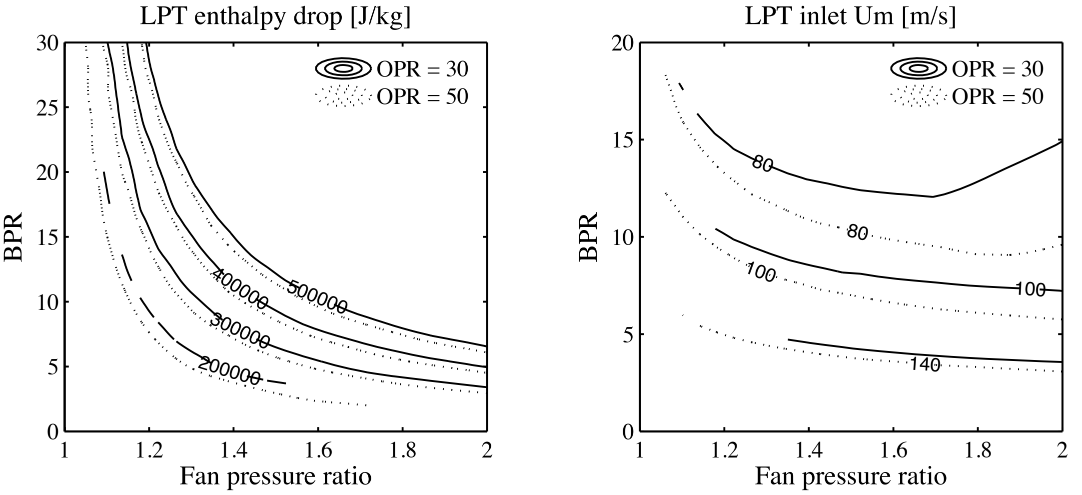

(a)

(b)

Figure 2.19: The effect of increased OPR on the LPT enthalpy drop and mean blade speed ($\eta = 85\%$).

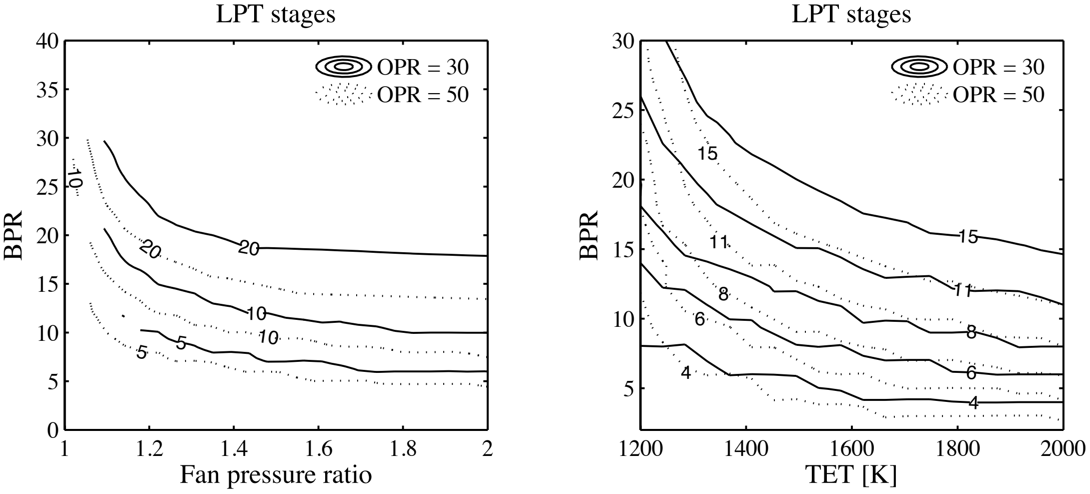

(a) FPR-BPR space

(b) TET-BPR space

Figure 2.20: The effect of increased OPR on the number of stages ($\eta = 85\%$).

2.9 Installed performance results

The title installed performance comprises all the previously analysed results in order to create a design space map that shows the position of the optimum short and long range engines and the technologies required to implement them. The preliminary design code has already calculated the weight of the engine and its dimensions, which are subsequently used in order to estimate its drag (see section 2.4.3). Table 2.3 lists the assumptions used in the installed performance analysis as discussed in section 2.4.3, with typical ranges for short and long range missions. A set of higher technology specifications is given in table 2.4 corresponding to a technology improvement typically taking place within approximately 20 years [10, 17, 62–67].

Table 2.3: Installed performance calculation assumptions

Parameter	Value
Short range	3000 km
Long range	14000 km
Drag coefficient C_D	0.002
Drag interference factor κ_i	1.2
Nacelle density factor κ_{nac}	24.88 kg/m^2
Cowl L/D ratio	1.5

Table 2.4: Low weight and drag case assumptions

Parameter	Value
Drag coefficient C_D	0.001
Drag interference factor κ_i	1.2
Nacelle density factor κ_{nac}	20 kg/m^2
Cowl L/D ratio	1
Fan & LPT weight	-50%
Other components weight	-15%

The design space maps for the short and long range missions are depicted in Fig. 2.21 and 2.22 respectively. Each sub-figure shows the variation of the range factor K_r in the TET-BPR design space, for given component efficiencies and OPR. The sub-figures 2.21d and 2.22d add the case of improved installation technology, according to the assumptions of table 2.4. The continuous lines represent the lines of equal specific thrust, the dashed lines show the number of LPT stages required and the dash-dot lines the TET at take-off conditions. The requirement for variable fan area as function of FPR, shown in Fig. 2.14c, has been translated into a function of ST using Fig. 2.8. This results in a requirement for 10% fan nozzle area increase for engines with ST lower than 130 m/s and 20% for the ones with ST lower than 80 m/s. Only the iso-stages line of 7 and 8 LPT stages are depicted, as after this threshold the number of LPT parts would be excessively high and a geared configuration would be possibly required.

As a preliminary step of this results analysis, table 2.5 presents the sensitivity of the range factor to the variation of SFC, drag and weight for the short and long range mission. The baseline reference values correspond to the square points of Fig. 2.21a and 2.22a for the short and long range engine respectively. As expected, the SFC dominates the installed performance, with a higher impact for the long range mission where the vast majority of the fuel is consumed at cruise. The weight has the second greatest influence, especially for the short range mission where the exchange rate is almost three times higher than the long range one. The influence of drag is much less, possibly due to optimistic assumptions in the calculation of nacelle drag.

2.9.1 Validation

The square point on Fig. 2.21a represents the baseline optimum, typical of engines currently in service in the short range market. With a bypass ratio around 5 and a diameter around 1.5m (Fig. 2.23), it is not far from the data published in Janes for the CFM and V2500 engines [62]. Furthermore, Fig. 2.21d shows that in the advanced installation technology case, the resulting optimum bypass ratio of about 8 (circle point) and the corresponding optimum diameter of about 1.7m are not far from the claimed values of the new LEAP engine [62].

Similarly, for the long range baseline case of Fig. 2.22a (square point), the bypass ratio of about 7 and the diameter of 3m are again not far from the values of the current GE90 and RR Trent 892 engines [17, 62].

In both short and long range engines, the turbine entry temperature is selected in order to have a good compromise and agreement with the published bypass ratios [62] and the estimated current and future levels of TET [6, 8, 29, 36, 37, 62].

Hence, it can be claimed that the used models and assumptions lead to realistic solutions and can be safely used in order to extract further conclusions.

2.9.2 Optimum specific thrust

The first observation that can be made for 2.21a, is that the optimum short range ST is around 260 m/s, which is much lower than the uninstalled optimum of 75 m/s (Fig.

2.9a). This significant difference between the two solutions is attributed to the inclusion of the engine weight and drag effects, which penalise higher diameter solutions. Secondly, it is readily observed from all the sub-cases of Fig. 2.21 that the optimum ST does not depend on the engine OPR or component efficiencies. It is only a function of the installed performance characteristics, which include the mission range and the variation of the engine weight and drag with ST. As seen in sub-figure 2.21d, a lower optimum ST can be attained only when the installation technology is improved.

Along the same lines, Fig. 2.22a shows that the optimum specific thrust for the baseline long range engine is significantly lower, with a value of 180 m/s. The corresponding advanced installation technology optimum falls to 142 m/s according to Fig. 2.22d. These significantly lower values of optimum ST are readily explained by the range factor exchange factors of table 2.5, which show the higher important of SFC for long range applications.

The above observations confirm the statements by Young [38] and Guha [29] regarding the optimisation of ST, which should be done independently from the other engine parameters and in close cooperation with the aircraft manufacturer.

2.9.3 TET limitation

Having chosen the specific thrust following the installed performance considerations, the design can then move on an iso-ST line in compliance with the constraints of TET. Applying a limit on the maximum TET at take-off immediately fixes the design point BPR. This is why the core of the engine is sized at take-off. The diameter is fixed by the selection of specific thrust and then the maximum allowable temperature gives the maximum allowable BPR and thus the minimum possible core size. The same limit on BPR can be applied by the top-of-climb temperature if it is higher than the take-off one, or if it is high enough to compromise the creep life of the engine.

2.9.4 HPC delivery temperature limitation

According to the analysis presented in section 2.7.2.2, a limitation on the high pressure compressor delivery temperature must also be taken into account. With the optimum specific thrust being defined by the installed performance, the only way to control the T_3 at take-off is via the overall pressure ratio for a given level of component efficiencies. Figures 2.12a and 2.21a show that current short range engines do not face an important restriction (the current levels of OPR being about 30), but a future increase of OPR up to 40 can only be brought about with a parallel increase of their compressor efficiency (Fig. 2.12b). On the other hand, a future amelioration of the installation technology would further decrease the optimum ST, relieving this way the HPC exit temperatures at take-off as shown by Fig. 2.12.

The long range engines are located closer to the T_3 limit due to their higher overall pressure ratios. Figure 2.12a shows that with a polytropic efficiency of 90% and using the optimum ST of 180 m/s (Fig. 2.22a), the attained level of T_3 would be higher than 950 K but still lower than 1000 K. This is an indication that current long range engines have probably compressor polytropic efficiencies higher than 90% or cruise OPR less than 40. In fact, these hypotheses are confirmed by the Trent 892 model of Jackson [17], which employs polytropic efficiencies of 92%, 92.5% and 88.6% for the fan hub, IPC and HPC respectively. With this set of efficiencies and with a cruise OPR level of 33 (versus 40 assumed here) Jackson's model generates a T_3 of 910 K at take-off. This value is already very close to the limit, proving the point that long range engines OPR is probably limited by the T_3 at take-off.

Once more, a possible future increase of OPR from 40 to 50 will be enabled by higher polytropic efficiencies, better materials and the lower optimum levels of specific thrust due to better installation technology.

2.9.5 Variable area fan nozzle

The results of Fig. 2.21 show that no variable fan nozzles are needed for the short range engine, even for the decreased optimum ST of 215 m/s (Fig. 2.21d). A geared configuration would probably result in a more aggressive relation between weight and diameter with the optimum translated towards lower ST. For example, if one follows the iso-TET@TO line of 2000 K up to the value of BPR equal to 13 (maximum value claimed in Janes for the GTF of Pratt & Whitney), they would end up with a design much closer to the requirement for variable fan nozzle.

On the other hand, the inherently lower ST long range engines are much closer to the limit of fixed geometry nozzle. According to Fig. 2.22d, the next generation of long range engines will most probably need the introduction of such a technology in order to ensure the safe operation of the fan at take-off.

The impact of the variable area fan nozzle on the selection of the optimum solution will be commented in section 2.9.7 with the help of the calculated performance exchange rates.

2.9.6 Gearbox

Figure 2.21a shows that the baseline short range engines are well inside the conventional turbofan design area, with a number of LPT stages below 8. A higher design turbine entry temperature, a higher OPR (Fig. 2.21b) or a higher level of component efficiencies (Fig. 2.21c) would not change the optimum ST but they would move the iso-stages lines downwards, compressing this way the available conventional turbofan area. The explanation of these trends has already been given in section 2.8.2. Finally, the lower optimum ST enabled by a low drag and weight installation would position the optimum design to the limit of the non-geared space (square point Fig. 2.21d) or even slightly inside the geared configuration area if the TET is also increased (circle point Fig. 2.21d). In reality the circle point of Fig. 2.21d could be still implemented without a gearbox if the number of stages was reduced to 7-8, 7 being the value claimed for the LEAP engine [68]. A possible way of achieving this is indicated by Eq. 2.26, which shows that an increase of the mean LPT radius could lead to a higher blade speed and a consequent decrease in the number of stages.

The schematic of GE-90 published in Janes [62] clearly shows the implementation of this practice, with the LPT inlet radius being significantly higher than the HPT exit. If a fictitious GE-90 engine was approximately positioned on the design map of Fig. 2.22a, using a value of TET at take-off equal to 1865 K and BPR equal to 8.1 as claimed in Janes [62], the resulting number of stages would be about 8. In reality the engine has only 6 stages, difference which is attributed in this study's design assumption of a hub radius which is constant and equal to the exit of the HPT.

Notwithstanding the above simplifying assumption regarding the LPT radius, it is evident from Fig. 2.22 that long range engines are much closer to the limit of non-geared configurations. This is not the result of a size effect between high and low thrust engines, but the outcome of the lower optimum specific thrusts inherent in long range applications. Figure 2.22d clearly illustrates that if the installation technology improves, the new long range optimum will move well inside the geared configuration space. This effect will be slightly delayed for three spool configurations which tend to have an inherently lower number of stages in the LPT (according to Jackson [17] the RR Trent 892 has 5 LPT stages versus the 6 of the GE-90).

In closing, it must be reminded that the geared configuration itself is likely to have a more aggressive relation between the engine diameter and its weight. This means that the engine weight would increase slower with diameter for a geared configuration than for a conventional. This argument is based on Riegler's argument [10] that for the same thermodynamic cycle, a geared configuration would have an LPT 40% lighter. Another proof that this argument might be correct is the higher diameters proposed by Pratt & Whitney relative to the ones proposed for the LEAP engines for the same applications [68]. This line of thought leads to the conclusion that a geared configuration will probably have a lower optimum ST, unlocking this way a further SFC benefit by better restraining the installation losses.

2.9.7 Exchange rates

This exchange rate analysis attempts to quantify all the design trends mentioned in the previous sections. Figure 2.24 shows the percentage change of SFC and K_r for given changes of OPR, TET, installation technology and specific thrust. The results are repeated for the short and long range engine, for component efficiencies of 90 and 95 percent. The short range baseline engine corresponds to the square point of Fig. 2.21a and the long range on the square point of Fig. 2.22a. The specific thrust and diameter are considered constant for all the step changes apart from the last which considers the reduction of specific thrust. As shown in Fig. 2.24, the improvement of component efficiencies brings in its own a significant improvement of performance and this a proof that engine design will definitely attempt to follow this path. Finally, with the drag playing a negligible role, the differences between the SFC and the K_r can be explained using the variation in SFC and weight and the exchange rates shown in table 2.5.

2.9.7.1 Overall pressure ratio

For all the cases of Fig. 2.24, the increase of OPR leads to a decrease in SFC with a lesser decrease in K_r due to the variations of engine weight. The SFC improvement is higher for the short range engine due to the lower baseline OPR of 30. This occurs because the curve between OPR and SFC demonstrates an asymptotic trend as OPR increases. Hence, a delta applied on a low OPR has a greater impact than the same delta applied on a higher OPR. Along the same lines, the improvement is higher for high efficiencies than for low, due to the shifting of the optimum OPR towards higher values as the efficiencies increase [27].

Regarding the installed performance, the preliminary design code predicts slight reductions of weight for the short range engine, while the opposite occurs for the long range. Although more investigation is required, this effect could be probably attributed to the lower fan weight as the OPR increases and the core gets bigger with a constant fan diameter. In the long range case, the opposite effect of increasing core size and engine length dominates, the weight increases and this widens the gap between SFC and K_r.

In summary, an increase of 25% in OPR can improve the SFC by 1-3% for a short range engine and by about 1% for a long range one. Depending on the variations of engine weight this can be translated in an improvement of fuel burn by 1-1.5% for the short range engine and up to 1% for the long range one.

2.9.7.2 Turbine entry temperature and Variable area fan nozzle

An increase of TET by 100 K brings at all cases an SFC improvement and an approximately equal or even higher improvement of fuel burn (proportional to K_r). This happens due to the reduction of weight due to the smaller size of the hotter engine core. The SFC improvement is lower for the higher efficiencies case due to the lower levels of the optimum TET, as described in section 2.2. Similarly, the SFC improvement is higher for the long range engine due to its higher OPR, which shifts the optimum TET towards higher values

[27]. The beneficial reduction of weight is more evident in the short range case, where the K_r improves more than the SFC. This happens because of the higher impact of engine weight on the short range fuel burn as proven by table 2.5.

As a general comment, the exchange rates of TET confirm the arguments of Kurzke [27], concerning the limited prospects of further TET increases. Especially if the component efficiencies continue to increase, the positive impact of TET will be extinguished or even reversed. This can be aggravated more if the negative effects of small size and higher cooling flows are taken into account.

In the light of the above observations, the benefits of introducing a variable area fan nozzle as a means of achieving a smaller and hotter core does not seem appealing. It has been shown in section 2.8.1 that a VFN could help increase the cruise TET by 15-50K. According to Fig. 2.24 this can bring a maximum K_r improvement of 1% which could easily reduce to zero if the aforementioned negative effects are taken into account. Considering the added complexity of a variable nozzle, its introduction is not justified from the results shown here.

2.9.7.3 Improved installation technology and lower specific thrust

The effect of improving the installation technology by reducing the engine drag and weight is immediately apparent from all the cases of Fig. 2.24. Without changing the engine cycle - hence SFC being constant - this technology step can deliver a fuel reduction of up to 13 and 7 percent for the short and long range engines respectively. This is why all the engine manufacturers invest a lot in composite and lightweight materials.

Moreover, this technology improvement can unlock a further 4.5 to 6.5 percent SFC improvement through a lower optimum specific thrust. The low value of 4.5% corresponds to the long range which already has a low ST and thus is less affected by the technology step change. The exact K_r potential of the 4.5-6.5% SFC improvement depends on the weight characteristics of the engine. Figure 2.24 demonstrates that it is easier to release this SFC potential in the long range case where efficiency is more important than engine weight. Based on the assumptions of this study, the reduction of ST could bring a maximum K_r reduction of 1.7 and 2.5 percent for the short and long range engines respectively.

The potential benefits of lighter geared configuration also become apparent. If a geared configuration could "soften" the relation between engine diameter and weight, the gap between SFC and K_r would further diminish. The exact amount of this potential can only be quantified with a more detailed engine design investigation, which is outside the scope of this work.

2.9.8 Some possible design paths

2.9.8.1 Short range engine

Starting from the baseline square point of Fig. 2.21a, the design will certainly go towards higher component efficiencies and lower installation losses. This is justified by the significant exchange rates shown in Fig. 2.24 for these two step changes, delivering a fuel decrease of up to 23%. The thermal efficiency will be then improved by increasing the OPR, with the T_3 being under control due to the higher compressor efficiencies. This would bring another 1.7% of fuel reduction. The specific thrust would be decreased moving to the new optimum of 215 m/s, reducing thereby the fuel by 1.2% (square point Fig. 2.21d). At this point the design is at the edge of the conventional non-geared design. A further increase in TET would be probably avoided, as it would lead to negligible fuel reductions (Fig. 2.24b) and would move the design towards the more complex geared configuration (circle point of Fig. 2.21d). The fuel burn difference between the baseline engine and the final one, could reach the total of 25.9%. In a most likely scenario where only half of the component and installation improvement were achieved, this fuel reduction would reduce down to 14.4%, which is close to the claimed improvement between the LEAP and the CFM56 engines [62, 68].

2.9.8.2 Long range engine

Following the same process for the long range engine, and starting again from the square point of Fig. 2.22a, the improved efficiencies and installation technology deliver a fuel decrease up to 19%. The increase of OPR would bring a fuel burn reduction of 0.8% and the new optimum ST of 142 m/s another 1.5%. At this point the solution lies in the triangle point of Fig. 2.22d, well inside the geared configuration space. A higher TET could potentially lead to a maximum improvement of 0.8%, which however could compromise the creep life of the engine.

At this point it would be quite interesting to contemplate the scenario where a geared configuration were to be avoided at all cost. In that case the design would have to move to a significantly lower TET at the square point of Fig. 2.22d. This would result in a fuel burn about 2% worse, but with a TET lower by 200 K and without the need for a gearbox. The fuel burn increase of 2% could be even smaller, if the reduced cooling requirement and the lower component size effects were taken into account. To sum up, if all the aforementioned improvements were introduced, the final engine (circle point in Fig. 2.22d) would have a fuel burn 22.1% lower than the baseline. Once again, in the most likely scenario where only half the improvement of efficiencies and installation were to take place, the reduction would reduce to 12.6%. If no gearbox were to be used, the maximum benefit would reduce to 19.3% and the most likely to 9.8%; i.e. a difference of 2.8% between the conventional and the geared configuration. This difference would be a bit higher, if the geared configuration resulted in a lower weight for the circle point of 2.22d, relative to the weight calculated here using the non-geared assumptions.

2.10 Conclusions

The aim of this chapter was to create a design space that shows the position of the optimum short and long range engines and to demonstrate which low pressure system technologies are required for their implementation.

An extensive literature review was conducted in order to clarify the parameters that drive engine efficiency, understand the current design trends and the enabling technologies required. The variable area fan nozzles and the geared architecture are the two technologies identified as the natural extension of the current design trends of turbofan engines. An analysis and optimisation framework was set up, comprising models that predict the engine performance, the dimensions and weight, the drag, and the installed performance. The engine performance model has been updated in order to correctly simulate the combustor balance, which results in the existence of a turbine entry temperature optimum. The principles of engine preliminary design were studied and translated into a numerical problem formulation using the created optimisation framework. The analysis was focused on a two-spool turbofan configuration for a short and a long range mission.

The uninstalled performance analysis established and clarified the relations between the specific thrust, the bypass ratio, the turbine entry temperature, the overall pressure ratio, the component efficiencies and the optimum value of the fan pressure ratio. The specific thrust was found as the parameter dominating the design, for it defines the fan pressure ratio, the propulsive efficiency, the engine diameter and the relation between the in-flight and the take-off turbine entry temperature. A lower specific thrust results in a cooler engine at take-off for a fixed value of turbine entry temperature at top-of-climb. "Relieving" the engine power setting at take-off also allows higher overall pressure ratios to be used at top-of-climb, improving thereby the engine thermal efficiency, without reaching excessive temperatures at the exit of the high-pressure compressor.

The requirement for a variable area fan nozzle was connected with the design fan pressure ratio of the engine. A relation was also found to exist between the required area increase and the fan pressure ratio, confirming this way the results of Jackson [17]. The strong relation between the fan pressure ratio and the engine specific thrust results in a law that defines the required area increase according to the specific thrust. Engines with specific thrust lower than 130 m/s require a nozzle area increase of 10%, while an increase of 20% is needed for engines with specific thrust lower than 80 m/s. The variable area fan nozzle can also be used in order to achieve the same take-off thrust with a lower turbine entry temperature, enabling this way the design of engines with cores smaller and hotter by up to 50 K.

The gearbox study related the number of low pressure turbine stages to the thermodynamic cycle characteristics. The fan pressure ratio and the bypass ratio are the dominant parameters. Increased bypass ratios increase the number of stages, due to the lower turbine blade speeds and the higher required turbine enthalpy drop. Increased fan pressure ratios increase the number of stages due to the higher fan work that increases the required turbine enthalpy drop. Increased overall pressure ratio and component efficiencies compress the conventional turbofan design space by increasing the number of stages needed for the same turbine entry temperature and bypass ratio. No size effect is found to exist and thus two engines sharing the same cycle and design but with different thrusts will have the same number of low pressure turbine stages.

The installed performance integrates all the results in order to create the final design space maps. The results showed good agreement against current and near future engines of the short and long range market. The optimum specific thrust is determined only by the installation characteristics and it is lower for engines with longer range, lower weight and lower drag. Having defined the specific thrust through the installed performance trade-offs, the limits of turbine entry temperature subsequently impose the minimum allowable engine core size. The optimum value of specific thrust, also fixes the maximum allowable design overall pressure ratio with respect to the compressor exit temperature restrictions at take-off.

The created design space maps show that the variable area fan nozzle will be probably required for the next generation of long range engines, due to their low optimum specific thrust. The gearbox will be also probably needed for both short and long range engines, as the lower specific thrust, higher overall pressure ratio and improved component efficiencies are pushing the conventional turbofan to its limits. The long range engines have the priority as they feature higher overall pressure ratios and lower specific thrusts.

Only mediocre improvements in thermal efficiency can be achieved by increasing the overall pressure ratio and turbine entry temperature relative to today's levels, confirming the statements of Kurzke [27, 36]. Increasing the overall pressure ratio by 25% can deliver a fuel burn improvement of 1.7 and 0.8 percent for the short and long range engines respectively. Increasing the TET by 100 K leads to almost no improvement for the short range and to a 0.8% improvement for the long range engine. The OPR benefit increases for higher component efficiencies, while the opposite happens with TET. The above trends mean that there is probably no benefit in using the variable area fan nozzle in order to achieve a smaller and hotter core design.

In an extreme scenario the turbine entry temperatures could even decrease by 200 K relative to today's levels, in order to decrease the bypass ratio and avoid completely the introduction of a gearbox. This scenario could result in an engine with potentially lower maintenance costs, lower cooling requirements and lower component size effects, without an excessive efficiency penalty as long as its weight is controlled.

Future fuel reductions are most likely to be sought by improvements of component efficiencies, reduced engine weight and drag, and lower specific thrusts.

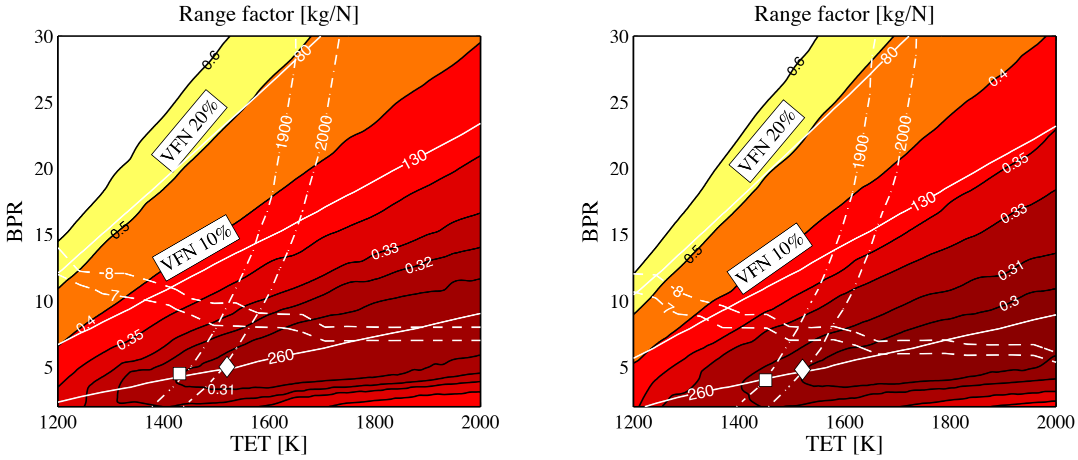

(a) OPR = 30 & $\eta = 90\%$ (b) OPR = 40 & $\eta = 90\%$

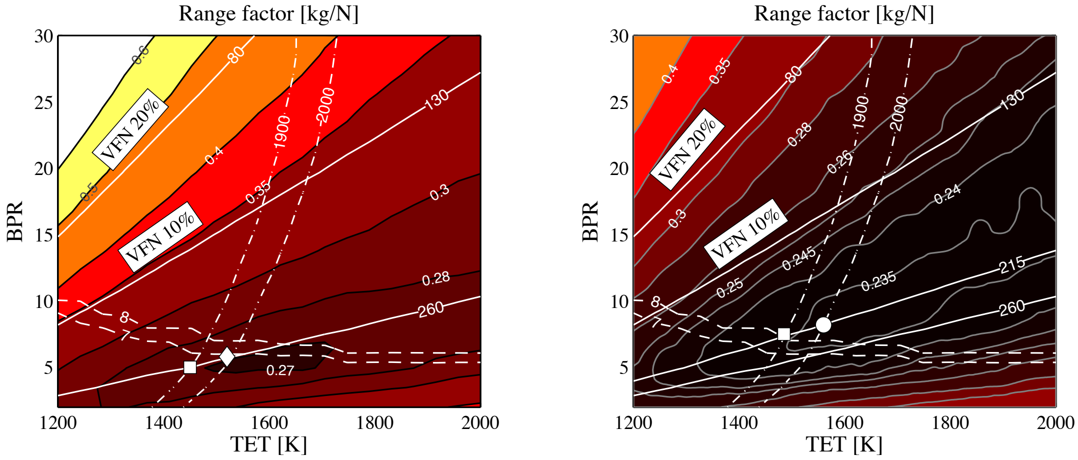

(c) OPR = 40 & $\eta = 95\%$ (d) OPR = 40 & $\eta = 95\%$
Low weight and drag

Figure 2.21: The short range design map for different OPR and component efficiencies. Square: baseline optimum. Diamond: increased TET optimum. Circle: Geared increased TET optimum. Continuous lines: iso ST [m/s] at ToC. Dotted lines: iso number of LPT stages. Dash-dot lines: iso TET [K] at TO.

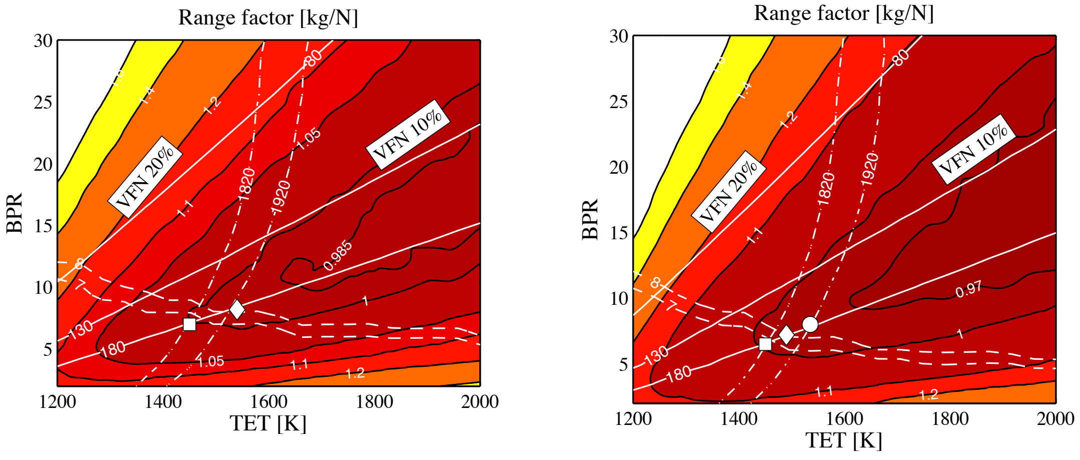

(a) OPR = 40 & $\eta = 90\%$

(b) OPR = 50 & $\eta = 90\%$

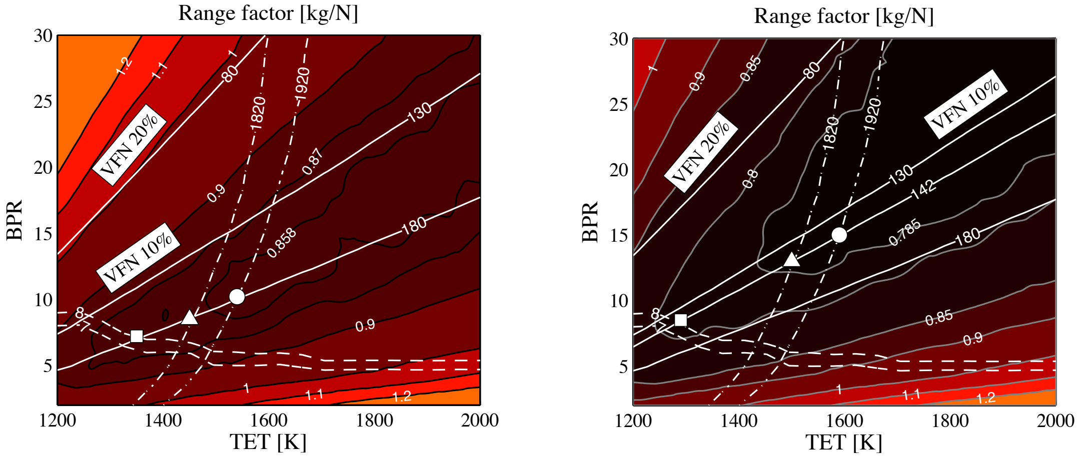

(c) OPR = 50 & $\eta = 95\%$

(d) OPR = 50 & $\eta = 95\%$
Low weight and drag

Figure 2.22: The long range design map for different OPR and component efficiencies. Square: baseline optimum. Diamond: increased TET optimum. Triangle: Geared optimum. Circle: Geared increased TET optimum. Continuous lines: iso ST [m/s] at ToC. Dotted lines: iso number of LPT stages. Dash-dot lines: iso TET [K] at TO.

Table 2.5: Range factor engine parameters exchange rates

Delta parameter	Delta K_r SR	Delta K_r LR
-1% SFC	-0.68%	-0.89%
-1% Drag	-0.01%	-0.02%
-1% Weight	-0.33%	-0.13%

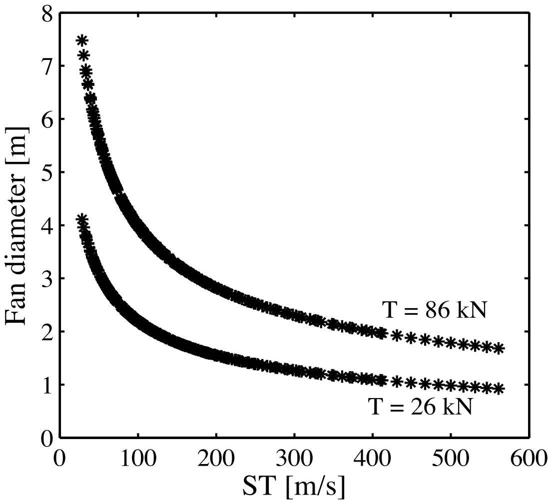

Figure 2.23: The relation between the specific thrust and the fan tip diameter for the short and long range engine ($\eta = 90\%$ $OPR = 40$).

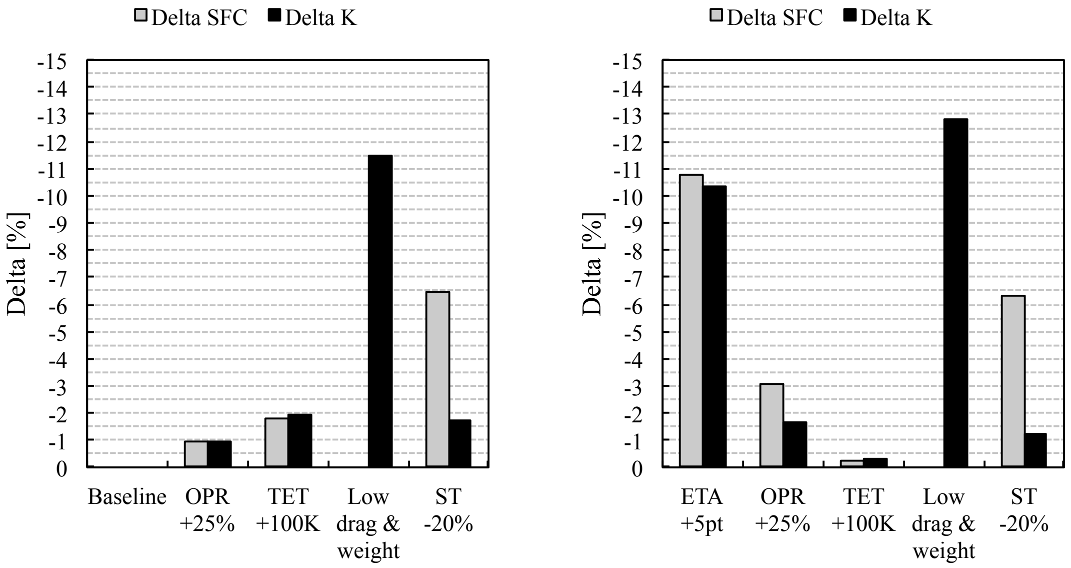

(a) Short range & $\eta = 90\%$ (b) Short range & $\eta = 95\%$

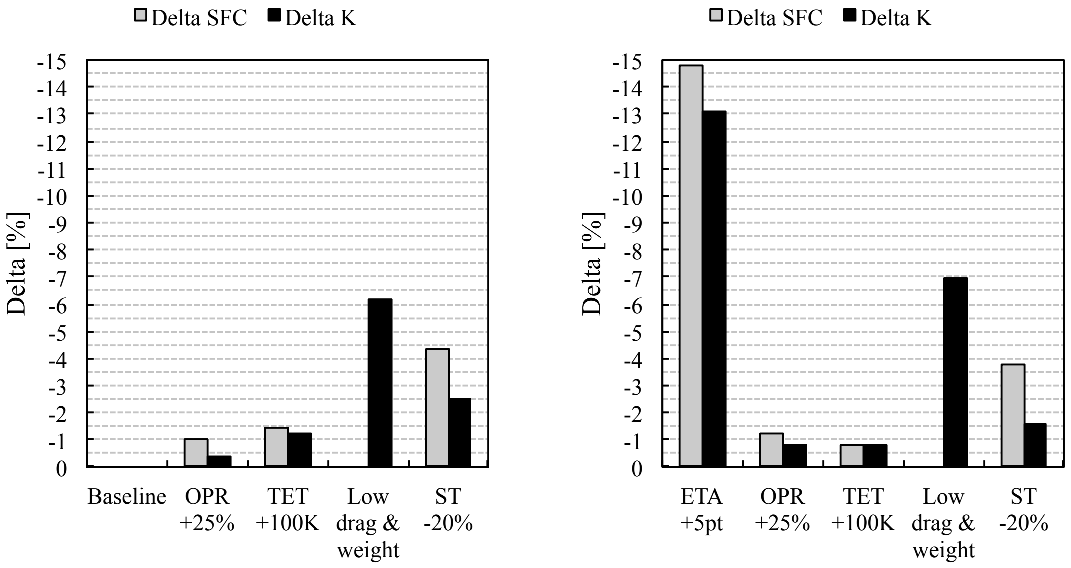

(c) Long range & $\eta = 90\%$ (d) Long range & $\eta = 95\%$

Figure 2.24: SFC and range factor (K) exchange rates for different missions and component efficiencies. The short and long range mission baseline engines correspond to the square symbols of Fig. 2.21a and Fig. 2.22a respectively. The low weight and drag case corresponds to: -50% drag and -35% weight for the SR and -45% for the LR.

Chapter 3

Secondary power extraction effects

3.1 Introduction

Aircraft engines are not merely a source of propulsive power but they also provide for the secondary power needs of the aircraft. Power is extracted from the engine core in the form of compressed air and shaft power in order to satisfy the requirements of the pneumatic, hydraulic, electric and cabin pressurization aircraft systems. The extraction of secondary power imposes an increase of about 1-4% in fuel consumption [4]. This chapter investigates how this fuel efficiency penalty varies for different engine designs by relating the main engine thermodynamic parameters with the magnitude of the penalty. The analysis presented here essentially complements the results presented in the previous chapter by adding the engine size effect of given bleed and power off-takes.

The effects of secondary power extraction were brought under investigation after the 1970s oil crises. The replacement of conventional secondary systems by one globally optimized all-electric system was contemplated in several studies published in the past [69–71]. Concerns were also focused on whether secondary power extraction would be heavier a burden for future high bypass ratio engines, due to their smaller engine cores [28, 69, 72].

Matching the engine for normal off-takes, which remain proportionally constant along the flight envelope, is a common practice to reduce the associated penalties [4, 73]. However there is still no single answer as to whether higher bypass ratio engines would suffer greater penalties than today's engines [4, 28, 69, 74]. Peacock stressed that the way the engine is resized to accommodate the off-takes plays a significant role in answering that question. The required resizing of the engine can be carried out either by keeping a constant diameter and specific thrust, while allowing the core size to float [75], or by keeping the bypass ratio constant and vary the size of the whole engine [76]. In that context, Peacock argued that if the first resizing method was employed no greater penalties would be imposed for higher bypass ratio engines, contrary to the second method where the penalties would increase.

Nowadays, secondary power extraction is still a current issue of research and discussion due to the continuous pursuit for more efficient aircraft/engines [12, 13]. Researchers continue to investigate the efficiency of different secondary power systems configurations [11, 14–16], and how this affects the whole aircraft performance [77].

This work aims to identify how secondary power extraction penalties relate to different engine thermodynamic designs. This entails testing the hypothesis that future engines with lower specific thrusts will suffer greater fuel efficiency penalties. An analytical method is used in order to derive expressions that relate the size of the off-take penalties to the design parameters of the engine. The analysis is based on the fundamentals of gas turbine aero engine efficiency and thermodynamics, and applies to the cruise design point of the engine, where fuel consumption is of utmost importance. The derived equations include design parameters that are known in the early preliminary design stages, and their validity is tested against Turbomatch. The conducted analysis offers physical insight on the parameters that drive the off-take penalties and has also been used to study the differences between the two resizing methods mentioned before. Finally, the developed analytical relations constitute a fast calculation tool in the hands of aircraft, engine, and secondary systems designers; any change in the characteristics of the engine and the secondary power systems can be translated to a fuel burn change, and subsequently, by applying the Breguet equation [32], to an aircraft range change.

3.2 Engine Core Efficiency Analysis

The determination of the secondary power extraction penalties is based upon estimating the changes in the individual efficiencies when bleed air or shaft power are taken off the engine. The enthalpy-entropy diagram will be used as a basis for the analysis, in order to determine the changes in the core efficiency. It is emphasized that the analysis applies to the design point of the engine, where the turbine entry temperature, overall pressure ratio and component efficiencies are kept constant.

The starting point will be a clean engine with zero bleed and shaft power off-takes. Then, shaft power and bleed air will be taken off the engine, with everything else kept constant. This will result in a reduction in thrust, which, for constant fuel inflow, will be translated to an equivalent reduction in efficiency. Therefore, to keep the thrust constant at its design value the engine has to be resized, and the reduction in efficiency will then be manifested as an increase in fuel flow.

3.2.1 Shaft power off-takes

Figure 3.1 shows how the extraction of shaft power affects the enthalpy-entropy diagram. The pressure ratio of the high-pressure turbine has to increase to cope with the increased demand in power and thus, everything else kept constant, the pressure at the exit of the core will fall. Consequently, the enthalpy produced by the core will also fall from Δh_{cp} to Δh^*_{cp} according to Eq. 3.1.

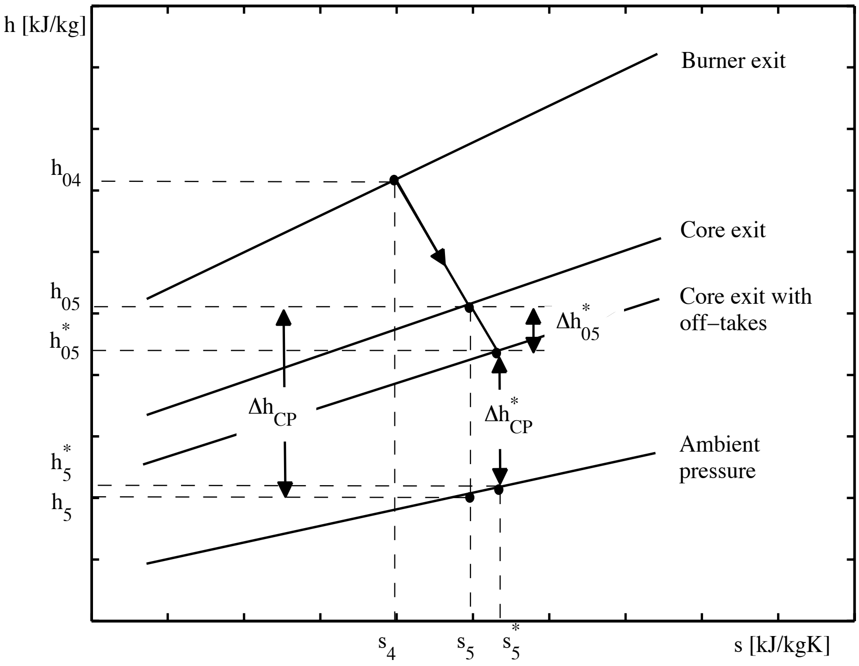

Figure 3.1: Enthalpy-entropy diagram at the core exit with and without off-takes.

$$\Delta h^*_{cp} = \Delta h_{cp} - \Delta h^*_{05} - (h^*_5 - h_5) \tag{3.1}$$

where Δh^*_{cp} represents the enthalpy produced by the core when secondary shaft power is extracted and Δh^*_{05} the enthalpy extracted as secondary power. If the losses due to the expansion to higher ambient temperature $(h^*_5 - h_5)$ are assumed equal to zero, Eq. 3.1 can be written in power terms as:

$$P^*_{cp} = P_{cp} - P_{po} \tag{3.2}$$

where $P_{po} = W_h \Delta h^*_{05}$ is the extracted shaft power. With the fuel flow kept constant, the above power drop will result in an equivalent drop in the efficiency of the core as described by Eq. 3.3, or by Eq. 3.4, relative to the clean engine efficiency.

$$\eta_{co}^{*} = \frac{P_{cp}^{*}}{W_{ff}FCV} = \frac{P_{cp} - P_{po}}{W_{ff}FCV} \tag{3.3}$$

$$\frac{\eta_{co}^{*}}{\eta_{co}} = 1 - \frac{P_{po}}{P_{cp}} \tag{3.4}$$

The power produced by the core of the clean engine (P_{cp}) can be calculated by rearranging Eq. 2.9 for a given thrust power ($Thrust[kN] \times Flight\,Velocity[m/s]$).

$$P_{cp} = \frac{T \cdot V_0}{\eta_{tr}\eta_{pr}} \tag{3.5}$$

Expressions 2.2, 2.3, 3.4, and 3.5 can now be combined to calculate the decrease in core efficiency.

$$\frac{\eta_{co}^{*}}{\eta_{co}} = 1 - \frac{P_{po} \cdot \eta_{tr} \cdot \eta_{pr}}{T \cdot V_0} = 1 - \frac{2 \cdot P_{po} \cdot (BPR + 1)}{T \cdot [BPR/(\eta_f \eta_{lpt}) + 1] \cdot (2V_0 + ST)} \tag{3.6}$$

3.2.2 Bleed air off-takes

A similar approach is followed for the case of bleed air extraction. First the change in the power required by the high-pressure turbine (HPT) is calculated, assuming that air mass flow of W_b is taken off the core, at a point in the compressor where the total air enthalpy increase is equal to Δh_b. The power balance for the high-pressure spool, assuming no mechanical shaft losses, will then be:

$$(W_h - W_b)\Delta h_{hpt}^{*} = (W_h - W_b)(h_{04} - h_{05}^{*}) = (W_h - W_b)\Delta h_{hpc} + W_b \Delta h_b \tag{3.7}$$

$$\Rightarrow \Delta h_{hpt}^{*} = (h_{04} - h_{05}^{*}) = \Delta h_{hpc} + \frac{W_b}{(W_h - W_b)}\Delta h_b = \Delta h_{hpc} + \frac{\beta}{(1-\beta)}\Delta h_b \tag{3.8}$$

Where β is the ratio of bleed air mass flow upon the core mass flow of the engine, W_b/W_h. It follows from the clean engine high-pressure spool power balance that Δh_{hpc} is equal to Δh_{hpt}, and hence the turbine power can be expressed as:

$$\Delta h_{hpt}^{*} = (h_{04} - h_{05}^{*}) = \Delta h_{hpt} + \frac{\beta}{(1-\beta)}\Delta h_b \tag{3.9}$$

The power produced by the core can now be calculated as:

$$\Delta h_{cp}^{*} = (h_{04} - h_5) - \Delta h_{hpt}^{*} - (h_5^{*} - h_5) \tag{3.10}$$

which combined with Eq. 3.9, and by assuming that $(h_5^* - h_5) \approx 0$ becomes,

$$\Delta h_{cp}^* = \Delta h_{cp} - \frac{\beta}{(1-\beta)} \Delta h_b \tag{3.11}$$

where $\Delta h_{cp} = (h_{04} - h_5) - \Delta h_{hpt}$. The expression can now be multiplied by the new core mass flow $(W_h - W_b)$, and after some algebraic manipulations be expressed in power terms as:

$$P_{cp}^* = (1-\beta) P_{cp} - W_b \Delta h_b \tag{3.12}$$

One can immediately observe that Eq. 3.12 is equivalent to Eq. 3.2. Consequently, the bleed air efficiency penalty can be calculated if Eq. 3.12 is divided by the new fuel energy $(1-\beta) W_{ff} FCV$ and by following the same procedure as for the derivation of Eq. 3.6.

$$\frac{\eta_{co}^*}{\eta_{co}} = 1 - \frac{2 \cdot W_b \Delta h_b \cdot (BPR + 1)}{(1-\beta) \cdot T \cdot [BPR/(\eta_f \eta_{lpt}) + 1] \cdot (2V_0 + ST)} \tag{3.13}$$

The relative bleed air mass flow β can be calculated from the thrust, bypass ratio and specific thrust of the engine as follows:

$$\beta = \frac{W_b}{W_h} = \frac{W_b}{W_{in}/(BPR + 1)} = \frac{W_b \cdot ST \cdot (BPR + 1)}{T} \tag{3.14}$$

3.3 Engine Total Efficiency Analysis

In the previous sections equations 3.6 and 3.13 were derived in order to calculate the core efficiency penalty when extracting shaft power and bleed air respectively. They can now be coupled with the changes in transmission and propulsive efficiency to estimate the total efficiency decrease. The analysis depends on the way the engine is resized to accommodate the secondary power extraction and keep the design point thrust constant. The first option is to keep the diameter and specific thrust of the engine constant, while the size of the core is allowed to increase, and the second to keep the bypass ratio constant and resize the whole engine. The derivation of the equations for both cases follows.

3.3.1 Constant Specific Thrust

A constant specific thrust will result in a constant propulsive efficiency, while the increase in the core size will cause an equal decrease in the bypass ratio and hence the transmission efficiency will improve, in accordance with Eq. 2.2. To keep the design thrust constant, the increase in core size will be assumed equal to the total decrease in efficiency. This can be justified as follows: for constant core size, and thus constant fuel energy input, the extraction of secondary power would decrease the thrust produced by the drop in total efficiency η_0^*/η_0. Therefore, to recover the thrust one would have to increase the energy input and core size to $((\eta_0^*/\eta_0)^{-1} \cdot W_h)$, and reduce the bypass ratio down to $(\eta_0^*/\eta_0 \cdot BPR)$. The above can be expressed with the following equations:

$$\frac{\eta_0^*}{\eta_0} = \frac{\eta_{co}^*}{\eta_{co}} \cdot \frac{\eta_{tr}^*}{\eta_{tr}} \cdot \frac{\eta_{pr}^*}{\eta_{pr}} = \frac{\eta_{co}^*}{\eta_{co}} \cdot \frac{\eta_{tr}^*}{\eta_{tr}} \cdot 1 \tag{3.15}$$

The transmission efficiency can be substituted with Eq. 2.2, where in the case of secondary power extraction $BPR \rightarrow (\eta_0^*/\eta_0 \cdot BPR)$:

$$\frac{\eta_0^*}{\eta_0} = \frac{\eta_{co}^*}{\eta_{co}} \cdot \frac{\dfrac{\eta_0^*/\eta_0 \cdot BPR + 1}{\eta_0^*/\eta_0 \cdot \dfrac{BPR}{\eta_f \eta_{lpt}} + 1}}{\dfrac{BPR + 1}{\dfrac{BPR}{\eta_f \eta_{lpt}} + 1}} \tag{3.16}$$

which after some algebraic manipulations, gives a quadratic equation for the total efficiency penalty:

$$\begin{aligned} \frac{\eta_0^*}{\eta_0} &= \frac{-b + \sqrt{b^2 - 4ac}}{2a} \\ a &= \frac{BPR(BPR + 1)}{\eta_f \eta_{lpt}} \\ b &= 1 + BPR - BPR \cdot \frac{\eta_{co}^*}{\eta_{co}} \cdot \left(1 + \frac{BPR}{\eta_f \eta_{lpt}}\right) \\ c &= -\frac{\eta_{co}^*}{\eta_{co}} \cdot \left(1 + \frac{BPR}{\eta_f \eta_{lpt}}\right) \end{aligned} \tag{3.17}$$

Equation 3.17 can now be combined with equations 3.6 and 3.13 to calculate the total efficiency penalty of secondary power extraction, when the engine core is resized while the engine diameter and specific thrust are kept constant.

3.3.2 Constant Bypass Ratio

The second design option involves the resizing of the whole engine while keeping the bypass ratio constant. In this case, the transmission efficiency before and after the extraction of secondary power will remain constant as the bypass ratio is fixed. This time the total engine mass flow will rise to $\left[(\eta_0^*/\eta_0)^{-1} \cdot W_{in}\right]$, in order to keep the thrust constant. Consequently, the specific thrust will fall to $(\eta_0^*/\eta_0 \cdot ST)$. The total efficiency is therefore given by:

Table 3.1: Engine specifications

Parameter	Value	Parameter	Value
T [kN]	50	TET [K]	1200-2000
Mach	0.8	Alt [m]	10668
V_0 [m/s]	237	η_f	0.9
OPR	40	η_{lpt}	0.86
BPR	2-50	η_{hpt}	0.88
Bypass $\Delta p/p$ [%]	1.5	η_{hpc}	0.86
Burner $\Delta p/p$ [%]	5.0	P_{po} [kW]	0, 250, 500
Δh_b [kJ/kg]	588	W_b [kg/s]	0, 0.425, 0.85

$$\frac{\eta_0^*}{\eta_0} = \frac{\eta_{co}^*}{\eta_{co}}\frac{\eta_{pr}^*}{\eta_{pr}} = \frac{\eta_{co}^*}{\eta_{co}} \cdot \frac{\dfrac{1}{1+\eta_0^*/\eta_0 \cdot \dfrac{ST}{2V_0}}}{\dfrac{1}{1+\dfrac{ST}{2V_0}}} \tag{3.18}$$

which after some algebra gives:

$$\frac{\eta_0^*}{\eta_0} = -\frac{V_0}{ST} + \frac{V_0}{ST}\sqrt{1+\frac{2ST}{V_0}\frac{\eta_{co}^*}{\eta_{co}}\left(1+\frac{ST}{2V_0}\right)} \tag{3.19}$$

3.4 Validation

The derived equations have been tested against numerical simulations for the engine specifications described in Table 3.1. The engine configuration resembles the one depicted in Fig. 2.1, with a single-spool core which comprises a high-pressure compressor, a burner, and a high-pressure turbine, followed by a low-pressure turbine driving a fan. The numerical simulations have been conducted with Turbomatch. In a manner similar to [34], the fan pressure ratio of each point on the graphs (representing a different engine) has been optimised for minimum specific fuel consumption. At the same time the engine mass flow has also been iterated in order to give a constant net thrust of 50 [kN].

Figures 3.2-3.5 compare the results of Eq. 3.6, 3.13, 3.17, and 3.19 with the simulation results of Turbomatch for a TET = 1650 [K]. The SFC penalty shown in the figures is calculated as $\left[(\eta_0^*/\eta_0)^{-1} - 1\right] \cdot 100\%$. The results include shaft power and bleed air offtakes and both the resizing methods described earlier. In all the cases the equations give very good agreement with the simulation data for the whole range of bypass ratio. The

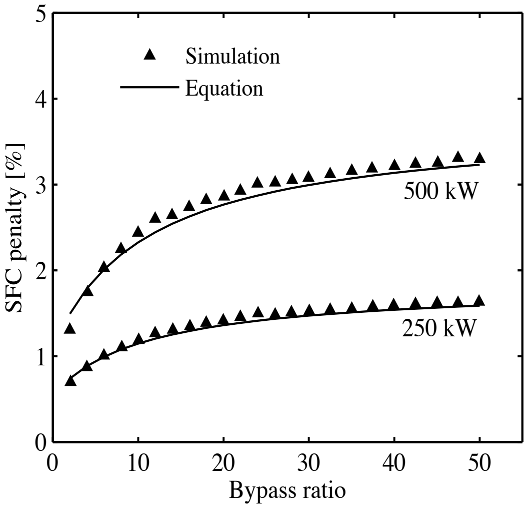

Figure 3.2: Variation of shaft power off-take penalties with bypass ratio. Resizing with constant bypass ratio. Shaft power extracted from the HP spool. TET = 1650 [K]. Predictions made with Eq. 3.6 and Eq. 3.19.

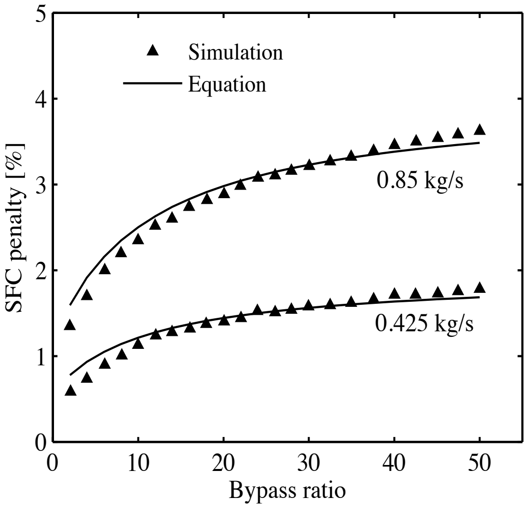

Figure 3.3: Variation of bleed air penalties with bypass ratio. Resizing with constant bypass ratio. Bleed air extracted from the HPC delivery. TET = 1650 [K]. Predictions made with Eq. 3.13 and Eq. 3.19.

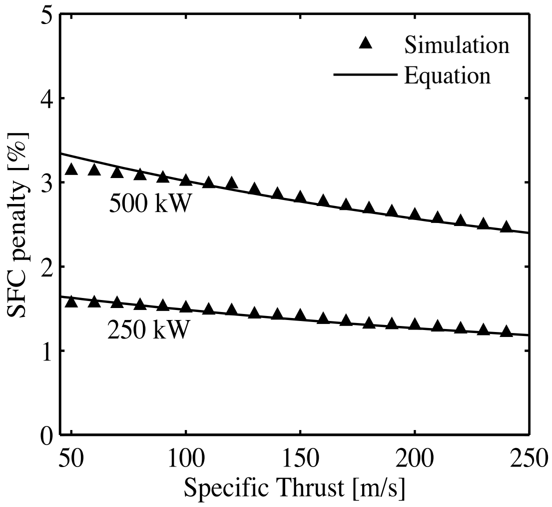

Figure 3.4: Variation of shaft power off-take penalties with specific thrust. Resizing with constant specific thrust. Shaft power extracted from the HP spool. TET = 1650 [K]. Predictions made with Eq. 3.6 and Eq. 3.17.

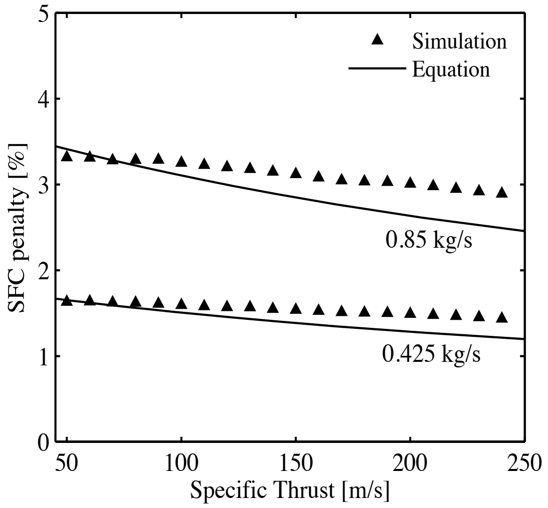

Figure 3.5: Variation of bleed air penalties with specific thrust. Resizing with constant specific thrust. Bleed air extracted from the HPC delivery. TET = 1650 [K]. Predictions made with Eq. 3.13 and Eq. 3.17.

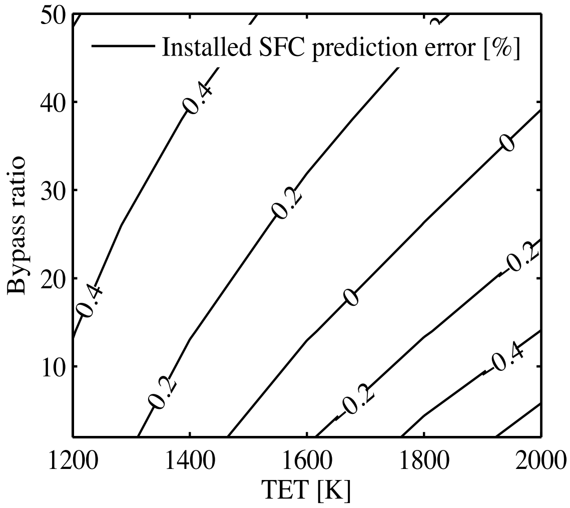

Figure 3.6: Installed SFC prediction error throughout the whole range of BPR and TET. Resizing with constant bypass ratio. 0.85 [kg/s] bleed air extracted from the HPC delivery. The term *installed SFC* includes only the secondary power extraction penalty; no other installation effect is included.

worst accuracy occurs in the case of the bleed air off-takes, where there is a deviation of up to 17%. This, however, can be mainly attributed to the approximate determination of the bleed enthalpy Δh_b, as Turbomatch returns the bleed temperature instead of the enthalpy. It has to be underlined here that a penalty prediction error of 20% corresponds approximately to an installed SFC prediction error of less than 0.5% (note here that the term *installed SFC* does not include any other installation penalties apart from the ones of secondary power extraction). For instance, if the real penalty is equal to 2% and the predicted value is equal to 2.4% (i.e. 20% error), then the predicted installed SFC will be $(1.024 * SFC_{bare})$ instead of $(1.02 * SFC_{bare})$. This translates to an installed SFC error of $(1.024 - 1.020)/1.020 * 100\% = 0.4\%$. Figure 3.6 shows the installed SFC prediction error for the whole design space of bypass ratio and turbine entry temperature for the worst-accuracy scenario of 0.85 kg/s bleed air. Even at the extremes of the design space the error lies below 0.5%.

Therefore, Eq. 3.6 and 3.13 combined with Eq. 3.17 and 3.19 can be used to predict the SFC penalty of shaft power and bleed air off-takes at the design point of the engine, for engines that range from a turbojet to an open rotor.

3.5 Future Engines Penalties

The derived expressions are not only a useful tool for the determination of installed SFC during the preliminary design phases but they also provide insight on how the extraction of secondary power affects the performance of different engine designs. Whether future engine designs such as ultra high bypass ratio engines or open rotors will face increasing fuel consumption penalties is a question that can be approached using the developed theory.

The first conclusion that can be drawn from the thermodynamic treatment of the problem is the primary effect of secondary power on the core efficiency of the engine. Secondary power reduces the core efficiency, as the definition of core efficiency (Eq. 2.9) does not include it as useful power output. Furthermore, Eq. 3.4 shows that for a given power off-take the core efficiency penalty increases as the power produced by the core decreases. The demand for core power does not come from the core per se, but from the demand for a certain thrust. That is the reason why the propulsive and transmission efficiencies of the engine dominate the magnitude of the penalty. For a given thrust requirement, the higher the propulsive and transmission efficiencies, the lower the demand for core power as shown by Eq. 3.5. Along these lines, the core efficiency and its drivers, i.e. the engine overall pressure ratio and the turbine entry temperature, do not directly affect the penalty, but they only have an indirect effect by defining the bypass ratio. More specifically, for a given specific thrust the selection of overall pressure ratio and turbine entry temperature fixes the value of bypass ratio, which in turn affects the transmission efficiency, and hence the efficiency penalty. This finding comes to confirm Codner's conclusions [74] about the lack of relationship between the core characteristics and the secondary power SFC penalties. Another way to justify the above is the following: by improving the core efficiency an equal reduction in fuel needed is achieved for both the secondary and mainstream core power, as they are both produced with the same efficiency; therefore the ratio between the two, and thus the penalty, remains constant. The actual size of the core in terms of mass flow has no effect either. For instance, if the TET and core specific power were increased, the size of the core would decrease but the power produced by the core would remain constant, as this is fixed by the thrust requirement and the propulsive and transmission efficiencies. Therefore, the TET and actual size of the core would have no direct effect on the penalty.

In addition to the primary effect on the core efficiency, the inclusion of secondary power in the design point of the engine will also have a secondary effect either on the transmission or the propulsive efficiency, depending on the resizing method employed. If the engine is resized by keeping constant the specific thrust and diameter, while the core mass flow is increased and the bypass ratio decreased, a transmission efficiency benefit will arise, as shown by Eq. 2.2. On the other hand, if the engine is resized with constant bypass ratio and increased diameter, the specific thrust will fall and therefore the propulsive efficiency will increase, as shown by Eq. 2.3. According to Peacock [4] it is this propulsive efficiency gain that decreases the penalties for higher specific thrust engines. Following this argument one could assume that if the engine was resized with constant specific thrust, hence without any propulsive efficiency gain, the penalty would be constant for different specific thrust engines. However, it has been shown in the thermodynamic analysis that the propulsive efficiency gain is only a secondary effect, which is added on the primary effect of the core efficiency drop. Even without any propulsive efficiency benefit the penalty is higher for lower specific thrust engines as they have a smaller core and therefore a higher core efficiency penalty (Fig. 3.4 and 3.5).

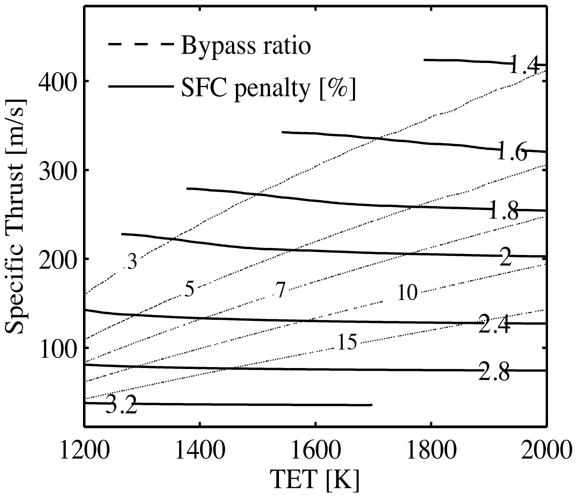

Figure 3.7: SFC penalty prediction throughout the whole range of Specific Thrust and TET. Resizing with constant bypass ratio. 500 [kW] of shaft power extracted from the HP spool.

The variation of the penalty throughout the whole design space of TET and specific thrust is shown in Fig. 3.7, for OPR = 40, resizing with constant bypass ratio, and 500 [kW] power extraction from the HP shaft. For a given TET as the specific thrust decreases, the propulsive efficiency improves, the core power decreases and hence the penalty increases. Similarly, for a given specific thrust as TET and hence bypass ratio increases, the transmission efficiency falls, the core power increases and therefore the penalty decreases. However, one can observe that this effect is weaker than the one of specific thrust and it wanes completely after a bypass ratio of about 10, as after this point the transmission efficiency decrease rate flattens out (Fig. 2.2).

Equations 3.6 and 3.13 reveal another cause of higher secondary power penalties for future engines, also mentioned by Peacock [4]. More fuel-efficient aircraft/engine designs will lead to lighter scaled-down aircraft with lower thrust requirements and, according to Eq. 3.6 and 3.13, higher SFC penalties. Moreover, it is very likely that future engines will face higher demands for secondary power due to the increased comfort offered to the passengers. Equation 3.6 shows that the effects of the thrust and off-take power demand can be combined into one non-dimensional power factor defined as $\frac{P_{po}}{T \cdot V_0}$. The power factor can increase either by increasing the size of off-takes or by decreasing the required thrust power.

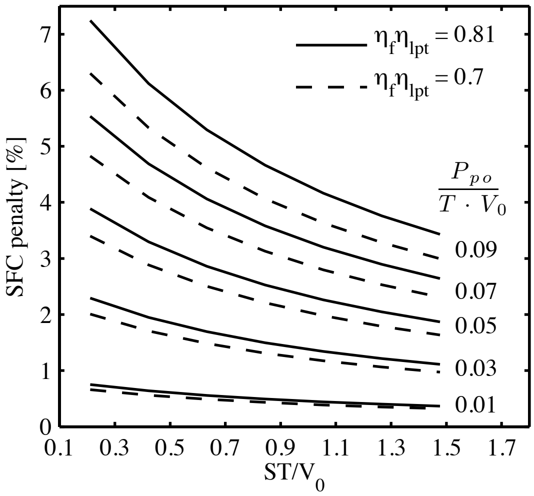

Figure 3.8: SFC penalty prediction of Eq. 3.19 and Eq. 3.6 for different specific thrusts and non-dimensional power factors. Resizing with constant bypass ratio. Shaft power extracted from the HP spool. BPR = 6.

Figure 3.8 shows the combined effect of the non-dimensional power factor and specific thrust on the level of the penalties. The specific thrust has been non-dimensionalized with the flight velocity. As shown earlier, bypass ratio has a lesser effect and can be neglected, but the effect of transmission efficiency is still taken into account through different fan and low-pressure turbine efficiencies. According to Fig. 3.8 lower specific thrusts, higher fan and turbine efficiencies, and higher power factors lead to higher SFC penalties. Furthermore, the higher the power factor, the more dependent is the penalty on specific thrust. Figure 3.8 can be used as a map that approximately identifies the SFC penalty for every engine and power off-take. It can also be used for the case of bleed air off-takes if $\frac{W_b \Delta h_b}{1-\beta}$ is used in the place of P_{po}.

To conclude, it can be argued that future engines will suffer greater secondary power SFC penalties due to:

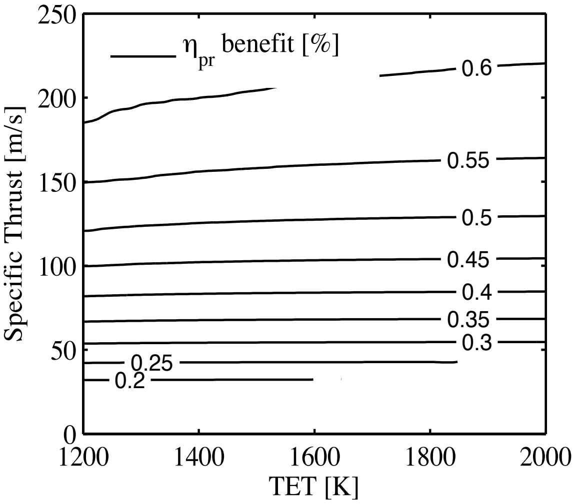

Figure 3.9: Propulsive efficiency gain when resizing with constant bypass ratio. 500 [kW] of shaft power extracted from the HP spool.

1. *Lower thrust requirements due to more efficient aircraft/engines.*
2. *Higher demand for secondary power.*
3. *Lower required core power for a given thrust, due to the more efficient conversion of core power into thrust power achieved by engines with low specific thrust and high fan and low-pressure turbine efficiencies.*

However in absolute terms, the fuel needed for a given demand in secondary power will remain constant unless improvements in core efficiency drive it down.

Altough the present study focuses on design point performance, a comment should be made here with respect to the off-design performance of future engines. The higher *(secondary power)/(core power)* ratio of future engines will also cause greater vertical movements of the compressor running lines when the operating conditions or secondary power requirements vary. This will affect the compressor surge margins and will also cause a variation of component efficiencies. These effects should not be disregarded, but a further off-design study is required in order to quantify them.

3.6 Resizing Methods Comparison

As described earlier, the two engine resizing methods only differ with respect to the secondary effect of propulsive or transmission efficiency gains. This section investigates the magnitude and variation of these gains, while it also compares the two methods in terms of SFC.

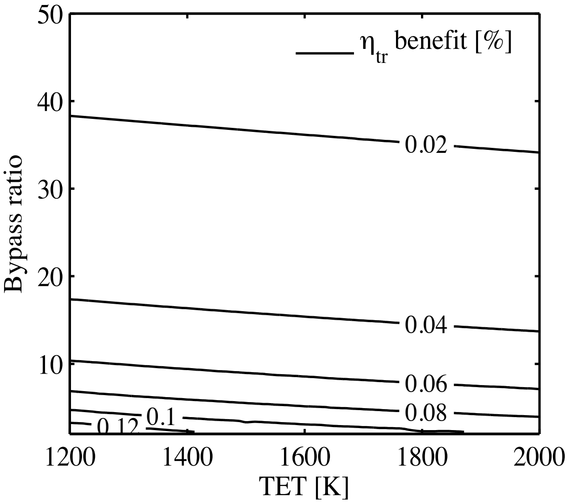

Figure 3.10: Transmission efficiency gain when resizing with constant specific thrust. 500 [kW] of shaft power extracted from the HP spool.

When the engine is resized with constant bypass ratio, the inlet mass flow increases and a propulsive efficiency benefit accrues. As shown in Fig. 3.9, this benefit ranges from 0.6% to 0.2% and decreases as the clean engine specific thrust falls. This happens because for an increase in mass flow x, the decrease in specific thrust is $\Delta ST = ST\,(1 - 1/x)$, which decreases when ST falls resulting in a lower propulsive efficiency gain.

On the other hand, when the engine is resized by keeping a constant diameter and allowing the core mass flow to increase and therefore the bypass ratio to decrease, a transmission efficiency gain is attained. Figure 3.10 shows that this benefit is much lower than the one achieved with the previous resizing method and depends only on bypass ratio. The benefit decreases as the bypass ratio increases and diminishes after a bypass ratio of 10. This behaviour is attributed to the steep variation of η_{tr} for low bypass ratios, which flattens out after a bypass ratio of 10 (Fig. 2.2).

Figure 3.11 shows the SFC benefit of the constant BPR method relative to the constant ST one. The relative benefit decreases: a) for lower STs following the trend shown in Fig. 3.9; b) for BPRs lower than 10 according to Fig. 3.10. However, the constant BPR method will result in a larger engine and consequently these small SFC benefits will diminish as the weight and drag penalties come into play.

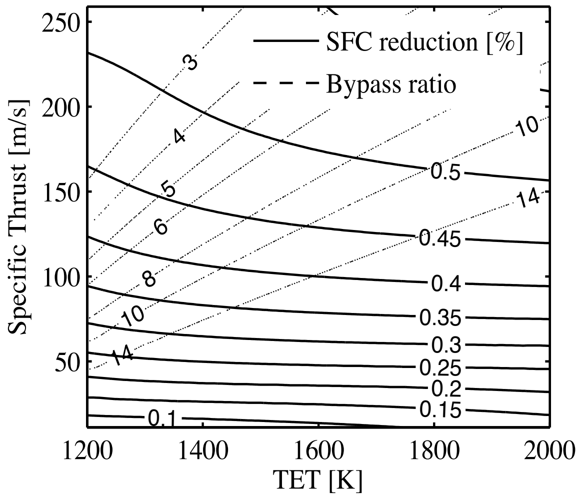

Figure 3.11: SFC benefit of engine resizing with constant bypass ratio relative to the constant specific thrust method. 500 [kW] of shaft power extracted from the HP spool.

3.7 Conclusions

A set of equations has been derived for the calculation of the SFC penalties when shaft power or bleed air is extracted at the design point of a gas turbine engine. The equations perform well against numerical simulation results and can be used during the preliminary design stages for the estimation of the installed specific fuel consumption of aero-engines ranging from a turbojet to an open rotor.

The thermodynamic analysis carried out demonstrated that the main factor driving the magnitude of the penalties is the size of the off-takes relative to the core power; the higher the relative size the higher the penalty. For fixed off-takes and thrust requirements the power produced by the core is determined by the propulsive and transmission efficiencies. The higher the efficiencies, the less the power needed by the core to produce a given thrust, and the greater the off-take penalties. Similarly, a lower thrust requirement would result in less demand for core power and therefore higher penalties.

As a result, the fan and low-pressure turbine efficiencies and the engine specific thrust are the main design parameters that drive the size of the penalties, since they govern the transmission and propulsive efficiency, respectively. Bypass ratio also drives the transmission efficiency, but has a lesser effect. The aforementioned design parameters have been grouped in three nondimensional numbers that affect the penalties in the following manner:

1. An increasing power factor $\frac{P_{po}}{T \cdot V_0}$ increases the SFC penalties. This means that future aircraft/engines with lower thrust requirements and higher passenger comfort,

and hence higher off-takes, will face increased SFC penalties.

2. Future engines are expected to have a decreased specific thrust factor $\frac{ST}{V_0}$, which will improve the propulsive efficiency, reduce the core power required for a given thrust, and increase the off-take penalties.

3. An increasing transmission efficiency factor $\eta_f \eta_{lpt}$ reduces the core power required for a given thrust and increases the off-take penalties.

The secondary-power SFC penalties are not high enough to affect the aforementioned future trends; in other words, the benefits arising from reduced specific thrust and improved transmission efficiency would outweigh the increased secondary-power penalties. Reducing the power factor appears to be the only way to improve the situation for future engines. This could be achieved by designing more efficient secondary systems, possibly within the context of an all-electric aircraft. The characteristics of the core (TET, OPR, core component efficiencies and pressure losses) do not directly affect the relative penalties, although they influence the absolute fuel needed for the provision of secondary power. In light of this, improvements in core efficiency should be further pursued to reduce the fuel burned for secondary systems and primary propulsive power.

When redesigning an engine to include the secondary power extraction in the design point, two methods exist to conduct the resizing:

1. Resize the whole engine by keeping the bypass ratio constant.

2. Resize the core by keeping the diameter and specific thrust constant.

Each method has a different secondary effect on the size of the penalties. The first method results in a propulsive efficiency benefit, accruing from the higher mass flow and lower specific thrust of the resized engine. The second method results in a lesser transmission efficiency benefit due to the lower bypass ratio of the resized engine. Although, the first method results in a better SFC the higher size of the engine is expected to increase its weight and drag and therefore eliminate or even reverse the fuel consumption benefit.

Chapter 4

Propeller modelling method development

4.1 Introduction

This chapter aims to develop a propeller performance modelling methodology suitable for the study of high speed prop-fans. This model constitutes the first step towards the implementation of an open-rotor simulation capability of equal maturity to the simulation of turbofans. The created tool will be used in the next chapter in order to devise a propeller map scaling technique, required for the integrated open-rotor engine performance prediction.

The chapter starts by identifying the main parameters that govern the propeller performance with a detailed analysis of the different sources of losses. This is followed by an extensive review of the different modelling approaches, leading to the selection of the lifting-line theory appropriately adapted for the simulation of advanced high speed prop-fan blades. The next sections detail the step by step development of the model, while special emphasis is given to the treatment of compressibility effects and the modelling of the propeller wake. The validity of the method is tested against experimental data and another higher fidelity numerical approach. The test case used for the validation is a swept prop-fan geometry designed by NASA and Hamilton Standard in the '70s.

4.2 Propeller fundamentals

The non-dimensional parameters most commonly used for the definition of propeller performance are the power coefficient C_P, the advance ratio J, the flight Mach number M_0, the thrust coefficient C_T, and the propeller efficiency η_{prop}, the last two being traditionally the dependent variables [78]. The operating Reynolds number also affects the propeller performance but its effect is usually considered secondary and it is not taken into account [79]. This is a good assumption if the the Reynolds number at the 0.75 radius is higher than 7×10^5, which is the case most of the times for full-scale propellers. The power and thrust coefficients are simply the non-dimensional forms of the power used and the thrust generated by the propeller and are defined according to Eq. 4.1 and Eq. 4.2 respectively. As shown by Eq. 4.3, the advance ratio is defined as the distance the propeller covers in one revolution divided by the propeller diameter. The propeller efficiency is defined as the ratio of thrust power upon input power and can be calculated by Eq. 4.4. Finally, a last parameter commonly used is the propeller disk loading, which - as shown by Eq. 4.5 - is defined as the ratio of the power input divided by the square of the propeller diameter. The disk loading is analogous to the fan pressure ratio of turbofan engines [80] and it shows the amount of kinetic energy imparted to the air as it passes through the propeller disk.

$$C_P = \frac{P}{\rho \cdot n^3 \cdot D^5} \tag{4.1}$$

$$C_T = \frac{T}{\rho \cdot n^2 \cdot D^4} \tag{4.2}$$

$$J = \frac{V_0}{n \cdot D} \tag{4.3}$$

$$\eta_{prop} = \frac{T \cdot V_0}{P} = \frac{C_T \cdot J}{C_P} \tag{4.4}$$

$$P/D^2 = \frac{C_P}{J^3} \cdot \rho \cdot {V_0}^2 \tag{4.5}$$

Propeller maps are usually presented as contour plots of efficiency as a function of C_P and J. For each different Mach number a different contour plot is required. For the benefit of easier digitization and numerical interpolation, sometimes efficiency is replaced by C_T [81].

It is useful at this point to make some comments on the losses impacting the propeller efficiency. An understanding of the losses breakdown will set the basis and the requirements for the selection of a propeller analysis method. For a propeller that measures 80% of efficiency, the 20% of losses can be broken down as follows. The axial and swirl momentum imparted to the air as it passes through the propeller disk represent approximately 3 and 7 percent units [82]. These momentum losses are higher the higher the loading of the propeller. As a notion these losses can be related to the propulsive efficiency of a jet engine, where the losses increase for higher jet velocities. For a finite number of blades there is also a 5% "tip-loss" connected to the reduction of lift near the blade edges, due to the presence of the tip vortices and the propeller wake [80]. This phenomenon corresponds to the induced drag of finite wings, and is aggravated as the loading increases (due to stronger vortices) and as the number of blades decreases. All the aforementioned losses, which so far account for 15% out of the 20% of total losses, are ideal losses [83]. This means that they are present even at the ideal condition of zero drag and hence zero viscous losses. Finally, viscous losses account for 5% of the total and can exceed the value of 7% as the Mach number increases [80]. This loss breakdown shows the importance of accurately modelling the ideal performance of the propeller, which must then be coupled with a reliable source of airfoil drag polars to account for the viscous losses.

4.3 Analysis methods

Wald [84] gives a very concise account of the historical evolution of propeller analysis methods. The beginning was made with the axial momentum theory by Rankine [85] and Froude [86], which, albeit their simplicity, only account for the axial momentum losses. Furthermore, these methods do not take into account the actual blade geometry since they model the propeller as an actuator disk. According to the propeller loss analysis presented in the previous section, these methods can only represent 3 percent units of the total losses. The Axial Momentum theory was extended by the General Momentum theory that is also capable of calculating the swirl induced velocity component [87–89].

A different path was followed by Drzewiecki, who developed the first blade-element theory [90]. This theory is the base of almost every modern preliminary propeller analysis method [79]. The fundamental assumption of this theory is that the blade is discretised in 2D ”strips” or ”blade elements” whose performance is independent of one another. The angle of attack of each blade element can be calculated by knowing the free-stream velocity components, which result from the axial flight velocity and the rotational propeller speed. This angle of attack is then used as an input to a 2D airfoil database to read the blade element lift and drag coefficients, and calculate the lift and drag forces. The integration of these forces along the blade will yield the total propeller performance. This method accounts for the actual blade geometry and is able to calculate the viscous drag losses. However, the viscous losses contribute only 5-7 percent units to the total losses figure. The prediction of such methods falls far from the truth, as in reality the blade elements are not independent [91]. Hence, the blade-element model needs to be coupled to another theory that is capable of calculating the induced velocities.

The Wright brothers are deemed as the first who coupled the two aforementioned modelling approaches and created the combined Blade-Element Momentum theory (BEM) [84], which was then described in detail by Glauert [89]. This method is able to describe the sum of momentum losses and viscous drag losses that amount to 15-17 percent units of the total losses. With the addition of the Prandtl tip loss function [89, 92], this method has survived until today due to its simplicity and its fairly good results [84, 87, 93, 94].

Nonetheless, albeit the correction introduced by the Prandtl tip loss function, the BEM method still assumes an averaged wake flow and is not able to accurately model the effect of the exact propeller wake. Furthermore, the method is not capable to calculate the velocity outside the defined flow stream-tube, or simulate the time-dependent performance of the rotor [95]. These shortcomings could limit future extension of the method to the field of noise estimation.

As described earlier, similarly to wings, there is a sheet of trailing vorticity shed in the wake of the blade, with the strongest vortices being at the tip of the blade [96]. Betz was the first to prove that for lightly-loaded optimum propellers the wake assumes the form of a rigid helical surface [92]. Prandtl calculated the induced velocity field produced by such a wake by approximating the wake by a set of equally spaced semi-infinite lamina and produced what is known as the Prandtl Tip Loss function [92]. The first exact algebraic solution to the wake defined by Betz was given by Goldstein in 1929 [97], who solved the potential flow equation problem by using Bessel functions. Theodorsen extended the applicability of the method to high loadings but used an electrical analogy of the helical wake, and a set of experiments to calculate the induced velocities [98]. These methods have been widely used until today for the design and performance prediction of straight blade single [84, 99–106] and contra-rotating propellers [22, 23, 107–109].

The advent of high-speed prop-fans which feature highly swept blades brought to the surface the main limitation of the Goldstein methods. For the case of straight blades one needs only to consider the effect of the trailing wake vorticity on the induced velocity, as the vorticity "bound" to the straight blades induces no velocity [84, 110]. However that is not the case for swept blades, as it will be shown in the next sections when the method development will be described. Hamilton Standard, the company who designed the SR prop-fan family in the '70s, identified that problem after designing the SR1 and SR2 propellers using a Goldstein method [80, 82, 103]. The modelling efforts by NASA [111–114] and ONERA [115] led to the same conclusion regarding the unsuitability of Goldstein based methods for the simulation of swept blades. Both NASA [114] and ONERA [115] found that neglecting the effect of bound vorticity displaces inboard the maximum loading of the blade.

Hamilton standard decided to design the rest of the SR family propellers by using the curved lifting-line method [100, 101, 105, 116] and the same approach was followed by NASA [117, 118] and by ONERA [115, 119–121]. This method is regarded as the extension of Prandtl's lifting-line wing method [122] to the case of swept propeller blades. According to its fundamental principle the blade is replaced by a curved vortex filament which passes through the quarter chord point of every section. As the circulation varies from one blade element to the next, trailing vortices spring from the blade-element boundaries according to the vortex theorems stated by Helmholtz [96]. These trailing vortices follow approximately a helical trajectory, which can be prescribed [123] or calculated freely

[124, 125]. The influence of the bound and trailing vortices on the blade is calculated by using the law of Biot-Savart [126, 127]. The approach is therefore capable of handling correctly the effect of bound and trailing vorticity, while taking into account a more realistic wake geometry.

Despite the development of more advanced lifting-surface, Euler and CFD techniques, the lifting-line approach is still used today during the propeller preliminary design stages, and in order to predict the propeller global performance [121, 128]. Furthermore, higher complexity methods do not always give higher fidelity results, an argument confirmed by Burger [129], who compared a lifting-surface and a lifting-line method. As this work focuses on the global performance of propellers, which represents a brick in the whole engine performance prediction, the lifting-line method has been chosen. This choice is also based on the experience gained by working with the Goldstein and Theodorsen methods within the MSc theses of Iosifidis [130] and Sanchez-Ortega [131], which confirmed the aforementioned shortcomings of these approaches. The details of the developed lifting-line approach will be presented in the next sections, while the validation of the method against experimental data and higher order methods will prove that not much accuracy has been sacrificed.

4.4 Lifting-line method development

4.4.1 Coordinate systems

Before presenting the details of the method it is crucial to first lay the foundations by discussing the coordinate systems used for the analysis. Figure 4.1 presents the global coordinate systems used. The first system is a cartesian XYZ orthogonal system that is fixed on the base of the pitch change mechanism and rotates with the propeller. This choice has been made instead of an inertial system, as in this way the unsteady flow problem is converted to a steady one. In this work the Z-axis, which is the axis of rotation, is also parallel to the direction of flight as no angle of attack is considered. The X-axis is aligned to the pitch change mechanism that passes through the middle of the base of the blade and together with the Y-axis define the plane of rotation. The cartesian XYZ system is used for the input of the geometry and also as the common base of reference for the calculations. The corresponding cylindrical $r\phi Z$ system is used when needed to facilitate the calculations by exploiting the symmetry of the geometry.

Apart from these global coordinate systems, another local one is defined at each blade element. As shown in Figs. 4.1 and 4.2 the s-axis is tangent to the meanline of the blade and points from the hub to the tip. The c-axis is parallel to the chord, perpendicular to the s-axis and points from the trailing edge to the leading edge of the airfoil. Finally the n-axis is normal to the other two and is a result of their cross product. The local

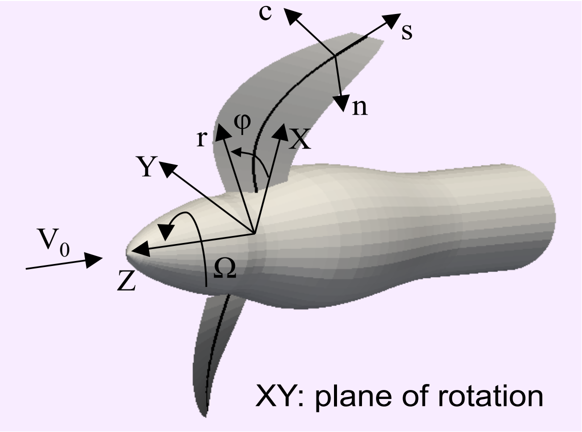

Figure 4.1: Coordinate systems used. XYZ: global cartesian system. $r\phi Z$: global cylindrical system. scn: local blade-element system. V_0: flight velocity. Ω: propeller rotational speed.

blade-element system is used for the calculation of the blade element performance and the solution of the induced velocities problem. As it will be shown later the linearisation of the problem is more accurate in this coordinate system because the dominant velocity component is in the c-axis direction.

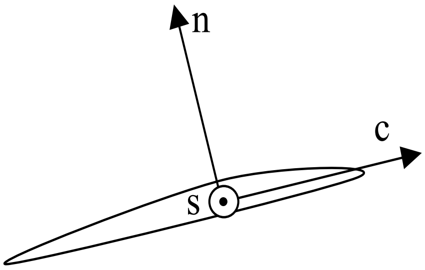

Figure 4.2: Local blade element coordinate system in the cn plane. s: spanwise unit vector. c: chordwise unit vector. n: normalwise unit vector

The definition of the local blade-element systems requires the knowledge of the blade geometry and thus it is essential to describe the way the geometry is input. The starting point is the meanline of a radially stacked set of airfoils. Apart from the points of the meanline, the starting coordinates of the quarter chord points are also stored. The quarter chord points are used to define the chordwise vector, which starts from the meanline point and ends in the quarter chord point. The first step is to rotate the airfoils about the radial direction (X-axis) according to the given twist angle. Only the quarter chord point coordinates are affected by this rotation as the meanline coincides with the rotation axis. The next step is to sweep back along the extended chord line. This geometry definition method is equivalent to the one used by Hamilton Standard for the design of the SR1 propeller [104]. The final step is to rotate the blade along the pitch change mechanism axis by the desired pitch angle. In this starting position the coordinates of the meanline and quarter chord line are known in the XYZ system. This geometry definition method can be used if the geometry is given as a table of chord, twist and sweep angle. If the exact 3D geometry is known, the exact XYZ coordinates of the meanline and quarter chord points can be given.

By knowing the coordinates of the meanline and quarter chord points for each blade station, the local blade-element unit vectors can be defined as follows. The spanwise unit vector is the difference between two adjacent meanline points (outboard minus inboard). The chordwise unit vector, as mentioned earlier, is the difference between the quarter chord point and the meanline point. The normalwise unit vector is the product vector of the two others and should point from the pressure side to the suction side of the airfoil. All the vectors should be divided by the scalar value of their magnitude to ensure that they have unit length. Their magnitude is defined as the square root of the sum of squares of the unit components. The above definitions are reflected on the Eqs. 4.6-4.8, which define the unit vectors for the center of each blade element i.

$$\vec{e}_{s,(i)} = \frac{\alpha_{s_X,(i)}}{d} \cdot \vec{e}_X + \frac{\alpha_{s_Y,(i)}}{d} \cdot \vec{e}_Y + \frac{\alpha_{s_Z,(i)}}{d} \cdot \vec{e}_Z \tag{4.6}$$

$$\begin{aligned} \alpha_{s_X,(i)} &= X_{m,(i+1)} - X_{m,(i)} \\ \alpha_{s_Y,(i)} &= Y_{m,(i+1)} - Y_{m,(i)} \\ \alpha_{s_Z,(i)} &= Z_{m,(i+1)} - Z_{m,(i)} \\ d &= \sqrt{\alpha^2_{s_X,(i)} + \alpha^2_{s_Y,(i)} + \alpha^2_{s_Z,(i)}} \end{aligned}$$

$$\vec{e}_{c,(i)} = \frac{\alpha_{c_X,(i)}}{d} \cdot \vec{e}_X + \frac{\alpha_{c_Y,(i)}}{d} \cdot \vec{e}_Y + \frac{\alpha_{c_Z,(i)}}{d} \cdot \vec{e}_Z \tag{4.7}$$

$$\begin{aligned} \alpha_{c_X,(i)} &= X_{1/4c,(i)} - X_{m,(i)} \\ \alpha_{c_Y,(i)} &= Y_{1/4c,(i)} - Y_{m,(i)} \\ \alpha_{c_Z,(i)} &= Z_{1/4c,(i)} - Z_{m,(i)} \\ d &= \sqrt{\alpha^2_{c_X,(i)} + \alpha^2_{c_Y,(i)} + \alpha^2_{c_Z,(i)}} \end{aligned}$$

$$\vec{e}_{n,(i)} = \frac{\alpha_{n_X,(i)}}{d}\cdot\vec{e}_X + \frac{\alpha_{n_Y,(i)}}{d}\cdot\vec{e}_Y + \frac{\alpha_{n_Z,(i)}}{d}\cdot\vec{e}_Z \tag{4.8}$$

$$\begin{aligned}
\alpha_{n_X,(i)} &= \alpha_{s_Y,(i)}\cdot\alpha_{c_Z,(i)} - \alpha_{s_Z,(i)}\cdot\alpha_{c_Y,(i)}\\
\alpha_{n_Y,(i)} &= \alpha_{s_Z,(i)}\cdot\alpha_{c_X,(i)} - \alpha_{s_X,(i)}\cdot\alpha_{c_Z,(i)}\\
\alpha_{n_Z,(i)} &= \alpha_{s_X,(i)}\cdot\alpha_{c_Y,(i)} - \alpha_{s_Y,(i)}\cdot\alpha_{c_X,(i)}\\
d &= \sqrt{\alpha^2_{n_X,(i)} + \alpha^2_{n_Y,(i)} + \alpha^2_{n_Z,(i)}}
\end{aligned}$$

After defining the local blade-element unit vector system, the transformation between global and local system is just a matter of a dot product operation. Equation 4.9 shows the transformation of a hypothetical vector $\vec{V} = V_X\vec{e}_X + V_Y\vec{e}_Y + V_Z\vec{e}_Z$ from the global XYZ system to the local *scn*. The reverse operation is given by Eq. 4.10 for a vector $\vec{V} = V_s\vec{e}_s + V_c\vec{e}_c + V_n\vec{e}_n$.

$$\begin{aligned}
\vec{V} &= V_s\vec{e}_s + V_c\vec{e}_c + V_n\vec{e}_n\\
V_s &= V_X\cdot\alpha_{s_X} + V_Y\cdot\alpha_{s_Y} + V_Z\cdot\alpha_{s_Z}\\
V_c &= V_X\cdot\alpha_{c_X} + V_Y\cdot\alpha_{c_Y} + V_Z\cdot\alpha_{c_Z}\\
V_n &= V_X\cdot\alpha_{n_X} + V_Y\cdot\alpha_{n_Y} + V_Z\cdot\alpha_{n_Z}
\end{aligned} \tag{4.9}$$

$$\begin{aligned}
\vec{V} &= V_X\vec{e}_X + V_Y\vec{e}_Y + V_Z\vec{e}_Z\\
V_X &= V_s\cdot\alpha_{s_X} + V_c\cdot\alpha_{c_X} + V_n\cdot\alpha_{n_X}\\
V_Y &= V_s\cdot\alpha_{s_Y} + V_c\cdot\alpha_{c_Y} + V_n\cdot\alpha_{n_Y}\\
V_Z &= V_s\cdot\alpha_{s_Z} + V_c\cdot\alpha_{c_Z} + V_n\cdot\alpha_{n_Z}
\end{aligned} \tag{4.10}$$

4.4.2 Blade-element velocity analysis

At each blade element, the total velocity vector can be broken down in three vectors as shown by Eq. 4.11, where i is the number of the blade-element. The vector $\vec{U}$ includes the free stream components which result from the flight speed and the rotation of the blade. Equation 4.12 defines these components in the global cylindrical system and Eq. 4.13 in the global cartesian. The position of the i^{th} blade-element center is defined by the position vector $\vec{r}_{BE,(i)} = X_{BE,(i)}\cdot\vec{e}_X + Y_{BE,(i)}\cdot\vec{e}_Y + Z_{BE,(i)}\cdot\vec{e}_Z$. The flight velocity is denoted by V_∞ and the rotational speed by Ω.

$$\vec{V}_{(i)} = \vec{U}_{(i)} + \vec{w}_{(i)} + \vec{u}_{(i)} \tag{4.11}$$

$$\vec{U}_{(i)} = \left(-\Omega \cdot \sqrt{X_{BE,(i)}^2 + Y_{BE,(i)}^2}\right) \cdot \vec{e}_{\phi} + (-V_{\infty}) \cdot \vec{e}_Z \tag{4.12}$$

$$\vec{U}_{(i)} = \left(\Omega \cdot Y_{BE,(i)}\right) \cdot \vec{e}_X + \left(-\Omega \cdot X_{BE,(i)}\right) \cdot \vec{e}_Y + (-V_{\infty}) \cdot \vec{e}_Z \tag{4.13}$$

The vector $\vec{u}$ describes the velocity components induced by the presence of a spinner and a nacelle. This velocity variation can be calculated by using a panel method which solves the potential flow equation [132] for a given spinner/nacelle geometry. Panel methods are extensively used in the industry as routine design tools for three-dimensional flows [133]. This work uses the publicly available code Panair, developed by Boeing, which has been extensively tested and validated in several cases for subsonic and supersonic flows [133]. A similar approach has been followed by Mikkelson et al [82] for the modelling of the SR1 and SR2 prop-fans. The schematic in Fig. 4.3 shows the way the code is used for the purposes of this work. The code requires the input of the flow velocity, the coordinates of the grid points that represent the nacelle geometry and the coordinates of the off-body points where the induced velocity needs to be calculated. The output includes the velocity vector $\vec{u}$ components at each off-body point which can then be used as an input in the lifting line method. For this work the off-body points of interest are the lifting-line points which are located at the quarter chord line of the blade.

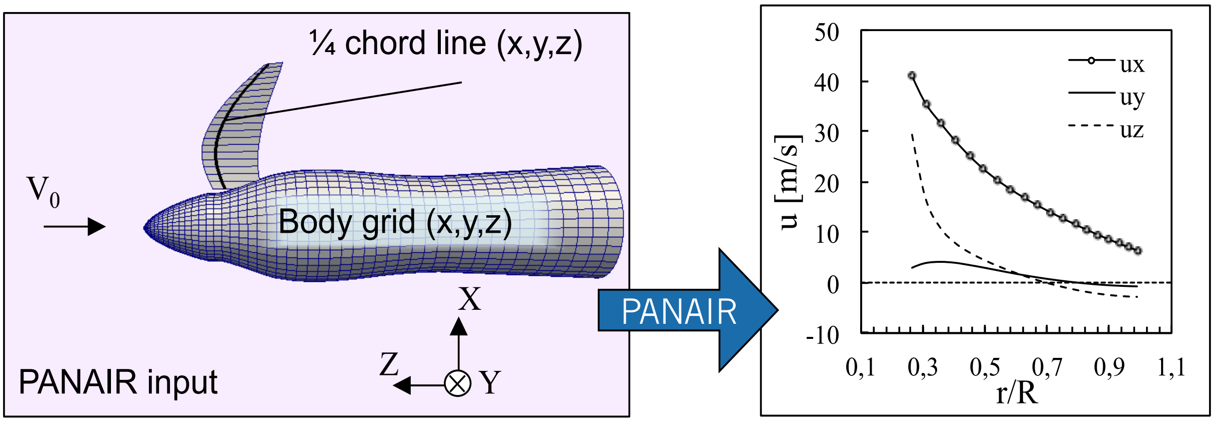

Figure 4.3: Panair input and output data.

The last vector $\vec{w}$ is the velocity induced by the trailing vortices of the wake and the bound vortices of the blades on each point of the blade. For simplicity henceforth it will be called vortex induced velocity. This induced velocity depends on the geometry of the wake, the geometry of the blades and on the operating conditions. Its calculation is the topic of the following sections. It has to be underlined here that in reality the nacelle induced and the vortex induced velocities interact with each other; i.e. the two calculations should be coupled in an iterative process. However for prop-fan applications this coupling is commonly omitted without a significant loss in accuracy [117].

4.4.3 Wake geometry definition

As mentioned in the literature review presented in section 4.3, the lifting line theory hypothesizes the existence of two types of vortices. Bound vortices that pass through the quarter chord line of the blades and corresponding trailing vortices that spring from the blade-element boundaries and constitute the wake of the propeller (Fig. 4.4). It is essential for the set-up and solution of the problem that a decision is made regarding the wake geometry. There are three main approaches:

1. The rigid wake which has been followed by Goldstein [97]. According to this method the wake assumes the shape of a rigid screw surface which follows a constant helix angle at every radius. This assumption neglects the influence of the induced velocity in the wake and can lead to significant inaccuracies at high loading conditions [113]. Furthermore, the wake is assumed to be non-contracted, i.e. there is no change in the radial position of the trailing vortices. This can again lead to inaccuracies when a static performance prediction is sought. The advantages of the method lies in the fact that the wake is defined a priori and remains constant throughout the entire iteration process [87].

2. The prescribed wake method. This method allows each helix to have a different angle by taking into account the local induced velocity [119]. It can also take into account the contraction by applying a set of correlations derived from experimental data [123], most notably the ones produced by Landgrebe [117, 123]. After the vortex is shed the helix angle remains constant [134]. It is evident that in this case the wake must be updated in each iteration as it is affected by the current value of the induced velocities. According to Young, 2-3 iteration are enough for the wake to assume its final shape [123].

3. The free wake method. This technique does not prescribe the wake geometry but it allows its real time calculation [124, 125]. It requires a much higher computational time than the other two methods and it is commonly used to calculate the static performance of propellers, where the contraction is significant. Alternatively it can be used to calibrate a prescribed wake model. At normal speed conditions it does not offer a higher accuracy advantage relative to the prescribed wake method as reported by Gur and Rosen [87].

This work focuses on the propeller global performance prediction for Mach greater than 0.2 which is a typical end-of-runway speed. The details of the wake geometry and

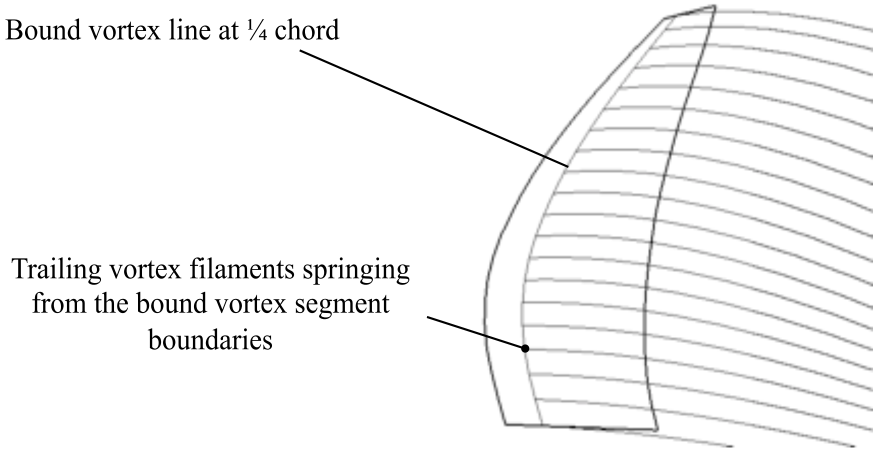

Figure 4.4: The modelling of the blade with a bound vortex and of the wake with a set of trailing vortex filaments.

the more complicated and resource demanding static performance prediction are outside the scope of work and therefore the selection of a free-wake model is not justified. The author has selected the prescribed wake formulation as presented by Egolf et al [117] for a similar prop-fan application. According to this model the local helix angle of the i^{th} filament is calculated by Eq. 4.14 where only the axial induced velocity is taken into account. Furthermore the speeds under which a prop-fan normally operates allow the omission of the wake contraction without a significant loss of accuracy. This is a common assumption used widely in the literature [118, 119, 134]. Nevertheless, the selection of a prescribed wake approach allows for future implementations of contraction prediction correlations, similar to Refs. [117] and [123].

$$\tan(\phi_{h,(i)}) = \frac{V_\infty + w_{Z,(i)}}{\Omega \cdot \sqrt{X^2_{W,(i)} + Y^2_{W,(i)}}} \tag{4.14}$$

Each vortex filament is segmented into straight vortices according to the geometric law described by Eq. 4.15. Equation 4.15 is a simple geometric series that gives the azimuthal angle of each vortex filament point in the cylindrical system. Two points define a straight segment.

$$\phi_{az,(j)} = N_{WT} \cdot 2\pi \cdot \left(\frac{j-1}{N_{WP}-1}\right)^{g_w} \tag{4.15}$$

In Eq. 4.15 N_{WT} is the number of turns a wake vortex filament is allowed to develop for, N_{WP} the number of points the vortex filament is split into and $j = 1..N_{WP}$ the current filament point. Normally 4 wake turns are sufficient, while the number of wake points has to be adjusted to give less than 2.5° for the first segment [127]. The parameter g_w

controls the grading of the grid and can take a value around 1.6. This way the first vortex segments that have the greatest impact on the performance calculations will be smaller than the vortex segments further from the blade.

The radius of each filament is kept constant and equal to the radius of the point on the bound vortex where the trailing filament springs from. The last coordinate to be defined is the Z which is given by Eq. 4.16 for the point j of the filament i. Equation 4.16 is consistent with the helix angle definition of Eq. 4.14. The result of this wake definition is shown in Fig. 4.5.

$$Z_{W,(i,j)} = \frac{\phi_{az,(j)}}{\Omega} \cdot \left(V_\infty + w_{Z,(i)}\right) \tag{4.16}$$

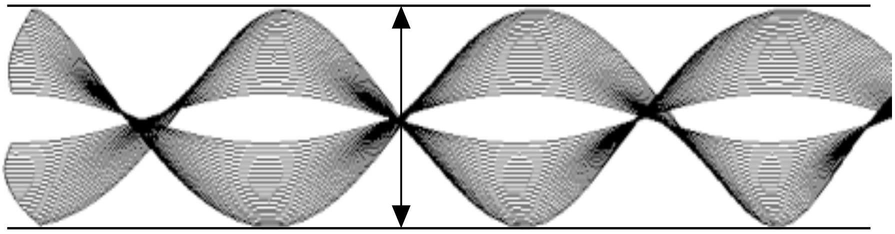

Figure 4.5: The resulting non-contracted prescribed wake geometry.

It is evident from Eq. 4.16 that the wake geometry depends on the variation of induced velocity along the blade radius. However this velocity is not known when the calculation begins and stems from the wake geometry itself. It is for this reason that the calculation requires a number of iterations, where for each calculation of induced velocities the wake geometry is updated. For the initial definition of the wake the induced velocities can be assumed to be zero, and hence the wake starts as a rigid helix surface.

4.4.4 Biot-Savart law

After the position of the bound and trailing vortices is defined, their influence can be calculated by using the law of Biot-Savart [127]. This law gives the velocity $\vec{w}$ induced at a point P by a vortex segment $\vec{l}_{AB}$ that has a constant circulation of Γ, as shown by Fig. 4.6 for a straight vortex segment.

$$\vec{w} = \frac{\Gamma}{4\pi} \frac{h}{\left(r_c^{2n} + h^{2n}\right)^{1/n}} \left(\cos\theta_1 - \cos\theta_2\right) \frac{\vec{l}_{AB} \times \vec{r}_1}{|\vec{l}_{AB} \times \vec{r}_1|} \tag{4.17}$$

$$\vec{r}_1 = \vec{r}_P - \vec{r}_A, \qquad \vec{r}_2 = \vec{r}_P - \vec{r}_B, \qquad \vec{l}_{AB} = \vec{r}_B - \vec{r}_A \tag{4.18}$$

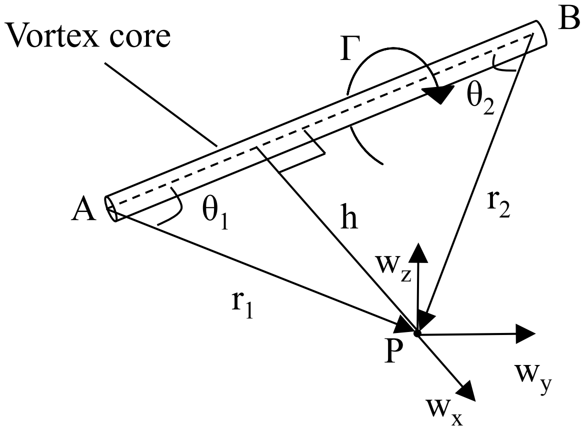

Figure 4.6: The Biot-Savart law, giving the velocity $\vec{w}$ induced by a straight vortex segment $\vec{l}_{AB}$ with a finite core radius as given by Leishman [127].

$$h = r_1 sin\theta_1 = r_2 sin\theta_2 \tag{4.19}$$

$$\cos\theta_1 = \frac{\vec{l}_{AB} \cdot \vec{r}_1}{|\vec{l}_{AB}| \cdot |\vec{r}_1|}, \qquad \cos\theta_2 = \frac{\vec{l}_{AB} \cdot \vec{r}_2}{|\vec{l}_{AB}| \cdot |\vec{r}_2|} \tag{4.20}$$

where r_p, r_A and r_B are the position vectors of the points P, A and B in the global XYZ system.

After all the wake segments are defined as described in the previous sections, the set of equations 4.17-4.20 can be used to find the velocity induced by each segment of bound and trailing vorticity. Some remarks should be made about the use of a "vortex core" in Eq. 4.17. If the Biot-Savart law is used without a vortex core ($r_c = 0$) Eq. 4.17 results in an infinite induced velocity when $h \to 0$. This behaviour of the Biot-Savart law results from its irrotational flow nature which is unrealistic as we move closer to the vortex core. Leishman [127] describes the salient points of different vortex core models and Eq. 4.17, which is taken from there, uses the Vatistas model. The parameter n in Eq. 4.17 defines the velocity profile in the vortex core according to the Vatistas method. In the context of this work the vortex core modelling is only a tool of de-singularisation and a more detailed treatment of vortex dynamics falls outside the scope of work. Szymendera [135] reports that different vortex core modelling choices have negligible effect on the global performance and therefore the author made the choice of $n = 2$ without any further investigation. The vortex core radius r_c is calculated using the Lamb-Oseen model as described by Ananthan et al [136].

Finally, an important observation can be made for Eq. 4.17. The induced velocity is equal to the product of the circulation of the vortex segment Γ with a vector geometric coefficient $\vec{GC}$, which is only a function of the geometry of the segment that in turn stems from the geometry of the wake. Therefore Eq. 4.17 can be conveniently rearranged to give Eq. 4.21.

$$\vec{w} = \Gamma \cdot \vec{GC} \tag{4.21}$$

4.4.5 Vortex induced velocity calculation

The calculation of the vortex induced velocity at any blade element of the lifting line can be conducted, starting from the simple Eq. 4.21. At this point the segmentation of the blade and wake must be recapitulated with the help of Fig. 4.7. Each one of the N_B blades is modelled as a bound vortex that is split into N blade elements. These elements have constant circulation and are bounded by $N+1$ points. From these points spring $N+1$ trailing vortex filaments that are split into $N_{WP}-1$ straight vortex segments (according to the discretisation of the wake as given by Eq. 4.15). The circulation is constant along the length of a trailing vortex filament and is equal to the circulation difference between the two bound vortex segments adjacent to the origin of the filament (Fig. 4.8).

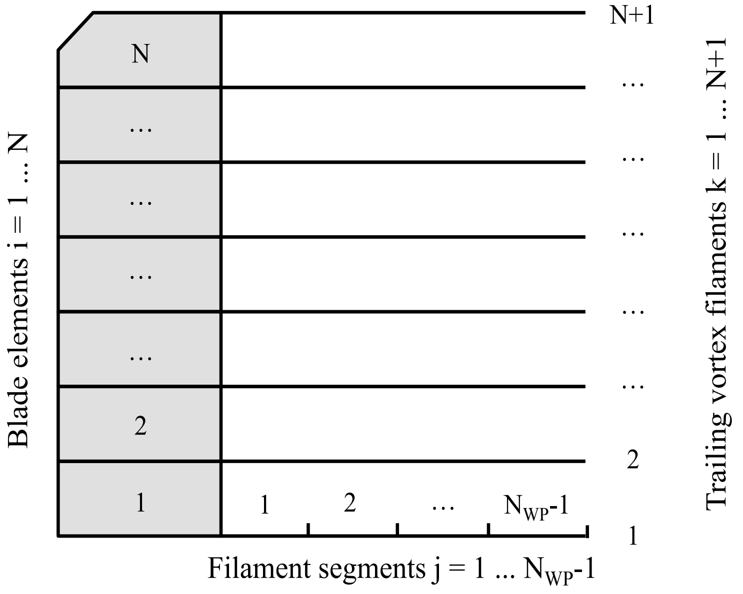

Figure 4.7: The discretisation of the blade and the wake. The blade is depicted with grey background.

The first step is the calculation of the velocity induced by the trailing vorticity. The velocity induced on the i^{th} blade element, by the j^{th} segment, of the k^{th} trailing filament, of the l^{th} blade is:

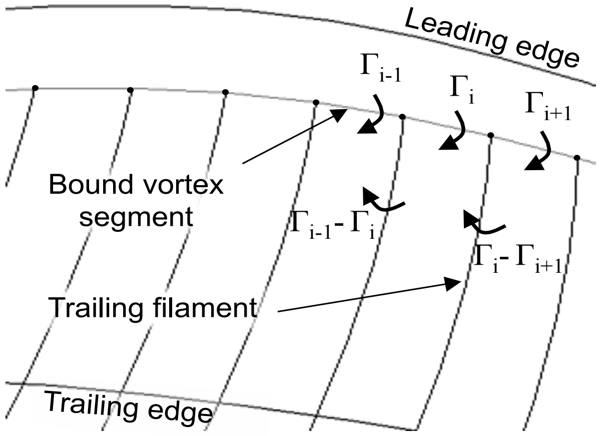

Figure 4.8: The relation between bound and trailing vortex circulation.

$$\vec{w}_{TR,(i,j,k,l)} = \Gamma_{TR,(k)} \cdot \vec{GC}_{TR,(i,j,k,l)} \tag{4.22}$$

where Γ_{TR} is the circulation of the trailing filament. Then the total induced velocity from the k^{th} trailing filament of all the blades is:

$$\vec{w}_{TR,(i,k)} = \Gamma_{TR,(k)} \cdot \sum_{l=1}^{N_B} \sum_{j=1}^{N_{WP}-1} \vec{GC}_{TR,(i,j,k,l)} = \Gamma_{TR,(k)} \cdot \vec{GC}_{TR,(i,k)} \tag{4.23}$$

Therefore the velocity induced by all the trailing vortex filaments is given by:

$$\vec{w}_{TR,(i)} = \sum_{k=1}^{N+1} \Gamma_{TR,(k)} \cdot \vec{GC}_{TR,(i,k)} \tag{4.24}$$

From Fig. 4.8 the trailing circulation of the k^{th} filament can be defined as $\Gamma_{TR,(k)} = \Gamma_{(k-1)} - \Gamma_{(k)}$, where $\Gamma_{(k)}$ is the circulation of the $i = k$ blade element. In the special cases where $k = 1$ or $k = N + 1 \Rightarrow \Gamma(k) = 0$. Hence Eq. 4.24 can be rewritten as:

$$\vec{w}_{TR,(i)} = \sum_{k=1}^{N+1} \left(\Gamma_{(k-1)} - \Gamma_{(k)}\right) \cdot \vec{GC}_{TR,(i,k)} \tag{4.25}$$

which can then be regrouped in terms of $\Gamma_{(k)}$ to give:

$$\vec{w}_{TR,(i)} = \sum_{k=1}^{N} \Gamma_{(k)} \cdot \left[\vec{GC}_{TR,(i,k+1)} - \vec{GC}_{TR,(i,k)}\right] = \sum_{k=1}^{N} \Gamma_{(k)} \cdot \vec{GC}^{*}_{TR,(i,k)} \tag{4.26}$$

Similarly, the velocity induced on the i^{th} blade element coming from the k^{th} bound vortex segment of the l^{th} blade is given by:

$$\vec{w}_{B,(i,k,l)} = \Gamma_{(k)} \cdot \vec{GC}_{B,(i,k,l)} \tag{4.27}$$

Hence, the total bound induced velocity on the i^{th} blade element can be calculated by:

$$\vec{w}_{B,(i)} = \sum_{k=1}^{N} \sum_{l=1}^{N_B} \Gamma_{(k)} \cdot \vec{GC}_{(i,k,l)} = \sum_{k=1}^{N} \Gamma_{(k)} \cdot \vec{GC}^*_{(i,k)} \tag{4.28}$$

And finally the total induced velocity of the i^{th} blade element can be calculated as a summation of the product of geometric coefficient vectors and the scalar circulation values of every blade element:

$$\vec{w}_{(i)} = \sum_{k=1}^{N} \Gamma_{(k)} \cdot \left[\vec{GC}^*_{TR,(i,k)} + \vec{GC}^*_{B,(i,k)}\right] = \sum_{k=1}^{N} \Gamma_{(k)} \cdot \vec{GC}^*_{(i,k)} \tag{4.29}$$

It must be noted for the sake of clarity that the index i represents the blade element of which the induced velocity is sought, and the index k the blade element whose circulation causes a part of the induced velocity at blade element i.

4.4.6 Calculation of circulation

The analysis has reached a point where the calculation of the induced velocity requires the calculation of the circulation at each blade element $\Gamma_{(i)}$. There are two methods to set up and solve the problem. The first method, which belongs to the family of vortex-lattice models, dictates that a control point is located at the three quarters chord point and the induced velocity is calculated there. The total normalwise velocity vector at that point must be equal to zero to satisfy the condition of non-permeability of the blade surface. This method has been used by Sullivan [118]. The vortex-lattice models work better if the blade is split in many elements in the spanwise and the chordwise direction (and that is why they are called vortex "lattice"). In the case where there is only one chordwise element, as for the lifting line assumption, the method fails to take into account any differences in the camber of the airfoils. That is because the condition of non-permeability in this case only depends on the location of the chord line which is independent of the mean camber line. If the camber line was discretised by more than one elements the effect of camber would be correctly accounted for, at the cost of higher computational effort. Phillips [137] identified this shortcoming of the single chordwise element vortex-lattice method and proposed an alternative method which he called the modern Prandtl lifting-line. However this method had already been used earlier for the case of prop-fans by Egolf et al. [117], and this is the one selected by the author. As the original method described by Egolf contained some ambiguities, the method will be redeveloped here with all the assumptions stated at every step.

The 2D lift at a blade element can be calculated by using the well known law of Kutta-Joukowski [96], as shown in Eq. 4.30.

$$L_{(i)} = \rho V_{cn,(i)} \Gamma_{(i)} \tag{4.30}$$

where ρ is the air density and $V_{cn,(i)}$ the total velocity at the i^{th} blade element in the cn local blade element plane. The spanwise component $V_{s,(i)}$ is not needed as it does not participate in the generation of lift. Another way to calculate the lift at the blade element is by using the lift coefficient definition:

$$L_{(i)} = \frac{1}{2} \rho c_{(i)} V_{cn,(i)}^2 C_{L,(i)} \tag{4.31}$$

where $c_{(i)}$ is the chord of the blade element i and $C_{L,(i)}$ the lift coefficient of the element. Equations 4.30 and 4.31 are two independent ways of calculating the blade-element lift. If equated they provide the boundary condition needed for the determination of the circulation of each blade element, Eq. 4.32.

$$\Gamma_{(i)} = \frac{1}{2} c_{(i)} V_{cn,(i)} C_{L,(i)} \tag{4.32}$$

Equation 4.32 takes into account the effect of camber by using the appropriate C_L for each airfoil. The equation applied to every blade element $i = 1..N$ gives a system of N non-linear equations for the determination of the circulation of each blade element. It can be solved either by using strong under-relaxation as suggested by Tremmel et al [134], or by a convenient linearisation as done by Egolf et al [117] and Young [123]. The second method has been chosen as it is faster and can be corrected for non-linear effects by using a fast iterative scheme. Figure 4.9 will be used as reference for the analysis.

It is readily seen from Fig. 4.9 that for small angles of attack the greatest component of the velocity V_{cn} will lie on the chordwise axis, i.e. $V_{cn} \simeq V_c$. Furthermore, one can assume that for high speed applications the vortex induced velocities have a much lower contribution than the free stream and nacelle induced ones and thus $V_c \simeq V_{f,c}$, where $V_{f,c} = U_c + u_c$. This way the velocity vector does not depend any more on the value of circulation. To compensate for the error introduced by the above simplifications the velocity $V_{f,c}$ must be corrected by a correction factor $C_{FV,(i,t-1)}$, where $(t-1)$ represents the previous iteration step. The calculation of all the correction factors will be given every time a simplification is introduced. The final expression for the velocity $V_{cn,(i)}$ is:

$$V_{cn,(i)} = V_{f,c,(i)} + C_{FV,(i,t-1)} \tag{4.33}$$

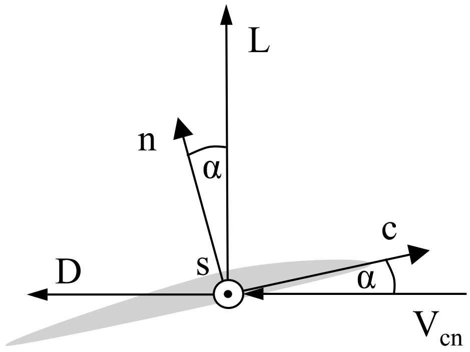

Figure 4.9: Blade-element aerodynamic performance described by the flow velocity in the *cn* plane and the lift and drag forces.

This equation is used inversely to calculate the correction factor of the current iteration step by using the known velocity values of the previous step, i.e.

$$C_{FV,(i,t-1)} = V_{cn,(i,t-1)} - V_{f,c,(i,t-1)} \tag{4.34}$$

and that is why the correction factor refers to the iteration step $(t-1)$. Where an iteration index is not used, the variable refers to the current iteration. Equation 4.32 becomes:

$$\Gamma_{(i)} = \frac{1}{2} c_{(i)} \left(V_{f,c,(i)} + C_{FV,(i,t-1)} \right) C_{L,(i)} \tag{4.35}$$

The next linearisation concerns the lift coefficient $C_{L,(i)}$ which as shown by Eq. 4.36 can be replaced by the product of the lift slope $C_{La,(i)}$ and the angle of attack $\alpha_{(i)}$ (in degrees), plus a correction factor which is defined by Eq. 4.37. Equation 4.35 is rearranged to give Eq. 4.38.

$$C_{L,(i)} = C_{La,(i)} \cdot \alpha_{(i)} + C_{FL,(i,t-1)} \tag{4.36}$$

$$C_{FL,(i,t-1)} = C_{L,(i,t-1)} - C_{La,(i,t-1)} \cdot \alpha_{(i,t-1)} \tag{4.37}$$

$$\Gamma_{(i)} = \frac{1}{2} c_{(i)} \left(V_{f,c,(i)} + C_{FV,(i,t-1)} \right) \cdot \left(C_{La,(i)} \cdot \alpha_{(i)} + C_{FL,(i,t-1)} \right) \tag{4.38}$$

Equation 4.38 is still non-linear due to the non-linear relation between the angle of attack and the circulation. Thus a linearised approximation of the angle of attack must be used. According to Fig. 4.9 the angle of attack can be defined by Eq. 4.39.

$$\alpha_{(i)} = \tan^{-1} \left(\frac{U_{n,(i)} + u_{n,(i)} + w_{n,(i)}}{U_{c,(i)} + c_{n,(i)} + w_{c,(i)}} \right) = \tan^{-1} \left(\frac{V_{f,n,(i)} + w_{n,(i)}}{V_{f,c,(i)} + w_{c,(i)}} \right) \tag{4.39}$$

for $V_{f,c,(i)} \gg w_{c,(i)}$ this becomes

$$\alpha_{(i)} = \tan^{-1}\left(\frac{V_{f,n,(i)}}{V_{f,c,(i)}} + \frac{w_{n,(i)}}{V_{f,c,(i)}}\right) \tag{4.40}$$

if the angle of attack is small the tan^{-1} can be omitted to give the simple expression:

$$\alpha_{(i)} = \theta_{B,(i)} + \frac{w_{n,(i)}}{V_{f,c,(i)}}\frac{180}{\pi} \tag{4.41}$$

where

$$\theta_{B,(i)} = \frac{180}{\pi}\frac{V_{f,n,(i)}}{V_{f,c,(i)}} \tag{4.42}$$

and both $\theta_{B,(i)}$ and $\alpha_{(i)}$ are given in degrees. Equation 4.41 is not the final one, as a correction factor is needed to produce the final Eq. 4.43. The correction factor $C_{F\phi,(i,t-1)}$ is defined by Eq. 4.44 using the values from the previous iteration step.

$$\alpha_{(i)} = \theta_{B,(i)} + \frac{w_{n,(i)}}{V_{f,c,(i)}}\frac{180}{\pi} + C_{F\phi,(i,t-1)} \tag{4.43}$$

$$C_{F\phi,(i,t-1)} = \alpha_{(i,t-1)} - \theta_{B,(i,t-1)} + \frac{w_{n,(i,t-1)}}{V_{f,c,(i,t-1)}}\frac{180}{\pi} \tag{4.44}$$

The angle correction Eq. 4.43 is coupled with Eq. 4.38 to give Eq. 4.45 below:

$$\begin{aligned}\Gamma_{(i)} =& \frac{1}{2}c_{(i)}\left(V_{f,c,(i)} + C_{FV,(i,t-1)}\right)\cdot \\ & \left[C_{La,(i)}\left(\theta_{B,(i)} + \frac{w_{n,(i)}}{V_{f,c,(i)}}\frac{180}{\pi} + C_{F\phi,(i,t-1)}\right) + C_{FL,(i,t-1)}\right]\end{aligned} \tag{4.45}$$

Equation 4.45 after some algebraic manipulations gives:

$$\Gamma_{(i)} = \frac{1}{2}c_{(i)}C_{La,(i)}\left[V_{f,c,(i)}\theta_{B,(i)} + \frac{180}{\pi}w_{n,(i)}\left(1 + \frac{C_{FV,(i,t-1)}}{V_{f,c,(i)}}\right) + C_{F,(i,t-1)}\right] \tag{4.46}$$

where

$$\begin{aligned}C_{F,(i,t-1)} =& V_{f,c,(i)}\left[\frac{C_{FL,(i,t-1)}}{C_{La,(i)}} + C_{F\phi,(i,t-1)}\right] + \\ & C_{FV,(i,t-1)}\left[\frac{C_{FL,(i,t-1)}}{C_{La,(i)}} + C_{F\phi,(i,t-1)} + \theta_{B,(i)}\right]\end{aligned} \tag{4.47}$$

The induced velocity $w_{n,(i)}$ can be calculated from Eq. 4.29, if the geometric vector coefficient $\vec{GC}^{*}_{(i,k)}$ is transformed from the XYZ system to the local scn system of every blade element by using the transformation Eq. 4.9. The result is shown below only for the required normalwise axis (i.e. only the normalwise component GC_n^* is used, instead of the whole vector $\vec{GC}^*$).

$$\vec{w}_{n,(i)} = \sum_{k=1}^{N} \Gamma_{(k)} \cdot GC^*_{n,(i,k)} \tag{4.48}$$

By substituting Eq. 4.48 to Eq. 4.46 the final circulation equation is produced:

$$\begin{aligned}\Gamma_{(i)} =& \frac{1}{2} c_{(i)} C_{La,(i)} \cdot \\ & \left[V_{f,c,(i)} \theta_{B,(i)} + \frac{180}{\pi} \sum_{k=1}^{N} \Gamma_{(k)} \cdot GC^*_{n,(i,k)} \left(1 + \frac{C_{FV,(i,t-1)}}{V_{f,c,(i)}} \right) + C_{F,(i,t-1)} \right]\end{aligned} \tag{4.49}$$

which, after a slight rearrangement, becomes:

$$\begin{aligned}\Gamma_{(i)} - \frac{1}{2} c_{(i)} C_{La,(i)} \frac{180}{\pi} \left(1 + \frac{C_{FV,(i,t-1)}}{V_{f,c,(i)}} \right) \sum_{k=1}^{N} \Gamma_{(k)} \cdot GC^*_{n,(i,k)} = \\ = \frac{1}{2} c_{(i)} C_{La,(i)} \left[V_{f,c,(i)} \theta_{B,(i)} + C_{F,(i,t-1)} \right]\end{aligned} \tag{4.50}$$

Equation 4.50 is a system of linear equations for $i = 1..N$, where N the number of blade elements; i.e. the system is of the form $[A]\Gamma = B$ and can be easily solved with a matrix inversion. Every term is known apart from the circulation $\Gamma_{(i)}$. The correction factors which are calculated from the results of the previous step are initially set to 0. The process converges when the change in circulation in all elements from one iteration to the next is less than a specified tolerance.

The circulation calculation procedure will be summarized here with the aid of Fig. 4.10. The geometry, operating conditions and method configuration are first loaded. The geometry and the location of the lifting line are fed in the Panair code, which calculates the nacelle induced velocities $\vec{u}$. The velocities are fed in the lifting-line code which initialises a wake geometry, by assuming zero vortex induced velocity. Using this wake definition a first set of geometric coefficients can be calculated and the linear system of Eq. 4.50 can be solved for the circulation. The knowledge of the circulation distribution allows the calculation of the vortex induced velocities $\vec{w}$, which in turn allow the determination of the correction factor C_{FV}. By knowing the total velocity vectors the angle of attack at each blade element can be determined together with the correction factor $C_{F\phi}$. The angle of attack is then translated to a lift coefficient C_L through a 2D airfoil database, and the correction factor C_{FL} is thereby defined. The convergence criterion is then checked, which is by default false for the first iteration. If more iterations are needed, then the

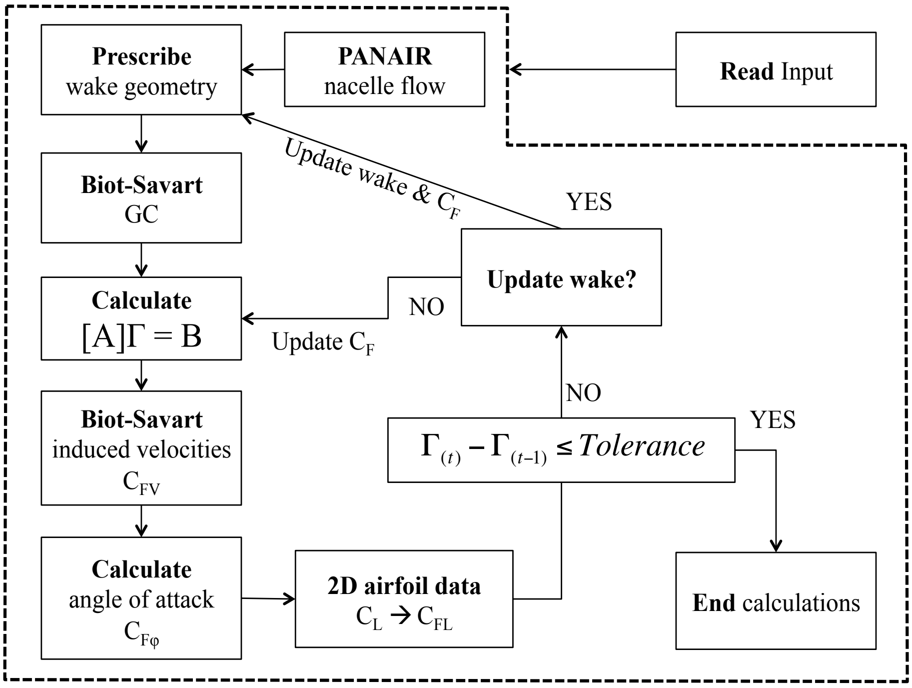

Figure 4.10: Overview of the blade circulation calculation process.

wake geometry is updated by taking into account the new velocity field as described in section 4.4.3 and the new geometric coefficients are calculated. The newly calculated factors are also used to update the system of Eq. 4.50. The wake geometry does not need to be updated more than approximately 3 times as further updates have a minor effect on the results and consume excessive computational resources. If the process converges the code passes to the final stage, which is the calculation of the lift and drag forces, which are then translated to thrust, torque and efficiency, as described in the next section.

4.4.7 Blade-element performance

The lift and drag forces in Fig. 4.9 can be calculated by using a 2D airfoil database. This database relates the angle of attack and Mach number of the flow with a lift and drag coefficient C_L and C_D, which can then be used to calculate the lift L and drag D. The 2D airfoil database used in this analysis is the one reported in References [99], [138] and [139]. This is probably the only one existing in the public domain which at the same time is so extensive. It contains C_L and C_D data for the NACA-16 and NACA-65 families, which are the ones commonly used in high-speed propellers. It covers Mach numbers upto 1.6 and angles of attack from -4. to +8 degrees. The data do not include the post-stall performance, therefore the performance prediction at operating conditions where a large part of the blade is stalled will not be reliable. However, it must be noted that propeller blades present a higher resistance to stall due to the three-dimensional spanwise flow which re-energises the boundary layer [140] and thus the blades are not expected to stall at the operating regions of interest. Some comments must also be made here regarding the Reynolds number (Re) effect. First of all, as mentioned in section 4.2, for propeller applications its quite common to ignore the effect of Re without a significant loss of accuracy. This is the case with this database which does not include a Re dependency. However, there is one more uncertainty in the database. First the corresponding Re value is not given, and secondly, as stated by Borst [99], the database is a compilation of all the test data available at that time. Consequently, not only the Re is not known, but it cannot even be asserted that it is consistent between different airfoils. Even at the same test it is unlikely that the Re has been kept constant as the Mach varied. Nevertheless, this database is the most reliable source of airfoil data, to the best of the authors knowledge, and it is deemed sufficient within the context of this work. It must be added that this airfoil database has been created especially for high-speed propeller modelling [99] and it has also been used in References [84] and [140] for similar propeller simulation efforts.

As mentioned earlier, one of the fundamental assumptions of blade-element theory is that only the velocity components which are normal to the airfoil participate in the generation of lift and drag. Hence, only the *cn* plane components are considered. However, the analysis also has to take into account the additional skin friction drag generated by the significant spanwise velocity components that are present in swept blades [102, 117]. This effect is taken into account in the analysis of the elemental lift and drag referred to the local *scn* coordinate system, Equations 4.51-4.53.

$$\begin{aligned} F_{c,(i)} =& 0.5 \cdot \rho \cdot A_{(i)} \cdot V_{cn,(i)}^2 \cdot \left(C_{L,(i)} \sin\alpha_{(i)} - C_{Dpr,(i)} \cos\alpha_{(i)}\right) + \\ & 0.5 \cdot \rho \cdot A_{(i)} \cdot C_{Df,(i)} \cdot V_{c,(i)} \cdot \sqrt{V_{s,(i)}^2 + V_{c,(i)}^2 + V_{n,(i)}^2} \end{aligned} \tag{4.51}$$

$$\begin{aligned} F_{n,(i)} =& 0.5 \cdot \rho \cdot A_{(i)} \cdot V_{cn,(i)}^2 \cdot \left(C_{Dpr,(i)} \sin\alpha_{(i)} + C_{L,(i)} \cos\alpha_{(i)}\right) + \\ & 0.5 \cdot \rho \cdot A_{(i)} \cdot C_{Df,(i)} \cdot V_{n,(i)} \cdot \sqrt{V_{s,(i)}^2 + V_{c,(i)}^2 + V_{n,(i)}^2} \end{aligned} \tag{4.52}$$

$$F_{s,(i)} = 0.5 \cdot \rho \cdot A_{(i)} \cdot C_{Df,(i)} \cdot V_{s,(i)} \cdot \sqrt{V_{s,(i)}^2 + V_{c,(i)}^2 + V_{n,(i)}^2} \tag{4.53}$$

$$\begin{aligned} \vec{D}_{(i)} =& 0.5 \cdot \rho \cdot A_{(i)} \cdot C_{Df,(i)} \cdot \left(V_{s,(i)}^2 + V_{c,(i)}^2 + V_{n,(i)}^2\right) \cdot \\ & \frac{V_{s,(i)}\vec{e}_s + V_{c,(i)}\vec{e}_c + V_{n,(i)}\vec{e}_n}{\sqrt{V_{s,(i)}^2 + V_{c,(i)}^2 + V_{n,(i)}^2}} \end{aligned} \tag{4.54}$$

In the above equations, $A_{(i)}$ is the area of the blade element i, C_{Dpr} is the pressure drag coefficient and C_{Df} the friction drag coefficient. This distinction between pressure and friction drag is made for the following reason. The pressure drag is only a result of the flow in the 2D *cn* plane, while the friction drag must also take into account the spanwise velocity component. Hence, the friction drag acts in the direction of the total velocity vector, while the pressure drag acts in the direction of the velocity $\vec{V}_{cn}$ that lies in the *cn* plane. This concept is represented by Eq. 4.54 which defines the friction drag vector. The term in the second line of the equation is the total velocity vector divided by its magnitude in order to give a unit vector. The spanwise force F_s includes the projection of the total friction drag to the spanwise direction, while the projections to the chordwise and normalwise axes are included as additional terms in the calculation of the force components F_c and F_n, Eq. 4.51 and Eq. 4.52. A last point must be made regarding the pressure and friction drag coefficients. The available airfoil database only gives a total drag coefficient C_D without differentiating between pressure and friction drag. According to Egolf et al [117] the friction drag coefficient C_{Df} can be approximated by the total drag coefficient for zero angle of attack; i.e. $C_{Df} = C_D(\alpha = 0)$. Then the pressure drag coefficient can be given by, $C_{Dpr} = C_D - C_{Df}$.

$$\vec{F}_{(i)} = F_{s,(i)} \cdot \vec{e}_s + F_{c,(i)} \cdot \vec{e}_c + F_{n,(i)} \cdot \vec{e}_n \tag{4.55}$$

$$\vec{F}_{(i)} = F_{X,(i)} \cdot \vec{e}_X + F_{Y,(i)} \cdot \vec{e}_Y + F_{Z,(i)} \cdot \vec{e}_Z \tag{4.56}$$

The element force analysis results in the final definition of the total force vector in the local *scn* system (Eq. 4.55), which can then be translated to the global XYZ system (Eq. 4.56) by using Eq. 4.10. The element thrust is then equal to the Z component of the force vector (Eq. 4.57), while the torque is calculated by the external product of the force and position vector, projected to the Z axis (Eq. 4.58). The position vector refers to the center (in the spanwise direction) of the blade element located on the quarter chord line of the blade.

$$T_{(i)} = F_{Z,(i)} \tag{4.57}$$

$$Q_{(i)} = \left(\vec{F}_{(i)} \times \vec{r}_{BE,(i)}\right) \cdot \vec{e}_Z = F_{X,(i)} \cdot r_{BE,Y,(i)} - F_{Y,(i)} \cdot r_{BE,X,(i)} \tag{4.58}$$

The total thrust and torque can now be calculated by Eq. 4.59 and Eq. 4.60 by a simple summation of the thrust of all the blade elements times the number of blades M. The propeller power is then given by Eq. 4.61 and the efficiency by Eq. 4.62, where Ω is the propeller rotational speed in [rad/s] and V_0 is the flight velocity in [m/s]. The calculation of the propeller performance has been completed.

$$T = N_B \cdot \sum_{i=1}^{N} T_{(i)} \tag{4.59}$$

$$Q = N_B \cdot \sum_{i=1}^{N} Q_{(i)} \tag{4.60}$$

$$P = Q \cdot \Omega \tag{4.61}$$

$$\eta_{prop} = \frac{T \cdot V_0}{P} \tag{4.62}$$

4.4.8 Compressibility effects

As confirmed by the literature survey of section 4.3, lifting-line methods similar to the one developed in the previous sections are the current state-of-the-art for prop-fan preliminary analysis and design. One of the very fundamental assumptions in the development of the lifting-line approach, is the hypothesis of a potential, incompressible flow [96]. This hypothesis, which is shared with the panel methods, leads to a convenient linear differential equation that describes the flow under investigation. The greatest advantage of a linear differential equation is that, if a set of solutions is known, any linear combination of this solution is also a solution [132]. The effect of a single straight vortex segment is an elementary solution (or singularity), which combined with the effect of all the other vortex segments through a simple summation gives the total flow velocities solution (see section 4.4.5).

Contrary to the lifting-line, which is strictly incompressible, the panel methods have been extended to compressible subsonic and supersonic applications without losing their linearity. The difference between subsonic and supersonic was described by Von Karman [141]. For subsonic flows the effect of a singularity, such as a vortex segment, is felt in the whole computational domain, while for supersonic flows it is only affecting regions within its aft Mach cone. This is what Von Karman called the "zone of action", while what is outside is called the "zone of silence". From a mathematical perspective the equation of the subsonic problem is of the elliptic type, while the supersonic flow equation is hyperbolic [137]. Unfortunately, a propeller usually operates in a completely transonic flow, where the hub Mach number is close to 0.8 and the tip close to 1.2. Anderson [96] explicitly states that a linearised solution is not valid in this range of Mach number. This is confirmed by Nixon (in Morino's edition [133]), who suggests that even the most primitive representation of the flow still requires a non-linear equation. From a mathematical perspective a transonic equation is of a mixed elliptic/hyperbolic type. Non-linear equations can only be solved by discretising the whole fluid volume and by solving with partial differences or other relevant methods that belong to the domain of CFD but not in the group of panel methods.

Despite the aforementioned difficulties, a few works where found in the literature that attempted to add some transonic capability to a linear propeller simulation method. The works will be commented in approximately chronological order. Davidson in 1953 [142] proposed a linearised solution to the potential problem for ducted fans. Wells [143] extended his work to the case of unducted propellers. There are three main problems with their approach. First the authors do not justify the linearisation of an equation which normally is not allowed to be linearised. Secondly, they did not report any results to prove the modelling reliability and fidelity of their approach. And thirdly, their approach follows the Goldstein [97] method, and thus it is only applicable to straight blades with rigid helical wakes. This assumption is not adequate for the case of prop-fan modelling as discussed in sections 4.3 and 4.4.3.

A different path was followed by Borst [99] who proposed two corrections applied to his baseline Goldstein/Theodorsen method. The same corrections were applied later by Egolf [117] and Rohrbach [105] to a lifting-line method. The first correction is an application of the "zones of silence" concept to the calculation of induced velocities as presented in sections 4.4.4 and 4.4.5. According to Borst, when summing the influence of every single vortex segment, one must only take into account the vortex segments which are inside the "zone of action". This is tested simply by checking whether the signal that was emitted from the location of the segment had the time to reach the current location of the blade element. As a result, the initial segments of a trailing vortex filament are likely to be outside the zone of action and therefore have no effect on the velocity. The second modification suggested by Borst was the application of a correction factor within the Mach cone of the tip of the blade. This was implemented by using results from a supersonic potential calculation conducted for a fixed wing flying with a constant speed along the span as reported by Evvard [144]. The estimated correction factors where applied on the lift and drag coefficients. The supersonic calculation by Evvard already includes the concept of hyperbolic flow and "zones of silence" and therefore it appears that the two corrections overlap. Furthermore, the calculation by Evvard was dealing with a completely supersonic flow of a wing and its applicability to a rotating transonic propeller is not justified. Finally, the combination of the "zones of silence" concept with the strictly incompressible Biot-Savart law is quite dubious. Therefore, the two modifications can only be seen as "engineering corrections", which attempt to model some real phenomena, but in a way that is not formally proven or justified. The concerns over validity of the correction are confirmed by the results from both studies [105] and [117]. The predictions seem unrealistic as they present a reversal of curvature in the efficiency-Mach curve after a Mach number of 0.80 (Fig. 4.11). This happens because of the de-activation of the vortex segments located close to the blade and outside the "zones of action", with a parallel reduction in ideal losses. At this point it is worth drawing the attention of the reader to the fact that Reference [105] was written by Hamilton Standard which is the company that designed the SR family of prop-fans. This fact highlights that the task of prop-fan modelling is far from being trivial.

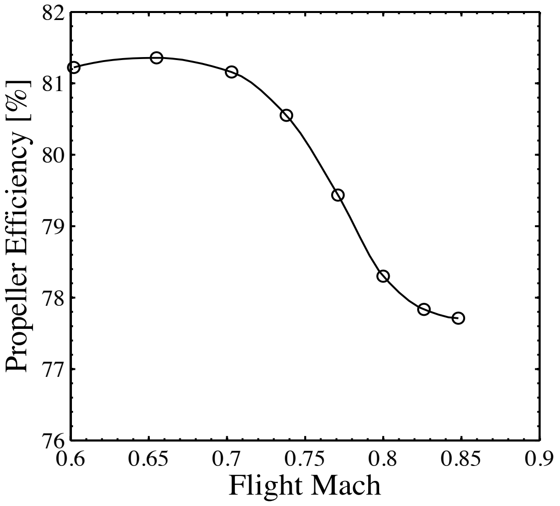

Figure 4.11: Efficiency prediction results from Rohrbach et al [105] using the Borst corrections. Prediction for the SR3 propeller, $J = 3.06$ and $C_P = 1.695$. Unrealistic change of curvature after Mach = 0.80.

The work of Hanson (also working in Hamilton Standard) in the 80s [83, 145, 146] is the most complete found by the author, and the only one that has a formal mathematical and physical formulation. Hanson built a lifting-surface method based on the linear wave equation in order to produce unsteady results for noise calculations. The method could also work in steady state for aerodynamic calculations and Hanson claimed that his prop-fan performance prediction was the most accurate at that time. The use of a linear equation was justified by using a criterion found in Bisplinghoff et al [147] and reproduced below:

$$AR^3 \cdot \delta \cdot \left[\ln\left(AR\delta^{1/3}\right)\right]^2 \ll 1 \tag{4.63}$$

where AR is the blade aspect ratio and δ the thickness ratio. By using the values $AR = 3$ and $\delta = 0.02$, which are typical of a prop-fan blade, Hanson calculated a value of $AR^3\delta\left[\ln\left(AR\delta^{1/3}\right)\right]^2$ equal to 0.023. This value satisfies the criterion of Eq. 4.63 and justifies the use of a linearised theory. Indeed the results at high Mach number looked promising but this was not the case for the low Mach number predictions. The theory assumed that the blades travel on a rigid helical wake and therefore did not take into account the effect of induced velocities on the wake. This effect introduced an important non-linearity to the flow which was not captured by the model. An attempt to rectify the problem was made through a coupling with a momentum theory but the results as reported by Hanson et al [83] were still unsatisfactory. Nevertheless, the high speed results will be kept as a reference base for the validation of this work. Another very interesting finding of his work, and more specifically of Reference [146], is the justification of using a simple lifting-line theory. By using a formal mathematical approach Hanson proved that the effect of modelling the blade with a single lifting line (thus neglecting the chordwise variations) cancels out with the effect of the incompressibility hypothesis. According to Hanson [146] this is the reason that lifting-line methods have been so successful in the design of prop-fans.

The most recent work found in the literature relative to the treatment of compressibility is the approach of Szymendera [135], which was also followed by Burger [129]. In this case, Szymendera assumed that each vortex segment performs an independent motion away from the control point which is located on the blade-element. He then performed a simple Prandtl-Glauert transformation of the domain to capture the stretching of the space due to compressibility as described in Anderson [96]. However, the treatment of each vortex segment as a separate flow was not justified by the author, and his results for the compressible case were less accurate than without the compressibility modification. Therefore, the suggested approach does not seem reliable.

Following this literature survey, it has been decided to follow a completely incompressible approach for the calculation of the vortex induced velocities; i.e. no modification is required to what has already been presented in the previous sections. This decision is based on: 1) the complexity of implementing Hanson's method which seems as the most well formulated, 2) the unsatisfactory results of the same method at take-off conditions, 3) the last argument of Hanson [146] regarding the suitability of simple lifting-line methods. As mentioned earlier, the high speed results of Hanson et al [83] will be kept as a comparison base for the validation of the method implemented. This will permit the evaluation of the error introduced by using a simpler modelling approach instead of a higher fidelity one. At the same time, it must be reminded that a part of the compressibility effects is captured through the airfoil database which includes the lift and drag coefficients as functions of Mach number. Furthermore, it must also be underlined that PANAIR models the compressible subsonic flow around the spinner/nacelle, although it has been decided to limit the input Mach number to 0.7. This has been done in order to ensure that the code operates in the Mach number domain suitable for linear potential theory (the upper limit being 0.7-0.8).

4.5 Method verification and validation

4.5.1 Case description

The SR3 prop-fan blade geometry has been chosen to test the validity of the developed method. This prop-fan has been designed in the 70s by Hamilton Standard and it is the one with the most data in the public domain. It features 8 swept blades, a hub/tip ratio of 0.2375 and the diameter of the model used in the experimental tests was 0.622 m. Table 4.1 gives the definition of the blade characteristics as reported by Rohrbach et al [105]. For each blade station, the table contains the radial position relative to the blade radius, the chord relative to the blade diameter, the twist angle $\Delta\beta$, and the sweep angle Λ. The last column gives the airfoil used at each station as reconstructed according to information given by Rohrbach [105]. Using this table the blade geometry has been reproduced according to the method described in section 4.4.1. The spinner/nacelle geometry are given by tables 4.2 and 4.3, with data retrieved from Stefko and Jeracki [148]. The reconstructed combination of blade/spinner/nacelle is shown in Fig. 4.12. The blade is represented by a mean surface formed by the chords of each blade station.

Table 4.1: SR3 blade geometry definition. Source: Rohrbach et al [105].

r/R	c/D	$\Delta\beta$ [°]	Λ [°]	Airfoil
0.25	0.164	+22.963	-24.640	NACA-65A-(-320)
0.30	0.171	+19.910	-21.525	NACA-65A-(-110)
0.35	0.180	+17.399	-14.908	NACA-65A-007
0.40	0.190	+14.706	-7.420	NACA-16-106
0.45	0.196	+12.376	+0.071	NACA-16-105
0.50	0.202	+10.046	+7.851	NACA-16-204
0.55	0.204	+7.896	+15.340	NACA-16-204
0.60	0.202	+5.927	+21.662	NACA-16-203
0.65	0.197	+3.598	+26.819	NACA-16-203
0.70	0.191	+1.810	+31.103	NACA-16-203
0.75	0.182	+0.022	+35.382	NACA-16-203
0.80	0.169	-1.945	+38.500	NACA-16-202
0.85	0.152	-3.371	+41.902	NACA-16-202
0.90	0.131	-4.797	+43.854	NACA-16-202
0.95	0.105	-6.402	+44.927	NACA-16-202
1.00	0.071	-7.647	+44.547	NACA-16-202

Table 4.2: SR3 spinner geometry definition. $R_{ref} = 0.1105$. Source: Stefko and Jeracki [148].

x/R_{ref}	r/R_{ref}	x/R_{ref}	r/R_{ref}
0.000	0.000	1.207	0.598
0.081	0.119	1.264	0.597
0.138	0.168	1.322	0.595
0.253	0.246	1.379	0.597
0.368	0.310	1.437	0.606
0.598	0.410	1.494	0.619
0.828	0.497	1.552	0.636
1.057	0.568	1.609	0.654
1.092	0.577	1.667	0.673
1.149	0.591	2.184	0.857

Table 4.3: SR3 nacelle geometry definition. $R_{ref} = 0.1105$. Source: Stefko and Jeracki [148].

x/R_{ref}	r/R_{ref}	x/R_{ref}	r/R_{ref}
2.199	0.860	3.136	0.999
2.216	0.866	3.214	1.000
2.239	0.873	3.366	0.999
2.262	0.881	3.596	0.990
2.285	0.888	3.825	0.975
2.308	0.895	4.055	0.956
2.331	0.902	4.285	0.933
2.354	0.908	4.515	0.911
2.377	0.915	4.745	0.894
2.400	0.920	4.975	0.883
2.423	0.926	5.205	0.874
2.446	0.931	5.251	0.873
2.561	0.946	5.297	0.871
2.676	0.970	5.400	0.871
2.791	0.982	5.417	0.865
2.906	0.990	8.659	1.046

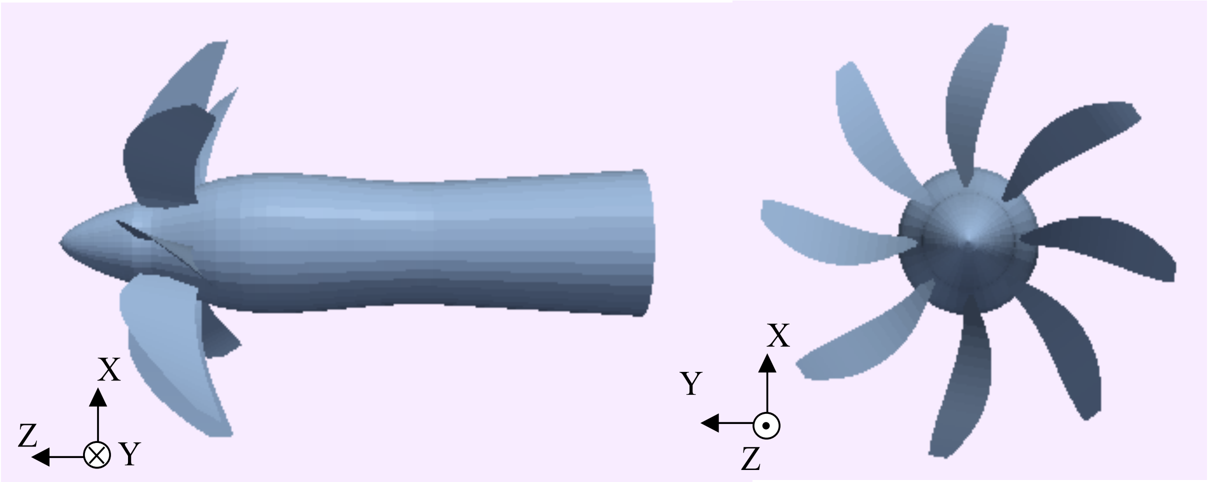

Figure 4.12: The SR3 blade/spinner/nacelle geometry as reconstructed by the developed code.

4.5.2 Model configuration

The set-up of the numerical model is given in table 4.4. The choice of the grid parameters is a result of a grid parametric study as shown in figures 4.13-4.14. The choice of 20 spanwise blade stations is in line with what is reported by Burger [129], while the respective grading parameter was chosen to give a denser distribution close to the blade tip. Traumel [134] suggested that only the first turn of the wake needs to be accounted for, while the rest of the wake can be taken into account by approximative methods. This statement is in part confirmed by Fig. 4.13b which shows that after two turns the result does not change. This is logical, as it is the wake segments closest to the blade that have the greatest impact on the performance. However, it has been decided to include four wake turns in order to accommodate cases where the advance ratio is low and therefore the wake segments are closer to the blades for the same number of turns. Once more, the wake azimuthal grading factor was set to 1.6, resulting in smaller segments close to the blades where the greatest accuracy is needed. For the same reason the wake points number has to be kept over 100 as shown by Fig. 4.13c; the smaller the wake vortex segments, the greater the accuracy of the induced velocities calculation. This wake configuration results in a first wake azimuthal angle less than 1 degree as recommended by Traumel [134] and Leishman [127].

Section 4.4.3 discussed the importance of taking into account the induced velocities in the calculation of the wake geometry. In section 4.4.8 this was also confirmed by the work of Hanson [83], who attempted to couple his high-fidelity code with a momentum model in order to capture this effect. Figure 4.13d is another proof that this statement

Table 4.4: Model configuration.

Parameter	Value
Number of blade grid spanwise stations	20
Wake turns	4
Number of wake azimuthal points	100
Blade radial grading parameter	1.2
Wake azimuthal grading parameter	1.6
Number of wake updates	3
Number of nacelle grid axial points	50
Number of nacelle grid azimuthal points	10
Nacelle azimuthal grading parameter	1.6
Circulation convergence tolerance	10^{-10}

holds true. A set-up with zero wake updates results in a wake that assumes a rigid helix form, where the vortex induced velocities are not taken into account. This leads to vortex segments that are closer to the blades, induce higher velocities and result in a lower efficiency. As soon as the wake is updated to account for the induced velocities, the vortex segments start moving further from the blades due to their own induced velocities and the efficiency increases. As shown in Fig. 4.13d two to three wake updates are enough to have an accurate prediction, result identical to what was reported by Young [123]. Regarding the spinner/nacelle grid, Fig. 4.14a shows that at least 50 axial elements are needed, with a grading value of 1.6 that results in a denser grid close to the spinner nose. Due to the axi-symmetric shape of the spinner/nacelle only a quadrant needs to be modelled, with at least 10 azimuthal elements as shown by Fig. 4.14b. The resulting grid for the combination of blade, wake, spinner and nacelle is shown in Fig. 4.15.

A last point needs to be underlined here regarding the model set-up for the simulation of the SR3 prop-fan. The blades used in the experimental tests are not completely rigid and present some elastic deformation in their twist angles; i.e. the blades tend to "detwist". This was reported by many studies in the open literature [80, 82, 83, 105, 111, 112, 149]. Bober et al [149] calculated the deformation for an operating point where the prop-fan rotated at 8440 rpm using a finite element analysis. The produced distribution of detwist along the blade was then used at other speeds, scaled by the square of rotational speed. As it will be shown in the next section, this detwisting effect has an important impact on performance and therefore it has to be taken into account for the comparison with the SR3 data. The results of Bober et al [149] were retrieved from Bober and Chang [111] and fitted by the curve given in Eq. 4.64. This curve is used in the model in order to compare with the experimental data in the next sections.

$$detwist = \left[-2.8964(r/R)^2 + 5.4457(r/R) - 0.959\right] \cdot (RPM/8440)^2 \tag{4.64}$$

4.5.3 Results

The first set of results presented in figure 4.16 verifies the modelling of the detwisting deformations effect. Figure 4.16a and Fig. 4.16b represent low Mach number conditions (M=0.2), while Fig. 4.16c and Fig. 4.16d depict the effect at high Mach conditions (M=0.8). Bober et al [111] reported that for the same conditions as Fig. 4.16c, an increase of C_P between 0.22 and 0.36 was observed for a rigid blade relative to a deformable one. Figure 4.16c shows a difference between 0.197 and 0.235. The effect is in the same order of magnitude but slightly under-predicted. The uncertainties in the actual aerodynamic and deformations modelling approach of Bober and Chang [111] do not allow further comments and the result is found satisfactory. According to Fig. 4.16d the increase in efficiency for the deformed blade is 3.2%, which again is in line with the 4% reported by Bober and Chang [111]. An interesting observation can be made if one studies the same effect for low Mach number this time. As shown by Fig. 4.16a and Fig. 4.16b the deformations impact is much lower for low Mach numbers. This can be explained by observing the change in the slope of the $C_L - angle$ curves for increasing Mach number (Fig. 4.17). The higher the Mach number the higher the slope of the curve and thus a change in angle of attack results in a higher change in performance for high Mach conditions. A detwisting deformation under constant advance ratio J, i.e. constant free stream velocity vector, results in a change in the blade angle and thus in the angle of attack. This change in the angle of attack is then translated to a lower change in C_P for lower Mach numbers and a higher C_P change for high Mach numbers.

The next step consists in verifying the accurate modelling of the flow around the spinner and nacelle. Egolf et al [117] quoted measured values of Mach number in the plane $Z/Lref = 0.09$ for an operating Mach number $Mref = 0.8$. The parameter Z represents the axial distance from the nose of the spinner. Figure 4.18 shows that PAN AIR is matching well the experimental data, especially in the high power outboard region of the blade. The inboard areas are less important because they are less loaded and thus affect less the performance.

The developed code was subsequently used in order to produce data in the form of propeller maps. These maps consist of lines of constant pitch angle, for different advance ratios. Each different advance ratio results in a different power coefficient and propeller efficiency. First the predicting capability for low Mach performance is compared in Fig. 4.19a and Fig. 4.19b against experimental data extracted from Stefko and Jeracki [148]. Both the power coefficient and efficiency compare very well with the test data, with higher

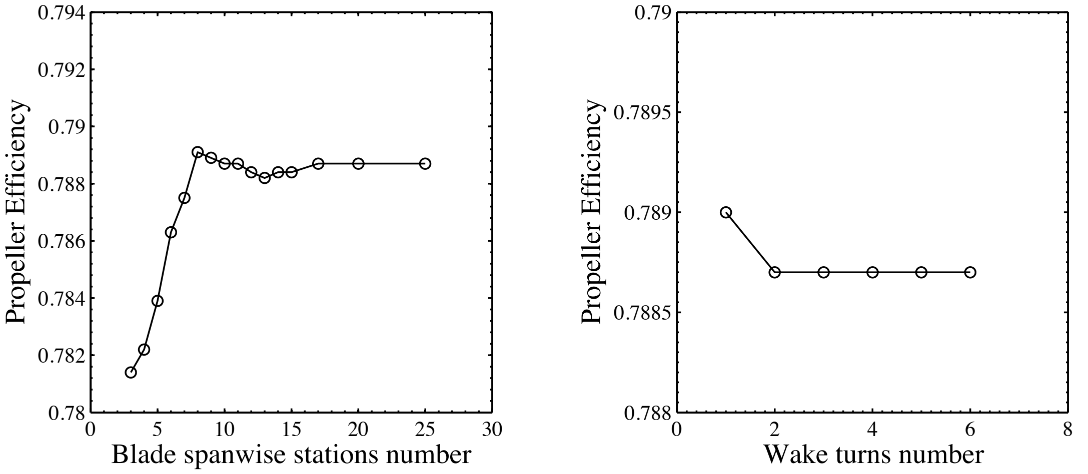

(a) Number of blade spanwise stations

(b) Number of wake turns calculated

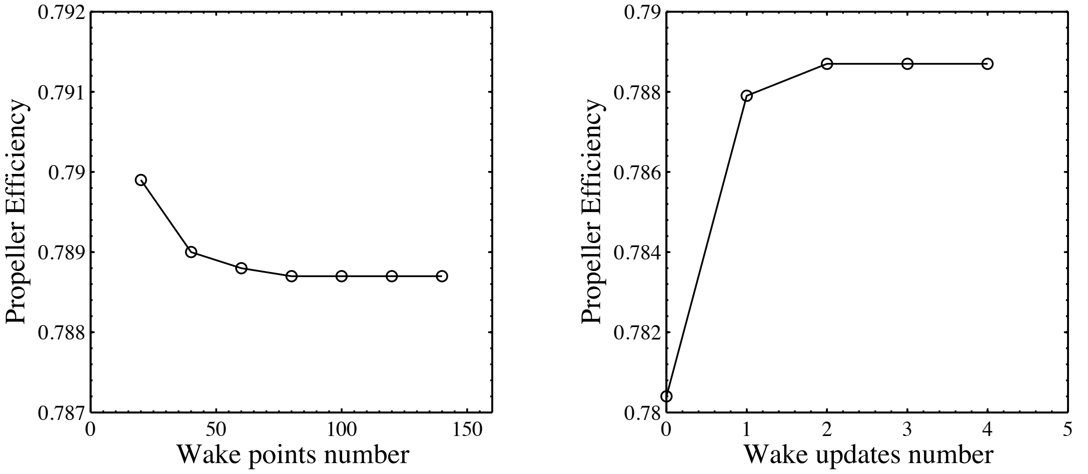

(c) Number of wake points calculated

(d) Number of wake updates

Figure 4.13: Grid independency study for the propeller modelling parameters. Operating conditions: M=0.8, J=3.06, Pitch=58.50°. All parameters are set to the values of table 4.4.

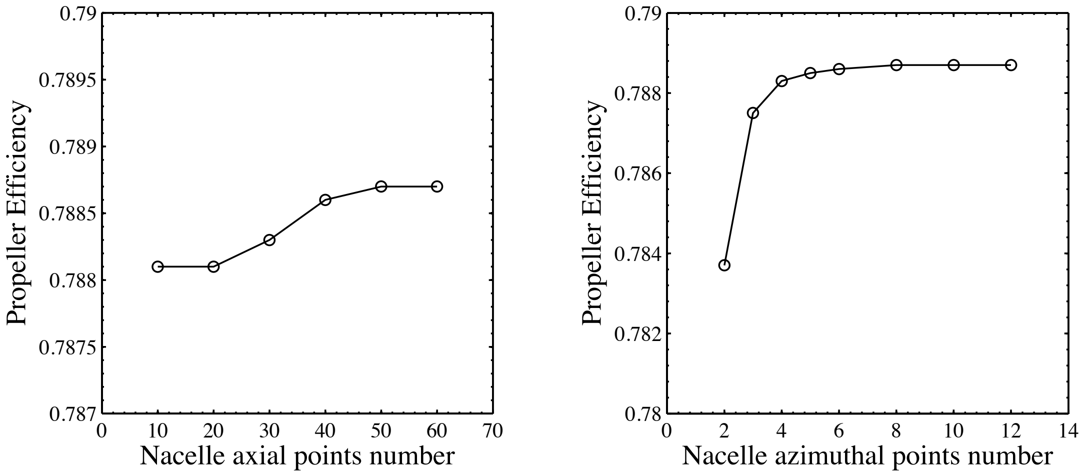

(a) Number of nacelle axial points

(b) Number of nacelle azimuthal points per quadrant

Figure 4.14: Grid independency study for the nacelle/spinner modelling parameters. Operating conditions: M=0.8, J=3.06, Pitch=58.50°. All parameters are set to the values of table 4.4.

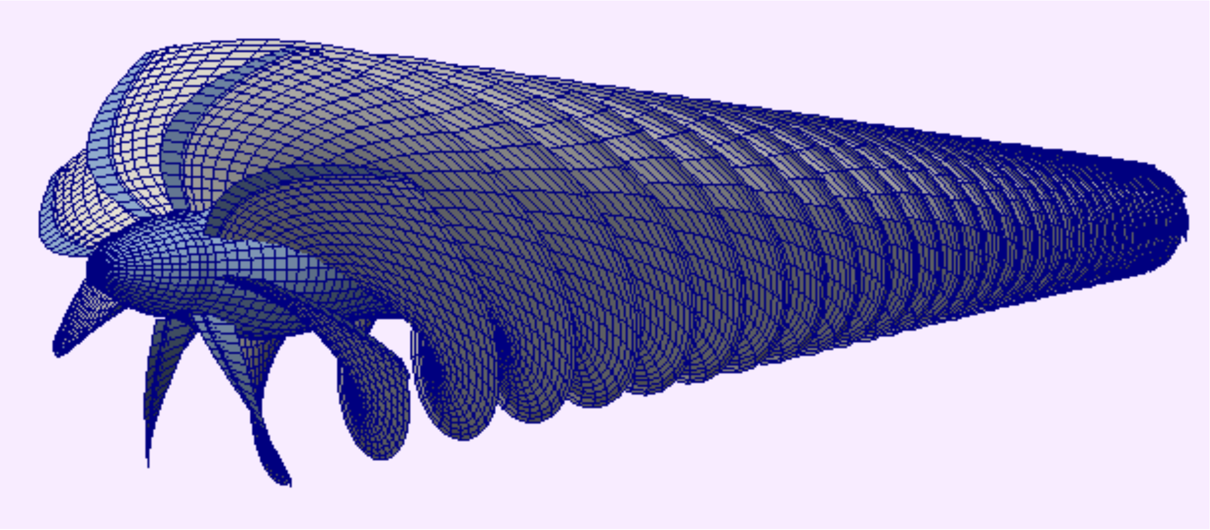

Figure 4.15: The SR3 blade/spinner/nacelle/wake grid as discretised by the developed code according to the settings given in table 4.4.

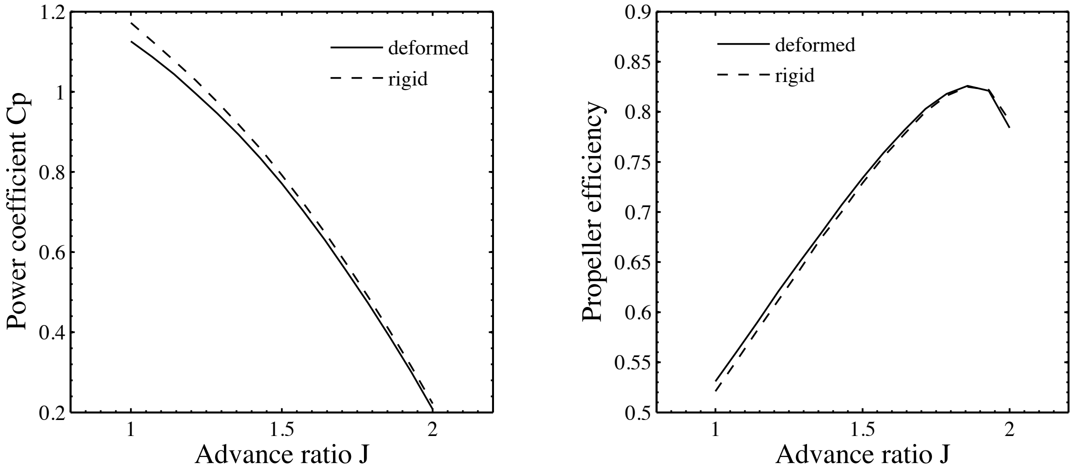

(a) Power coefficient
M=0.2, Pitch=41.9

(b) Efficiency
M=0.2, Pitch=41.9

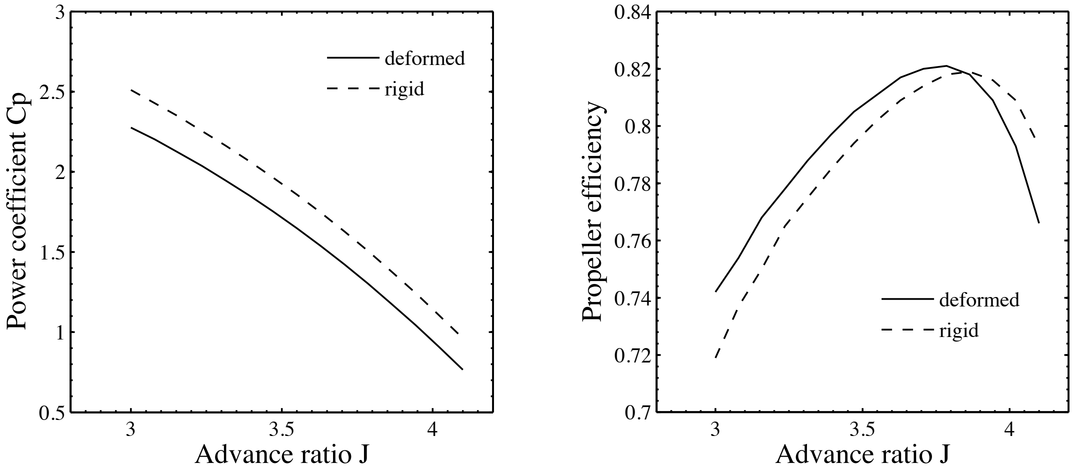

(c) Power coefficient
M=0.8, Pitch=60.4

(d) Efficiency
M=0.8, Pitch=60.4

Figure 4.16: The effect of blade deformations on the power coefficient and efficiency.

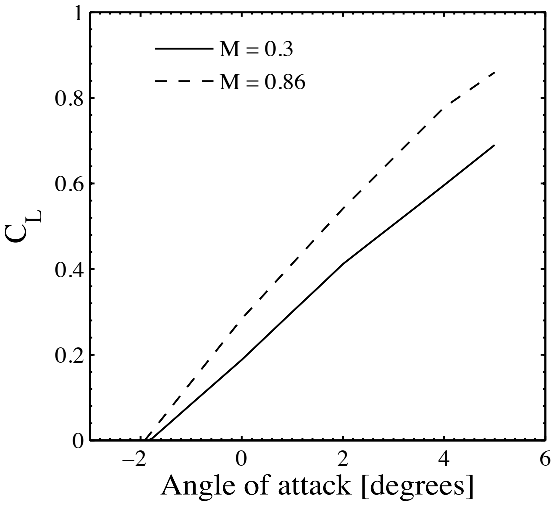

Figure 4.17: The effect of Mach number on the lift coefficient C_L for the NACA-16-204 airfoil.

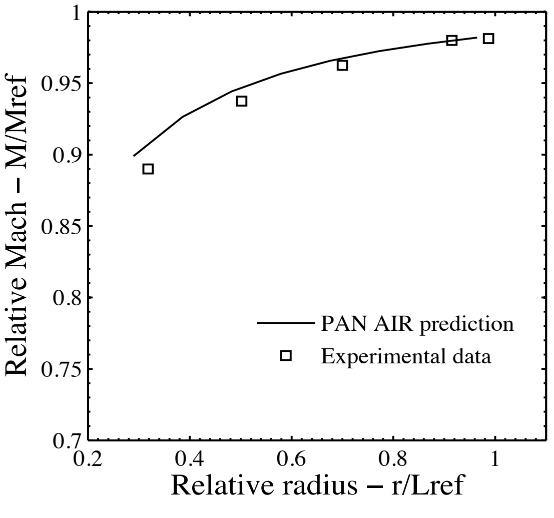

Figure 4.18: Comparison of Mach number profile predicted by PAN AIR with test data extracted from Egolf et al [117]. Measurements taken at plane $Z/Lref = 0.09$ for Mref=0.8. Lref=12.25 inches.

discrepancies occurring in the low advance ratios of the $C_P - J$ lines. In this operating region the angles of attack are the highest and flow separation is very likely. As discussed in 4.4.7 the airfoil data do not predict well the stalled operating regime, which can partly explain the observed discrepancies. As shown by Fig. 4.20a and Fig. 4.20b the code also matches very well the experimental data extracted from Jeracki et al [150] for $M = 0.6$. However, this time the calculated angles had to be reduced by 1.5-2 degrees due to the deformation effects which are higher for higher Mach numbers.

The predicted performance at the high speed condition $M = 0.8$ is compared in Fig. 4.21 against experimental data from Rohrbach et al [105]. The predictions of the compressible lifting-surface code by Hanson [83] are also shown. Both the developed method and the Hanson code predict well the shape of the 59.3° iso-pitch line. The 57.3° is better predicted by the Hanson code, while the 60.5° is matched better by the developed code. Similarly to the case of $M = 0.6$, there is a under-prediction of the pitch angles by around 2 degrees. Hanson [83] reported that according to the experience of Hamilton Standard these two degrees are attributed to the flexibility of the blade retention system. Thus their effect is not included in the detwisting model of Eq. 4.64, which only includes the deformations of the blade. The different predictions between the developed code and the one by Hanson can either be due to different deformation models or due to the differences in the aerodynamic modelling. As mentioned earlier, Hanson's method better captures the linear compressibility effects but lacks accuracy regarding the non-linear impact of the induced velocities. These are better captured by the developed code, which however does not model the effect of compressibility on the calculation of the induced flow. The similar accuracies between the two approaches justifies the earlier selection regarding the modelling of compressibility, as discussed in section 4.4.8. With the respect to the propeller global performance prediction, a simple incompressible lifting-line method is equally good with a higher-fidelity compressible lifting-surface model.

A way to partially eliminate the effect of deformations and focus on the effect of compressibility is to predict the performance at given power coefficient and advance ratio; i.e. leave the pitch angle out of the equation. Figure 4.22 attempts to perform this exercise and compare against the ideal and measured real efficiencies quoted by Jeracki et al [150]. The ideal efficiency is the efficiency of the propeller for zero drag conditions, while the no-induced efficiency is the efficiency with all the induced velocities set to zero; i.e. only the viscous drag losses are taken into account. This is done in order to isolate the different modelling features and check separately their predictive capability. The first conclusion that can be drawn from Fig. 4.22 is that the ideal efficiency is very well predicted. That shows that the wake modelling and the calculation of the induced velocities are quite accurate. It must be underlined here that the value of the ideal efficiency is shown to be constant because the impact of compressibility is not accounted for. In this case, as stated by Mikkelson et al [80], the ideal efficiency is only a function of the power coefficient and advance ratio. This also means that the quoted ideal efficiency value of Jeracki et al [150] also lacks accounting for the compressibility effect. If the attention is now focused on the total real efficiency prediction, it is apparent that the code is in agreement with the test data with a discrepancy of less than 0.5%. That means that the airfoil data for this case were also quite close to the true performance of the blade. It can be seen from the no-induced efficiency that the shape of the real efficiency curve is a replica of the shape of the no-induced efficiency. This was expected as the ideal efficiency is shown as constant. This observation also shows the great importance of the airfoil database; there is no use modelling correctly the ideal flow, without an accurate drag calculation.

Before concluding this validation effort a comment must be made regarding the experimental data used as a reference. First of all, Black et al [104] claim that any efficiency reported in propeller maps is accurate within one percent. Secondly, as highlighted by Stefko et al [112], the accuracy of the experimental rig has a significant effect on the peak efficiency measurements, where the thrust values are quite low. These two arguments attempt to underline that although the experimental data are used as a reference base, there is some uncertainty hidden in them too.

It can be concluded that the performance prediction of the SR3 prop-fan agrees well with the experimental data and shows similar accuracy to the higher fidelity method of Hanson et al [83]. This establishes the confidence around the developed method, which can then be used to perform the map scaling analysis described in the next chapter.

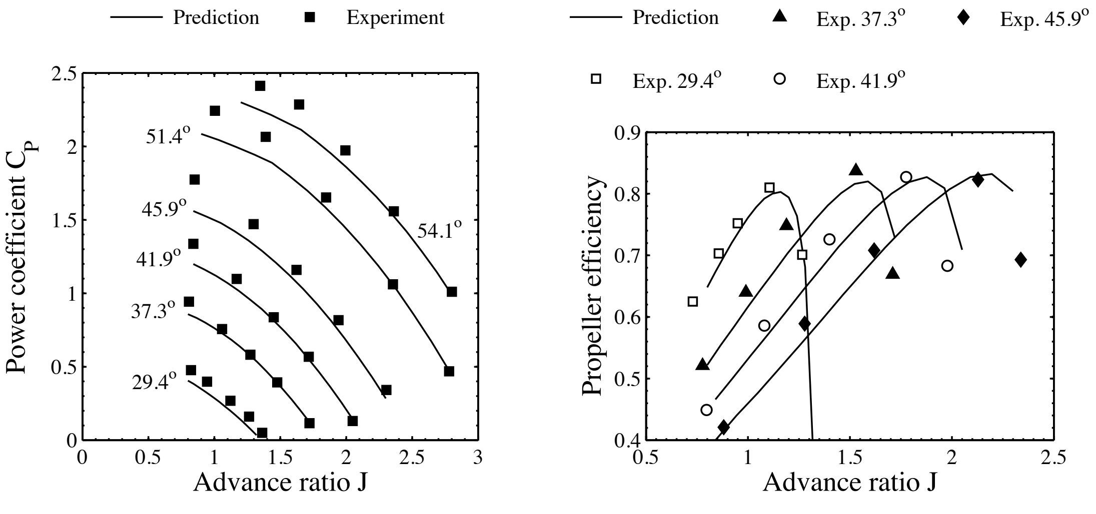

(a) Power coefficient

(b) Efficiency

Figure 4.19: Validation of the power coefficient and efficiency predicted by the lifting-line method against experimental data extracted from Stefko and Jeracki [148] for M=0.2.

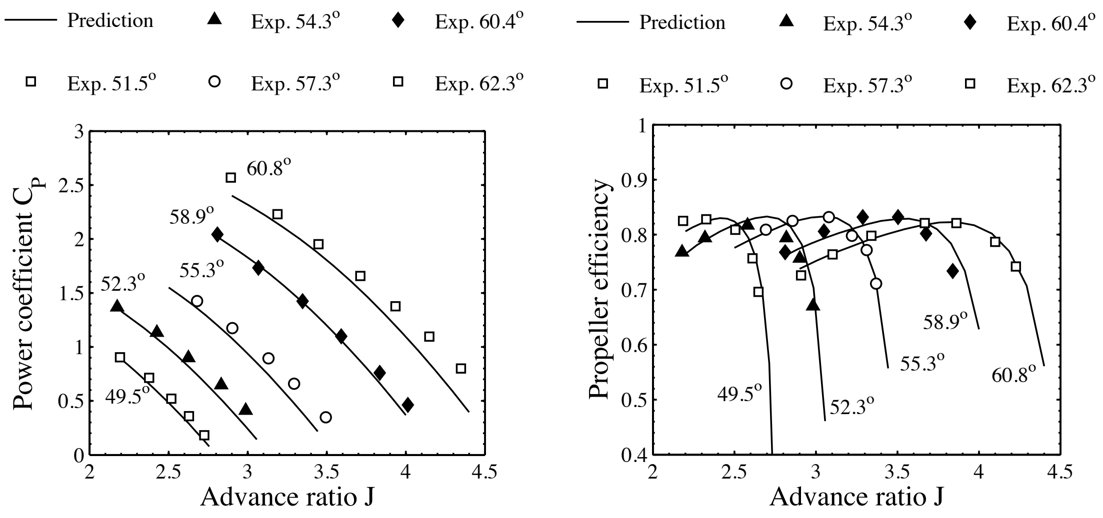

(a) Power coefficient (b) Efficiency

Figure 4.20: Validation of the power coefficient and efficiency predicted by the lifting-line method against experimental data extracted from Jeracki et al [150] for M=0.6.

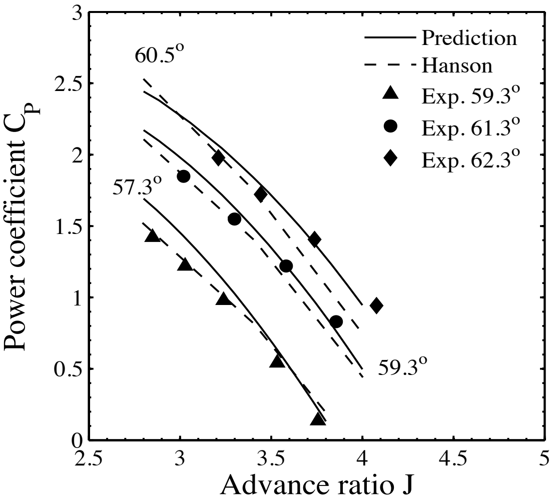

Figure 4.21: Validation of the power coefficient predicted by the lifting-line method against experimental data extracted from Rohrbach et al [105] for M=0.8. The predictions by Hanson et al [83] have also been added as a comparison base.

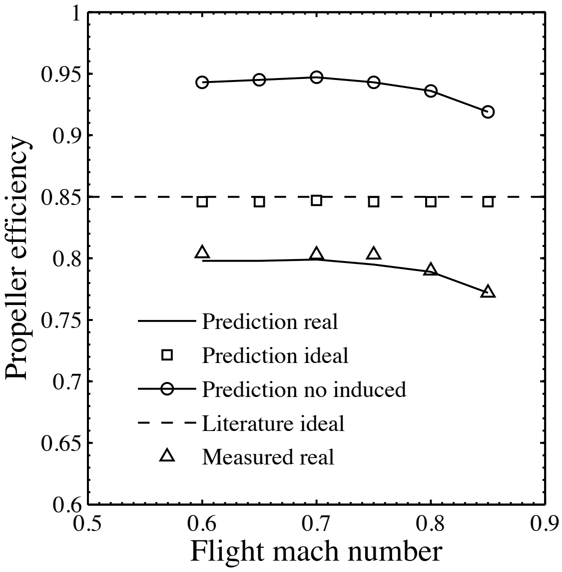

Figure 4.22: Validation against the ideal efficiency and measured real efficiency quoted by Jeracki et al [150]. The no-induced prediction represents the predicted efficiency if the induced velocities are set to zero. The ideal efficiency represents the efficiency with zero drag. C_P=1.7, J=3.06.

4.6 Conclusions

This chapter presents the development of a numerical method aiming to model the aerodynamic performance of high speed propellers. This is an essential task, as the accurate prediction of propeller efficiency is translated into an accurate prediction of open-rotor engine thrust. A description of the fundamentals of propeller performance and a breaking down of the propeller losses allows a better understanding of the characteristics required from a propeller modelling method. An extensive literature survey leads to the selection of the lifting-line method, which was extensively used in the past for the design of propfan geometries. That approach is able to capture satisfactorily the performance of highly swept blades, and take into account the induced and viscous losses.

The description of the method development focuses mainly on the modelling of the wake geometry and the calculation of the induced velocities through the use of the Biot-Savart law. Special attention is given to the modelling of the compressibility effects relative to the calculation of the induced flow-field. The analysis of previous studies pointed towards an incompressible approach, due to its simplicity and to the unsatisfactory results of more complex solutions. Amongst them, the well formulated compressible lifting-surface of Hanson et al [83] is retained as a comparison base.

The numerical method is configured in order to simulate the performance of the well-documented SR3 prop-fan geometry, created by Hamilton Standard in 1970s. The selection of the model configuration parameters is conducted by using an extensive sensitivity analysis. In addition to setting up the model, this analysis sheds light to many interesting modelling aspects. Most notably, the results confirm the selection of the prescribed wake model against the rigid helical one, which would lead in a severe under-prediction of efficiency. Furthermore, the effect of blade deformations is proven to induce a reduction in the power coefficient of about 0.22, especially at high mach numbers. The nacelle modelling using the public domain potential flow code PAN AIR, is found to predict well the flow around the SR3 spinner and nacelle, especially in the high power blade region.

Having verified the code set-up, the modelling of deformations and the accuracy of the nacelle prediction, the code is validated against experimental data. At low Mach number (M=0.2) the predictions show very good agreement with the test data, both for the power coefficient and the efficiency. At M=0.6 the agreement is still very good but the pitch angle is under-predicted by 2 degrees due to the increased effect of the deformations. This effect is attributed to the elastic behaviour of the blade retention system, which was not captured by the implemented modelling. At M=0.8 the agreement is not as good, due to the combined effect of deformations and compressibility. Nevertheless, the prediction is in the same order of accuracy as the higher fidelity compressible lifting-surface method of Hanson et al [83]. This result further reinforces the choice for an incompressible calculation of the induced velocities. In an attempt to reduce the effect of deformations, a last validation exercise is conducted with constant power coefficient and advance ratio. This time the agreement with the experimental data is excellent throughout the whole Mach number range, proving the suitability of the code for the performance predictions required in the context of this work.

Chapter 5

The development of a scalable propeller map representation

5.1 Introduction

The aim of this chapter is to devise a propeller map representation approach able to capture the performance of different propeller designs. This can also be achieved by the method developed in the previous chapter if the geometry of the propeller is known. However, this is not the case during the early stages of engine parametric studies and design space explorations. Normally at this early phase the designer has access to a limited set of maps which correspond to specific propeller geometries. The effect of varying the propeller design is captured by scaling and interpolating between the existing maps, with the design space being limited by the availability of data. For the scaling to be generic, it must be physics based and should only use global propeller design parameters that can be available at the preliminary design phases. The generation of such a generic scaling method is the ultimate objective of this chapter.

The chapter begins with a literature survey that details previous attempts to give a generic propeller representation within the context of an engine design study. The lifting-line method described in the previous chapter is used in order to produce a complete propeller map in the conventional form described in section 4.2. At this point, the focus turns to selecting a convenient way of capturing the effect of Mach number. Subsequently, the propeller model is used within a sequential quadratic programming framework in order to optimise the blade twist and chord distribution for different sets of design parameters. A complete propeller performance map is then generated for each one of the optimised designs. The generated maps are analysed with the sole purpose of identifying a propeller performance representation method that is scalable between different propeller designs.

5.2 Propeller map scaling literature

As described in section 4.2 the traditional representation of propeller performance consists of tables or graphs that give the efficiency or thrust coefficient as a function of advance ratio and power coefficient. The effect of compressibility is then captured either by additional data tables for each Mach number [79], or with a correlation which corrects the efficiency as a function of Mach [81]. This data pack is repeated for different propeller geometries that cover a wide range of ”prime geometry variables” as mentioned in Wainauski et al [79]. These variables can include the tip speed, diameter, horsepower, blade number, integrated lift coefficient and activity factor just to mention the most important ones. It must be noted here that the integrated lift coefficient represents the average section design lift coefficient weighted by the radius cubed, while the activity factor is a measure of the solidity and chord of the blade [79]. Designers can then interpolate in this bulky set of data in order to perform trade-off studies between the different parameters [151].

Borst [99] noted that in order to cover the necessary range, numerous maps of coherent characteristics would be required and therefore suggested a more convenient process. More specifically, he recommended the use of propeller theory in order to minimise the required amount of data. In doing so, he separated the ideal and viscous losses and modelled the blade in a simplified way by assuming that the performance at the 3/4 of the radius represents the performance of the whole blade. This helped him understand the different loss sources and how they change for different designs. For example, the viscous losses are connected to the aerodynamic efficiency of the airfoil section which is equal to C_L/C_D. This in turn depends on the lift coefficient C_L of the section. For given operating conditions, power can be produced either by higher lift coefficients or by higher blade chords. This means that for a given power, the higher the blade chord the lower the required lift coefficient [148]. Borst formulated this relationship as shown in Eq. 5.1, where N_B is the number of blades. He then used a propeller simulation code to produce his results and populate graphs that depict this relation. These graphs were contour plots where the x-axis was the advance ratio J (representing the operating conditions), the y-axis the ”loading factor” $\frac{C_P}{N_B \cdot AF}$ and the contours the ratio C_L/C_D representing the viscous losses.

$$C_L = f\left(\frac{C_P}{N_B \cdot AF}\right) \Rightarrow C_L/C_D = f\left(\frac{C_P}{N_B \cdot AF}\right) \tag{5.1}$$

It must be noted here that C_P is the operating power coefficient and not the design one. The design power coefficient is implicitly taken into account by the activity factor AF; i.e. a propeller of higher power would eventually (but not necessarily) have a higher activity factor. Hence, the selection of the activity factor is left on the user of the method, as according to Borst's approach this is the parameter that distinguishes one propeller from the other. To summarize, by using the aforementioned graph of Eq. 5.1, the designer can estimate the C_L/C_D ratio for a given number of blades, activity factor, advance ratio and power coefficient (the last two representing the operating conditions).

After having estimated the viscous losses through the calculation of C_L/C_D the final efficiency is calculated according to a second graph given by Borst. This graph uses advance ratio, power coefficient and C_L/C_D as the independent variables and the propeller efficiency as the dependent. More precisely, a different graph corresponds to each value of C_L/C_D, and this is repeated also for different blade numbers. By this second graphical correlation, Borst essentially adds the effect of ideal losses which only depend on the advance ratio and power coefficient as discussed in section 4.5.3. Following Borst's approach a designer could model the performance of propellers of different activity factors and different blade numbers.

However, to the best of the author's knowledge the method has never been used in the public domain. Some possible explanations can be given by carefully examining the salient features of the method. First of all, the selection of the activity factor as the main design parameter is not convenient for engine design studies. The main parameters used interchangeably in this kind of studies is the power coefficient or the disk loading P/D^2, supplemented by the advance ratio. These parameters can readily be calculated by the definition of macroscopic variables such as the propeller diameter, rotational speed, flight speed and the power supplied. If one wanted to use Borst's approach, they should be able to relate the changes in the design power coefficient or advance ratio to the changes in activity factor. Secondly, the method uses the aerodynamic efficiency as a parameter in the graphs. This was possible because the graphs were populated by simulation results, where these variables are conveniently available in the output file. However, if one wanted to use the method in conjunction with a measured set of data, he would only have in hand the efficiency, power/thrust coefficient and advance ratio. Thus the method would not be applicable to maps already existing in the public domain in the aforementioned format. Thirdly, the method does not seem to take into account the effect of flight Mach number and the associated compressibility effects. Finally, although the number of required graphs has been greatly reduced, the second set of graphs still requires a set of data equal to: (number of different blade numbers) × (number of different C_L/C_D). Notwithstanding its disadvantages this work was the first attempt to use a physics-based map representation by separating the induced and viscous losses and it was one of the studies that instigated the method presented later in this chapter.

The propeller method by S.B.A.C. [152], albeit being computational and not relevant to map scaling, supplied useful ideas towards the development of a scalable map. This approach consists in simple calculations conducted for the 3/4 radius point of the blade. The method itself is not very accurate, as it is based on approximative solutions of the Goldstein equation and on the performance of a single blade point. Nevertheless, the important element is that once again the method splits the ideal and viscous efficiencies and calculates a total efficiency as their product. This technique, together with the selection of the 3/4 point as representative of the whole blade performance, will be retained as useful elements for the subsequent developments.

As the open-rotor concept has been historically connected to the level of fuel prices, there was no continuous development of the modelling methodology [79]. Nowadays, the simulation capability is being reinvented and references [19–24] are modern studies on the topic. Hendricks [20] implemented the open-rotor capability in the NPSS code simply by adding a given map corresponding to a specific geometry. This method was then used by the studies [19, 21, 24]. Seitz [22, 23] followed a more generic approach by using a Theodorsen design code, to calculate the design point efficiency and with this scale a given map. However, Seitz never proved the suitability of his method and the error it introduces. It seems that the know-how and the ideas developed by Borst and S.B.A.C. were not taken on-board by contemporary researchers. It this gap in the development of propeller map representation methods that this chapter aims to fill.

5.3 SR3 prop-fan map

Before studying the effect of different designs, it is essential to study the variation within a map of a given design. More specifically, the method developed in the previous chapter is used in order to produce complete performances maps for the SR3 propeller. As shown in Fig. 5.1a, the map is in the form of efficiency contours, with the advance ratio and power coefficient being the independent variables and the flight Mach number being constant (M=0.2 in this case). The iso-pitch-angle lines, which are also depicted, are not used for the performance calculations but are useful in explaining the different phenomena taking place.

As one observes from Fig. 5.1a, the efficiency of a constant pitch angle line increases until an optimum is reached and then decreases. This variation can be explained by studying the effect of advance ratio on the ideal and viscous losses. Starting from the ideal losses, lower advance ratio means that the wake helical vortices will be closer to the blades and therefore impact more their performance. Furthermore, a decrease in advance ratio also leads to an increase in the power coefficient, which in turn intensifies the strength of the trailing vortices and increases the ideal losses. Figure 5.1b depicts the variation of ideal efficiency and confirms these arguments. It must be reminded here that the ideal efficiency is the efficiency of the propeller calculated by setting the drag to zero. In summary, the ideal losses increase monotonously as the advance ratio decreases. This means that the effect of non-optimal distribution of loading reported by Mikkelson et al [80] seems to have a negligible impact, or else a region of optimum ideal efficiency would occur.

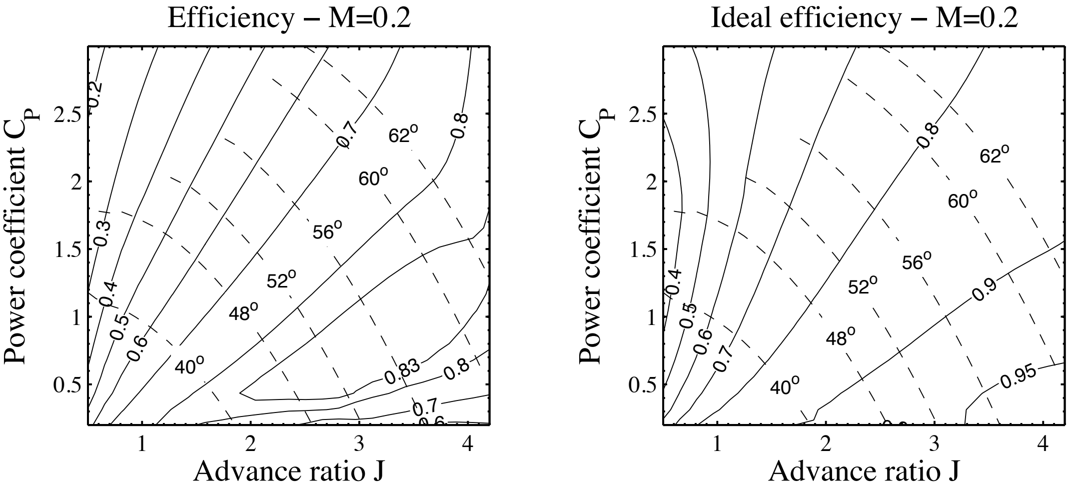

(a) Efficiency

(b) Ideal efficiency

Figure 5.1: A full performance map for the SR3 propeller at low speed conditions M=0.2. The contours represent the real or ideal efficiency, while the iso-pitch-angle lines are depicted in dashed style.

The presence of an optimum efficiency is thus expected to be due to the viscous losses behaviour, explained hereafter. The aforementioned increase in the power coefficient for a decreasing advance ratio, comes about due to an increase in the angle of attack seen by the blade elements. This results from the increased rotational speed Ω and peripheral velocity, which rise for a decreasing advance ratio when the flight speed V_0 is kept constant (as it is fixed by the flight Mach number). The variation of the angle of attack is confirmed by the results shown in Fig. 5.2. The points of the graph falling in the region where the angle is higher than 8 degrees represent operating conditions where the blade stall starts expanding and thus are less accurate. The rising angle of attack results in a variation in the aerodynamic efficiency of the blades (L/D), which reaches an optimum value as the angle increases and then decreases.

In addition to the angle of attack effect there is also the effect of rising compressibility losses due to the higher Mach number seen by the airfoils for decreasing advance ratio. This is explained clearly by examining the Eq. 5.2 that gives the definition of helical Mach number for a given r/R ratio of the blade radius. This variable is a simple vector sum of the axial and rotational Mach numbers and it gives an approximation of the total Mach number seen the blade element at that radius (it is not 100% accurate, as it neglects the effect of induced velocities and blade sweep). It is clear from Eq. 5.2 that a decrease in J leads to a monotonous increase in M_h, which in turn aggravates the compressibility losses and decreases the efficiency.

Thus, it can be concluded that it is the viscous losses variation that leads to the

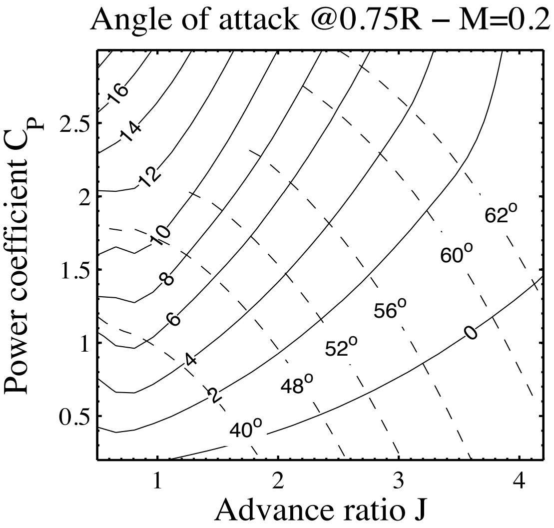

Figure 5.2: The variation of the angle of attack at the 3/4 blade radius for the SR3 propeller at low speed conditions M=0.2. The angles are in degrees, while the iso-pitch-angle lines are depicted in dashed style.

presence of an optimum in the efficiency variation at constant pitch angle.

$$M_h = M \cdot \sqrt{1 + \left(\frac{r}{R}\frac{\pi}{J}\right)^2} \tag{5.2}$$

The same logic applies if one tries to explain the variation of efficiency for constant advance ratio J when the pitch angle varies. This time the wind angle of attack is fixed by the advance ratio and the blade pitch angle is the one varying. On the other hand, the effect of varying the advance ratio at constant C_P is more complicated to explain and the simplified blade element of Fig. 5.3 will be used as an aid. This figure represents the performance of a simplified case, where the blade is straight, there is no drag, no induced velocities and no effect of nacelle. Under these conditions no transformation of coordinate systems is required and the free-stream flight speed and rotational velocity directly define the angle of attack for a given pitch angle B.

Equation 5.3 gives the definition of the power coefficient of the element i, with the power being replaced by the product of torque and rotational speed. Then, the torque is replaced by the appropriate component of the element lift, which is calculated by the definition of the lift coefficient C_L as shown in Eq. 5.4. Then the angle ϕ and the total velocity V_{cn} are calculated by the axial and rotational velocity components as shown in Eq. 5.5. Finally, by introducing the definition of the advance ratio J (Eq. 4.3) and after some algebraic manipulations, Eq. 5.6 is derived.

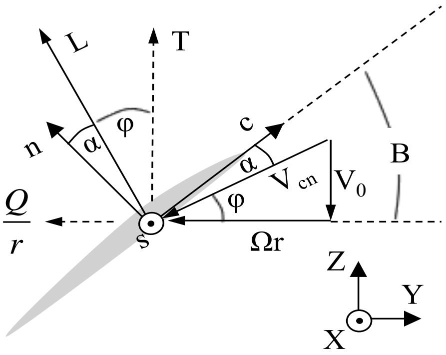

Figure 5.3: Simplified blade element performance. The schematic assumes a straight blade with zero induced velocities, zero drag and no effect of nacelle.

$$C_{P,(i)} = \frac{P_{(i)}}{\rho \cdot n^3 \cdot D^5} = \frac{\Omega \cdot Q_{(i)}}{\rho \cdot n^3 \cdot D^5} \tag{5.3}$$

$$C_{P,(i)} = \frac{\Omega}{\rho \cdot n^3 \cdot D^5} \cdot \frac{1}{2}\rho c_{(i)} C_{L,(i)} \cdot V^2_{cn,(i)} \cdot \sin\phi_{(i)} \cdot r_{(i)} \tag{5.4}$$

$$C_{P,(i)} = \frac{\Omega}{\rho \cdot n^3 \cdot D^5} \cdot \frac{1}{2}\rho c_{(i)} C_{L,(i)} \left[V_0^2 + \left(\Omega r_{(i)}\right)^2\right] \cdot \sin\left[\tan^{-1}\left(\frac{V_0}{\Omega r_{(i)}}\right)\right] \cdot r_{(i)} \tag{5.5}$$

$$C_{P,(i)} = \frac{\pi M c_{(i)} V_0^2}{D^3} \cdot C_{L,(i)} \cdot \sin\left[\tan^{-1}\left(\frac{J}{\frac{r_{(i)}}{R}\pi}\right)\right] \cdot \left[1 + \left(\frac{r_{(i)}}{R}\frac{\pi}{J}\right)^2\right] \cdot r_{(i)} \tag{5.6}$$

The first term of Eq. 5.6 is constant, the second is the lift coefficient C_L and the terms three and four depend on the advance ratio. More specifically, term three increases with increasing advance ratio, while term four decreases. Amongst them, term three is more powerful and dominates. Thus the ensemble of terms three and four increases with advance ratio. This means that for a constant power coefficient, when the advance ratio increases, the increase of the advance ratio term will need to be compensated by a corresponding decrease of the lift coefficient. This is confirmed by Fig. 5.2 which shows that for constant power coefficient, the angle of attack falls when the advance ratio increases. At the same time the pitch angle increases in order to follow the blade element ϕ angle increase. More precisely, the increase of advance ratio leads to a decrease in the Ωr velocity component and a corresponding increase in the angle ϕ, as shown in Fig. 5.3. For a constant angle of attack this would lead to a parallel increase of the pitch angle; i.e.

the increasing ϕ would "push" the pitch angle B towards the axial direction. In this case the angle of attack decreases, a fact which slightly abates the increasing pitch effect.

Finally, Fig. 5.4 shows an alternative representation of performance using the thrust coefficient C_T in the place of efficiency. As seen in the figure, the variation of C_T is more "linear" and therefore more adapted for computerisation and interpolation. However, within the context of this chapter the efficiency map is preferred as it facilitates the explanation of the different phenomena.

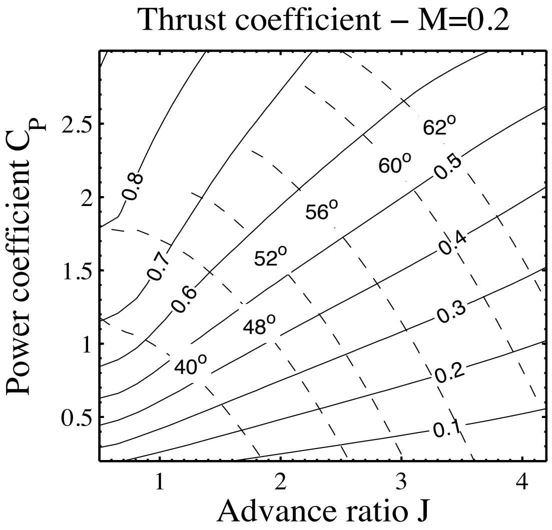

Figure 5.4: An alternative C_T performance map for the SR3 propeller at low speed conditions M=0.2. The contours represent the thrust coefficient, while the iso-pitch-angle lines are depicted in dashed style.

5.3.1 The Mach number effect

Having established the performance representation for a single flight Mach number, the next step is to investigate the effect of different flight speeds. This has been traditionally taken into account either by multiple maps, one for each Mach, or by using a correlation that corrects the efficiency in function with the Mach number. The first solution offers potentially higher accuracy at the cost of larger data tables, while the second offers the opposite. However, the difference in accuracy between the two methods has never been tested before.

Figures 5.5a and 5.5b show the efficiency map of the SR3 propeller for Mach numbers equal to 0.6 and 0.8 respectively. The comparison between these maps and the one shown earlier in Fig. 5.1a illustrates that the efficiency contours are compressed towards the high advance ratio region. This means that the efficiency in the lower advance ratio region gets lower as the Mach increases. Recalling the concept of helical Mach number introduced by Eq. 5.2, it becomes apparent that this behaviour occurs due to the higher helical Machs experienced at low advance ratios. These higher helical Mach numbers induce stronger compressibility losses and diminish the efficiency of the blade at low advance ratios.

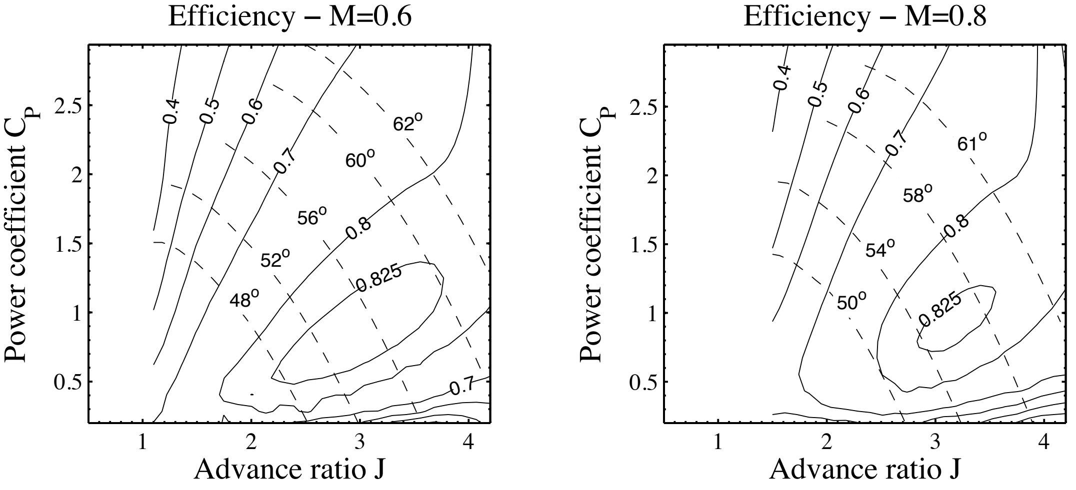

(a) M=0.6

(b) M=0.8

Figure 5.5: A full performance map for the SR3 propeller at high speed conditions M=0.6-0.8. The contours represent the efficiency, while the iso-pitch-angle lines are depicted in dashed style.

In order to clarify this differentiation between the low and high advance ratios, Fig. 5.6a shows the variation of efficiency with the flight Mach number for three different values of advance ratio. It is evident that the lower the advance ratio the faster the compressibility losses kick in. A side product of this figure is the observation that the shape of the curves is similar; i.e. a flat part is followed by a region of decreasing efficiency. The only difference observed is the absolute level of efficiency (depending on advance ratio as explained earlier), and the point where the efficiency starts to deteriorate. This offset due to the advance ratio is also explained if one observes the helical Mach numbers plotted in Fig. 5.7 for the three cases. It is shown that the lower the advance ratio the higher the helical Mach for the same flight Mach. This confirms the explanation given earlier regarding the higher compressibility losses for lower advance ratios.

Figure 5.6b turns the attention to the compressibility losses of points on the map that have the same advance ratio but different power coefficient. This time the only difference between the curves is the absolute level of efficiency stemming from the different power coefficients. To summarize the observations made from these three last figures, the following statement can be made. It seems that if the efficiency is non-dimensionalised by its maximum value and the flight Mach number is replaced by the helical Mach (automatically taking into account the different advance ratios), the different curves should collapse into one. This statement is confirmed by Fig. 5.8 where the concept is applied for all the different operating points depicted.

These results demonstrate that a single curve can be used for the entirety of the propeller map. In summary, the performance of a given propeller can be described by a low speed map similar to the one shown in Fig. 5.1a and a curve like the one shown in Fig. 5.8. This achieves similar accuracy to having multiple maps without the higher cost of larger data tables. However, this ensemble of data is expected to change for different propeller designs. Surely the performance will be different if the blading is different; i.e. if the airfoils used are different or if a different sweep angle distribution is used. Nonetheless, it remains to be confirmed whether this representation is able to be scaled between propellers that use the same blading but different design power coefficient and advance ratio. More precisely, the next sections will investigate how the map changes if the airfoil distribution and the sweep angle are constant, but the twist angle, design pitch angle and chord distribution are allowed to be optimised for different design C_P and J.

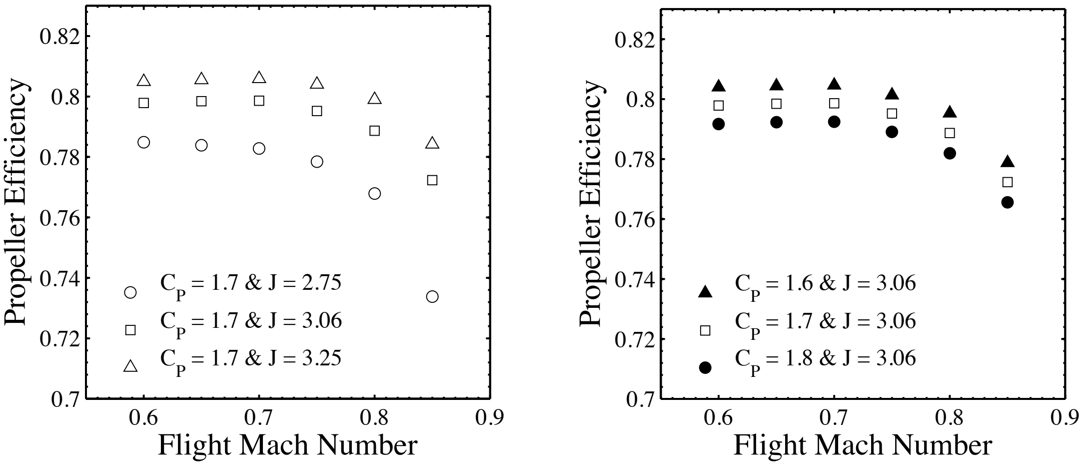

(a) Varying advance ratio

(b) Varying power coefficient

Figure 5.6: The effect of flight Mach number on propeller efficiency for different operating power advance ratios and power coefficients.

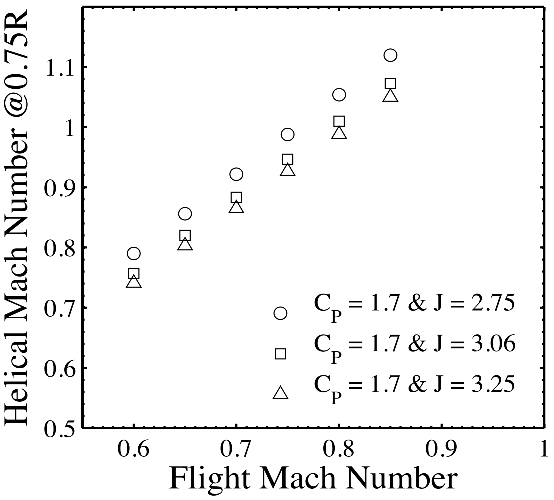

Figure 5.7: The variation of helical mach number at the 3/4 of the blade radius for different flight mach numbers and advance ratios.

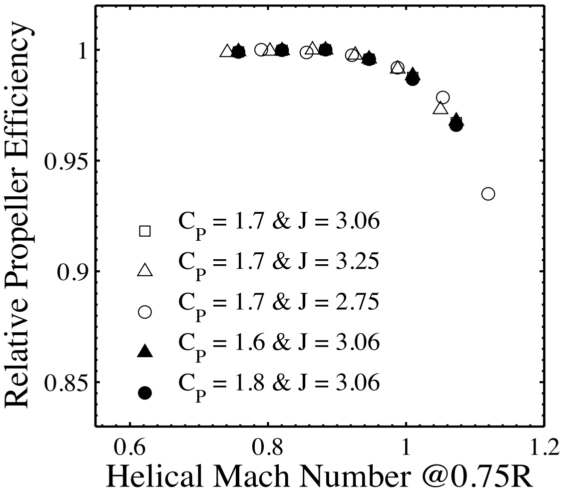

Figure 5.8: The variation of relative efficiency with helical mach number at 0.75R for different operating advance ratios and power coefficients. The relative efficiency is defined as the efficiency divided by the maximum efficiency for a given advance ratio and power coefficient.

5.4 Design and optimisation

5.4.1 The propeller design problem

Before starting the propeller design exercise, the design problem must first be briefly described. That is the problem of selecting all the parameters that define the geometry of the propeller, as described by numerous studies conducted by Hamilton Standard and NASA [82, 104, 112, 148, 150]. To begin with, the number of blades is normally selected as high as possible in order to minimise the ideal losses. However, after a certain number the blades encounter an efficiency loss due to choking at the propeller hub [112]. Furthermore, a higher number of blades is also translated in a higher propeller weight and cost. The thickness to chord ratio of the airfoils is normally selected as the lowest allowed by the stress limits, aeroelastic response considerations and fabrication state-of-the-art [82]. According to Stefko and Jeracki [148] the design lift coefficient of the airfoils is selected in a way that maximises the aerodynamic efficiency for a given power and minimises the drag. Finally, the selection of the sweep angle distribution aims to achieve subcritical Mach numbers along the blade and reduce the compressibility losses [104]. However, during the design of the SR3 prop-fan the sweep was varied in a way that reduces the emitted noise [101].

All the aforementioned design parameters belong to the sphere of propeller design and fall outside the context of this work. In the context of whole engine design, this work focuses only on the variation of macroscopic design parameters. These macroscopic parameters are the design power coefficient and design advance ratio, which are directly related to the power, shaft speed, diameter restriction and flight speed of the engine. For each set of macroscopic design parameters the propeller performance is optimised by selecting the values of the propeller twist angle and chord distribution. The twist distribution is mainly connected to the ideal performance, whilst the chord distribution affects the viscous drag losses [106]. The blade characteristics described in the previous paragraph are considered constant and related to the specific propeller design.

In summary, within the context of this chapter a propeller of given blading is taken and its design power coefficient and advance ratio are varied. The twist and chord distributions are redesigned in order to minimise the ideal and viscous losses for the new propeller. The new propeller geometry is used in order to generate a complete performance map and study how this has changed relative to the baseline design.

5.4.2 Method selection

There are two main approaches to conduct the propeller design exercise. The first is the fastest but more old fashioned, as it is based on the theories of Goldstein and Theodorsen. This approach has been used in the studies by Davidson [109], McKay [108] and Adkins et al. [106]. The method is based on the optimality condition first stated by Betz [92] and subsequently used by Goldstein [97], which says that an ideal propeller generates a wake of rigid helical shape. As described by Wald [84], this rigid wake requires a constant wake displacement velocity, which is the only unknown variable in the optimisation problem (at least at its simplest version). The wake displacement velocity is the velocity with which the rigid helix travels backwards. This variable, coupled with a specified lift coefficient distribution, is iterated in order to match a specified design power coefficient. After the power coefficient is matched, the method gives automatically the twist and chord distribution. The distribution of lift coefficient should be chosen in a way that optimises the L/D at each airfoil station. The method gives a clear vision of the physics involved and more specifically, it shows the independence between the optimisation of the ideal losses and the viscous losses. This fact was also described by Adkins et al. [106] and by Borst [99], who reported that the ideal losses are minimised through the selection of twist, while the viscous losses via the selection of the chord or L/D of each section.

Although this method is extremely fast (it takes less than a few seconds), it inherits all the shortcomings of the Goldstein approach. The greatest among them, it cannot handle correctly swept blades. Mikkelson et al. [80] mentioned this problem for the swept SR1 propeller, which was designed using a Goldstein approach. According to them, the designed twist resulted in a non-optimal loading distribution and the blade needed to be retwisted. They finally had to turn to a lifting-line method, similar to the one developed in the previous chapter. The transition to lifting-line methods comes at the cost of higher computational requirements. The method is not able to "reverse engineer" the optimum distribution of twist and chord by imposing a rigid wake and an optimisation method is required.

Chang and Sullivan [153] chose a gradient based penalty method to translate the constrained optimisation problem to a sequence of corresponding unconstrained ones. This optimisation method adds a penalty term to the objective function that corresponds to the violation of the constraint specified. At each different step of the solution the weight of the penalty term is increased and in the end the unconstrained problem converges towards the constrained. Chang and Sullivan used this method to optimise the twist of a swept blade for a given pitch angle, under the constraint of a specified power coefficient. The authors also proved that their approach is consistent with the traditional Goldstein method when the propeller blades are straight.

Cho and Lee [154] used a gradient based optimisation technique similar to the one of Chang and Sullivan [153], which was once more coupled with a lifting-line code. In addition to optimising the twist they also calculated the optimal distribution of chord. Interestingly, they did the optimisation in two steps: first they optimised the twist and then the chord. Although the authors did not comment on this choice, it can be assumed that it is due to the independence of the two figures of merit; i.e. the ideal and viscous losses. Another interesting finding of their work concerns the selection of the number of blade elements. They reported that around 10 elements are enough for the result to converge to an optimum, while more elements would increase the numerical difficulty of the problem and they could also result in a "wiggly" variation of twist and chord.

Gur and Rosen [93] proposed a combination of three optimisation methods in order to achieve a high optimisation robustness and also produce a smooth variation of twist and chord. In the first stage a genetic algorithm was used in order to bring the solution closer to the global optimum. The authors argued that this algorithm could not handle well multiple constraints and also produced non-smooth results. Thus, they decided to add a linear simplex method at the second stage. This time, the smoothness of the design variation was achieved by constraining the second derivative of twist and chord at each blade element. The smoother result of the simplex method was finally input to a gradient based method which climbed the rest of the hill to reach the optimum value. As with the two previous cases, Gur and Rosen also used penalty functions, but contrary to the others based their predictions to a simpler blade-element/momentum propeller model. However, it has to be noted that they limited their study to low speed straight blades. The use of three consecutive optimisation techniques was justified due to the high number of variables used in this study, which optimised in parallel the aerodynamics, acoustics and structural integrity. Within this chapter, the optimisation problem is limited to the aerodynamic design of twist and chord and thus such a hybrid scheme would lead to unnecessary excessive evaluations.

The design method chosen for this work follows the approach of references [153] and [154], by coupling the developed lifting-line method with a gradient based optimiser. More specifically the author chose the Sequential Quadratic Programming method available in the non-linear optimisation toolkit of the Matlab platform. This approach was preferred to the classic Goldstein one, firstly because it can take advantage of the higher fidelity lifting-line method and secondly because in future developments it could also incorporate disciplines other than aerodynamics, as done by Gur and Rosen [93].

5.4.3 Optimisation problem formulation

According to what was discussed in sections 5.4.1 and 5.4.2, the optimisation problem can be stated as follows. For a given blade geometry, optimise the pitch angle and the twist/chord distributions in order to achieve optimum propeller efficiency for a given flight Mach number, advance ratio and power coefficient. As discussed in section 5.4.1 the rest of the blade characteristics falls in the domain of hardcore propeller design and are not relevant to the global performance investigations of this work.

The given blade geometry includes:

- the number of blades

- the blade hub to tip ratio
- the sweep angle distribution
- the selection of airfoils

The non-linear optimisation problem is thus formulated as:

Maximise the objective function

$$\eta_{prop}(B, \vec{\Delta\beta}, \vec{c}) \tag{5.7}$$

Subject to the constraints

$$C_P(B, \vec{\Delta\beta}, \vec{c}) - C_{P,des} = 0$$

$$0 \leq B \leq 90^\circ$$

$$-45 \leq \Delta\beta_i \leq +45, \quad i = 1..(N+1)$$

$$0 \leq c_i \leq R, \quad i = 1..(N+1)$$

$$\left| \frac{d^2(\Delta\beta_i)}{dr^2} \right| \leq C_1, \quad i = 1..(N-1)$$

$$\left| \frac{d^2(c_i)}{dr^2} \right| \leq C_2, \quad i = 1..(N-1)$$

Where B is the blade pitch angle, $\vec{\Delta\beta} = [\Delta\beta_1, \Delta\beta_2, ...\Delta\beta_{N+1}]^T$ the design vector of twist, $\vec{c} = [c_1, c_2, ...c_{N+1}]^T$ the design vector of chord, r the local blade radius, R the blade tip radius and N is the number of blade elements (it is reminded that N blade elements are bounded by $N+1$ blade geometry points). The advance ratio J is an input of the lifting-line method, while the power coefficient C_P is an output and hence it has to be added as an equality constraint. The constraints in the second derivatives ensure a smooth variation of the twist and chord of the blade, as done by Gur and Rosen [93]. Experience with the model showed that the values of $C_1 = 100$ and $C_2 = 3$ give satisfactory results.

In order to isolate the different effects and especially the ideal and viscous losses, the optimisation exercise will be carried out in two phases. In the first phase only the twist and pitch will be optimised, which are expected to have an impact only in the ideal performance. This phase corresponds to the work carried out by Chang and Sullivan [153], who only optimised the ideal efficiency. The second phase also adds the chord distribution in the set of variables and solves the entirety of the design problem. This stepped approach is expected to give a better visibility and insight into the phenomena taking place. The results of the two steps are given in the next sections.

5.4.4 Optimisation results

The baseline geometry is that of the SR3 prop-fan as described in section 4.5.1. Following the recommendation of Cho and Lee [154] the twist and chord are optimised for 10 blade points (which define 9 blade elements). The effect of the nacelle is deactivated in order to speed up the optimisation process, with no important effect on the final conclusions of the study. Following a common practice of propeller design, the twist at the 0.75 blade radius is set equal to zero. In order to do that, the pitch angle is ”freed” to accommodate any variation of power, instead of varying uniformly the twist of all the blade stations. Had the blade been straight, this would not be required as the pitch would simply be set equal to the final optimal twist angle at the 0.75 blade radius. This angle would then be set as the design pitch and subsequently be subtracted from all the blade station twists, setting the angle at $0.75R$ automatically to zero.

5.4.4.1 Step 1: optimise twist and pitch with constant chord

As mentioned earlier during the first step of the study the chord distribution is kept the same to the baseline blade. The five cases optimised are shown in the table 5.1. The design Mach number for all the cases is equal to 0.8. The power coefficient C_P and the advance ratio J represent the chosen design conditions for each case, while the pitch is the result of the optimisation process. The first observation is that the pitch increases for increasing C_P or increasing J. These trends will be more easily explained by first examining the variation of optimal twist in Fig. 5.9 for different design advance ratios. It is seen that there is no significant variation of the twist distribution, especially at the more important outboard blade region. The same trend is identified for different design power coefficients, although not shown here. This essentially means that the blade geometry is the same for the different design conditions, the chord distribution also being constant. The geometry being constant, the propeller just has to change its operating point on the map. Therefore, for this case the explanations for the variations in performance have already been given in section 5.3. An increase in C_P under constant J leads to an increase in the pitch angle and a parallel increase in the lift coefficient as shown by Fig. 5.10a. This means that the increase in the power has to be achieved by an increase in the lift coefficient as the chord of the blade cannot change. On the other hand, an increase in the design advance ratio leads to a decrease of the lift coefficient as proven by Eq. 5.6 and shown in Fig. 5.10b. As explained in section 5.3, the increase in advance ratio aligns the velocity component closer to the axial direction, while the increase in the lift coefficient slightly lessens the effect. The effect of aligning the blade towards the axial direction dominates and the pitch increases for increasing advance ratio. To conclude, as the chord remains constant, any variation of the design conditions has to be accommodated by a corresponding change of the lift coefficient and pitch angle.

The variations of efficiency as shown in Fig. 5.11a and Fig. 5.11b have also been explained in section 5.3. The ideal efficiency decreases for increasing power coefficient and decreasing advance ratio and is minimized by the optimisation of the twist distribution. At the same time the total efficiency is also affected by the viscous losses, which are driven by the variation of C_L for the different design conditions. This means that contrary to the ideal losses, the viscous losses are not optimised by a variation of the chord distribution but have to follow the variations of C_L.

Table 5.1: The optimum pitch angle for each optimisation case at constant chord. Design Mach number equal to 0.8.

C_P	J	Pitch [degrees]
1.13	3.06	55.36
1.70	3.06	57.22
2.55	3.06	61.04
1.70	2.75	55.57
1.70	3.25	58.26

5.4.4.2 Step 2: optimise twist, pitch and chord

If now the chord distribution is also added in the set of the optimisation variables, the final results behave quite differently. Once more the design Mach number used is equal to 0.8. The four cases studied are defined in table 5.2, together with the resulting pitch angles and activity factors. It is reminded that the activity factor is an indicator of the blade solidity and, as described in section 5.2, it has been used by Borst[99] as the parameter distinguishing different blade designs. Table 5.2 shows that the trends in the variation of pitch are the same as for the constant chord case. However, relative to the previous variations, this time the variation is lower when the design C_P changes and higher when the design J changes. At the same time, the results show that the activity factor AF increases for increasing design C_P and decreasing J. The aforementioned trends can be explained by studying the variations in the blade geometry and lift coefficient as shown by Fig. 5.12-5.13.

First of all, no clear trend is visible for the variation of the twist distribution (Fig.

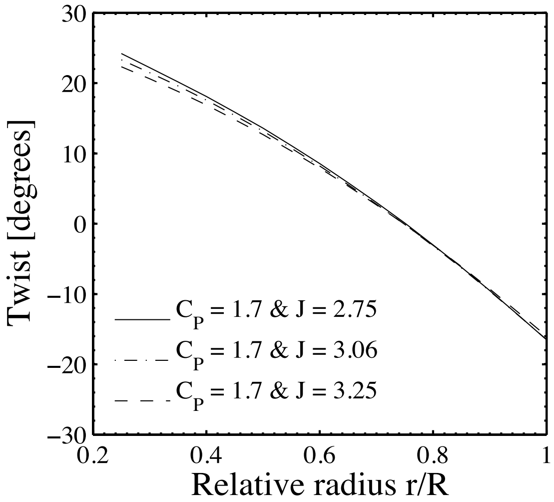

Figure 5.9: The optimum distribution of twist for different design advance ratios J. The blade chord distribution is held constant. Design Mach number equal to 0.8.

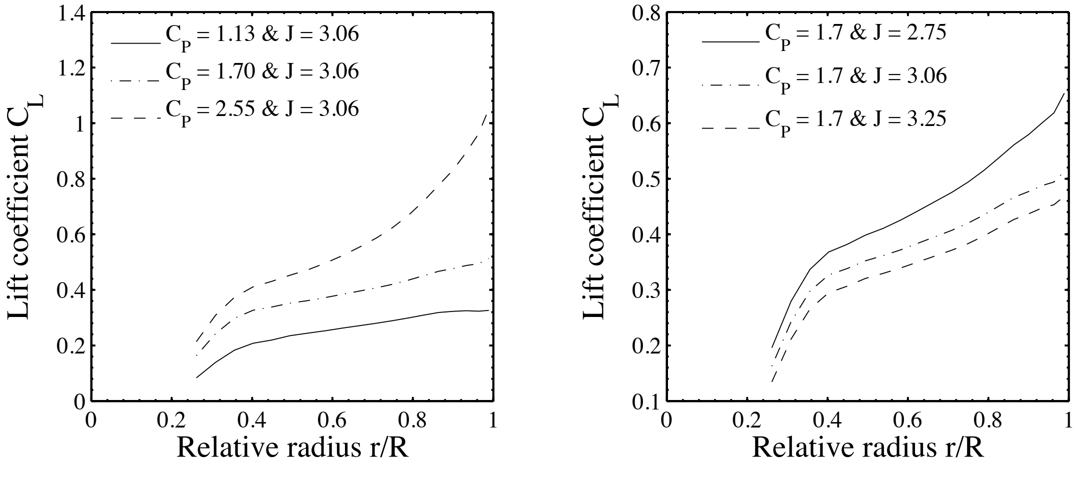

(a) Varying design power coefficients C_P

(b) Varying design advance ratio J

Figure 5.10: The change in the lift coefficient distribution for different design power coefficients C_P and advance ratios J. The blade chord distribution is held constant. Design Mach number equal to 0.8.

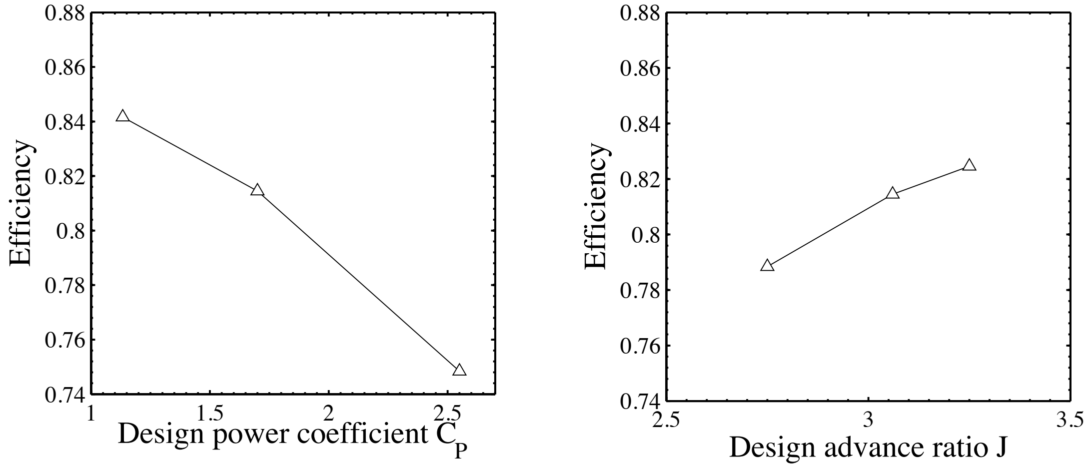

(a) Varying design power coefficients C_P (b) Varying design advance ratios J

Figure 5.11: The change in the propeller efficiency for different design power coefficients C_P and advance ratios J. The blade chord distribution is held constant. Design Mach number equal to 0.8.

5.12a, which again remains approximately unchanged at the outboard high loading region. On the other hand, significant variations occur for the chord distribution as shown by Fig. 5.12b. Recalling the results shown in Fig. 5.10a and Fig. 5.10b, it is evident that the variations of chord come to replace the corresponding variations of the lift coefficient; i.e. where for the constant chord case there was an increase in C_L, now there is a corresponding increase in the chord. This way, the optimiser is able to keep the lift distribution at an optimal L/D value for all the design cases, minimising thereby the viscous losses. This can be observed in Fig. 5.13, where it is apparent that the optimiser tries to keep the same C_L distribution. At the hub this is not possible, due to a constraint set for the minimum chord allowable. As mentioned by Adkins [106], at the hub and tip the circulation is zero and thus the only way to keep a finite value of C_L is to have a zero chord. This is what the optimiser tries for both ends of the blade, although not so visible for the tip. The reason for this is that at the tip contrary to the hub, the loading is higher and therefore higher chords are required for the elements adjacent to the tip. This phenomenon coupled with the use of a second derivative constraint which stiffens the variations of the chord, leads to the non-zero values of chord at the tip.

The variations of the chord and C_L distribution can now be used to explain the changes in the pitch angle and the activity factor. First of all, higher chords lead directly to higher activity factors and higher solidity. Secondly, changes in the power coefficient are now accommodated by higher chords with the C_L changing much less. This is why the pitch angle also changes less. In an ideal optimal case where no constraints limited the optimiser and the C_L was exactly constant, the pitch would be expected to also remain constant. Regarding the variation of design advance ratio, the changes are more pronounced relative to the constant chord case, as seen from tables 5.1 and 5.2. It was explained in the previous section that there are two effects that contribute to the change of the pitch angle. The one is the aligning of the blade towards the axial direction as the advance ratio increases and the other is the parallel decrease in the angle of attack, which has an opposing but lesser impact. Figure 5.13 proved that the lift coefficient and thus the angle of attack are kept approximately constant for the optimal chord case. Therefore, the second abating factor affecting the pitch angle, is eliminated and the variation of pitch becomes more pronounced.

Figures 5.14a and 5.14b show the variation of efficiency for different design C_P and J, in relation to the constant chord results showed in the previous section. It can be seen that the trends are the same as before, but this time the efficiencies are higher. This is normal, as this time the optimiser also minimises the viscous losses. Finally, it can be seen from Fig. 5.14a that the initial chord distribution was closer to the optimal for the $C_P = 1.7, J = 3.06$ case, and that is why the distance between the constant chord and the optimal chord efficiencies is the lowest.

Table 5.2: The optimum pitch angle for each optimisation case when the chord distribution is also optimised. Design Mach number equal to 0.8.

C_P	J	Pitch [degrees]	AF
1.13	3.06	56.24	178
1.70	3.06	57.00	271
2.55	3.06	59.16	439
1.70	2.75	54.66	326

5.5 Results analysis to devise a map scaling technique

Having optimised the blade for the different design cases, the next step consists in generating a propeller map for each one of them. The produced maps will then be analysed in order to identify how they change according to the design. To be consistent with the maps produced earlier for the baseline SR3 prop-fan, the effect of the nacelle will be reactivated. The maps will be produced for the low speed Mach number of 0.2 and the effect of Mach will be studied in a separate section. It must be noted here that in order to facilitate the

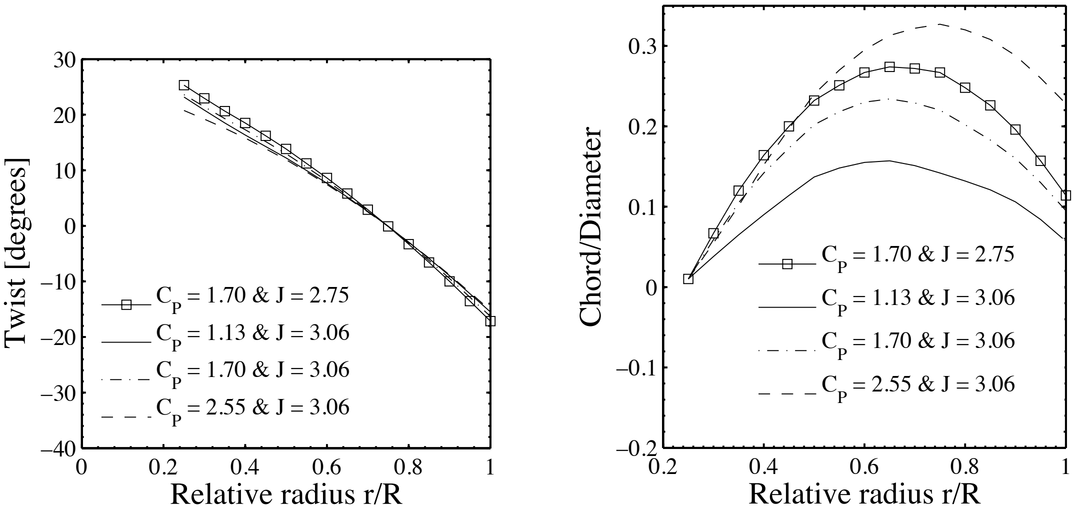

(a) Twist

(b) Chord

Figure 5.12: The optimum distribution of twist and chord for different design C_P and J. The blade chord distribution is optimised. Design Mach number equal to 0.8.

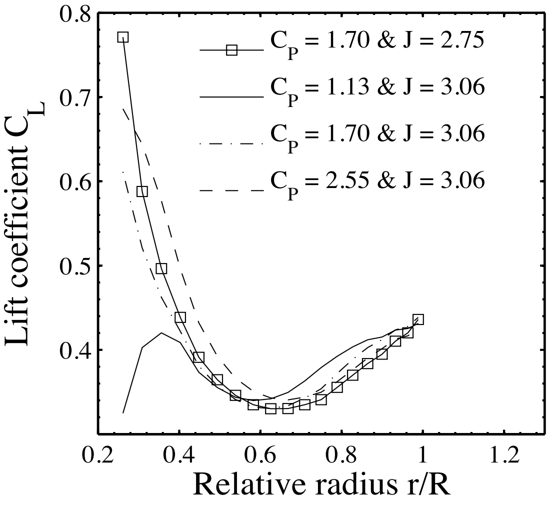

Figure 5.13: The change in the lift coefficient distribution for different design C_P and J. The blade chord distribution is optimised. Design Mach number equal to 0.8.

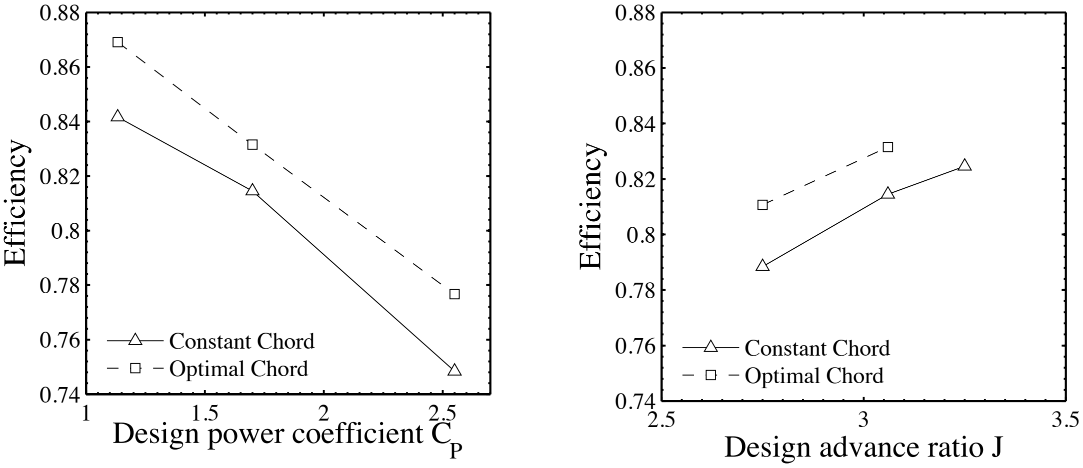

(a) Varying design power coefficients C_P (b) Varying design advance ratios J

Figure 5.14: The change in the propeller efficiency for different design power coefficients C_P and advance ratios J. The blade chord distribution is optimised. Design Mach number equal to 0.8.

analysis, the performance results will not be presented in the traditional contour plot of efficiencies. Instead, the efficiency will be plotted in a "parametric map" format, i.e. as a function of the power coefficient for different advance ratios. Furthermore, the efficiency will be broken into two parts: the ideal efficiency, which is the efficiency when the drag is set to zero and the viscous losses. The viscous losses are defined as the difference between the ideal efficiency and the real efficiency; i.e. *viscous losses = ideal efficiency - efficiency.*

5.5.1 Step 1: optimise twist and pitch with constant chord

The results of the constant chord design cases are analysed first. Figure 5.15a shows the effect of different design power coefficients on the parametric map of ideal efficiency. The points for the three designs collapse onto single curves, apart from some deviations observed at the low C_P region. This discrepancy occurs because this region is in the edge of the propeller map, where some extrapolation is used. The extrapolation is used to fill uniformly the $C_P - J$ space, from data points that are produced for given J and pitch angle; i.e. its not the C_P that is an input in the code but the pitch angle. Therefore it can occur that the results do not cover uniformly the map space and some extrapolation is required in the edges. As seen in Fig. 5.15a, this time there is an optimum ideal efficiency point occurring towards the low end of C_P. Nonetheless, the results confirm that the variations in the design do not change the map of ideal efficiency which depends strongly on the actual value of C_P and J regardless the design point of optimal performance. This result comes to confirm the observation made in section 5.3 regarding the ideal efficiency map as shown in Fig. 5.1b.

Having in mind that the chord was kept constant and the viscous losses where not re-optimised for each design, the results shown in Fig. 5.15b are not unexpected. The variation of viscous losses in the parametric map is the same for all three designs. Only the operating point of the propeller changes, with the losses being increased or decreased according to the location of the new point on the map. This is also justified if one recalls that the three optimised designs have the same chord and approximately the same twist distributions. Hence, they are essentially the same blade operating at a different point. The efficiency parametric map of Fig. 5.16a concludes this argument by showing the same exactly performance variation for the three design C_P, while Fig. 5.16b proves that the same applies for different design advance ratios J.

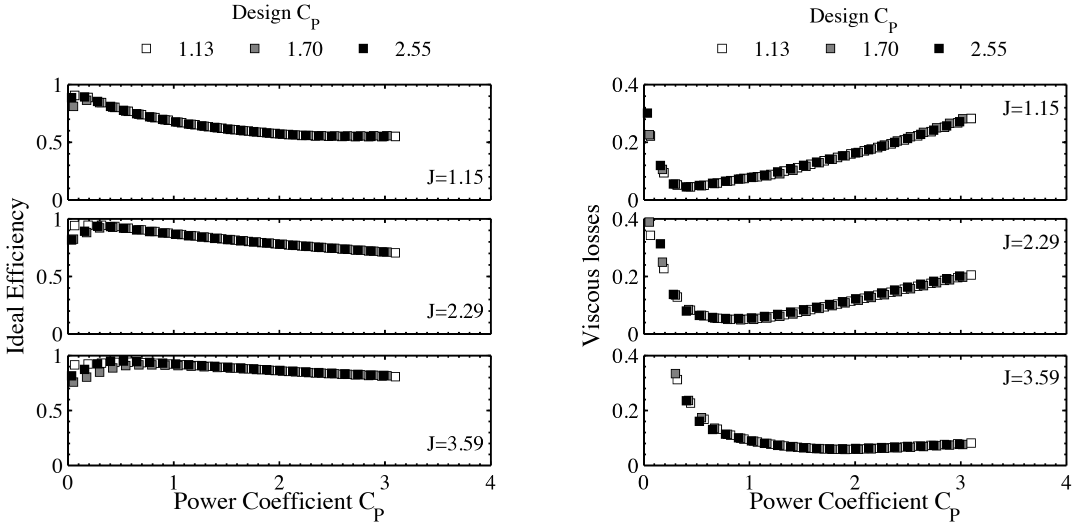

(a) Ideal efficiency

(b) Viscous losses

Figure 5.15: The change in the ideal efficiency and viscous losses map for different design power coefficients C_P. The blade chord distribution is held constant. Mach = 0.2.

5.5.2 Step 2: optimise twist, pitch and chord

The next step consists in analysing the map generated for propellers of which the distribution of chord has also been optimised. Figure 5.17a shows that the ideal efficiency is still unaffected. There is a slight divergence of the points for low C_P and for high C_P at the lowest advance ratio. Once more the explanation can be sought in the extrapolation taking place in these regions, as mentioned earlier. Furthermore, this graph is another proof

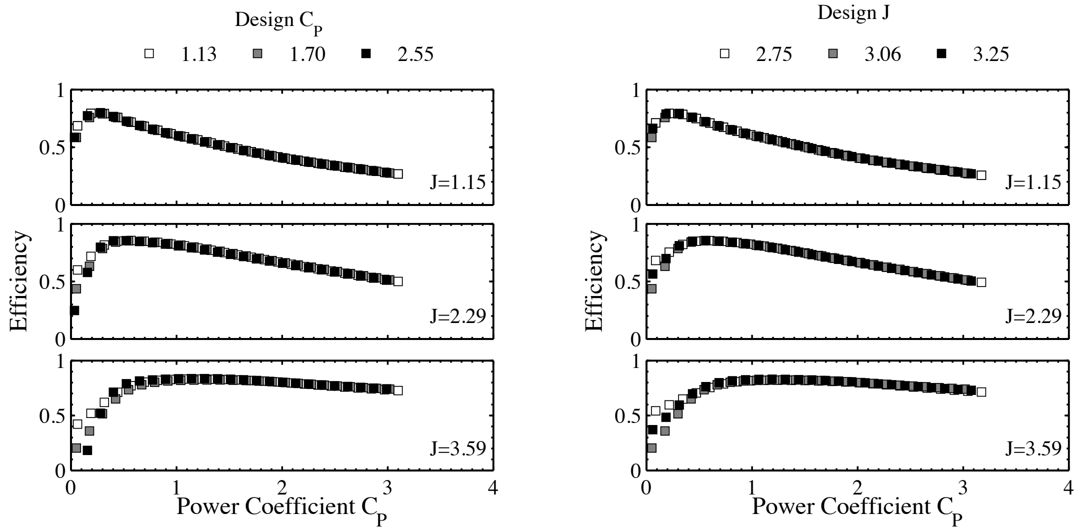

(a) Varying design power coefficients C_P

(b) Varying design advance ratios J

Figure 5.16: The variation of the efficiency map, for different design power coefficients C_P and advance ratios J. The blade chord distribution is held constant. Mach = 0.2.

of the independence between the ideal performance and the chord distribution, discussed in section 5.4.2.

On the other hand, Fig. 5.17b shows that the different chord distributions have a substantial impact on the viscous losses. The parametric maps for the three different design power coefficients do not collapse any more onto single curves, but there is an offset between the points. This offset occurs due to the optimisation of the viscous losses that forces the minimum loss point to occur as close as possible to the corresponding design point. As shown in section 5.4.4.2 the optimiser achieves that by setting the lift coefficient always at the value that optimises the aerodynamic efficiency L/D. This is also proven by Fig. 5.18, which serves to illustrate that the lift coefficients move towards a lower C_P when the design C_P decreases; i.e. the optimum lift always moves towards the design point C_P. Hence, the minimum losses also move towards a lower C_P when the design C_P decreases, as seen in Fig. 5.17b. Figure 5.19 demonstrates that if one plots the losses as a function of the lift coefficient instead of using C_P, there will be no offset between the different designs as the losses depend only on the corresponding C_L. At the same time, the lift coefficient variation is centred around the design point of the propeller and hence remains constant for different propeller designs if the relative $(J/J_{des}, C_P/C_{Pdes})$ coordinates are used (Fig. 5.20a).

The above arguments can be summarised in the following statements:

1. The viscous losses depend only on the lift coefficient.

2. The lift coefficient is always at the optimal value at the design point.
3. Hence the minimum losses will always move to the design point.

Therefore, if the coordinates of the viscous losses map are non-dimensionalised by dividing them with their design values, the viscous losses will always stay constant and centred at the point $J/J_{des} = 1$ and $C_P/C_{Pdes} = 1$. This is illustrated by Fig. 5.20b, where the relative C_P is used and all the points collapse onto single curves. Although not shown here, the same principle applies for different design advance ratios according to the analysis in section 5.4.4.2.

In conclusion, a propeller of whichever design power coefficient and advance ratio, which is based on the same blading characteristics, can be described by a single set of two maps. One that describes the variation of ideal efficiency as a function of the absolute values of advance ratio and power coefficient, and one that determines the viscous losses as a function of the same coordinates divided by their design point values. It remains to be seen in the next section, whether these different designs also share the same Mach number efficiency correction.

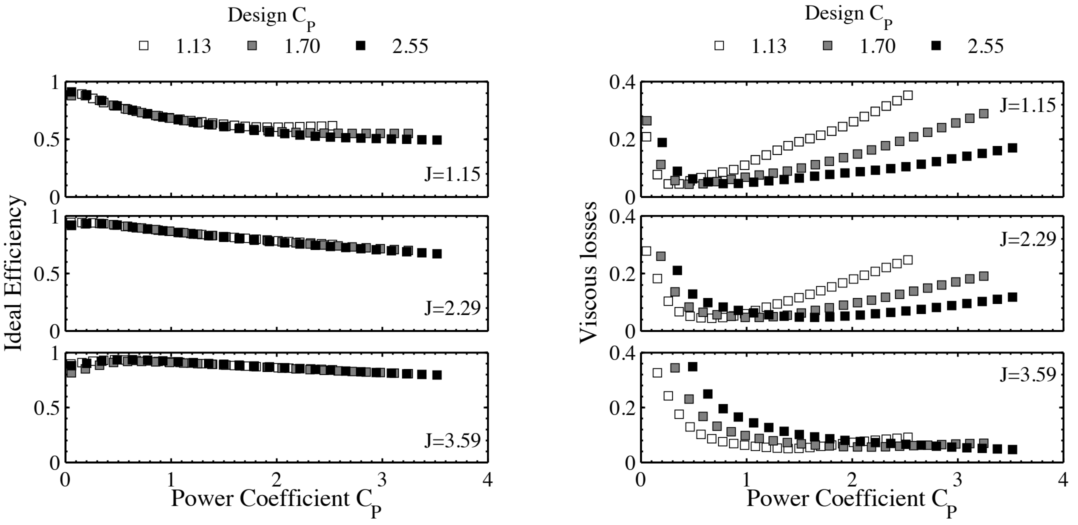

(a) Ideal efficiency

(b) Viscous losses

Figure 5.17: The change in the ideal efficiency and viscous losses map for different design power coefficients C_P. The blade chord distribution is optimised. Mach = 0.2.

5.5.3 The Mach number effect for different designs

In order to test the impact of Mach number on propeller efficiency, each propeller design is operated at its design power coefficient and advance ratio while the Mach number

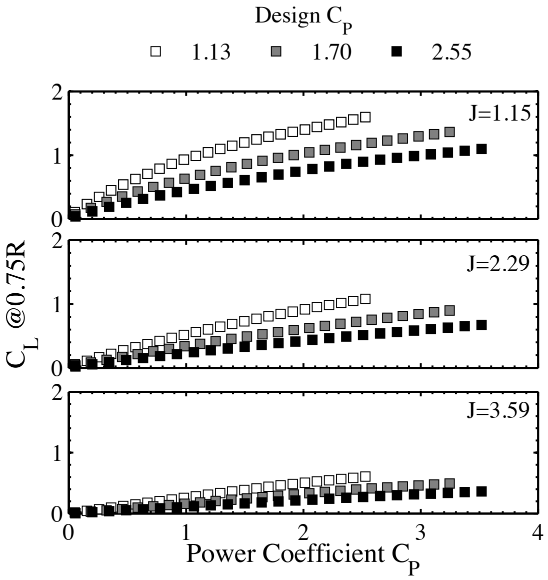

Figure 5.18: The variation of the lift coefficient in the relative coordinates map, for different design power coefficients C_P. The map uses the C_L at the 0.75R point as typical of the blade performance. The blade chord distribution is optimal. Mach = 0.2.

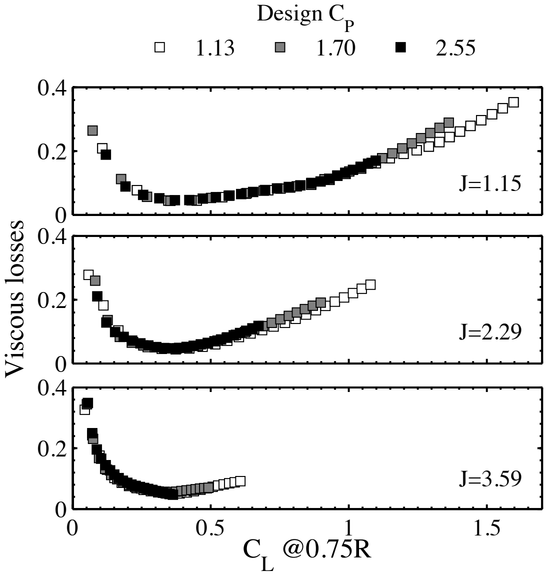

Figure 5.19: The variation of viscous losses as a function of the operating $C_L@0.75R$ and the operating advance ratio, for different design power coefficients C_P. The blade chord distribution is optimal. Mach = 0.2.

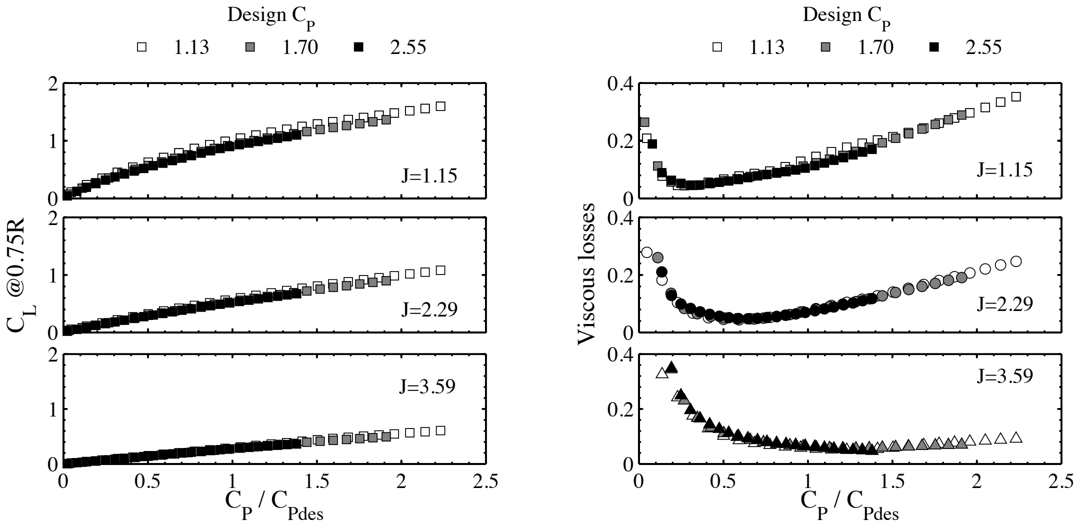

(a) C_L

(b) Viscous losses

Figure 5.20: The variation of C_L and the viscous losses in the relative coordinates map, for different design power coefficients C_P. The blade chord distribution is optimal. Mach = 0.2.

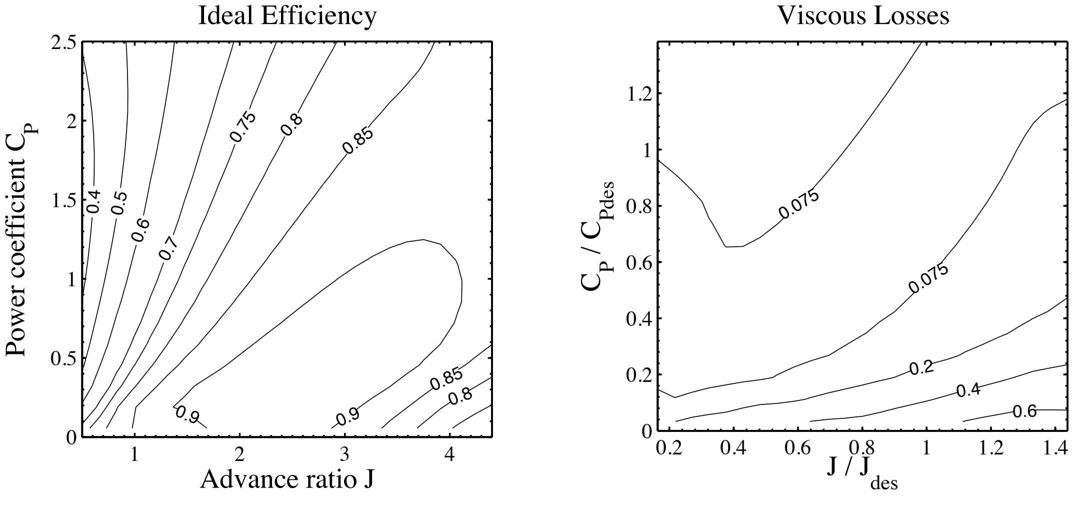

(a) Ideal efficiency map

(b) Viscous losses map

Figure 5.21: The scalable ideal efficiency and viscous losses maps for the SR3 prop-fan. Mach = 0.2.

gradually increases. The aim is to verify whether the single curve of Fig. 5.8 can be used for all the prop-fan designs. Figure 5.22 shows the results for the five different designs of table 5.2, each one operating at their design point conditions. It is confirmed that the points collapse on a single curve, which can be used to describe the correlation between Mach number and efficiency regardless of the blade design point C_P and J. This was expected as the five designs studied share the same blade characteristics (except for the twist and chord distributions), and thus their airfoils are expected to show the same behaviour with Mach number.

The effect of varying both the operating advance ratio and power coefficient was investigated in section 5.3.1. The first was incorporated in the definition of helical Mach number, while the second was found not to affect the results. This was somewhat unexpected as a higher power coefficient leads to higher angles of attack, which are more sensitive to increases in Mach number. However, the variations of power coefficient used in section 5.3.1 were quite close to the design point conditions. It was found as part of this design study, that the relation with Mach number is also a function of the angle of attack seen by the airfoils, if the propeller is operated far from its design point. The design point conditions used for Fig. 5.22 correspond approximately to a C_L@0.75 equal to 0.36 (as observed from Fig. 5.13). This time the value of 0.60 was tested for the cases of $C_{Pdes} = 1.13$ and $C_{Pdes} = 1.70$ (for both cases $J_{des} = 3.06$). The desired C_L was achieved by appropriately adjusting the values of the operating advance ratio and power coefficient. The final values used are indicated in the caption of Fig. 5.23. Figure 5.23 shows that the points collapse again on a single curve, which nonetheless is different to the one corresponding to the design conditions. As expected, the higher C_L curve is more sensitive to an increase of Mach number and the efficiency starts deteriorating faster.

The above observation leads to the conclusion that for an accurate modelling of the Mach number effect, a different curve is required for each C_L. This entails that an additional graph similar to Fig. 5.20a is required, in order to relate the operating C_P and J with an operating C_L, which can then be translated to a Mach number correction. Thus, in total four maps would be required to describe the ensemble of propellers that have a different design point (C_P, J), but are based on the same baseline blade characteristics. Alternatively, instead of using a Mach number correction, a different Fig. 5.21b could be used for each Mach number, improving this way the accuracy by sacrificing some more computing resources. As proven by Fig. 5.23 these maps are still independent of propeller design C_P and J. Furthermore, the latter method is also preferred when existing propeller test data are used, as these do not include an indication of the operating lift coefficient. This would have to be modelled by a simulation code, which however would necessitate the knowledge of the propeller geometry.

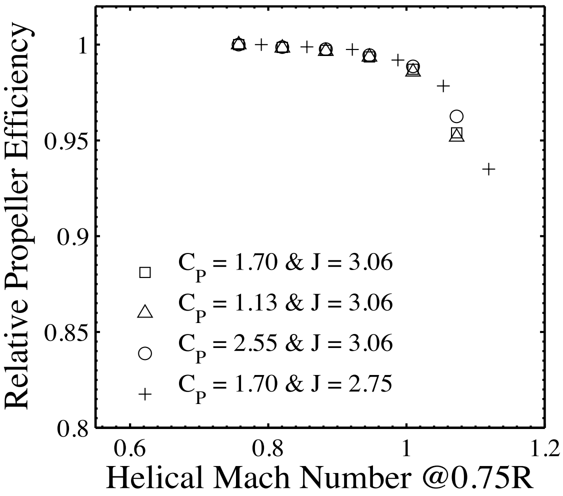

Figure 5.22: The mach number correction curve for four different design conditions. Each propeller operates at the design power coefficient and advance ratio. The twist and chord are optimal.

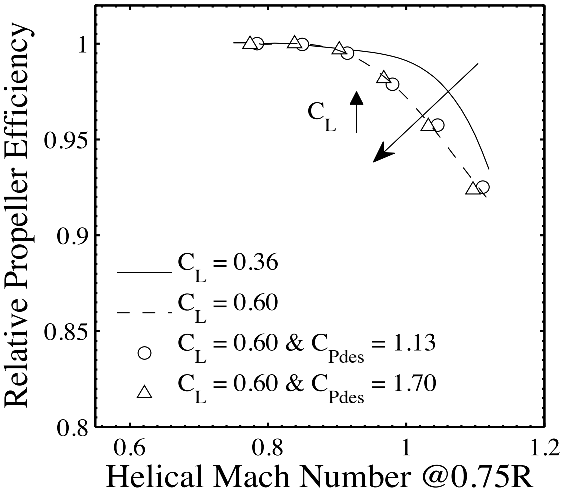

Figure 5.23: The effect of the operating C_L on the mach number correction curve. The C_L at the $0.75R$ is used. The $C_{Pdes} = 1.13$ propeller operates at $(C_P = 1.58, J = 2.80)$, while the $C_{Pdes} = 1.70$ propeller operates at $(C_P = 2.72, J = 2.89)$. The $C_L = 0.36$ curve represents the results of Fig. 5.22. The twist and chord of each design are optimal.

5.5.4 Discussion

The propeller map representation developed in this chapter is superior to the one used by Seitz [22, 23], while it improves Borst's approach [99], the principles of which are used as a basis. Seitz used an efficiency contour map, which used the relative coordinates of C_P/C_{Pdes} and J/J_{des}. The design point efficiency was predicted using the design technique formulated by Davidson [109]. The calculated efficiency was used to scale all the efficiencies of the map by multiplying with the ratio of calculated design point efficiency divided by the map design point efficiency.

The first shortcoming identified in this approach is the approximate accounting of the blade sweep, stemming from the fact that the method by Davidson is based on the Goldstein/Theodorsen modelling. The second disadvantage is the requirement for a design code that calculates the design point efficiency for each different propeller design. Alternatively, the method would require that such a code was used to produce a design point map that relates the design point efficiency with the design point power coefficient and advance ratio. The third and last disadvantage comes from the map scaling per se. The implemented scaling assumes that the shape of the efficiency contours remain unchanged as the design point efficiency changes. It has been shown in section 5.5.2 that the use of the (C_P, J) coordinates results in the ideal efficiency contours being constant between different designs (Fig. 5.17a). On the other hand, as illustrated by Fig. 5.20b, the relative coordinates $(C_P/C_{Pdes}, J/J_{des})$ result in constant viscous losses contours. This implies that the total efficiency contours, being the difference of the two previous efficiency terms, are not constant in either coordinate system. Figure 5.24 proves this argument by showing the difference between the relative efficiency contours of two propellers which have different design point power coefficients. The relative efficiency is defined as the efficiency defined by its maximum value on the map. In order to facilitate the comparison the same contours are plotted in both sub-figures. It is evident that not only the location of the maximum efficiency changes, but also the efficiency varies more rapidly for the higher power coefficient design. It can be concluded that the approach followed by Seitz does not reflect the physical phenomena taking place and can lead to high inaccuracies.

Contrary to Seitz's approach, the method proposed by Borst identifies correctly the different phenomena and devises a map representation in the form of a set of graphs that can generically model a family of prop-fans. The method developed in this chapter is based on the same principles and at the same time enhances the following points:

1. The activity factor design parameter has been replaced by the design point power coefficient and advance ratio. Contrary to the activity factor, these parameters can be calculated from variables readily available during the preliminary thermodynamic design of the whole engine.

2. The Mach number can be taken into account either by multiple viscous losses map

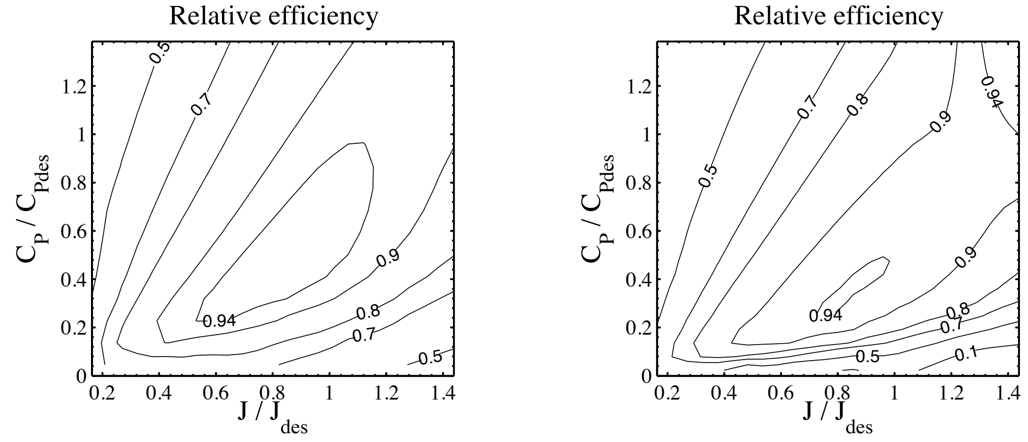

(a) $C_{Pdes} = 1.13$

(b) $C_{Pdes} = 2.55$

Figure 5.24: The change of the relative efficiency contours plotted using the relative C_P and J for two different design power coefficients. The relative efficiency is defined as the efficiency of each point divided by the maximum efficiency of the map.

(one for each Mach number) or by a graph that corrects the efficiency as a function of the lift coefficient and the helical Mach number at the 3/4 of the blade radius. This graph must be accompanied by a graph connecting the relative power coefficient and advance ratio with the lift coefficient. Furthermore, the viscous losses and Mach correction maps could be integrated into a single graph that gives the total viscous losses (including the compressibility effect) as a function of the lift coefficient and the helical Mach number. Nonetheless, this requires further work and can be part of future work on the topic.

3. The method is easily applicable to existing propeller maps which give efficiency as a function of C_P, J and Mach. The only requirement is the generation of an ideal efficiency map, which can be easily produced by a simulation code as complicated as a lifting-line or as simple as a Goldstein/Theodorsen method. Moreover, the propeller decks supplied by the manufacturers often include the option of running the deck in zero drag mode, producing this way the ideal efficiency table. Contrary to the data required by the Borst approach, no knowledge of the airfoil drag is required in this case. This map will be used to expand the given experimental data to other design power coefficients and advance ratios in the following way: the available real efficiency data will be subtracted from the corresponding ideal efficiencies in order to produce the viscous losses map. It comes without saying that the higher the accuracy of the ideal performance prediction, the better the repartition between ideal and viscous losses and the better the generalisation of the

performance map.

4. For a single Mach number Borst's method requires the storage of a number of graphs equal to (number of different blade numbers) × (number of different C_L/C_D). The proposed method requires a number of ideal efficiency maps equal to (number of different blade numbers), but this is accompanied by a unique viscous losses map.

Another positive aspect of the approach developed in this chapter is the quick evaluations it offers regarding the design point performance of propellers with different design C_P and J. For instance, according to Fig. 5.17a a propeller having a design C_P and J equal to 1. and 3. respectively operates with an ideal efficiency of approximately 92%. At the same time, according to Fig. 5.20b the minimum losses for this blade design are around 0.04. This leads to the conclusion that a propeller designed at these conditions would have an efficiency of 88%. Finally, according to Eq. 5.2 a flight Mach of 0.8 would result in a helical Mach of 1 at 0.75R, which would be translated by Fig. 5.22 to a compressibility correction equal to 0.99. The final efficiency would therefore be equal to approximately 87%, value not far from the ones given by table 5.2.

Before closing, a limitation of the proposed method must be discussed. The basic underlying assumption is that for each propeller design the viscous losses are minimised. This is indeed one of the most critical targets of propeller optimisation, which nonetheless can be constrained by different limitations. More precisely, it has been shown earlier that the minimisation of the viscous losses is mainly achieved by adjusting the blade chord distribution. However, the variation of the blade chord can be constrained by considerations of structural integrity, which would keep the final design solution further from the losses minimum. In that case, the accuracy of the map representation would decrease. This design exercise has been tried by the author and has been found to have a negligible impact on the results, as the constraints mainly affect the hub blade region which is not as important as the outboard one. Furthermore, it must be reminded that regardless of the structural constraints, the design would always drive the chord distribution close to the minimum losses value, validating this way the propeller map representation proposed here.

5.6 Conclusions

The aim of this chapter was to produce a propeller map representation which remains unchanged when the propeller design point changes and allows the preliminary engine designer to conduct extensive parametric studies.

The propeller modelling method developed in the previous chapter was used in order to generate a full performance map for the SR3 prop-fan. The map was subsequently used in order to understand the phenomena taking place. An increase in the power coefficient or a decrease in the advance ratio result in a drop of the ideal efficiency. The off-design migrations from the optimal design loading seem to have a secondary effect on the ideal performance. On the other hand, the viscous losses depend on the actual lift coefficient of the blade - the value at 0.75R being used as reference - and exhibit a locus of optimum performance at a specific lift coefficient, which corresponds to the optimum L/D ratio. At the same time, lower advance ratios lead to higher helical Mach numbers which tend to increase the compressibility losses.

The effect of Mach number can be captured in two ways. Either by having a different propeller map for each Mach number, or by using a correlation that corrects the efficiency as a function of the helical Mach number and the operating lift coefficient. The former provides higher accuracy and it can be more convenient as data are often available in this format. The latter can offer computer resources savings and potentially the same accuracy, but some post-processing of the existing propeller data is required in order to create the correlation map.

The change of the propeller map for different design point power coefficients and advance ratios was investigated. For this purpose, the twist and chord distributions are varied - all the other blade characteristics being constant - in order to achieve an optimum propeller efficiency for the given specifications. When the chord distribution is also kept constant, the blade shape effectively stays the same between the different design points and only the operating pitch angle changes. The propeller essentially operates at a different angle of attack and lift coefficient within the same propeller map, which remains constant.

On the other hand, the variation of the chord distribution allows the lift coefficient to be always at the same optimal value for all different designs. This leads to the minimisation of the viscous losses around the respective design point and thus the shape of the map is not constant any more. Breaking down the efficiency in ideal efficiency and viscous losses allows to create a set of maps that is common between the different propeller designs. The first map expresses the ideal efficiency as a function of the absolute values of C_P and J, while the second expresses the viscous losses as a function of the relative coordinates C_P/C_{Pdes} and J/J_{des}. The compressibility losses are added as a correction factor which is a function of the lift coefficient and the helical Mach number, supplemented by a map of the lift coefficient in terms of the aforementioned relative coordinates. Alternatively, a separate map can be used for the viscous losses of each flight Mach number. The latter would be preferred if existing experimental data were to be used.

The analysis of the results demonstrated that the map representation approach used by Seitz [22, 23] was not accurate, as it assumed a single efficiency map that was expressed in relative coordinates. It has been proven that this map would change between different designs, leading this way to important discrepancies in the modelling. On the other hand, the proposed method is based on the same principles with Borst's method [99], which was enhanced in the following ways:

1. The activity factor design parameter has been replaced by the more convenient design point power coefficient and advance ratio.
2. The effect of the flight Mach number has been taken into account.
3. The method is easily applicable to existing propeller maps which give efficiency as a function of C_P, J and Mach.
4. Less computer resources are required as only one viscous losses map is used for every flight Mach number.

Chapter 6

Conclusions & Future work

6.1 Summarising the key elements

6.1.1 Advanced turbofan design space exploration

Chapter 2 aims to create a design space map that shows the position of the optimum short and long range engines and demonstrates which low pressure system technologies are required.

The literature is reviewed in order to clarify the thermodynamic cycle parameters that drive engine efficiency, understand the current design trends and identify the enabling technologies required. According to the literature, if the engine industry keeps walking on the current path of turbofan design, the variable area fan nozzle and the geared architecture are the two major enabling technologies that will be needed. Explaining why, is part of the objectives of this chapter.

An analysis and optimisation framework is set up, comprising models that predict the engine performance, the dimensions and weight, the drag and the installed performance. The engine performance model has been updated in order to correctly simulate the combustor balance, which results in the existence of a turbine entry temperature optimum. The numerical stability of the model has also been significantly improved, allowing the fast and automated generation of the engine design data required for the analysis. The principles of engine preliminary design were studied and translated into a numerical problem formulation using the created optimisation framework. The analysis was focused on a two-spool turbofan configuration for a short and a long range mission, studying in turn the uninstalled performance, the need for enabling technologies and the integrated installed performance. The main conclusions are as follows:

1. There is an optimum turbine entry temperature for a given level of overall pressure ratio and component efficiencies. The optimum value is higher for higher overall

pressure ratio and lower for higher component efficiencies. In the ideal case of isentropic components the turbine entry temperature has a negative impact on engine efficiency, but still a positive impact on core size. In order to capture the effect of optimum turbine entry temperature, the combustor balance needs to take into account the fuel added mass flow in the calculation of the exit gas enthalpy.

2. There is a strong dependency between the engine specific thrust and the optimum fan pressure ratio. A lower specific thrust leads to a lower fan pressure ratio. A higher overall pressure ratio decreases the specific power of the core and thus decreases the optimum fan pressure ratio. The opposite happens for higher component efficiencies.
3. Under constant turbine entry temperature, the optimum specific thrust is determined by the trade-off between the propulsive and the transmission efficiency. A lower specific thrust improves the propulsive efficiency, but increases the bypass ratio and deteriorates the transmission efficiency. The results show that the value which optimises the uninstalled performance and hence the SFC is equal to 75 m/s.
4. Under constant specific thrust, the optimum turbine entry temperature and bypass ratio are determined by the trade-off between core and transmission efficiency. Higher TET leads to higher bypass ratio and lower transmission efficiency, while the effect of TET on the core efficiency has been described above in point 1. The optimum level of TET is not far from the currently used values of 1800-2000 K and further increases are unlikely to bring important benefits, especially considering the increased cooling requirements and component losses due to small size effects.
5. The specific thrust defines the TET ratio between top-of-climb and take-off. For the same take-off temperatures, a lower specific thrust results in higher top-of-climb TET due to the lower jet velocities and the higher thrust lapse rate.
6. An increase of the overall pressure ratio can improve the core efficiency but the maximum compressor exit temperature at take-off must be always respected. For a given level of top-of-climb OPR and TET, a lower specific thrust ”relieves” the take-off power setting and reduces the compressor exit temperatures. This positive effect of lower ST and the continuous research for higher compressor efficiencies can enable the use of higher top-of-climb OPR.
7. The need for a variable area fan nozzle is dictated by the fan surge problems at take-off. Fans with lower pressure ratio operate unchoked at take-off and therefore their surge margin reduces. The lower the fan pressure ratio the lower the surge margin at take-off. An increase of the fan nozzle area at take-off can augment the nozzle capacity and increase the fan surge margin. The results show that there is strong relation between the required nozzle area increase and the fan pressure ratio,

which in turn is strongly dependent on the specific thrust. Engines with specific thrust lower than 130 m/s need a 10% increase of the nozzle area at take-off, while 20% is required for specific thrusts lower than 80 m/s.

8. The variable area fan nozzle can also be used to achieve the same take-off thrust with a lower turbine entry temperature. When the area increases, the same fan power is distributed to a higher mass flow with a lower jet velocity and the propulsive efficiency increases. The turbine entry temperature can then fall as long as the fan efficiency stays at high levels. The results show that a reduction of upto 50 K can be achieved at take-off.

9. The gearbox study relates the required number of turbine stages to the thermodynamic cycle parameters. The fan pressure ratio and the bypass ratio are the two dominant parameters. Increased bypass ratios increase the number of stages, due to the lower turbine blade speeds and the higher required turbine enthalpy drop. Increased fan pressure ratios increase the number of stages due to the higher fan work that also increases the required turbine enthalpy drop. No size effect is found to exist and thus two engines sharing the same cycle and design but with different thrusts will have the same number of low pressure turbine stages.

10. Increased overall pressure ratio and component efficiencies compress the conventional turbofan design space by increasing the number of stages needed for the same turbine entry temperature and bypass ratio.

11. The installed performance integrates all the results in order to create the final design space maps. The results showed good agreement against current and future engines of the short and long range market.

12. The engine specific thrust at top-of-climb uniquely defines its diameter for a chosen inlet hub/tip ratio and axial Mach number. The optimum specific thrust is determined by the trade-off between, propulsive efficiency, engine weight and drag for a given aircraft application. The optimum value is lower for long range missions where the fuel efficiency is the dominant parameter. Higher engine weight and drag decrease the optimum value, especially for short range missions, for which the impact of weight is three times higher than the long range case.

13. Having defined the specific thrust through the installed performance trade-offs, the limits of turbine entry temperature subsequently impose the minimum allowable engine core size. The higher the temperature, the higher the bypass ratio and the lower the core size. The optimum value of specific thrust, also fixes the maximum allowable design overall pressure ratio which respects the compressor exit temperature restrictions at take-off.

14. The created design space maps show that the variable area fan nozzle will be probably required for the next generation of long range engines, due to their low optimum specific thrust. The replacements of the current CMF56 engines, will probably still operate safely without a variable nozzle. This conclusion can change if lower optimum specific thrusts are attained, through a more aggressive installation, potentially provided by a geared configuration.
15. Based on the generated results, the gearbox will be needed for both short and long range engines, as the lower specific thrust, higher overall pressure ratio and improved component efficiencies are pushing the conventional turbofan to its limits. The long range engines have the priority as they feature higher overall pressure ratios and lower specific thrusts.
16. Only mediocre improvements in thermal efficiency can be achieved by increasing the overall pressure ratio and turbine entry temperature relative to today's levels. Increasing the overall pressure ratio by 25% can deliver a fuel burn improvement of 1.7 and 0.8 percent for the short and long range engines respectively. Increasing the TET by 100 K leads to almost no improvement for the short range and to a 0.8% improvement for the long range engine. The OPR benefit increases for higher component efficiencies, while the opposite happens with TET. The above trends mean that there is probably no benefit in using the variable area fan nozzle in order to achieve a smaller and hotter core design.
17. In an extreme scenario the turbine entry temperatures could even decrease by 200 K relative to today's levels, in order to decrease the bypass ratio and avoid completely the introduction of a gearbox. This scenario could result in an engine with potentially lower maintenance costs, lower cooling requirements and lower component size effects, without an excessive efficiency penalty as long as its weight is controlled.
18. Future fuel reductions are most likely to be sought by improvements of component efficiencies, reduced engine weight and drag, and lower specific thrusts.

6.1.2 Secondary power extraction effects

The work presented in chapter 3 aims to complement the conclusions of chapter 2 by adding the size effect of given bleed and power off-takes. The analysis is based on the fundamentals of engine efficiency and on the typical enthalpy entropy diagram. A set of equations is derived in order to calculate the SFC penalties when shaft power or bleed air is extracted at the design point of a gas turbine engine. The equations perform well against numerical simulation results and can be used during the preliminary design stages for the estimation of the installed specific fuel consumption of aero-engines ranging from a turbojet to an open rotor. The thermodynamic analysis carried out leads to the following findings:

1. The main factor driving the magnitude of the penalties is the size of the off-takes relative to the core power; the higher the relative size the higher the penalty. For fixed off-takes and thrust requirements the power produced by the core is determined by the propulsive and transmission efficiencies. The higher the efficiencies, the less the power needed by the core to produce a given thrust, and the greater the off-take penalties. Similarly, a lower thrust requirement would result in less demand for core power and therefore higher penalties.

2. The fan and low-pressure turbine efficiencies and the engine specific thrust are the main design parameters that drive the size of the penalties, since they govern the transmission and propulsive efficiency, respectively. Bypass ratio also drives the transmission efficiency, but has a lesser effect. The aforementioned design parameters have been grouped in three nondimensional numbers that affect the penalties in the following manner:

    (a) An increasing power factor $\frac{P_{po}}{T \cdot V_0}$ increases the SFC penalties. This means that future aircraft/engines with lower thrust requirements and higher passenger comfort, and hence higher off-takes, will face increased SFC penalties.

    (b) Future engines are expected to have a decreased specific thrust factor $\frac{ST}{V_0}$, which will improve the propulsive efficiency, reduce the core power required for a given thrust, and increase the off-take penalties.

    (c) An increasing transmission efficiency factor $\eta_f \eta_{lpt}$ reduces the core power required for a given thrust and increases the off-take penalties.

3. The secondary-power SFC penalties are not high enough to affect the aforementioned future trends; in other words, the benefits arising from reduced specific thrust and improved transmission efficiency would outweigh the increased secondary-power penalties. Reducing the power factor appears to be the only way to improve the situation for future engines. This could be achieved by designing more efficient secondary systems, possibly within the context of an all-electric aircraft.

4. The characteristics of the core (TET, OPR, core component efficiencies and pressure losses) do not directly affect the relative penalties, although they influence the absolute fuel needed for the provision of secondary power. In light of this, improvements in core efficiency should be further pursued to reduce the fuel burned for secondary systems and primary propulsive power.

5. When redesigning an engine to include the secondary power extraction in the design point, two methods exist to conduct the resizing:

    (a) Resize the whole engine by keeping the bypass ratio constant.

    (b) Resize the core by keeping the diameter and specific thrust constant.

    Each method has a different secondary effect on the size of the penalties. The first method results in a propulsive efficiency benefit, accruing from the higher mass flow and lower specific thrust of the resized engine. The second method results in a lesser transmission efficiency benefit due to the lower bypass ratio of the resized engine. Although, the first method results in a better SFC the higher size of the engine is expected to increase its weight and drag and therefore eliminate or even reverse the fuel consumption benefit.

6.1.3 Propeller modelling method development

This chapter presents the development of a simulation method aiming to model the aerodynamic performance of high speed propellers. This is an essential task, as the accurate prediction of propeller efficiency is translated into an accurate prediction of open-rotor engine thrust. A description of the fundamentals of propeller performance and a breaking down of the propeller losses allows a better understanding of the characteristics required from a propeller modelling method. An extensive literature survey leads to the selection of the lifting-line method which was extensively used in the past for the design of prop-fan geometries. That approach is able to capture satisfactorily the performance of highly swept blades, and to take into account the induced and viscous losses.

The description of the method development focuses mainly on the modelling of the wake geometry and the calculation of the induced velocities through the use of the Biot-Savart law. Special attention is given to the modelling of the compressibility effects involved in the calculation of the induced flow-field. The study conclusions are listed below:

1. The analysis of previous studies pointed towards an incompressible lifting-line approach, due to its simplicity and to the unsatisfactory results of more complex solutions. Amongst them, the well formulated compressible lifting-surface of Hanson et al [83] is retained as a comparison base.

2. The numerical method is configured in order to simulate the performance of the well-documented SR3 prop-fan geometry, created by Hamilton Standard in 1970s. The selection of the model configuration parameters is conducted by using an extensive sensitivity analysis. The number of spanwise blade stations is set to 20, the model calculates 4 wake turns, while the wake geometry is updated 3 times.

3. In addition to setting up the model, this analysis sheds light to many interesting modelling aspects. Most notably, the results confirm the selection of the prescribed wake model against the rigid helical one, which would lead in a under-prediction of efficiency by 1.2%.
4. The effect of blade deformations is proven to reduce the slope of the $J - C_P$ curve and to induce a reduction in the power coefficient of about 0.22, especially at high mach numbers.
5. The nacelle modelling using the public domain potential flow code PAN AIR, is found to predict well the flow around the SR3 spinner and nacelle, especially in the high power blade region.
6. Having verified the code set-up, the modelling of deformations and the accuracy of the nacelle prediction, the code is validated against experimental data. At low Mach number (M=0.2) the predictions show very good agreement with the test data, both for the power coefficient and the efficiency. At M=0.6 the agreement is still very good but the pitch angle is under-predicted by 2 degrees due to the increased effect of the deformations. This effect is attributed to the elastic behaviour of the blade retention system, which was not captured by the implemented modelling.
7. At M=0.8 the agreement is not as good, due to the combined effect of deformations and compressibility. Nevertheless, the prediction is in the same order of accuracy as the higher fidelity compressible lifting-surface method of Hanson et al [83]. The above result further reinforces the choice for an incompressible calculation of the induced velocities.
8. In an attempt to reduce the effect of deformations, a last validation exercise is conducted with constant power coefficient and advance ratio. This time the agreement with the experimental data is excellent throughout the whole Mach number range, proving the suitability of the code for the performance predictions required in the context of this work.

6.1.4 The development of a scalable propeller map representation

The aim of chapter 5 is to produce a propeller map representation which remains unchanged when the propeller design point changes and allows the preliminary engine designer to conduct extensive parametric studies.

The propeller modelling method developed in chapter 4 is used in order to generate a full performance map for the SR3 prop-fan. The map is subsequently used in order to understand the phenomena taking place. The major findings are listed below:

1. Within a given propeller map, an increase in the power coefficient or a decrease in the advance ratio result in a drop of the ideal efficiency. The off-design migrations from the optimal design loading seem to have a secondary effect on the ideal performance.
2. On the other hand, the viscous losses depend on the actual lift coefficient of the blade - the value at 0.75R being used as reference - and exhibit a locus of optimum performance at a specific lift coefficient, which corresponds to the optimum L/D ratio. At the same time, lower advance ratios lead to higher helical Mach numbers which tend to increase the compressibility losses.
3. The effect of Mach number can be captured in two ways. Either by having a different propeller map for each Mach number, or by using a correlation that corrects the efficiency as a function of the helical Mach number and the operating lift coefficient. The former provides higher accuracy and it can be more convenient as data are often available in this format. The latter can save computer resources and offers potentially the same accuracy, but some post-processing of the existing propeller data is required in order to create the correlation map.

The change of the propeller map for different design point power coefficients and advance ratios is investigated. For this purpose, the twist and chord distributions were varied - all the other blade characteristics being constant - in order to achieve an optimum propeller efficiency for the given specifications. This design study produces the following principal conclusions:

4. When the chord distribution is kept constant, the blade shape effectively stays the same between the different design points and only the operating pitch angle changes. The propeller essentially operates at a different angle of attack and lift coefficient within the same propeller map, which remains constant.
5. The variation of the chord distribution by the optimiser allows the lift coefficient to be always at the same optimal value for all different designs. This leads to the minimisation of the viscous losses around the respective design point and thus the shape of the map is not constant any more.
6. Breaking down the efficiency in ideal efficiency and viscous losses allows to create a set of maps that is common between the different propeller designs. The first map expresses the ideal efficiency as a function of the absolute values of C_P and J, while the second expresses the viscous losses as a function of the relative coordinates C_P/C_{Pdes} and J/J_{des}.
7. The compressibility losses are added as a correction factor which is a function of the lift coefficient and the helical Mach number, supplemented by a map of the

lift coefficient in terms of the aforementioned C_P/C_{Pdes} and J/J_{des} coordinates. Alternatively, a separate map can be used for the viscous losses of each flight Mach number. The latter would be preferred if existing experimental data were to be used.

8. The analysis of the results demonstrated that the map representation approach used by Seitz [22, 23] is not accurate, as it assumes a single efficiency map which is expressed in relative coordinates. It has been proven that this map would change between different designs, leading this way to important discrepancies in the modelling.
9. On the other hand, the method proposed here is based on the same principles with Borst's method [99], which was enhanced in the following ways:
    (a) The activity factor design parameter has been replaced by the more convenient design point power coefficient and advance ratio.
    (b) The effect of the flight Mach number has been taken into account.
    (c) The method is easily applicable to existing propeller maps which give efficiency as a function of C_P, J and Mach.
    (d) Less computer resources are required as only one viscous losses map is used for every flight Mach number.

6.2 Author's contribution

Taking into account the studies already existing in the literature, this work contributes in the following aspects:

1. The work presented in chapter 2 concerning the design space exploration of advanced turbofan engines, is the first study that achieves to correlate the thermodynamic cycle parameters to the number of the low pressure turbine stages. The thermodynamic based analysis clearly demonstrates the possible paths future turbofan engine design can take. Furthermore, the study sheds light on concepts that are often a source of misconception. The notion of the optimum turbine entry temperature, the selection of a specific thrust and its importance as a design parameter have been clearly demonstrated and clarified. The installed performance analysis showed that without significant reductions in the engine weight and drag, the design will not go towards lower specific thrusts and thus towards the need for a variable area fan nozzle. Finally, the technique of using the variable nozzle as a means of achieving a smaller and hotter core is shown not to deliver significant benefits mainly due to the already ”saturated” optimal values of temperatures.

2. The "preparatory" work of improving the engine performance code Turbomatch, in order to use it for the thermodynamic analysis of chapter 2, is a significant contribution to the department of Power and Propulsion. The stability of the code has been significantly improved, making its integration within an automated optimisation framework possible. The addition of a propeller brick enables future open-rotor and turboprop studies, while the correction of the combustor balance has a significant impact on capturing correctly the effect of turbine entry temperature. The upgraded code is a great asset for the department.

3. Chapter 3 presents the formulation of simple algebraic relations that calculate the specific fuel consumption increase when customer bleed or power is extracted from the engine. Using the derived relations the study determines the relation between the SFC penalties and the thermodynamic cycle parameters of the engine and thereby proves the future increase of the penalties. This is the first study formally demonstrating that engines with lower specific thrust will suffer from higher secondary power extraction penalties. Furthermore, the derived equations are a fast way to calculate the impact of extracting secondary power for any engine configuration. The work has been published in the AIAA Journal of Propulsion and Power [155].

4. Before developing the propeller simulation code described in chapter 4, the author conducted an extensive literature review, spanning from the beginning of the 20th century until today. Most peculiarly, the propeller topic seems to come and go over the years, with many works re-inventing the wheel and without a continuous development of the modelling methods. The review of the available modelling methods, with special focus on prop-fans and compressibility effects is a piece of work not existing in the literature at the moment. Furthermore, the clear step-by-step formulation and validation of the lifting-line model clarifies many misty points on the topic, while the comparison with a compressible lifting-surface method is a proof that lifting-line methods will continue to be a useful tool for prop-fan analysis. Finally, the lifting-line code itself is an important addition to the simulation capability of the department, on which many future design and analysis projects can be based.

5. Chapter 5 describes a novel propeller representation approach, which is generic between propellers of different design power coefficient and advance ratio. This approach can be used in design studies where the design point varies without the need for re-generating the propeller map. Furthermore, using this method the unknown map of an existing propeller can be deduced from the map of another propeller of similar technology level but with a different design point. This is a novel approach not existing in the literature.

6.3 Future work

The following aspects could be further pursued in the future in order to improve and continue the work presented in this thesis:

1. The turbofan analysis of chapter 2 uses a conventional two-spool architecture, with the focus being on the thermodynamic aspects of the engine and on the extraction of qualitative trends. The thermodynamic aspects could be further improved by adding the interaction between the component design and their efficiencies assumed in the cycle. The optimisation could be more realistic if a multi-design point approach was used even for the optimisation of the fan pressure ratio, which in this study was only conducted considering the cruise design point. The effect of small size losses and increased cooling requirements could also add value and lead to more quantitative results. The preliminary design aspect could be enriched by investigating different design assumptions and by studying a three-spool or a geared configuration.

2. The secondary power extraction penalties study considers only the impact on the design point of the engine. The analysis could be extended to off-design in order to investigate the effect of the design cycle parameters on the excursions of the component running lines due to the extraction of bleed and power. Finally, in the light of more-electric concepts, a study could investigate what is the potential fuel saving offered by such technologies for different aircraft applications and engine designs.

3. The lifting-line method developed in chapter 4 could be enhanced by adding the effect of Reynolds to the two dimensional airfoil database. Extending the database by including more airfoils and higher accuracy data could also significantly improve the method's predicting capability. The wake representation could be improved by adding a prescribed wake model, enabling this way the prediction at low Mach or even static conditions. Finally, it is very important that the model is extended by adding the capability of modelling contra-rotating fans.

4. The map representation method presented in chapter 5 is based on the hypothesis of similar primary blade characteristics. This means that for the map to be used for two different propellers, these must share the same airfoils and sweep angle distribution. The analysis can thus be extended in order to cover cases where there are gradually more geometrical differences. For example, the effect of increasing the sweep angle can be taken into account for the generation of a more generic Mach number correction curve. On another aspect, the representation proposed can be further elaborated in order to simplify the characteristic curves used and reduce their number, saving this way valuable computer resources. Finally, the

blade optimisations could be repeated by also including the discipline of structural integrity. This would change the optimal chord distribution and thus it would be interesting to see whether the conclusions still remain the same.

References

[1] Advisory Council for Aeronautics Research in Europe (ACARE). European aeronautics: A vision for 2020, January 2001.

[2] N. T. Birch. 2020 vision: the prospects for large civil aircraft propulsion. *Aeronautical Journal*, 104(1038):347–352, 2000.

[3] J. A. Borradaile. Towards the optimum ducted uhbr engine. In *Proceedings of 24th AIAA/ASME/SAE/ASEE Joint Propulsion Conference and Exhibit*, number AIAA-88-2954, Boston, Massachusetts, July 1988.

[4] N. J. Peacock and J. H. R. Sadler. Advanced propulsion systems for large subsonic transports. *Journal of Propulsion and Power*, 8(3), May-June 1992.

[5] D. L. Daggett, S. T. Brown, and R. T. Kawai. Ultra-efficient engine diameter study. Technical Report CR-2003-212309, NASA, 2003.

[6] M. T. Tong. An assessment of the impact of emerging high-temperature materials on engine cycle performance. In *Proceedings of the ASME Turbo Expo*, number GT2010-22361, Glasgow, Scotland, June 2010. ASME.

[7] A. J. B. Jackson. Some future trends in aero engine design for sub-sonic transport. *Journal of Engineering for Power*, 98:281–289, April 1976.

[8] R. A. Zimbrick and J. L. Colehour. An investigation of very high bypass ratio engines for subsonic transports. In *Proceedings of 24th AIAA/ASME/SAE/ASEE Joint Propulsion Conference and Exhibit*, Boston, Massachusetts, July 1988.

[9] V. E. Kyritsis. *Thermodynamic preliminary design of civil turbofans and variable geometry implementation.* PhD thesis, Cranfield University, School of Engineering, Dept of Power and Propulsion, 2006.

[10] C. Riegler and C. Bichlmaier. The geared turbofan technology - opportunities, challenges and readiness status. Technical report, MTU Aero Engines GmbH, 2008.

[11] P. Laskaridis. *Performance Investigations and Systems Integration for the More Electric Aircraft*. PhD thesis, Power and Propulsion Dept., Cranfield University, 2004.

[12] M. A. Dornheim. Electric cabin: The 787 generates at least four times more electricity than normal. traditionally bleed-powered systems now use volts, 28 March 2005.

[13] B. Sweetman. Unlaunched a350 jet takes shape very publicly. *Aviation Week Show News, Paris Air Show 2005*, 13 June 2005.

[14] P. Laskaridis. Effects of engine parameters on secondary power extraction and evaluation of engine performance penalties. In *AIAA 19th International Symposium on Air Breathing Engines (ISABE)*, number ISABE-2009-1275, Montreal, Canada, 2009.

[15] R. Slingerland and S. Zandstra. Bleed air versus electric power off-takes from a turbofan gas turbine over the flight cycle. In *AIAA 7th Aviation Technology, Integration and Operations Conference (ATIO)*, number AIAA 2007-7848, Belfast, Northern Ireland, 2007.

[16] R. Gandolfi, L. F. Pellegrini, and S. de Oliveira. More electric aircraft analysis using exergy as a design comparison tool. In *AIAA 48th Aerospace Sciences Meeting Including the New Horizons Forum and Aerospace Exposition*, number AIAA 2010-809, Orlando, Florida, 2010.

[17] A. J. B. Jackson. *Optimisation of aero and industrial gas turbine design for the environment*. PhD thesis, School of Engineering, Cranfield University, 2009.

[18] R. D. Hager and D. Vrabel. Advanced turboprop project. Technical Report SP-495, NASA, 1988.

[19] M. T. Tong, D. R. Thurman, and M. D. Guynn. Conceptual design study of an advanced open-rotor propulsion system. In *Proceedings of the 20th International Symposium on Air Breathing Engines*, number ISABE-2011-1311, Göteberg, Sweden, September 2011. AIAA.

[20] E. S. Hendricks. Development of an open rotor cycle model in npss using a multi-design point approach. In *Proceedings of ASME Turbo Expo*, number GT2011-46694, Vancouver, Canada, June 2011. ASME.

[21] M. D. Guynn, J. J. Berton, E. S. Hendricks, M. T. Tong, J. W. Haller, and D. R. Thurman. Initial assessment of open rotor propulsion applied to an advanced

single-aisle aircraft. In *11th AIAA Aviation Technology, Integration, and Operations (ATIO) Conference*, Virginia Beach, VA; United States, September 2011. NASA.

[22] A. Seitz, D. Schmitt, and S. Donnerhack. Emission comparison of turbofan and open rotor engines under special consideration of aircraft and mission design aspects. *The Aeronautical Journal*, 115(1168):351–360, June 2011.

[23] A. Seitz. *Advanced Methods for Propulsion System Integration in Aircraft Conceptual Design*. PhD thesis, Technische Universität München, 2011.

[24] C. A. Perullo, J. C. M. Tai, and D. N. Mavris. Effects of advanced engine technology on open rotor cycle selection and performance. In *Proceedings of ASME Turbo Expo*, number GT2012-69331, Copenhagen, Denmark, June 2012. ASME.

[25] R. C. Wilcock, J. B. Young, and J. H. Horlock. Gas properties as a limit to gas turbine performance. In *Proceedings of the ASME Turbo Expo*, number GT-2002-30517, 2002.

[26] A. Guha. Effects of internal combustion and non-perfect gas properties on the optimum performance of gas turbines. *Proceedings of the Inst. of Mechanical Engineers, Part C: J. Mechanical Engineering Science*, 217:1085–1099, 2003.

[27] J. Kurzke. Achieving maximum thermal efficiency with the simple gas turbine cycle. In *Proceedings of the 9th CEAS European Propulsion Forum: "Virtual Engine - A challenge for integrated computer modelling"*, Roma, Italy, October 2003.

[28] P. P. Walsh and P. Fletcher. *Gas turbine performance*. Blackwell Science, 2nd edition, 2004.

[29] A. Guha. Optimization of aero gas turbine engines. *Aeronautical Journal*, 105(1049):345–358, 2001.

[30] H. W. Bennett. Aero engine development for the future. *Proceedings of the Inst. of Mechanical Engineers, Part A: Power and Process Engineering*, 197:149–157, July 1983.

[31] E. Schwartz and C. Hall. Assessment of future aircraft technologies on engine noise and fuel consumption. In *AIAA 18th International Symposium on Air Breathing Engines (ISABE)*, number ISABE-2007-1142, Beijing, China, 2007.

[32] L. R. Jenkinson, P. Simpkin, and D. Rhodes. *Civil jet aircraft design*. Arnold, 1999.

[33] G. C. Oates. *Aerothermodynamics of Gas Turbine and Rocket Propulsion.* AIAA Education Series, Washington, DC, revised and enlarged edition edition, 1988.

[34] A. Guha. Optimum fan pressure ratio for bypass engines with seperate or mixed exhaust streams. *Journal of Propulsion and Power*, 17(5), 2001.

[35] B. G. Bruni. Performance investigations of turbofan aero engines. Master's thesis, School of Engineering, Cranfield University, 2010.

[36] J. Kurzke. Fundamental differences between conventional and geared turbofans. In *Proceedings of ASME Turbo Expo*, number GT2009-59745. ASME, 2009.

[37] R. E. Owens, K. L. Hasel, and D. E. Mapes. Ultra high bypass turbofan technologies for the twenty-first century. In *Proceedings of 26th AIAA/ASME/SAE/ASEE Joint Propulsion Conference*, number AIAA-90-2397, Orlando, Florida, July 1990.

[38] P. H. Young. The future shape of medium and long-range civil engines. *Aeronautical Journal*, February 1979.

[39] G. L. Wilde. Future large civil turbofans and powerplants. *Aeronautical Journal*, 82:281–299, July 1978.

[40] D. J. Karanja and R. A. Harvey. Optimization studies for the pw305 turbofan. In *Proceedings of 26th AIAA/ASME/SAE/ASEE Joint Propulsion Conference*, number AIAA 90-2520, Orlando, Florida, 1990.

[41] J-M. Jacquet and D. L. Seiwert. Methodology for commercial engine/aircraft optimization. In *Proceedings of 29th AIAA/SAE/ASME/ASEE Joint Propulsion Conference and Exhibit*, number AIAA 93-1807, Monterey, CA, 1993.

[42] Cranfield University. *The turbomatch scheme*, October 1999.

[43] W. H. Press, S. A. Teukolsky, W. T. Vetterling, and B. P. Flannery. *Numerical Recipes in Fortran 90.* Cambridge University Press, 1996.

[44] H. I. H. Saravanamuttoo, G. F. C. Rogers, and H. Cohen. *Gas turbine theory.* Prentice Hall, 5th edition, 2001.

[45] P. Lolis. *Preliminary gas turbine weight estimation methods.* PhD thesis, Cranfield University, 2013.

[46] L. Davis, editor. *Handbook of genetic algorithms.* Van Nostrand Reinhold, New York, US, 1991.

[47] M. Gen and R. Cheng. *Genetic algorithms and engineering optimization.* John Wiley and Sons Inc., Chichester, UK, 2000.

[48] J. M. Rogero. *A genetic algorithms-based optimisation tool for the preliminary design of gas turbine combustors.* PhD thesis, School of Engineering, Cranfield University, 2002.

[49] C. Celis. *Evaluation and optimisation of environmentally friendly aircraft propulsion systems.* PhD thesis, School of Engineering, Cranfield University, 2010.

[50] T. Gronstedt. Advanced solvers for general high performance transient gas turbine simulation tools. In *14th International Symposium on Air Breathing Engines*, Florence, Italy, September 1999.

[51] M. W. Whellens, R. Singh, and P. Pilidis. Genetic algorithm based optimisation of intercooled recuperated turbofan design. In *Proceedings of 41st AIAA Aerospace Sciences Meeting and Exhibit*, number AIAA 2003-1210, Reno, Nevada, January 2003. AIAA.

[52] A. Gulati. *An optimisation tool for gas turbine engine diagnostics.* PhD thesis, School of Engineering, Cranfield University, 2001.

[53] S. Sampath. *Fault diagnostics for advanced cycle marine gas turbine using genetic algorithms.* PhD thesis, School of Engineering, Cranfield University, 2003.

[54] M. W. Whellens. *Multidisciplinary optimisation of aero-engines using genetic algorithms and preliminary design tools.* PhD thesis, School of Engineering, Cranfield University, 2003.

[55] P. Jeschke, J. Kurzke, R. Schaber, and C. Riegler. Preliminary gas turbine design using the multidisciplinary design system mopeds. In *Proceedings of the ASME Turbo Expo*, number GT-2002-30496, Amsterdam, The Netherlands, June 2002.

[56] V. E. Kyritsis and P. Pilidis. Performance evaluation for the application of variable turbine-cooling-bleeds in civil turbofans. In *Proceedings of the ASME Turbo Expo*, number GT2007-27224, Montreal, Canada, May 2007.

[57] V. E. Kyritsis and P. Pilidis. Principles of thermodynamic preliminary design of civil turbofan engines. In *Proceedings of the ASME Turbo Expo*, number GT2009-58815, Orlando, Florida, June 2009. ASME.

[58] J. Kurzke. *Preliminary design.* Lecture Series 2002-2003, Aero-engine design: a state of the art. von Karman Institute for Fluid Dynamics, April 2003.

[59] J. Kurzke. Gas turbine cycle design methodology: A comparison of parameter variation with numerical optimization. *Journal of Engineering for Gas Turbines and Power*, 121, January 1999.

[60] S. Kawada. Calculation of induced velocity by helical vortices and its application to propeller theory. Technical Report 172, Aeronautical Research Institute, Tokyo Imperial University, 1939.

[61] J. S. Schutte. *Simultaneous multi-design point approach to gas turbine on-design cycle analysis for aircraft engines.* PhD thesis, Georgia Institute of Technology, 2009.

[62] B. Gunston. *Jane's: Aero-engines.* Jane's Information Group, 2010.

[63] D. Riordan. Environmentally friendly engine nacelle technology development. `http://flygreen.info/wp-content/uploads/2012/10/bombardier_driordan_ppt_w2.pdf`, 2012 (Accessed on 28/04/2013).

[64] S. Lott. One giant leap. `http://www.aero-mag.com/features/19/20121/1206/`, 2012 (Accessed on 28/04/2013).

[65] A. Schonland. The foundation behind the leap-x. `http://airinsight.com/2011/01/31/the-foundation-behind-the-leap-x/`, 2011 (Accessed on 28/04/2013).

[66] Low density materials. `http://www.rolls-royce.com/about/technology/material_tech/low_density_materials.jsp`, Accessed on 28/04/2013.

[67] Leap-x, a trailblazer for tomorrow's aero-engines. `http://www.safran-group.com/IMG/pdf/EN_mag5_p8-9-2.pdf`, 2009 (Accessed on 28/04/2013).

[68] E. S. Arvai. Comparing the new technology narrow-body engines: Gtf vs leap maintenance costs. `http://airinsight.com/2011/11/09/`, 2011 (Accessed on 13/03/2013).

[69] A. G. Hoffman, I. G. Hansen, R. F. Beach, R. M. Plencher, R. P. Dengler, K. S. Jefferies, and R. J. Frye. Advanced secondary power system for transport aircraft. Technical Report 2463, NASA, May 1985.

[70] G.E. Tagge, L. A. Irish, and A. R. Bailey. Systems study for an integrated digital/electric aircraft (idea). Technical Report NASA CR 3840, Boeing Commercial Airplane Company, 1985.

[71] M. J. Cronin, A. P. Hays, F. B. Green, N. A. Radovcich, C. W. Helsley, and W. L. Rutchik. Integrated digital/electric aircraft concepts study. Technical Report NASA CR 3841, Lockheed California, 1985.

[72] R. I. Jones. Considerations of the all electric (accessory) engine concept. *Proceedings of the Institution of Mechanical Engineers, Part G: Journal of Aerospace Engineering*, 209, 1995.

[73] R. I. Jones. The more electric aircraft—assessing the benefits. *Proceedings of the Institution of Mechanical Engineers, Part G: Journal of Aerospace Engineering*, 216(5):259–269, 2002.

[74] G. Codner. The implication of advanced engines for the airframe systems of transport aircraft. Master's thesis, Aircraft Design Dept., Cranfield University, 1988.

[75] G. B. Toyne and G. S. Hodges. 'all-electric' accessory drive systems: Implications on engine design and performance. In *In Auxiliary Power Systems Meeting*, volume AGARD CP-352, Copenhagen, 1983.

[76] H. M. Helm. Study of a zero bleed engine and a new secondary power system for large aircraft. Technical Report RR-PNR-92634, Rolls-Royce plc., 1999.

[77] T. R. Ensign. Sensitivity studies of electric systems on business jet range. In *AIAA 46th Aerospace Sciences Meeting and Exhibit*, number AIAA 2008-147, Reno, Nevada, 2008.

[78] R. D. Archer and M. Saarlas. *An Introduction to Aerospace Propulsion*, chapter 3, pages 68–127. Prentice Hall, 1996.

[79] H. S. Wainauski, C. Rohrbach, and T.A. Wynosky. Prop-fan performance terminology. In *Proceedings of Aerospace Technology Conference and Exposition*, number 871838, Long Beach, California, October 1987. Society of Automotive Engineers.

[80] D. C. Mikkelson, G. A. Mitchell, and L. Bober. Summary of recent nasa propeller research. Technical Report TM-83733, NASA, 1984.

[81] R. Worobel and M. G. Mayo. Advanced general aviation propeller study. Technical Report CR-114289, NASA, April 1971.

[82] D. C. Mikkelson, B. J. Blaha, G. A. Mitchell, and J. E. Wikete. Design and performance of energy efficient propellers for mach 0.8 cruise. Technical Report 770458, Society of Automotive Engineers, 1977.

[83] D. B. Hanson, C. J. McColgan, R. M. Ladden, and R. J. Klatte. Unified aeroacoustics analysis for high speed turboprop aerodynamics and noise. Technical Report CR-185193, NASA, 1991.

[84] Q. R. Wald. The aerodynamics of propellers. *Progress in Aerospace Sciences*, 42:85–128, 2006.

[85] W. J. M. Rankine. On the mechanical principles of the action of propellers. *Trans Inst Naval Architects (British)*, 6(13), 1865.

[86] R. E. Froude. *Trans Inst Naval Architects*, 30:390, 1889.

[87] O. Gur and A. Rosen. Comparison between blade-element models of propellers. *The Aeronautical Journal*, 112(1138):689–704, December 2008.

[88] A. Rosen and O. Gur. Novel approach to axisymmetric actuator disk modeling. *AIAA Journal*, 46(11):2914–2925, November 2008.

[89] H. Glauert. *Aerodynamic Theory: A General Review of Progress*, volume IV, chapter Airplane Propellers, pages 169–310, 341–344. Julius Springer, 1935.

[90] S. Drzewiecki. *Théorie générale de l'hélice.* Gauthier-Villars et cie., Paris, France, 1920.

[91] G. J. D. Zondervan. A review of propeller modelling techniques based on euler methods. Technical Report LR-797, Delft University of Technology, November 1995.

[92] A. Betz and L. Prandtl. Schraubenpropeller mit geringstem energieverlust. Technical report, Goettinger Nachrichten, 1919.

[93] O. Gur and A. Rosen. Optimization of propeller based propulsion system. *Journal of Aircraft*, 46(1):95–106, 2009.

[94] M. A. Takallu and D. M. Dunham. A hybrid method of prediction for propeller performance. In *Proceedings of 28th AIAA Aerospace Sciences Meeting*, number AIAA-90-0440, Reno, Nevada, January 1990. AIAA.

[95] W. Z. Stepniewski and C. N. Keys. *Rotary-Wing Aerodynamics*, chapter 4 - Vortex Theory, pages 141–159. Dover Publications, 1984.

[96] J. D. Anderson. *Fundamentals of Aerodynamics*, pages 668–674. McGraw-Hill International Edition, 4th edition, 2007.

[97] S. Goldstein. On the vortex theory of screw propellers. In *Proceedings of the Royal Society*, volume 123 of *A, Containing Papers of a Mathematical and Physical Character*, pages 440–465, 1929.

[98] Theodore Theodorsen. *Theory of Propellers.* McGraw-Hill Publications in Aeronautical Science, April 1954.

[99] H. V. Borst. Summary of propeller design procedures and data volume i: Aerodynamic design and installation. Technical Report 73-34A, USAAMRDL, 1973.

[100] C. Rohrbach. A report on the aerodynamic design and wind tunnel test of a prop-fan model. In *Proceedings of 12th AIAA/SAE Propulsion Conference*, number AIAA-76-667, Palo Alto, California, July 1976. AIAA.

[101] F. B. Metzger and C. Rohrbach. Aeroacoustic design of the prop-fan. In *Proceedings of the 5th AIAA Aeroacoustics Conference*, number AIAA-79-0610, Seattle, Washington, March 1979. AIAA.

[102] Y. Sandak and A. Rosen. Aeroelastically adaptive propeller using blades' root flexibility. *The Aeronautical Journal*, pages 411–418, August 2004.

[103] R. J. Jeracki and G. A. Mitchell. Low and high speed propellers for general aviation - performance potential and recent wind tunnel test results. Technical Report TM-81745, NASA, 1981.

[104] D. M. Black, R. W. Menthe, and H. S. Wainauski. Aerodynamic design and performance testing of an advanced 30o swept, eight bladed propeller at mach numbers from 0.2 to 0.85. Technical Report CR-3047, NASA, 1978.

[105] C. Rohrbach, F. B. Metzger, D. M. Black, and R. M. Ladden. Evaluation of wind tunnel performance testings of an advanced 45 swept eight-bladed propeller at mach numbers from 0.45 to 0.85. Technical Report CR-3505, NASA, 1982.

[106] C. N. Adkins and R. H. Liebeck. Design of optimum propellers. *Journal of Propulsion and Power*, 10(5):676–682, September-October 1994.

[107] M. Olausson, R. Avellán, N. Sörman, F. Rudebeck, and L. Eriksson. Aeroacoustics and performance modeling of a counter-rotating propfan. In *Proceedings of ASME Turbo Expo*, number GT2010-22543, Glasgow, Scotland, June 2010. ASME.

[108] B. G. McKay. Ideal optimization of counterrotating propellers. In *Proceedings of 24th ASME, SAE, ASEE Joint Propulsion Conference*, number AIAA-1988-2801, Boston, MA, July 1988.

[109] R. E. Davidson. Optimization and performance calculation of dual-rotation propellers. Technical Report TM-1948, NASA, 1981.

[110] W. F. Phillips and D. O. Snyder. Modern adaptation of prandtl's classic lifting-line theory. *Journal of Aircraft*, 37(4):662–670, July-August 2000.

[111] L. Bober and L. Chang. Factors influencing the predicted performance of advanced propeller designs. Technical Report TM-82676, NASA, 1981.

[112] G. L. Stefko, L. J. Bober, and H. E. Neumann. New test techniques and analytical procedures for understanding the behavior of advnaced propellers. Technical Report TM-83360, NASA, 1983.

[113] L. J. Bober. Advanced propeller aerodynamic analysis. Technical report, NASA, 1980.

[114] L. J. Bober and G. A. Mitchell. Summary of advanced methods for predicting high speed propeller performance. In *Proceedings of 18th AIAA Aerospace Sciences Meeting*, number AIAA-80-0225, Pasadena, California, January 1980. AIAA.

[115] J. M. Bousquet. Etude de l'aerodynamique des helices pour avions rapides. In *Proceedings of Advanced Technology for Aero Gas Turbine Components AGARD Conference*, number CP-421. AGARD, 1987.

[116] W. A. Campbell, H. S. Wainauski, and P. R. Bushnell. A report on high speed wind tunnel testing of the large scale advanced prop-fan. In *Proceedings of 24th AIAA/ASME/SAE/ASEE Joint Propulsion Conference and Exhibit*, number AIAA-88-2802, Boston, Massachusetts, July 1988. AIAA.

[117] T. A. Egolf, O. L. Anderson, D. E. Edwards, and A. J. Landgrebe. An analysis for high speed propeller-nacelle aerodynamic performance prediction, volume i: Theory and application. Technical Report CR-169450, NASA, 1988.

[118] J. P. Sullivan. The effect of blade sweep on propeller performance. In *Proceedings of the 10th AIAA Fluid and Plasma Dynamics Conference*, number AIAA-1977-716, Albuquerque, New Mexico, June 1977. AIAA.

[119] J. M. Bousquet. Theoretical and experimental analysis of highspeed propeller aerodynamics. In *Proceedings of 22nd AIAA/ASME/SAE/ASEE Joint Propulsion Conference and Exhibit*, Huntsville, Alabama, June 1986.

[120] J. M. Bousquet. Methodes aerodynamiques utilisees en france pour l'etude des helices pour avions rapides. In *Proceedings of Aerodynamics and Acoustics of Propellers AGARD Conference*, number CP-366. AGARD, 1984.

[121] J. M. Bousquet and P. Gardarein. Recent improvements in propeller aerodynamic computations. In *Proceedings of 18th AIAA Applied Aerodynamics Conference*, number AIAA-2000-4124. AIAA, 2000.

[122] L. Prandtl. Application of modern hydrodynamics to aeronautics. Technical Report TR-116, NACA, 1923.

[123] C. Young. The prediciton of helicopter rotor hover performance using a prescribed wake analysis. Technical Report CP 1341, Aeronautical Research Council, 1976.

[124] R. D. Clark and C. A. Leiper. The free wake analysis. a method for the prediction of helicopter rotor hovering performance. *Journal of the American Helicopter Society*, 15(1):3–11, 1970.

[125] C. S. Chen, H. R. Velkoff, and C. Tung. Free-wake analysis of a rotor in hover. In *Proceedings of 19th AIAA Fluid Dynamics, Plasma Dynamics and Lasers Conference*, number AIAA-87-1245, Honolulu, Hawaii, June 1987. AIAA.

[126] K. Karamcheti. *Principles of Ideal-Fluid Aerodynamics.* Krieger, 1980.

[127] J. G. Leishman. *Principles of Helicopter Aerodynamics.* Cambridge University Press, 2nd edition, 2006.

[128] S. Béchet, C. A. Negulescu, V. Chapin, and F. Simon. Integration of cfd tools in aerodynamic design of contra-rotating propeller blades. In *CEAS 2011 The International Conference of the European Aerospace Societies*, 2011.

[129] C. Burger. *Propeller performance analysis and multidisciplinary optimization using a genetic algorithm.* PhD thesis, Auburn University, Auburn, Alabama, 2007.

[130] G. Iosifidis. Single-rotation advanced performance modelling. Master's thesis, School of Engineering, Cranfield University, 2011.

[131] A. Sanchez-Ortega. Performance modelling of advanced propellers. Master's thesis, Cranfield University, School of Engineering, 2011.

[132] L. L. Erickson. Panel methods - an introduction. Technical Paper 2995, NASA, 1990.

[133] L. Morino, editor. *Computational Methods in Potential Aerodynamics.* Springer-Verlag, 1985.

[134] M. Tremmel, D. B. Taulbee, and J. R. Sonnenmeier. Numerical determination of circulation for a swept propeller. *Journal of Aircraft*, 38(6):1085–1092, November-December 2001.

[135] C. J. Szymendera. Computational free wake analysis of a helicopter rotor. Master's thesis, The Pensylvania State University, Dept of Aerospace Engineering, May 2002.

[136] S. Ananthan, J. G. Leishman, and M. Ramasamy. The role of filament stretching in the free-vortex modeling of rotor wakes. In *Proceedings of the 58th Annual Forum and Technology Display of the American Helicopter Society International*, Montreal, Canada, June 2002. American Helicopter Society.

[137] A. F. Donovan and H. R. Lawrence, editors. *Aerodynamic Components of Aircraft at High Speeds*, volume Volume VII High Speed Aerodynamics and Jet Propulsion. Princeton University Press, 1957.

[138] E. Sand, D. A. Elliott, and H. V. Borst. Summary of propeller design procedures and data volume iii: hub, actuator and control designs. Technical Report 73-34C, USAAMRDL, Fort Eustis, VA, November 1973.

[139] C. M. Maksymiuk and S. A. Watson. A computer program for estimating the aerodynamic characteristics of naca 16-series airfoils. Technical Report TM-85696, NASA, 1983.

[140] O. Gur and A. Rosen. Propeller performance at low advance ratio. *Journal of Aircraft*, 42(2):435–441, March-April 2005.

[141] T. Von Karman. Supersonic aerodynamics - principles and applications. *Journal of the Aeronautical Sciences*, 14(7), 1947.

[142] R. E. Davidson. Linearized potential theory of propeller induction in a compressible flow. Technical Note 2983, NACA, 1953.

[143] V. L. Wells. Propellers in compressible flow. In *Proceedings of 14th Congress of the International Council of the Aeronautical Sciences*, pages 697–707, Toulouse, France, September 1984. ICAS, American Institute of Aeronautics and Astronautics.

[144] J. C. Evvard. Distribution of wave drag and lift in the vicinity of wing tips at supersonic speeds. Technical Report TN-1382, NACA, July 1947.

[145] D. B. Hanson. Compressible helicoidal surface theory for propeller aerodynamics and noise. *AIAA Journal*, 21(6):881–889, June 1983.

[146] D. B. Hanson. Compressible lifting surface theory for propeller performance calculation. *Journal of Aircraft*, 22(1), January 1985.

[147] R. L. Bisplinghoff, H. Ashley, and R. L. Halfman. *Aeroelasticity.* Dover Publications, 1996.

[148] G. L. Stefko and R. J. Jeracki. Wind-tunnel results of advanced high- speed propellers at takeoff, climb, and landing mach numbers. Technical Report TM-87030, NASA, November 1985.

[149] L. J. Bober, D. S. Chaussee, and P. Kutler. Prediction of high speed propeller flow fields using a three-dimensional euler analysis. Technical Report TM-83065, NASA, 1983.

[150] R. J. Jeracki, D. C. Mikkelson, and B. J. Blaha. Wind tunnel performance of four energy efficient propellers designed for mach 0.8 cruise. Technical Report TM-79124, NASA, 1979.

[151] R. M. Plencher, P. Senty, and T.J. Wickenheiser. Propeller performance and weight predictions appended to the navy/nasa engine program. Technical Report TM-83458, NASA, 1983.

[152] S.B.A.C. Standard method of propeller performance estimation. Technical report, Society of British Aircraft Constructors Ltd., 1943.

[153] L. K. Chang and J. P. Sullivan. Optimization of propeller blade twist by an analytical method. *AIAA Journal*, 22(2):252–255, February 1984.

[154] J. Cho and S. C. Lee. Propeller blade shape optimization for efficiency improvement. *Computers & Fluids*, 27(3):407–419, 1998.

[155] P. Giannakakis, P. Laskaridis, and P. Pilidis. Effects of offtakes for aircraft secondary-power systems on jet engine efficiency. *Journal of Propulsion and Power*, 27(5), 2011.